Transport signatures of topological and trivial states in the three-dimensional topological insulator HgTe

Dissertation zur Erlangung des naturwissenschaftlichen Doktorgrades der Julius-Maximilians-Universität Würzburg

vorgelegt von

Valentin Leander Müller

aus Hüttenberg

Würzburg, 2021

This document is licensed under the Creative Commons Attribution-NonCommercial-ShareAlike 4.0 International License (CC BY-NC-SA 4.0): http://creativecommons.org/licenses/by-nc-sa/4.0 This CC license does not apply to third party material (attributed to another source) in this publication.

Eingereicht am: 05.10.2021
bei der Fakultät für Physik und Astronomie

1. Gutachter: Prof. Dr. H. Buhmann
2. Gutachter: Prof. Dr. B. Trauzettel
3. Gutachter:
der Dissertation

Vorsitzende(r): Prof. Dr. P. Jakob
1. Prüfer: Prof. Dr. H. Buhmann
2. Prüfer: Prof. Dr. B. Trauzettel
3. Prüfer: Prof. Dr. F. Reinert
im Promotionskolloquium

Tag des Promotionskolloquiums: 18.02.2022

Doktorurkunde ausgehändigt am: ....

Contents

Acronyms **5**

Summary **7**

Zusammenfassung **9**

1 Introduction **13**
1.1 Motivation 13
1.2 Introducing HgTe as prototypical topological material 14
1.3 Thesis outline 16

I Low-damage lithographic processes for HgTe 19

2 State of the art of lithographic processes in our group **21**
2.1 Introduction 21
2.2 Hall bar standard process: Optical resist mask and ion beam milling 22
2.3 Microstructures: Wet etching 24

3 BaF_2 hard masks for dry etching of HgTe layers **27**
3.1 Deposition of structured BaF_2 hard masks 27
3.2 Removal of BaF_2 hard masks 30
3.3 Application to HgTe Hall bar structures 34

4 Inductively coupled plasma etching for structuring HgTe transport devices **41**
4.1 Introduction to ICP etching 42
4.2 Performance of the etching process and selection of etch mask . . 43
4.3 Comparison with other etching methods 51
4.4 Application to microstructures 55

5 Conclusion: A well-controlled, minimally invasive lithography process for HgTe transport devices **59**

II Surface states in HgTe 3D TIs 61

6 Introduction to HgTe-based 3D TIs **63**
6.1 Overview 63
6.2 Previous work on transport properties of HgTe 3D TIs 63

7 Solving known issues of HgTe 3D TI measurements **67**
7.1 Improving general device quality by introducing thick capping layers 67

7.2 Avoiding destructive lithography processes 70
7.3 Problems with contacting devices in magnetic fields 76

8 Identification and manipulation of topological and trivial surface states in HgTe 3D TIs 81
8.1 Experimental identification of surface states of pristine HgTe layers in low magnetic fields 81
8.2 Manipulating both topological surface states 87
8.3 Comparison of experimental data with k·p calculations including electrostatics 101

9 Interplay of Landau levels in high-quality HgTe 3D TIs 107
9.1 Mutual screening and avoided crossings of Landau levels 107
9.2 Evolution of Landau levels in high magnetic fields 114
9.3 Coexistence of topological surface states and Volkov-Pankratov states 118

10 Conclusion: Refined model for surface state transport in HgTe 123

III Transport properties of HgTe-based microstructures 125

11 Fingerprints of ballistic effects in surface state transport 127
11.1 Signatures of ballistic transport in the semiclassical transport picture 127
11.2 Magnetosize effect in HgTe 3D TI surface state transport 130

12 Temperature-dependent transport in HgTe microstructures: Signatures of intercarrier scattering 139
12.1 Electron-electron scattering and its impact on resistance 139
12.2 Temperature dependence of resistance in HgTe 3D TIs 141
12.3 Temperature dependence in other HgTe systems 159

13 Conclusion and outlook 169

References 173

Appendix 188
Appendix A: Recipes 188
Appendix B: List of material 195
Appendix C: List of samples 196
Appendix D: Details of transport measurements 198
List of publications 200
Acknowledgments 201

Acronyms

2D EG two-dimensional electron gas

2D TI two-dimensional topological insulator

3D TI three-dimensional topological insulator

DOS density of states

DQW double quantum well

EBL electron beam lithography

EBPVD electron beam-physical vapor deposition

FFT fast Fourier transformation

IBE ion beam etching

ICP inductively coupled plasma

LL Landau level

MBE molecular beam epitaxy

PECVD plasma-enhanced chemical vapor deposition

QHE quantum Hall effect

QPC quantum point contact

QSH quantum spin Hall

QW quantum well

RF radio frequency

RIE reactive ion etching

SdH Shubnikov-de Haas

SEM scanning electron microscopy

TI topological insulator

TPVD thermal evaporation

TSS topological surface state

VPS Volkov-Pankratov state

WAL weak anti-localization

WL weak localization

XPS X-ray photoelectron spectroscopy

Summary

The thesis at hand is concerned with improving our understanding of and our control over transport properties of the three-dimensional topological insulator HgTe. Topological insulators are characterized by an insulating bulk and symmetry-protected metallic surface states. These topological surface states hold great promise for research and technology; at the same time, many properties of experimentally accessible topological insulator materials still need to be explored thoroughly. The overall aim of this thesis was to experimentally investigate micrometer-sized HgTe transport devices to observe the ballistic transport regime as well as intercarrier scattering and possibly identify special properties of the topological surface states.

Part I of the thesis presents lithographic developments concerned with etching small HgTe devices. The aim was to replace existing processes which relied on dry etching with high-energy Ar^+ ions and an organic etch mask. This etching method is known to degrade the HgTe crystal quality. In addition, the etch mask turned out to be not durable for long etching processes and difficult to remove completely after etching. First, BaF_2 was introduced as a new etch mask for dry etching to replace the organic etch mask. With common surface characterization techniques like SEM and XPS it was shown that BaF_2 etch masks are easy to deposit, highly durable in common dry etching processes for $Hg_{1-x}Cd_xTe$, and easy to remove in deionized water. Transport results of HgTe devices fabricated with the new etch mask are comparable to results obtained with the old process. At the same time, the new etch mask can withstand longer etching times and does not cause problems due to incomplete removal. Second, a new inductively coupled plasma dry etching process based on CH_4 and Ar was introduced. This etching process is compatible with BaF_2 etch masks and yields highly reproducible results. Transport results indicate that the new etching process does not degrade the crystal quality and is suitable to produce high-quality transport devices even in the micrometer range. A comparison with wet-etched samples shows that inductively coupled plasma etching introduces a pronounced edge roughness. This – usually undesirable – property is actually beneficial for some of the experiments in this study and mostly irrelevant for others. Therefore, most samples appearing in this thesis were fabricated with the new process.

Part II of the thesis details the advancements made in identifying topological and trivial states which contribute to transport in HgTe three-dimensional topological insulators. To this end, macroscopic Hall bar samples were fabricated from high-quality tensilely strained HgTe layers by means of the improved lithographic processes. All samples were equipped with a top gate electrode, and some also with a modulation doping layer or a back gate electrode to modify the carrier density of

the surface states on both sides of the HgTe layer. Due to the high sample quality, Landau levels could be well-resolved in standard transport measurements down to magnetic fields of less than 0.5 T. High-resolution measurements of the Landau level dispersion with gate voltage and magnetic field allowed disentangling different transport channels. The main result here is that the upper (electron) branches of the two topological surface states contribute to transport in all experimentally relevant density regimes, while the hole branch is not accessible. Far in n-regime bulk conduction band states give a minor contribution to transport. More importantly, trivial bulk valence band holes come into play close to the charge neutrality point. Further in p-regime, the strong applied gate voltage leads to the formation of two-dimensional, massive hole states at the HgTe surface. The interplay of different states gives rise to rich physics: Top gate-back gate maps revealed that an anticrossing of Landau levels from the two topological surface states occurs at equal filling. A possible explanation for this effect is a weak hybridization of the surface states; however, future studies need to further clarify this point. Furthermore, the superposition of n-type topological and p-type trivial surface states leads to an intriguing Landau level dispersion. The good quantization of the Hall conductance in this situation indicates that the counterpropagating edge states interact with each other. The nature of this interaction will be the topic of further research.

Part III of the thesis is focused on HgTe microstructures. These "channel samples" have a typical width of 0.5 to 4 µm and a typical length of 5 to 80 µm. The quality of these devices benefits particularly from the improved lithographic processes. As a result, the impurity mean free path of the topological surface state electrons is on the order of the device width and transport becomes semiballistic. This was verified by measuring the channel resistance in small magnetic fields in n-regime. The deflection of carriers towards the dissipative channel walls results in a pronounced peak in the magnetoresistance, which scales in a predictable manner with the channel width. To investigate transport effects due to mutual scattering of charge carriers, the differential resistance of channel samples was measured as a function of carrier temperature. Selective heating of the charge carriers – but not the lattice – was achieved by passing a heating current through the channel. Increasing the carrier temperature has two pronounced effects when the Fermi level is situated in proximity to the bulk valence band maximum where the density of states is large. First, when both topological surface state electrons and bulk holes are present, electron-hole scattering leads to a pronounced increase in resistance with increasing carrier temperature. Second, a thermally induced increase of the electron and hole carrier densities reduces the resistance again at higher temperatures. A model considering these two effects was developed, which can well reproduce the experimental results. Current heating experiments in zero-gap HgTe quantum wells and compressively strained HgTe layers are consistent with this model. These observations raise the question as to how electron-hole scattering may affect other transport properties of HgTe-based three-dimensional topological insulators, which is briefly discussed in the outlook.

Zusammenfassung

Die vorliegende Arbeit beschäftigt sich mit dem dreidimensionalen topologischen Isolator HgTe. Als topologische Isolatoren bezeichnet man Materialien, die in ihrem Inneren elektrisch isolierend sind, auf ihrer Oberfläche jedoch symmetriegeschützte metallische Zustände aufweisen. Diese topologischen Oberflächenzustände sind aufgrund ihrer speziellen Eigenschaften für die Grundlagenforschung und praktische Anwendungen von großem Interesse. Die Erforschung topologischer Isolatoren ist ein relativ junges Forschungsgebiet, sodass viele Eigenschaften dieser Materialien noch besser verstanden werden müssen. Das übergeordnete Anliegen dieser Arbeit war die experimentelle Untersuchung von HgTe Mikrostrukturen mithilfe von Transportexperimenten. Das Ziel war hier, sowohl das ballistische Transportregime als auch die Streuung von Ladungsträgern untereinander zu beobachten und möglicherweise Besonderheiten der topologischen Oberflächenzustände zu finden.

Teil I der Arbeit stellt die Weiterentwicklung lithographischer Prozesse zur Herstellung von HgTe-Mikrostrukturen vor. Der zu Beginn dieser Arbeit genutzte Prozess basierte auf einem Trockenätzprozess mit hochenergetischen Ar^+ Ionen. Dieses Ionenstrahlätzen beschädigt jedoch die HgTe-Kristallstruktur. Zudem war die verwendete organische Ätzmaske nicht sehr widerstandsfähig gegen Ionenbeschuss und nach dem Ätzvorgang nur schwer zu entfernen. Um diese Probleme zu umgehen, wurde zunächst BaF_2 als mögliche Alternative zur bestehenden Ätzmaske untersucht. Mithilfe verschiedener Techniken zur Oberflächencharakterisierung wie SEM und XPS konnte gezeigt werden, dass BaF_2 Ätzmasken einfach herzustellen, sehr widerstandsfähig gegenüber gängigen Trockenätzprozessen für $Hg_{1-x}Cd_xTe$, und leicht in deionisiertem Wasser zu entfernen sind. Probenpaare, die entweder mit der alten oder der neuen Ätzmaske hergestellt wurden, haben vergleichbare Transporteigenschaften. Allerdings ist die neue BaF_2 Ätzmaske deutlich robuster gegenüber Trockenätzprozessen und einfacher zu entfernen, was für die weitere Prozessierung eine entscheidende Verbesserung darstellt. Zusätzlich zur neuen Ätzmaske wurde auch induktiv gekoppeltes Plasmaätzen mit CH_4 und Ar als Prozessgasen eingeführt. Dieses Trockenätzverfahren zeichnet sich durch sehr reproduzierbare Ergebnisse aus. Die Transporteigenschaften der so hergestellten Proben deuten darauf hin, dass induktiv gekoppeltes Plasmaätzen die Kristallqualität nicht merklich beeinträchtigt und dementsprechend auch zur Herstellung kleiner Proben geeignet ist. Der direkte Vergleich mit nasschemisch geätzten Proben zeigt, dass die Kanten der trockengeätzten Proben eine ausgeprägtere Rauigkeit aufweisen. Tatsächlich ist diese – meist unerwünschte – Eigenschaft für einige Experimente in dieser Arbeit von Vorteil oder zumindest nicht problematisch. Die meisten Proben wurden daher mit dem neuen Verfahren hergestellt.

Teil II der Arbeit zeigt detailliert, welche topologischen und trivialen Zustände im dreidimensionalen topologischen Isolator HgTe für den Ladungstransport relevant sind. Die zugrundeliegenden Transportexperimente wurden an qualitativ hochwertigen, makroskopischen „Hall bar“ Proben aus zugverspannten HgTe-Schichten durchgeführt. Auf alle diese Proben wurde eine „Top Gate“-Elektrode aufgebracht. Zusätzlich waren einige Proben mit einer Modulationsdotierung oder einer weiteren „Back Gate“-Elektrode unter der HgTe Schicht ausgestattet, sodass die Ladungsträgerdichte beider topologischer Oberflächenzustände beeinflusst werden konnte. Aufgrund der hohen Probenqualität konnten bereits bei kleinen Magnetfeldern von weniger als 0.5 T Landau-Niveaus aufgelöst werden. Detaillierte Messungen der Landau-Niveaus mit veränderlichen Gatespannungen und Magnetfeldern ermöglichten es, die relevanten Transportkanäle einzeln zu identifizieren. Die wichtigste Erkenntnis ist hierbei, dass die elektronenartigen topologischen Oberflächenzustände in allen experimentell relevanten Dichtebereichen die Transporteigenschaften dominieren, der lochartige Teil dieser Bänder jedoch nicht erreicht werden kann. Weit im n-Bereich werden auch die volumenartigen Zustände des Leitungsbandes besetzt, die jedoch nur einen kleinen Einfluss auf die Transporteigenschaften haben. Die volumenartigen Zustände des Valenzbandes haben hingegen einen großen Einfluss auf Transporteigenschaften, wenn die Gesamtladungsträgerdichte des Systems klein wird. Das Anlegen einer hohen Gatespannung führt weiter im p-Bereich zur Bildung von zweidimensionalen, lochartigen Zuständen an der dem Gate zugewandten HgTe Oberfläche. Aus dem Zusammenspiel dieser Zustände ergeben sich mehrere interessante Effekte: Top- und Back-Gate-abhängige Messungen zeigen deutlich, dass bei gleicher Besetzungszahl die Landau-Niveaus der beiden topologischen Oberflächenzustände nicht direkt kreuzen. Eine mögliche Erklärung für dieses Phänomen ist eine schwache Hybridisierung der Oberflächenzustände, die in weiterführenden Studien genauer untersucht werden sollte. Darüber hinaus führt die Überlagerung von elektronenartigen und lochartigen Zuständen zu einem komplexen Verlauf der Landau-Niveaus im Magnetfeld. Die Hall-Leitfähigkeit ist in dieser Situation exakt quantisiert, was auf eine Wechselwirkung zwischen den gegenläufigen Randzuständen schließen lässt. Eine weiterführende Studie wird sich detaillierter mit dieser Wechselwirkung auseinandersetzen.

Teil III der Arbeit konzentriert sich auf HgTe Mikrostrukturen. Diese „Kanalproben“ haben üblicherweise eine Breite von 0.5 bis 4 µm und eine Länge von 5 bis 80 µm. Die weiterentwickelten lithographischen Prozesse erlauben die Herstellung solcher Strukturen mit ausreichend hoher Qualität, um im n-Bereich das quasi-ballistische Transportregime zu erreichen. Hier liegt die mittlere freie Weglänge von Elektronen in den topologischen Oberflächenzuständen in derselben Größenordnung wie die Kanalbreite. Dies konnte durch Messung des Kanalwiderstands in kleinen Magnetfeldern nachgewiesen werden. Die Ladungsträger werden hierbei zu den Kanalwänden hin abgelenkt und streuen dort vermehrt. Der Magnetowiderstand zeigt dann ein ausgeprägtes Maximum, was vorhersagbar mit der Kanalbreite skaliert. Die Ladungsträger können auch untereinander streuen. Um diesen Effekt zu untersuchen, wurde der differentielle Kanalwiderstand als

Funktion der Ladungsträgertemperatur gemessen. Für diese Messungen wurde ein Heizstrom direkt durch den Kanal geschickt, um die Ladungsträgertemperatur – nicht jedoch die Gittertemperatur – zu erhöhen. Wenn das Fermi-Niveau nah am Valenzbandmaximum mit seiner sehr großen Zustandsdichte liegt, hat die Erhöhung der Ladungsträgertemperatur zwei sehr ausgeprägte Konsequenzen: Zum einen kommt es zu einem starken Anstieg des Widerstands mit steigender Temperatur, verursacht durch die Streuung von Elektronen aus den topologischen Oberflächenzuständen mit Löchern aus dem Valenzband. Zum anderen führt die thermische Umverteilung von Ladungsträgen bei höheren Temperaturen zu einem Abfall des Widerstands. Basierend auf diesen beiden Effekten wurde ein Modell entwickelt, was die experimentellen Beobachtungen zufriedenstellend reproduziert. Dieses Modell fand weitere Bestätigung durch ähnliche Messungen an HgTe Quantentrögen und druckverspannten HgTe Schichten. Diese Ergebnisse führen zu der Frage, inwiefern die Elektronen-Loch Streuung andere Transporteigenschaften des dreidimensionalen topologischen Isolators HgTe beeinflusst. Ein kurzer Ausblick erörtert, wie diese Frage in weiterführenden Studien untersucht werden kann.

1 Introduction

1.1 Motivation

Solid state physics is one of the largest branches of physics and arguably one of the most influential to humankind. The results of this field of research often have direct technological applications. Semiconductor technology, for example, which enabled the rise of compact, yet immensely powerful computers, is directly based on solid state physics. There is still a plethora of fundamental physics principles with unlimited technological potential that wait to be explored more deeply. An example of the latter is the fast-growing field of topological materials. These are materials that are classified by so-called topological invariants. In simple terms, these invariants distinguish whether materials can be continuously transformed into or connected to one another without changing a characteristic property of the material. Topological insulators (TIs) are to date the most extensively studied materials which are best described by such a classification. These materials themselves are insulating, but their electronic structure differs in a subtle way from conventional insulators. If a TI and a conventional, often called trivial, insulator are brought in contact, a metallic state will inevitably form at their interface. In the language of electronic band structures, the bulk band gap (a characteristic property of both materials) must be closed (i. e. vanish) at the interface between the two materials. The metallic surface states which form at the interface due to the band closing are usually referred to as topological surface states (TSSs) to distinguish them from conventional surface states which naturally occur at interfaces.

Why is it so important to investigate TSSs? Take for example a three-dimensional topological insulator (3D TI). It supports on its boundaries two-dimensional TSSs, similar to other two-dimensional electron systems like the ones found in semiconductor heterostructures or graphene. The TSSs, however, come with very special properties: They have a linear energy dispersion, described by the Dirac equation, and their spin is locked to their propagation direction. These properties lead to a suppression of backscattering, resulting in a low material resistance. The spin structure is also extremely interesting for the field of spintronics which is concerned with using the electron spin to process data more efficiently than conventional electronics.

Any application in basic research or technology of course requires first a sound understanding of the systems hosting TSSs. In a nutshell, the thesis at hand is concerned with increasing our knowledge and understanding of TSSs, as well as

improving our ability to control them. More specifically, the thesis tackles the question of how the interaction between charge carriers in the TSSs and other carriers – either from the TSSs or other bands – influences their transport properties. The model system to do so experimentally is HgTe, which will be introduced briefly in the next section.

1.2 Introducing HgTe as prototypical topological material

The development of topological concepts in solid state physics has a long history. In a more general sense the first experimental observation of a TI was the discovery of the quantum Hall state in 1980 [1]. However, what is usually meant nowadays (and throughout this thesis) by the term TI are time-reversal invariant TIs, which were theoretically predicted in 2005/2006 [2, 3]. Soon after, the two-dimensional topological insulator (2D TI) phase of HgTe was predicted and experimentally realized in Würzburg [4, 5]. The concept was extended to three-dimensional systems and the first 3D TI to be confirmed experimentally was $Bi_{1-x}Sb_x$ in 2008 [6]. Already before that, however, it was predicted that strained HgTe also belongs to the class of 3D TIs [7]. The experimental confirmation for this prediction followed in 2011 [8]. After the discovery of TIs, the concept of topological materials has become extremely important in solid state physics and many other topological phases of matter have been predicted and some observed experimentally [9]. Among these are topological semimetals, which can also be realized in HgTe [10]. We nowadays have an extensive theoretical understanding of topological properties of solids, which is in contrast to the relatively small number of experimentally verified topological materials [11]. HgTe is thus an indispensable model system for different topological phases, most importantly the TI phase.

One might wonder at this point: What is it that makes HgTe so versatile in terms of topological phenomena? The special property of HgTe is the unusual ordering of electronic bands, which is brought about by strong relativistic corrections related to the large atomic mass of Hg and Te [12]. Figure 1.1 compares the schematic band structures of the two zinc-blende crystals CdTe and HgTe around the band extrema at the Γ point. The Γ_6 band with s-symmetry forms the conduction band in CdTe and the Γ_8 bands with p-symmetry form the valence band, which is the most common band ordering for zinc-blende crystals [12]. The band gap E_g has a value of roughly 1.6 eV [12]. Next to the band structure is a sketch of how energy levels without relativistic corrections (H_{NR}) are shifted due to these corrections ($H_{\mathrm{NR}} + H_{\mathrm{R}}$), including the Darwin interaction, the mass-velocity interaction, and the spin-orbit interaction [12]. Importantly, though, the ordering of states remains the same. In HgTe, however, the relativistic corrections are strong enough to cause an inversion of the Γ_6 and Γ_8 bands. The "band gap", of roughly -0.3 eV, is often denoted with a negative sign in this case to emphasize this inversion [12]. (Note,

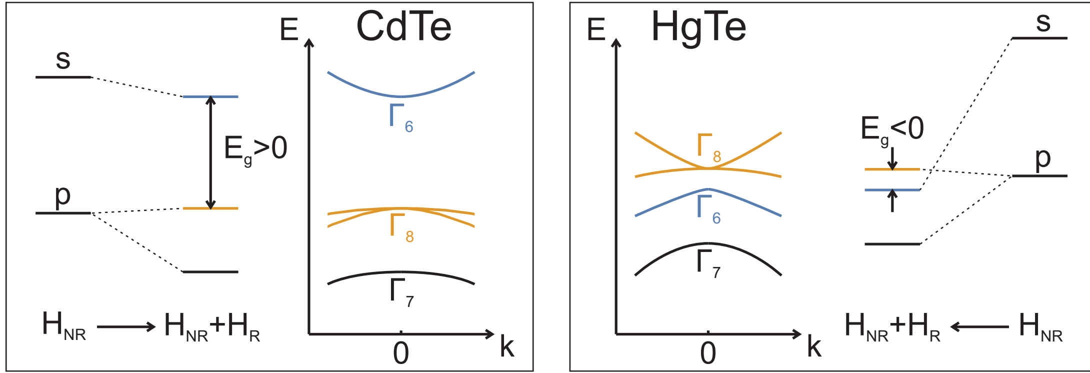

Figure 1.1: Schematic illustration of the band structure in CdTe (left) and HgTe (right) around the Γ point. Also included are the level shifts due to relativistic corrections H_{R}, as compared to the case without relativistic corrections H_{NR}. Figure based on information from References [12] and [4].

however, that the Fermi level is situated at the degeneracy point of the two Γ_8 bands, rendering intrinsic HgTe a semimetal.)

It was already noticed in the 1980s that such a mutual inversion of bands can lead to the formation of special surface states at material interfaces, see e. g. References [13, 14]. However, a band inversion alone does not automatically guarantee a certain topological property. PbTe and SnTe, for example, have mutually inverted bands and yet both materials are not time-reversal symmetric topological insulators [7].[1] A careful analysis – based on determining an appropriate topological invariant – is needed to determine the topological characteristics of the system. This analysis shows that HgTe is in fact a 3D TI once a small band gap is opened[2] between the two Γ_8 bands [7]. CdTe and (the experimentally relevant) $Cd_{0.7}Hg_{0.3}Te$, on the contrary, are trivial insulators. TSSs are thus guaranteed to exist at the interface between HgTe and CdTe or $Cd_{0.7}Hg_{0.3}Te$. The band inversion in HgTe also occurs in thin quantum wells (QWs) above a critical thickness, giving rise to the 2D TI phase of HgTe [4, 5]. A more detailed discussion of topological invariants, often including the specific case of HgTe, can be found in several textbooks and review articles (see e. g. Reference [16]).

Besides its interesting topological properties, there is also a number of practical benefits of working with HgTe. The synthesis of mercury cadmium telluride alloys was first reported as early as 1959 [17]. It turned out that this material system is ideal to build infrared detectors [18], causing intense research related to these alloys. Decades later, we have a number of well-established techniques to fabricate

[1] Note, however, that only PbTe is a topologically trivial material, while SnTe is a crystalline topological insulator [15]. In other words: PbTe and SnTe are topologically distinct, but not in the same way as HgTe and CdTe.

[2] This may be achieved by applying strain and will be discussed in some more detail in Part II of this thesis.

high-quality crystals of $Hg_{1-x}Cd_xTe$. The growth method of choice in our group is molecular beam epitaxy (MBE), which allows the growth of thin $Hg_{1-x}Cd_xTe$ layers and heterostructures thereof (for a general review on MBE, see e. g. Reference [19], and for more details on HgCdTe growth e. g. References [20, 21, 22]). The basis for MBE growth is a crystalline substrate, kept in an ultrahigh vacuum environment to minimize adsorption of residual gas particles. The constituents of the layer to be grown are provided, as a directed beam of neutral atoms or molecules, by appropriate effusion cells. A portion of the effused particles stick to the substrate surface. If the substrate temperature and material fluxes are chosen appropriately, the particles remain mobile to find a suitable position to be incorporated in the crystal growth front. The result is a well-defined crystalline layer, which adopts the lattice structure of the substrate. Substrates for HgTe/CdHgTe heterostructures include commercially available CdTe and CdZnTe wafers [23], as well as a number of virtual substrates, e. g. based on GaAs wafers [20, 21]. MBE growth is indispensable for the preparation of HgTe layers in different topological phases. First, this technique allows for a very accurate control of the layer thicknesses. The layer thickness determines to a large degree the band structure of the system. With MBE it is possible to grow noninverted and inverted QWs, as well as thicker "bulk" layers with 3D character. Second, the MBE-grown layer adopts the lattice constant of the substrate. A slight lattice mismatch between the two thus introduces strain in the grown layer. The latter is necessary to access the 3D TI phase as well as the semimetallic phases of HgTe. Third, the resulting HgTe layers can have an exceptionally high quality. The long impurity mean free path allows the observation of subtle transport features. Furthermore, high-quality HgTe layers have low intrinsic doping, so that the Fermi level can be controlled by means of gate electrodes.

All of these special properties, as well as practical advantages, make HgTe so precious for basic solid state physics research.

1.3 Thesis outline

At the beginning of this PhD project in 2015, the 3D TI phase of HgTe had been well established experimentally by transport experiments with macroscopic Hall bars [8, 24, 25]. The focus of research was thus shifted towards slightly more advanced experiments. These were for example concerned with induced superconductivity [26, 27], thermoelectric properties [28], and ballistic transport effects in small structures [29, 30].

Likewise, the idea for this thesis was to combine another hot topic of contemporary solid state physics with HgTe 3D TIs. It has been established since the 1990s that very clean two-dimensional electron systems can reach a special transport regime, known as "hydrodynamic electron flow" [31, 32], in which transport properties are strongly influenced by intercarrier scattering. This phenomenon has received considerable attention since studies of electron hydrodynamics in graphene

[33, 34] and $PdCoO_2$ [35] were published in 2016. It was suggested by Prof. Dr. Laurens Molenkamp and Prof. Dr. Hartmut Buhmann to check for the occurrence of hydrodynamic electron flow in two-dimensional Dirac systems in zero-gap HgTe QWs and – most important for this thesis – the TSSs of HgTe 3D TIs. We decided to follow the same experimental approach as the one used in the original papers on hydrodynamic electron flow [31, 32]; that is, by measuring the resistance of micrometer sized HgTe devices while changing the electron temperature.

As often in research, even the most straightforward approach can contain a number of unexpected detours. The first step was to develop the lithographic processes necessary to reliably produce high-quality HgTe devices in the micrometer range. A detailed description of lithographic developments made during this project is given in Part I of the thesis. The first experimental results in 3D TI microstructures were exiting, but also difficult to interpret in terms of hydrodynamic electron flow in the TSSs. It was thus necessary to take a step back and develop a model for transport in HgTe 3D TIs, which explicitly takes into account additional states derived from the bulk band structure. Strong experimental evidence for this refined model is presented in Part II of the thesis. This part also contains a short digression on the interplay of different bands in magnetic fields, which raises several questions for further research. Finally, Part III of the thesis focuses on transport properties of HgTe 3D TI microstructures. It includes a short discussion of ballistic transport effects and then focuses on one of the central results of this thesis, which was published already in a peer-reviewed journal [36]: the observation of electron-hole scattering. Each of these parts is almost self-contained and includes both a more detailed topical introduction as well as a conclusion.

The thesis is accompanied by an extensive appendix, which includes details regarding lithographic processes, a list of wafers, a complete list of transport devices which appear throughout the thesis, and details regarding the transport measurements. The list of transport devices also includes dates of when the fabrication of a particular sample started. The reader should note, however, that the order of results in the thesis is not chronological, but intended to be readable and compact.

Part I

Low-damage lithographic processes for HgTe

2 State of the art of lithographic processes in our group

2.1 Introduction

Building well-defined devices out of the high-quality MBE-grown HgTe/CdHgTe[1] heterostructures is one of the most important steps required for research on this material system. The central step is the definition of the device layout itself. A very common and successful approach in semiconductor science to define device layouts is the so-called split gate technology (see e. g. References [37, 38] for important early applications of this technique). In this approach, top gate electrodes are deposited on top of a semiconductor heterostructure. The application of a suitable gate voltage depletes the area beneath the top gates of free charge carriers. The gates can thus define a device structure with a very smooth confining potential, virtually without affecting transport properties of the system (cf. Reference [39]). This elegant approach can not be used for HgTe structures, however. First of all, all HgTe systems of current interest either have a small bulk band gap (compared to potential fluctuations and thermal energy) or are semimetallic to begin with. It is thus not practical to tune the Fermi level in the band gap and in this way fully deplete a region of free charge carriers. Second, the most exciting physics is found in HgTe systems which are topological insulators and as such unavoidably feature gapless states at the surface. In these systems the conducting edge states are defined only by the structure of the HgTe layer itself and cannot be redirected with top gate electrodes (cf. discussion in Reference [40]). Hence, building a device from an extended HgTe/CdHgTe heterostructure layer always includes an etching step to fabricate a so-called mesa structure which includes the remaining (conducting) HgTe layer.

A large variety of etching methods has been developed in order to structure CdHgTe devices, mostly with the goal to produce infrared photodetectors. Etching methods include wet chemical etching, purely physical dry etching, and combined chemical and physical dry etching (see e. g. Reference [41] for an overview). Many of these etching methods can be used also to structure HgTe/CdHgTe heterostructures with the goal to produce devices for transport experiments. Mainly two methods had been in use in our group when the work for the current thesis began: Physical dry etching with high-energy Ar^+ ions and wet chemical etching with an aqueous solution of $KI/I_2/HBr$. The corresponding processes will be introduced in the

[1] "CdHgTe" will henceforth be used as abbreviation for $Cd_{0.7}Hg_{0.3}Te$.

following sections, together with a brief discussion regarding their advantages and disadvantages. As part of this thesis, the existing dry etching process was first modified by introducing BaF_2 as an etch mask (Chapter 3). This new etch mask later allowed the use of a new dry etching technique based on inductively coupled plasma (ICP) etching, which combines chemical and physical dry etching (Chapter 4). Most samples used in this thesis have been prepared with ICP etching.

2.2 Hall bar standard process: Optical resist mask and ion beam milling

The following lithographic process was used in order to fabricate Hall bar samples from HgTe/CdHgTe heterostructures. A very detailed description of this process can be found in Reference [42] and the parameters are listed in Appendix A. The typical sample layout includes two six-terminal devices with dimensions 200 µm × 600 µm and 10 µm × 30 µm in between the voltage probes. Both devices are equipped with a top gate electrode to change the carrier density in the HgTe layer. Starting from an as-grown HgTe/CdHgTe heterostructure, the process includes the following steps:

Mesa The positive-tone resist ECI 3012 (AZ ECI 3012, MicroChemicals GmbH, Ulm, Germany) is structured by means of optical lithography and used as an etch mask to define the mesa. The etching itself is achieved by ion beam etching (IBE) with Ar^+-ions accelerated to 1 keV with a Tectra Gen2 plasma source. The resist mask is stripped by first immersing the sample in Acetone and subsequently in Technistrip (Technistrip P1316, Technic Inc., Cranston (RI), US).

Top gate The mesa is covered in a 110 nm thick SiO_2/Si_3N_4 insulating superlattice, deposited by plasma-enhanced chemical vapor deposition (PECVD) (Plasmalab 80 plus, Oxford instruments, Bristol, UK). This superlattice consists of 11 alternating layers of SiO_2 and Si_3N_4 to reduce strain in the insulating layer and improve adhesion [40]. The negative-tone resist AR-N 4340 (AR-N 4340, Allresist GmbH, Strausberg, Germany) is used for a lift-off process to structure the top gate electrode, consisting of a 5 nm thick Ti sticking layer and a 100 nm thick Au layer, deposited by electron beam-physical vapor deposition (EBPVD). The top gate electrode is covered with the resist ECI 3012 and the part of the insulator layer which covers the ohmic contact regions is removed by wet etching in HF (BOE 7-1, Technic, Noyarey, France).

Ohmic contacts The resist AR-N 4340 is used for a lift-off process to structure the ohmic contacts. Before the deposition of a contact metal, the top cap layer is partially removed by IBE with Ar^+-ions, accelerated to 400 eV. The sample is then transferred in situ to the metallization chamber, where 50 nm

AuGe and 50 nm Au are deposited by EBPVD to contact the HgTe layer. After the lift-off the sample itself is ready.

After this process, the sample is glued to a standardized sample carrier and the contact pads are connected to the contacts on the sample carrier with a thin Au wire by means of wedge bonding. The standardized sample carriers fit on the sample sticks which can be inserted in a cryostat in order to perform low-temperature transport experiments.

This standard Hall bar process is quite reliable, but two issues remain unsolved. The first problem arises from the combination of the organic resist ECI 3012 and IBE with high-energy Ar^+ ions. This purely physical etching mechanism attacks the resist and for extended etching times can cause the formation of bubbles. In these spots the underlying heterostructure is partially etched as well, which destroys the device. Another resist-related issue is the redeposition of etched material (most likely Cd and Te in unknown composition) and resist hardening at the sides of the resist mask. When most of the etch mask is removed in acetone, these hardened sidewalls often remain on the sample and may cause serious problems for the gate structure (including inhomogenous gating, poor insulator adhesion, and discontinuous, i. e. disconnected, gold layers). As discussed in References [42, 43], the sidewalls can often be removed with Technistrip, an aggressive stripping agent. This chemical occasionally also attacks the HgTe/CdHgTe heterostructure itself and it seems desirable to avoid its use entirely. A new etch mask for dry etching of HgTe/CdHgTe heterostructures was needed and a possible solution will be presented in Chapter 3 of this thesis.

The second problem arises from the etching process itself, independent of the etch mask. HgTe and CdHgTe are very sensitive materials due to the high volatility of Hg. IBE with high-energy Ar^+ ions provides sufficient energy to Hg atoms that they can diffusive into the surrounding material, which causes p-to-n type conversion [44, 45] and possibly an overall degradation of the crystal quality. These damages extend both vertically and laterally over the range of several micrometers [44, 45]. Reference [42] discusses in detail that this lateral damage severely degrades the quality of HgTe/CdHgTe transport devices along the mesa edge. In micrometer-sized samples the damaged layer can extend over the full width of the device and generate a variety of artifacts. In thin HgTe QWs the main artifacts are a dramatic decrease in the charge carrier mobilities and deviations from proper quantization in the quantum spin Hall (QSH) regime [46]. As will be discussed in Section 7.2, several pronounced artifacts are also observed in thick ($\approx$ 70 nm) HgTe layers. Different etching techniques were thus needed in order to avoid this problem. To this end, Bendias et al. have implemented a wet etching process which will briefly be described in the following section. An alternative approach is the use of a noninvasive dry etching technique as presented in Chapter 4 of this thesis.

2.3 Microstructures: Wet etching

The most common wet etching processes for CdHgTe utilize Br_2-based chemistry [41], which is disadvantageous for practical as well as principle reasons [42]. The process implemented by Bendias et al. is based on an aqueous I:KI:HBr solution [47]. It is used heavily in our group to fabricate micrometer-sized HgTe transport devices, typically six-terminal Hall bar structures. The definition of a micrometer-sized HgTe mesa structure by wet etching usually consists of two steps:

Inner mesa The PMMA etch mask (AR-P 679.03, Allresist GmbH, Strausberg, Germany) is prepared on top of the HgTe/CdHgTe heterostructure by low-energy electron beam lithography (EBL) (extraction voltage of 2.5 kV). The PMMA exposed to electron irradiation is dissolved in the developer. During this step only the innermost part of the device mesa is structured, typically restricted to a write field with approximate dimensions of 200 µm × 200 µm. Right before the etching step the natural oxide on top of the CdHgTe cap layer is removed in diluted HF. Subsequently, the wet etching step is performed under a constant vertical flow of fresh etchant onto the sample surface. The sample is immersed in etchant throughout the etching process. The etchant is a solution of $(KI_{4.15\,g}/I_{2,\,0.1\,g}/HBr_{12.5\,ml})_{to\ 50\,ml\ H_2O}$ 1:8 H_2O. Etching is stopped in H_2O and the mask is stripped in acetone.

Outer mesa Only the innermost part of the final device is structured in the first etching step. All of the surrounding area still contains the conducting HgTe layer, most of which needs to be removed in a second etching step. The etch mask can be prepared by means of optical lithography using the resist ECI 3012. The inner mesa is completely covered by the etch mask, which additionally defines the outer mesa, including bond pads and leads to the inner mesa. The etching step is performed with the same wet etchant as in the previous step. Etching is stopped in H_2O and the mask removed in acetone.

These two steps are necessary to structure the device mesa, and are therefore comparable to the first process step in the standard Hall bar process. Further steps crucially depend on the particular device that is fabricated. Usually the process continues with the fabrication of AuGe/Au ohmic contacts and a top gate electrode (both may include EBL and optical lithography, cf. Appendix A).

The main advantage of this wet etching process is that it does not affect the unetched HgTe/CdHgTe heterostructure unlike IBE for example. Wet etching also results in very smooth mesa edges which presumably reduces scattering at the device walls. It even allows the fabrication of nanometer-sized structures like quantum point contacts (QPCs) without a loss of material quality [48]. This etching method is thus the method of choice whenever the main imperative is to preserve the layer's quality.

However, wet etching also has a number of drawbacks worth mentioning. First of all, the etching is almost isotropic, so that a certain amount of lateral etching will always occur. This has to be taken into consideration when designing the etch mask and every variation of etch depth will lead to changes in lateral device dimensions. Second, our wet etching process is diffusion-controlled [42], so that the etch rate is enhanced in the vicinity of the etch mask edge [49]. Narrow trenches are thus etched considerably faster than wide areas [42]. The combination of isotropic etching and mask-dependent inhomogeneities implies that the etching process needs to be optimized whenever the device layout is changed. For complicated device geometries or situations where structural fidelity is the main imperative, the wet etching process might not be ideal. Third, the etch rate critically depends on several details of the process and the samples. These details include the exact time between preparation of the etch solution and the etching process, the exact shape of the sample and its positioning in the flow of etchant, and the presence of contaminations (such as In, which is used as glue on the back side of the wafers during MBE growth of the heterostructure).

Especially the last issue – poor reducibility – was mostly unsolved when the work for the current thesis began and even most pronounced in samples with thick HgTe layers and large device dimensions such as in macroscopic Hall bar structures. For some of the experiments in this thesis it also seemed beneficial to have samples with rough edges to enhance diffusive boundary scattering (see Chapters 11 and 12). It was thus decided that a minimally invasive dry etching technique for HgTe/CdHgTe should be implemented as well, details of which are found in Chapter 4 of this thesis.

3 BaF_2 hard masks for dry etching of HgTe layers

The search for a new etch mask for dry etching of HgTe/CdHgTe layer stacks was guided by several requirements:

- The mask should be easy to fabricate and ideally suitable for defining both large and small structures.
- The mask material should be durable when exposed to IBE with Ar^+ ions in order to achieve a good selectivity over HgTe/CdHgTe and enable long etching times.
- The etch mask should be easy to remove completely without the need of aggressive chemicals that may harm the heterostructures.
- The new process should avoid the use of dangerous chemicals.

Since the 1980's, metal fluorides – including BaF_2 – have been used as etch masks for dry etching of common semiconductor materials. Most studies focused on the possibility to use metal fluorides as EBL resist (see e. g. References [50, 51]), but in some studies the masks were structured with conventional lift-off processes [52, 53]. Metal fluorides are favorable as mask material, since they are easy to deposit as thin films, adhere well to untreated surfaces of many semiconductor materials, and are very resistant in common dry etching processes [52]. The latter implies that rather thin etch masks are sufficient for long etching steps, which completely avoids the issue of sidewall formation. BaF_2 in particular has the advantage that it is soluble in water and thus easy to remove [53]. These advantages were the reason for Dr. J. Kleinlein to suggest BaF_2 as an etch mask for dry etching of HgTe/CdHgTe heterostructures.

Some of the following results have been obtained together with J. Strunz and have been included in his Master's thesis [54].

3.1 Deposition of structured BaF_2 hard masks

Thin BaF_2 films can be deposited by various techniques, including EBPVD and thermal evaporation (TPVD). In our group, BaF_2 layers are deposited in a home-built vapor deposition chamber at a base pressure of 5×10^{-5} mbar. BaF_2 grains (99.9 %, 3 to 6 mm, ChemPUR GmbH, Karlsruhe, Germany) are heated either

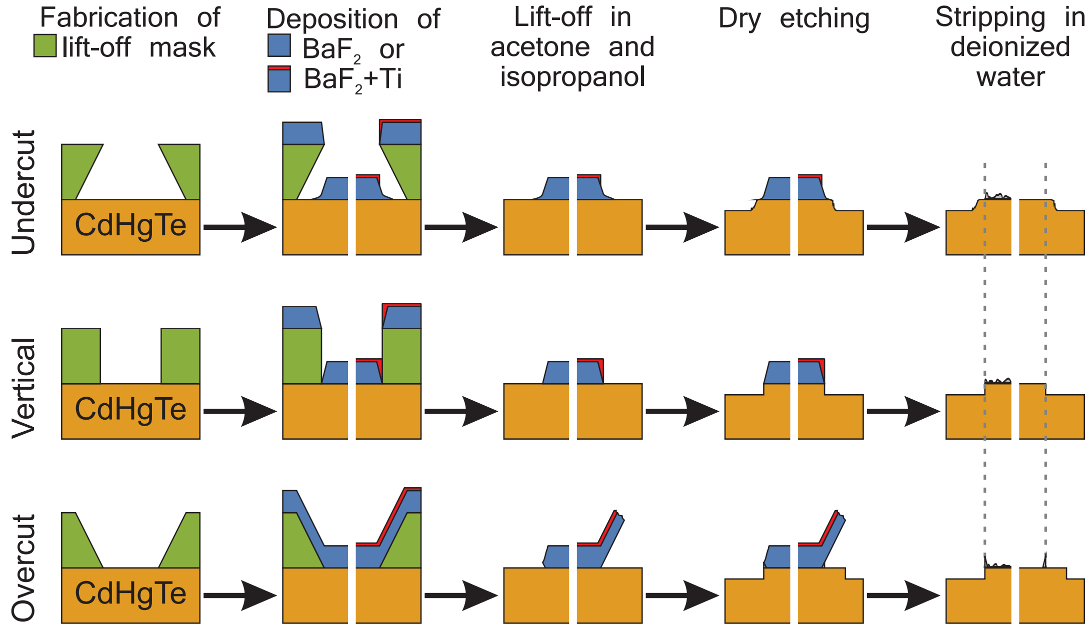

Figure 3.1: Schematic depiction of lift-off processes used to structure BaF_2 etch masks and the resulting structure after etching and BaF_2 removal.

thermally or by means of electron bombardement (e-gun: AP&T HVP4, acceleration voltage 7.8 kV), until a stable evaporation rate is monitored by means of a quartz microbalance mounted in the vicinity of the sample. To make the deposition process as reproducible as possible, the sample is always kept at room temperature and the deposition rate is tuned to $\approx 1\,\text{nm/s}$. X-ray photoelectron spectroscopy (XPS) measurements show that the thin films prepared in this way contain both Ba and F (cf. Figure 3.4 and related discussion). Typical BaF_2 layer thicknesses are on the order of 100 nm, which is sufficient for most etching processes. For certain processes it is beneficial to reinforce the BaF_2 layer in situ with a thin layer of Ti ($\approx 10\,\text{nm}$). The BaF_2 layers obtained in this way adhere well to HgTe, CdHgTe, and Si (with SiO_2 termination). The layers do not detach from the surface when rinsing the samples with acetone or isopropanol, even under ultrasonic excitation.

The good adhesion and stability in common organic solvents allow the use of well-established lift-off processes to structure BaF_2 layers. Figure 3.1 schematically shows this approach. In the first step, a lift-off mask is structured, which covers the whole sample surface except the parts where the BaF_2 mask is supposed to cover the sample later on. Then BaF_2 is deposited and if necessary also covered in situ with a thin Ti sheet. The lift-off mask as well as the BaF_2 on top of it are removed with a suitable solvent. The remaining BaF_2 mask has the desired shape, can be used during the etching process, and is removed subsequently. The properties of the BaF_2 etch mask depend to a certain degree on the exact profile of the lift-off mask, as will be explained in the following. The most common optical resist for

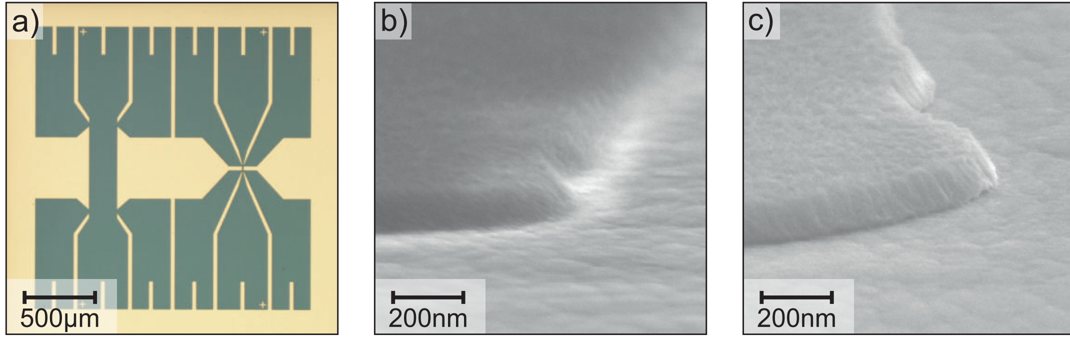

Figure 3.2: Nominally 100 nm thick BaF_2 etch masks, structured with lift-off processes. a) Optical microscopy image of a BaF_2 mask in the shape of the standard Hall bar design, prepared with an AR-N 4340 lift-off mask. b) SEM image of a BaF_2 mask prepared with AR-N 4340 lift-off mask. c) SEM image of a BaF_2 mask prepared with ECI 3012 lift-off mask. SEM images are taken with the SE2 detector at an acceleration voltage of 20 kV, a working distance of 10 mm, and under an angle of approximately 80°.

lift-off processes in our group is the negative-tone resist AR-N 4340. Using the standard deposition parameters (see Appendix A) this resist has a thickness of ≈ 1.3 µm and, depending on the development time, a large undercut (i. e. negative edge profile) on the order of 1 µm. A common EBL resist for lift-off processes is PMMA 950 K 3 % (AR-P 679.03, Allresist GmbH, Strausberg, Germany). Using the standard deposition parameters (see Appendix A), this resist has a thickness of only ≈ 160 nm and a smaller undercut. Another optical resist that can be used for a lift-off process is the positive tone resist ECI 3012. It is not ideal for this purpose, since it has a positive edge profile instead of an undercut. With standard parameters it has a thickness of ≈ 1.4 µm. For these three resist masks, the lift-off is done in acetone under ultrasonic excitation to avoid redeposition of BaF_2 flakes. Subsequently the sample is rinsed in isopropanol and blown dry with a nitrogen spray gun to avoid drying residues on the sample surface. Further process details are listed in Appendix A.

Figure 3.2a) shows an optical image of a BaF_2 mask with nominal thickness of 100 nm, prepared with an AR-N 4340 lift-off mask and EBPVD. The shape of the mask is the standard Hall bar design[1], with two six-terminal devices (the bigger one on the left, the smaller one on the right). A high-resolution SEM image of such a BaF_2 mask is shown in b), in direct comparison to a BaF_2 mask prepared with the ECI 3012 resist shown in c).[2] Clearly visible are the grainy structure of

[1]The current "standard Hall bar design" in our group is an 8-terminal Hall bar device and thus differs from Figure 3.2a). Throughout this thesis, the term "standard Hall bar design" refers to the old standard design, which is shown in Figure 3.2a).

[2]Note that Figure 3.2b) and c) show 90° corners of structures similar to those in a). In the

the layers, which have previously been reported to have a typical grain size of 30 to 100 nm [51, 52]. Also visible is the pronounced sidewall slope that is characteristic for patterned fluoride layers [51]. In the case of the positive tone resist, c), the BaF_2 mask has a sharp and well-defined edge. However, the positive edge profile frequently causes problems due to remaining sidewalls as sketched in the bottom row of Figure 3.1. In the case of the negative resist, Figure 3.2b), the mask seems to gently fall off towards the substrate. The latter is likely caused by diffusion of a small amount of BaF_2 in the shadow region of the resist mask with large undercut. As sketched in the top row of Figure 3.1 and shown explicitly in the context of ICP etching (cf. Figure 4.3) this effect can result in a sloped mesa edge, which is beneficial for further processing steps. At the same time it can cause the formation of hillocks around the mesa, which may be detrimental to transport properties (cf. Section 4.3). The cleanest results can be obtained by using a resist with a vertical edge profile as sketched in the center row of Figure 3.1. In practice, the aforementioned EBL process with a small undercut corresponds to this situation.

On the whole, it is fairly straightforward to produce high-quality BaF_2 etch masks of arbitrary shape on CdHgTe (and other substrates, including Si) by means of standard evaporation and lift-off processes.

3.2 Removal of BaF_2 hard masks

One of the major advantages of BaF_2 etch masks is that they can be removed in deionized water without the need of aggressive stripping agents [51]. If a thin Ti reinforcement layer on top of BaF_2 is used, it will detach from the surface as well, similar to a normal lift-off process. The result of this gentle stripping process can be inspected by means of SEM imaging and XPS measurements. SEM imaging is extremely useful to detect residues, such as remaining particles, which do not form a closed film but rather alter the surface topography of the mesa. XPS measurements on the contrary are very useful to detect closed layers of residues by revealing the elements present at the sample surface [56]. XPS is an extremely surface-sensitive technique [57], meaning that a residual layer of even a few nanometers in thickness can be reliably detected. Optical microscopy images are of course also useful, but usually do not provide sufficient resolution to detect small amounts of residues.

Figure 3.3a) shows an optical image of a mesa structure fabricated with a BaF_2 etch mask and IBE after removal of the etch mask in water. The central mesa structure appears homogeneous and bright, similar to the etched parts. Also in higher magnifications (not shown), there are no signs of sidewalls or incomplete mask removal.

Figure 3.3b) shows a SEM image of a mesa structure fabricated with a BaF_2+Ti etch mask and ICP dry etching after removal of the etch mask. The edged part (left

SEM images they appear rounded, however. This is due to diffraction of light at the optical mask, which reduces the structural fidelity of the resulting resist mask [55]. It is important to note that the rounded corners are not related to the use of BaF_2.

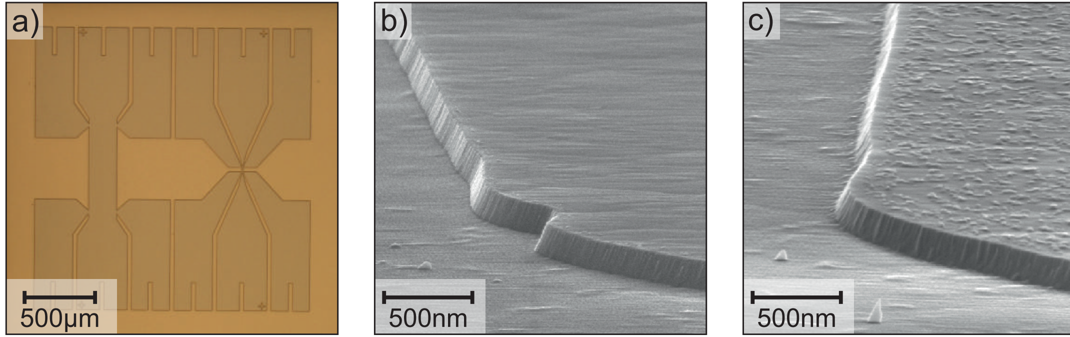

Figure 3.3: Mesa structures after removal of a BaF_2 etch mask in deionized water. a) Optical microscopy image of a HgTe/CdHgTe mesa structure after IBE dry etching and removal of the BaF_2 etch mask. Same sample as shown in Figure 3.2a). b) SEM image of a CdHgTe mesa edge after ICP dry etching and removal of the BaF_2+Ti etch mask. c) SEM image of a CdHgTe mesa edge after ICP dry etching and removal of the BaF_2 etch mask. SEM images are taken with the In-Lens detector at an acceleration voltage of 20 kV, a working distance of 6 mm, and under an angle of approximately 80°.

lower half of the image) as well as the mesa surface (right upper half of the image) have a similar appearance. They show similar surface corrugations, which are comparable to the corrugations found in as-grown samples. Except for some small spots right at the mesa edge the mesa surface appears to be clean. No obvious mask residues are visible. For comparison, Figure 3.3c) shows an SEM image of a mesa structure, where mask residues are found. It has been fabricated with a BaF_2 etch mask (without an additional Ti layer) and ICP dry etching. The mask has been partially removed in deionized water. The etched parts look very similar to those in Figure b), while the mesa surface clearly shows mask residues which were not removed during the stripping procedure. This comparison demonstrates that SEM imaging is well-suited to detect mask residues. As will be discussed in more detail in Section 4.2.2, the difficulties in stripping appear only after ICP etching when no additional Ti layer is used. When pure BaF_2 etch masks are used for IBE, stripping in deionized water does not leave mask residues on the mesa surface.

Further XPS measurements have been performed to check whether the BaF_2 layer can be removed completely in water and whether the sample surface is altered by deposition and removal of BaF_2. Figure 3.4 shows XPS spectra of a MBE-grown CdHgTe layer and a commercially available Si substrate before deposition and after removal of a BaF_2 layer. These spectra are compared to the XPS spectra of BaF_2 layers on CdHgTe. The Si substrate is included in this discussion since it has a relatively simple XPS spectrum which makes it easier to detect BaF_2 residuals. XPS measurements were performed in a customized measurement setup (x-ray source: Riber CX700, analyzer based on Omicron parts), at a base pressure

of 5×10^{-10} mbar. The samples were excited with Al K_α X-rays with an energy of 1486.6 eV. Only the spectrum shown in Figure 3.4d) had to be recorded with Mg K_α X-rays with an energy of 1253.6 eV due to a failure of our Al anode. The spectra were recorded in an energy range of 0 eV to 1100 eV with a step size of 0.5 eV and an integration time of either 10 s or 20 s per data point. In order to correct for charging effects, the spectra are shifted so that the binding energy of the contaminant C 1s peak falls onto 284.8 eV. To enhance the ease of interpretation the Si and CdHgTe spectra are normalized to the height of the O 1s or the Cd $3d_{5/2}$ peak, respectively, and vertically shifted with respect to each other. If not otherwise mentioned, peak identification is accomplished by comparison with spectra from Reference [56].

The XPS spectrum of a 100 nm thick BaF_2 layer deposited on CdHgTe is shown in Figure 3.4b). One can identify the Ba 4d, Ba 4p, Ba 4s, Ba 3d (splitted into $3d_{5/2}$ and $3d_{3/2}$), and Ba $3p_{3/2}$, as well as the F 1s core level principal peaks. Furthermore, some Ba MNN and F KLL Auger transitions are resolved. There are also some less pronounced peaks visible, which are roughly 233 eV above the main peaks described before. They are most likely caused by ionization due to Mg K_α X-rays, which is a common artifact of X-ray sources with two anode materials [56].

The XPS spectra of p-type Si and CdHgTe before deposition and after removal of a BaF_2 based etch mask are shown in Figures 3.4a) and c). The Si sample was covered with a nominally 100 nm thick BaF_2 layer. The CdHgTe sample was covered with 100 nm of BaF_2 and 20 nm of Ti, and exposed to our ICP etching process prior to removal of the BaF_2+Ti layer in water. For the Si substrate with native oxide, the Si 2p, Si 2s, and O 1s core level principal peaks as well as corresponding plasmon loss lines can be observed. Furthermore, some O KLL Auger transitions are resolved. For the CdHgTe substrate, the assignment of peaks is complicated by the fact that some of the core level peaks partly overlap with each other. The most prominent features, however, can be identified as Cd 3d (splitted into $3d_{5/2}$ and $3d_{3/2}$), Cd 3p (splitted into $3p_{3/2}$ and $3p_{1/2}$), Hg 4f (splitted into $4f_{7/2}$ and $4f_{5/2}$), Hg 4d (splitted into $4d_{5/2}$ and $4d_{3/2}$), O 1s, Te 4d, Te 3d (splitted into $3d_{5/2}$ and $3d_{3/2}$), and Te 3p (splitted into $3p_{3/2}$ and $3p_{1/2}$) core level peaks. Also visible, but more difficult to assign unambiguously are the overlapping Te 3s and Te MNN peaks as well as the O KLL Auger transitions. The two Te 3d core level principal peaks are notably splitted into two pairs of peaks (cf. inset in c), with a zoom-in). This feature is commonly observed in CdHgTe XPS spectra with native oxide and occurs due to two different chemical states of Te [58]. The peaks corresponding to Te-O bonds are shifted about 3.2 eV towards higher binding energies as compared to those corresponding to Te-Cd and Te-Hg bonds [58].

The most important result from the XPS experiments is that no traces of BaF_2 are found on the Si and CdHgTe surfaces after the removal step in water. This becomes evident from the absence of any Ba or F core level peaks, which are very prominent in the spectrum of the pristine BaF_2 layer (cf. gray vertical lines in Figure 3.4). Even a very thin remaining layer of BaF_2 residues will lead to notable modifications of the Si and CdHgTe XPS spectra. This statement is supported

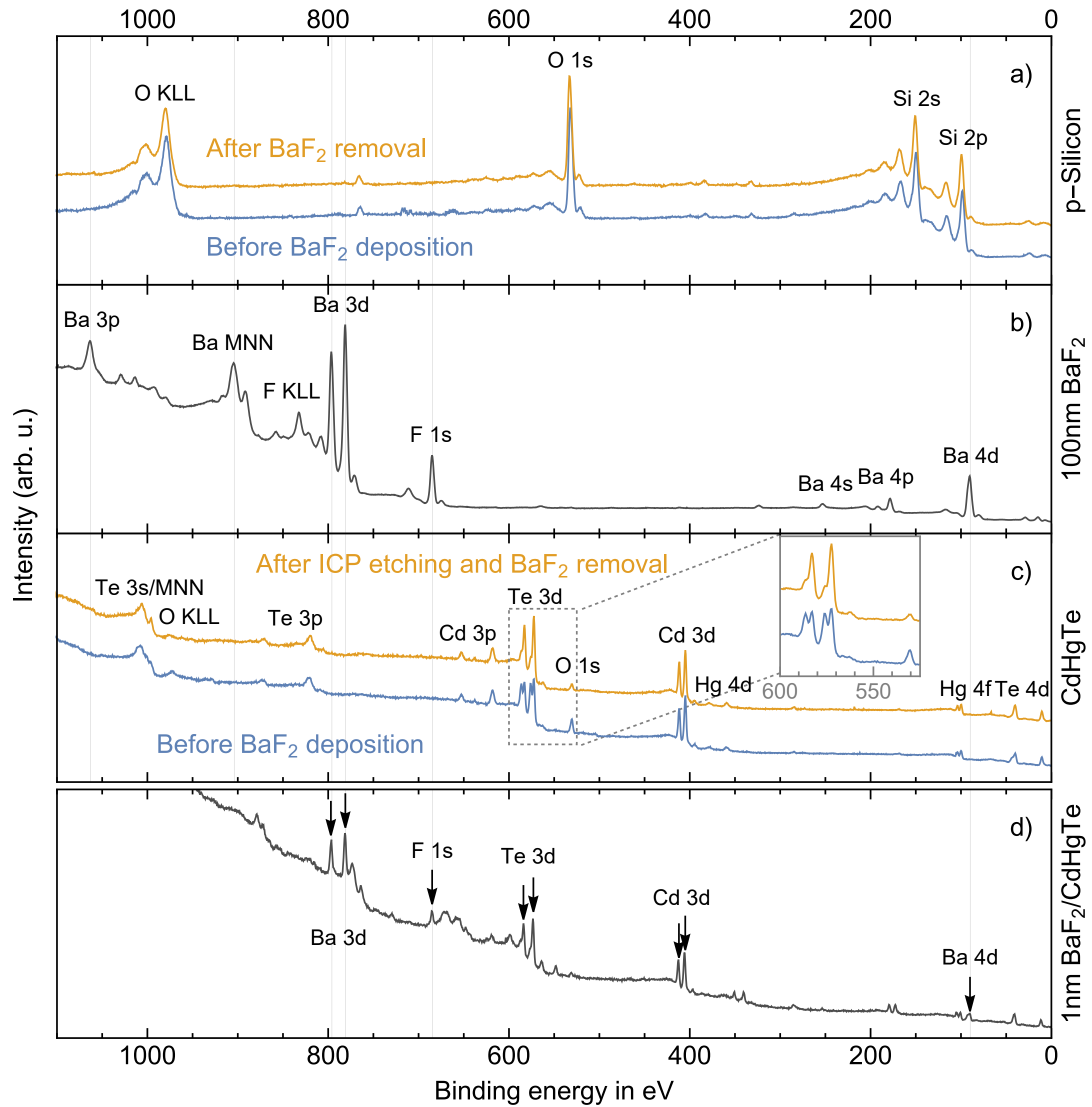

Figure 3.4: XPS spectra of a Si wafer (a) and a MBE-grown CdHgTe layer (c) before deposition (blue line) and after removal (orange line) of a BaF_2 (+Ti) layer. The inset in c) shows a zoom of the CdHgTe spectra. Also shown for comparison are the XPS spectra of BaF_2 layers deposited on CdHgTe with a nominal thickness of 100 nm (b) and 1 nm (d). Important core level principal peaks and Auger transitions are indicated.

by Figure 3.4d), which shows the spectrum of a CdHgTe layer with a nominally 1 nm thick BaF_2 layer. One can clearly identify the pronounced Ba 4d, Ba 3d, and F 1s core level peaks, proving the existence of a BaF_2 layer. At the same time one can distinguish the Te 3d and Cd 3d core level peaks of the underlying substrate, proving that the BaF_2 layer has indeed a thickness of at most a few nanometers. Furthermore, the spectra of the Si and the CdHgTe surfaces are qualitatively left unchanged by the deposition and removal of the BaF_2 hard mask. Only in the case of CdHgTe there are some quantitative differences concerning the Te 3d and O 1s peaks: The O 1s peak and the chemically shifted Te 3d peaks, related to Tellurium Oxides, are less pronounced. Both changes indicate that the amount of TeO_2 has been reduced. The reason cannot be identified at this point because contact to BaF_2 as well as immersing the sample in water [59] might be the cause for a removal of surface oxides. A mild oxygen plasma cleaning step might be sufficient to restore the surface oxide.

On the whole, the results of SEM imaging and XPS inspection of the CdHgTe surfaces before deposition and after removal of BaF_2 proof that a BaF_2 hard mask system can be removed simply by immersing the sample in deionized water. The same holds true for untreated Si surfaces, which demonstrates that BaF_2 hard masks may also be used on other substrate materials. This gentle, yet efficient stripping procedure is the key advantage of BaF_2 as hard mask material.

3.3 Application to HgTe Hall bar structures

After exploring how BaF_2 layers can be structured, and verifying that they can be removed completely, the new etch mask can be incorporated in an existing lithography process. The transport devices fabricated with the new lithography process can then be characterized thoroughly and compared with devices that have been fabricated with the already established process.

The new BaF_2 hard mask can be easily incorporated into the previously developed standard Hall bar process (see Section 2.2), based on dry etching a mesa with Ar^+ ion milling. Only the steps for structuring the sample mesa need to be adapted. Instead of the ECI 3012 optical resist, the etch mask is obtained by using the AR-N 4340 lift-off resist to structure a 100 nm thick BaF_2 layer. The BaF_2 layer has low ion sputter yields [52], so that this mask is very resistant to ion milling. For IBE with 1 kV Ar^+ ions the etch rate of BaF_2 is on the order of 0.25 nm/s. This value corresponds to a selectivity better than 1 : 3 compared to CdHgTe and 1 : 6 compared to HgTe. After removal of the etch mask in deionized water, the sample needs to be cleaned in a mild oxygen plasma. This cleaning step is necessary for two reasons: First, the optical resist AR-N 4340 leaves a thin layer of residues in the unexposed areas (i. e. the area below the BaF_2 layer, which after etching is equivalent to the mesa area). This problem is unrelated to BaF_2 and occurs in related lithography processes with AR-N 4340 as well (e. g. when the AR-N 4340 is used as etch mask for wet etching of the SiO_2/Si_3N_4 superlattice

insulator). These residues lead to poor adhesion of the PECVD gate insulator, which can result in gate rip-offs and device failure. Second, the surface of the etched areas is not terminated with native oxide after the etching process. In the old Hall bar process it was suggested to let the sample oxidize in ambient conditions for at least one night, since the PECVD insulator adheres better to the oxidized surface. The oxygen plasma cleaning step in the modified process reliably oxidizes the etched areas and makes this step less time-consuming and more reproducible. A summary of the new Hall bar process including a BaF_2 dry etch mask is provided in Appendix A with all process parameters.

The similarity between the old and the new Hall bar process makes it possible to fabricate sample pairs, which differ only in the etch mask for dry etching (and mask-related processing steps, e. g. stripping of the mask after etching). Most process steps can be done with both samples simultaneously, including the dry etching with high-energy Ar^+ ions and the metallization steps. Transport properties of these samples can then be compared and significant differences may be attributed to the differing process steps. For these tests it is beneficial to work with HgTe QWs slightly above the critical thickness (i. e. in the inverted regime). The main reason is that layers of this thickness are relevant for many experiments in our group concerned with 2D TIs. They are readily available in high quality also for the purpose of lithography tests. Furthermore, they offer a simple band structure (at least in n-regime, cf. Section 12.3.1) which facilitates a quantitative assessment of sample quality.

A Hall bar device (sample *QC0333 HB 1*), which is ready for measurements, is shown on the left side of Figure 3.5. The upper half of the visible structures belongs to the big Hall bar, with dimensions of $W \times L = 200\,\mu\text{m} \times 600\,\mu\text{m}$ between voltage probes. The central structure with golden color is the top gate electrode (TG), the darker green frame is the insulator, which protrudes under the gate electrode. The darker golden structures on the outside are the AuGe/Au ohmic contact pads, numbered from 1 to 6. The lower half of the structures belongs to the small Hall bar, with dimensions $10\,\mu\text{m} \times 30\,\mu\text{m}$ between voltage probes. Also visible are the Au bond wires, which connect the sample to the standardized chip carrier (not visible). This chip carrier can be inserted into the sample stick and placed in a cryostat to do low-temperature transport measurements. The right side of Figure 3.5 shows a schematic of the typical measurement circuit. An excitation voltage V_{exc} is applied to send a small current through the sample and a reference resistor R_{ref} with known resistance. The measured voltages V_{ref}, V_{xx}, and V_{xy} contain information about the current through the sample $I = V_{\text{ref}}/R_{\text{ref}}$, the longitudinal resistance $R_{\text{xx}} = R_{\text{ref}} V_{\text{xx}}/V_{\text{ref}}$, and the transverse (Hall) resistance $R_{\text{xy}} = R_{\text{ref}} V_{\text{xy}}/V_{\text{ref}}$. Technical details regarding transport measurements can be found in Appendix D. A magnetic field B can be applied perpendicular to the HgTe plane (which is the orientation of choice throughout this thesis). In the classical Drude model for two-dimensional charge carriers the longitudinal and

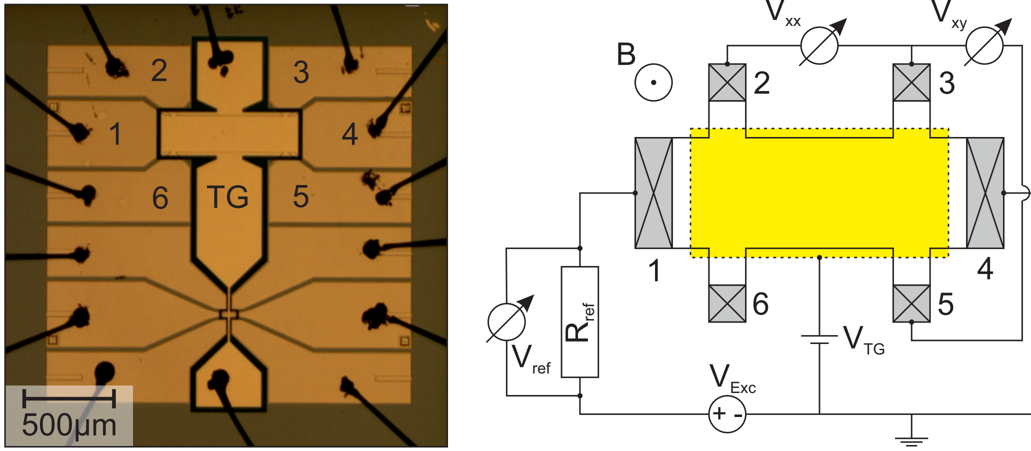

Figure 3.5: (Left) Optical microscopy image of a HgTe Hall bar device (sample *QC0333 HB 1*), ready for transport measurements. Superimposed numbers (1-6) refer to ohmic contacts, (TG) refers to the top gate electrode. (Right) Schematic of the typical measurement circuit, including the externally applied excitation voltage V_{exc}, the top gate voltage V_{T} and magnetic field B. Measured voltages are V_{ref}, V_{xx}, and V_{xy}.

transverse resistances in a magnetic field are given by [60]

$$R_{\text{xx}} = \frac{L}{W} \times \rho_{\text{xx}} = \frac{L}{W} \times \frac{1}{en\mu} \tag{3.1}$$

$$R_{\text{xy}} = \rho_{\text{xy}} = \frac{B}{en}, \tag{3.2}$$

where e is the elementary charge, n is the charge carrier density, and μ the carrier mobility. ρ_{xx} and ρ_{xy} are the entries of the resistivity tensor. The carrier density can be found from a measurement of R_{xy} in small magnetic fields and Equation 3.2. With this information and R_{xx} at zero magnetic field one can then calculate the mobility via Equation 3.1.

Figure 3.6 compares results of transport measurement for two samples, *QC0332 HB 1* and *QC0332 HB 2*, which have been fabricated using either the old ECI 3012 etch mask (*HB 1*) or the new BaF_2 etch mask (*HB 2*) for the dry etching step. Following the etching of the mesa and removal of the etch mask, all processing was done in parallel for these two samples. The samples contain a 8 nm thick HgTe QW, encapsulated in 100 nm thick CdHgTe bottom and top barrier layers. Figure 3.6a) shows the longitudinal resistance of these samples as a function of top gate voltage. Sample *QC0332 HB 1* (ECI 3012) has a slightly higher resistance at all gate voltages. The hysteresis-free gate range, which can be addressed without introducing a permanent density shift [61, 62] is slightly higher in the ECI 3012 sample (±2 V as compared to -2 to 1 V in the BaF_2 sample). Also

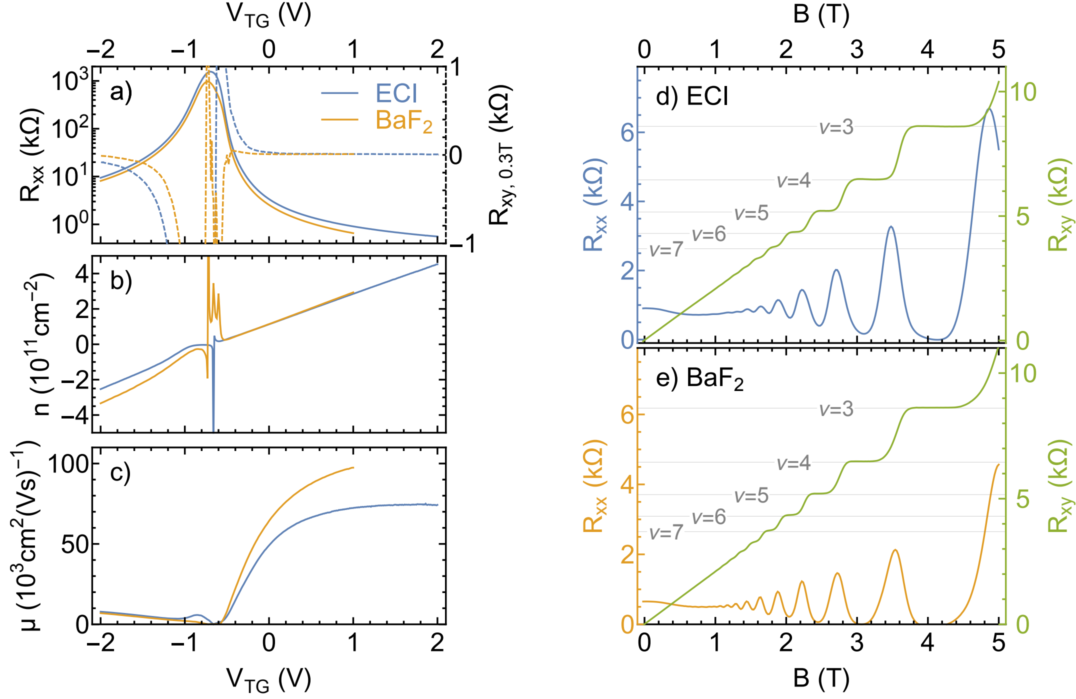

Figure 3.6: Transport characteristics of HgTe 2D EG samples *QC0332 HB 1* and *QC0332 HB 2* processed using an ECI 3012 etch mask or a BaF_2 etch mask. a) Longitudinal resistance R_{xx} (solid lines) at zero magnetic field and transverse resistance R_{xy} (dashed lines) at a magnetic field of 0.3 T as a function of top gate voltage V_{TG}. b) and c) Total carrier density n and carrier mobility μ as a function of V_{TG}. d) and e) R_{xx} and R_{xy} as a function of magnetic field B for samples *QC0332 HB 1* and *QC0332 HB 2*, respectively. Vertical lines and indices ν indicate quantum Hall plateaus. All measurements were done at 4.2 K.

shown is the transverse resistance at a perpendicular magnetic field of 0.3 T. The transverse resistance and Equation 3.2 provide an estimate of the total carrier density at all gate voltages. The results are shown in Figure 3.6b). In overall n-regime ($V_{TG} \gtrsim -0.5\,\mathrm{V}$), the density to gate relation is very linear and can be analyzed with a linear fit. The gate action, i. e. density shift per gate voltage, is $(1.73 \pm 0.05) \times 10^{11}\,\mathrm{cm^2V^{-1}}$ for *HB 1* and $(1.788 \pm 0.005) \times 10^{11}\,\mathrm{cm^2V^{-1}}$ for sample *HB 2*. The zero density point (found by extrapolating the linear fit) is at $(-0.6 \pm 0.1)\,\mathrm{V}$ for *HB 1* and $(-0.62 \pm 0.03)\,\mathrm{V}$ for *HB 2*. The indicated errors are the deviation between measurements with differing contact pairs (on the same Hall bar structure), since these exceed other uncertainties by at least one order of magnitude. The estimated carrier mobilities, found from the density data and Equation 3.1, are shown in Figure 3.6c). As expected from the lower resistance, the BaF_2 sample has a slightly higher mobility in n-regime. When the Fermi level is in the bandgap or in overall p-regime ($V_{TG} \lesssim -0.5\,\mathrm{V}$) the values for the total

density and carrier mobility are not reliable due to division by zero or a nonlinear transverse resistance due to the complex valence band structure (cf. Section 12.3.1). The small deviations between the samples in this gate regime are thus difficult to interpret.

Another important criterion for the sample quality are transport results in high magnetic fields. Figures 3.6d) and e) show the longitudinal and transverse resistance for both samples at a gate voltage of 1 V up to a magnetic field of 5 T. Up to roughly 1 T, the longitudinal resistance decreases slightly in both samples and the transverse resistance increases linearly. For higher fields, both samples enter the quantum Hall effect (QHE) regime: The longitudinal resistance shows pronounced Shubnikov-de Haas (SdH) oscillations, accompanied by a step-like increase of the transverse resistance. The QHE is caused by the formation of Landau levels (LLs) in sufficiently clean samples in high magnetic fields. This behavior is equally observed in both samples, irrespective of the etch mask used.

On the whole, the two samples *QC0332 HB 1* and *QC0332 HB 2* display very similar transport properties. The small variations in carrier mobility and accessible hysteresis-free density range may be caused by slight quality variations in the sample wafer, e. g. due to a inhomogeneous distribution of defects. In order to consolidate this result, it is necessary to consider several sample pairs and compare a representative set of sample properties. A suitable choice of sample properties is given in the following:

Carrier density with grounded top gate. It is determined from a Hall measurement, which is done directly after cooling the sample to liquid Helium temperature and before applying a finite top gate voltage. Statistically meaningful differences between samples with differing etch masks may indicate that the change in lithography induces n- or p-doping.

Carrier mobility at a specified carrier density of $2 \times 10^{11}\,\mathrm{cm}^{-2}$. The latter is important, since the mobility is usually depending on the carrier density, cf. Figure 3.6c). Differences in the carrier mobility may indicate the formation of potential fluctuations and defects due to changes in the lithography process. This value is extracted from the gate-dependent longitudinal and transverse resistance data at zero magnetic field and 0.3 T, cf. Figures 3.6a) through c) and related explanations.

Uncertainties are estimated as the maximum deviation between the results from differing contact pairs. These exceed all other experimental uncertainties by at least one order of magnitude.

Table 3.1 shows these properties for five sample pairs, including the two samples from wafer *QC0332* which were mentioned before. All wafers contain a HgTe layer with a nominal thickness of 7.5 to 9.2 nm and cap layers with a nominal thickness of 42 to 100 nm. All samples contain a big Hall bar (“gHB”) and a small Hall bar (“kHB”). Only one structure, the kHB of *QC0327* fabricated with the ECI resist, could not be measured due to a short between two contacts.

Sample		$n_{\text{gnd}}^{\text{BaF}_2}$ $10^{11}\,\text{cm}^{-2}$			$n_{\text{gnd}}^{\text{ECI}}$ $10^{11}\,\text{cm}^{-2}$			μ^{BaF_2} $10^3\,\text{cm}^2(\text{Vs})^{-1}$			μ^{ECI} $10^3\,\text{cm}^2(\text{Vs})^{-1}$		
QC0327	gHB	1.98	±	0.07	0.72	±	0.06	165	±	7	221	±	5
	kHB	2.55	±	0.04	-	±	-	86	±	4	-	±	-
QC0331	gHB	2.65	±	0.01	1.72	±	0.05	99.7	±	0.5	105	±	6
	kHB	2.07	±	0.05	1.59	±	0.08	51	±	2	51	±	7
QC0332	gHB	1.99	±	0.04	1.2	±	0.2	89	±	5	71	±	9
	kHB	2.10	±	0.02	0.81	±	0.09	47	±	2	45	±	6
QC0333	gHB	3.58	±	0.08	1.7	±	0.3	120	±	4	152	±	3
	kHB	4.0	±	0.2	1.0	±	0.1	94	±	7	92	±	30
QC0336	gHB	0.52	±	0.09	1.18	±	0.04	130	±	40	235	±	40
	kHB	0.32	±	0.02	1.28	±	0.02	140	±	30	151	±	30

Table 3.1: Transport characterization data for sample pairs, fabricated either with a BaF_2 or an ECI 3012 etch mask. n_{gnd} is the carrier density at grounded top gate and μ is the carrier mobility at a carrier density of approximately $2 \times 10^{11}\,\text{cm}^{-2}$.

The first important observation is that both lithography processes yield reasonable sample properties: None of the measured structure has an extremely high ground density (i. e. exceeding $10 \times 10^{11}\,\text{cm}^{-2}$) or an extremely low carrier mobility (i. e. falling short of $10 \times 10^3\,\text{cm}^2(\text{Vs})^{-1}$), which would be problematic for most experiments.

A quantitative comparison within the individual sample pairs does not give a clear trend for either process. The ground density is higher in four of the BaF_2 samples as compared to the ECI samples. The opposite is the case in sample pair *QC0336*. The differences in the ground density seem dramatic for some sample pairs (cf. *QC0333*). However, there is also a considerable variation of values when comparing gHB and kHB on the same sample, as for example in *QC0333*. This variation is surprising, since the values are extracted from measurements performed directly after the cooldown, before applying a finite voltage to the top gate. The reason for this is unclear as of now. It is important to note in this context that a sample may show a certain density shift from cooldown to cooldown as well (personal observation). One possible explanation is that the contact to the gate electrode is lost during the cooldown from room temperature to liquid Helium temperature. This can happen due to different thermal expansion of the sample holder and the metal pins which connect to the chip carrier. Insulating behavior is sometimes observed when monitoring the contact resistances during cooldown (personal observation). In this case, the gate would not be grounded all the time and electrostatic charging could induce a persistent change of the potential landscape. Another possible explanation for deviations between gHB and kHB are inhomogeneities in the samples themselves. The values which are extracted by measuring differing contact pairs always deviate to a certain degree. It is possible that variations occur across the full wafer, so that different sample

pieces have slightly different properties.

The second set of transport parameters are the carrier mobilities. Also these do not show a clear trend in favor of either lithography process. In the big Hall bar structures, the mobilities are either higher in the ECI samples (*QC0327*, *QC0333*, *QC0336*), higher in the BaF_2 samples (*QC0332*) or the same within experimental uncertainty (*QC0331*). In the small Hall bar structures, the carrier mobilities are always reduced with respect to the big Hall bars and the same (within experimental uncertainty) for both lithography processes. The similarity in the carrier mobilities indicates that both lithography processes preserve the sample quality in a similar manner.

On the whole, the two lithography processes for fabrication of gated HgTe Hall bar structures both yield working samples. Neither of the two processes shows obvious advantages in terms of sample quality. If any, there might be a tendency that the BaF_2-based process slightly increases the ground density, but not to a worrying degree. A more thorough investigation of this effect would require to first understand and reduce sample-to-sample as well as cooldown-to-cooldown variations of the measured transport parameters. The BaF_2 etch mask has the crucial advantage that it withstands long etch times, notably without mask failure or formation of problematic sidewalls. Based on the results presented in this section, the BaF_2 Hall bar process had been chosen as standard process in our group. It was in use for fabrication of characterization samples from 2016 to 2019.[3]

[3] The standard process was then changed to a wet-etching process. The reason for this choice was that dry etching with high-energy Ar^+ ions induces a number of artifacts as explained in more detail in Sections 4.3 and 7.2.

4 Inductively coupled plasma etching for structuring HgTe transport devices

At the beginning of my PhD project, our group's standard etching technique of dry etching with high-energy Ar^+ ions had already been suspected to induce artifacts. Thus, a novel wet etching process was introduced. However, this wet etching process did not get fully developed at the time. Furthermore, it has some principal limitations that have been discussed in Section 2.3.

A widely used etching method for CdHgTe in industrial applications is nowadays reactive ion etching in high-density plasmas, commonly achieved in ICP plasma sources [63]. Such an etching process has several advantages:

- The combination of physical and chemical dry etching requires only low ion energies, thus avoiding a type conversion as seen in purely physical dry etching of CdHgTe and HgTe.

- Dry etching processes are suitable for achieving a high anisotropy, which avoids lateral etching and thus favors structural fidelity.

- Precise control over the process parameters and the etch duration results in a high reproducibility and user independence of dry etching methods.

- Dry etching is also convenient from a practical point of view, since handling of dangerous chemicals (such as HBr) is not necessary.

For the particular project presented in this thesis, ICP etching was also favored for another reason: Dry etching usually results in rough mesa sidewalls and thus diffusive boundary scattering. As explained in Chapters 11 and 12, enhanced boundary scattering may allow the observation of several interesting physical phenomena in micrometer-sized structures. It was thus an obvious choice to introduce an ICP-based etching process for our HgTe/CdHgTe heterostructures. The following chapter is concerned with the basic properties of this etching process and the performance of devices fabricated with this process. Some of the results have been obtained together with J. Werther and have been included in his Bachelor's thesis [64].

4.1 Introduction to ICP etching

ICP etching relies on the generation of a quasi-neutral plasma by inductive power transfer to the process gas. Our ICP etching process for CdHgTe/HgTe was developed by Oxford Instruments and uses Ar and CH_4.

The principle of ICP plasma generation and etching will be briefly explained in the following, based on the much more detailed treatment in References [63] and [65], and the actual geometry and process in our ICP tool. Figure 4.1 shows a schematic drawing of our ICP tool (PlasmaPro 100, Oxford instruments, Bristol, UK). Ar gas is introduced to the sample chamber via a showerhead gas inlet. A radio frequency (RF) power at 13.56 MHz is applied to the ICP coil, which is wound around the upper part of the sample chamber. The AC electromagnetic field accelerates electrons while the much more massive ions can hardly respond to this excitation. A small amount of gas atoms dissociate spontaneously. Collisions of accelerated electrons with neutral gas atoms further increase the degree of dissociation and lead to the formation of a high-density plasma. The RF power is coupled inductively to the plasma, which may be regarded a coil with a single turn. The gas inlet for methane is close to the sample table to avoid excessive formation and deposition of hydrocarbon polymers.

The rather fast electrons in the plasma have a higher probability of reaching the chamber walls than the heavy (and slow) ions. This leads to the formation of positively charged sheath regions, where the net concentration of positively charged ions exceeds the concentration of negatively charged electrons. As a consequence, ions are accelerated towards the chamber walls and the sample. This acceleration can be quantified via the potential difference across the sheath regions, usually called “DC bias” U_{DC}. This DC bias can be further enhanced and controlled by capacitively coupling RF power to the sample electrode (i. e. the sample table). This

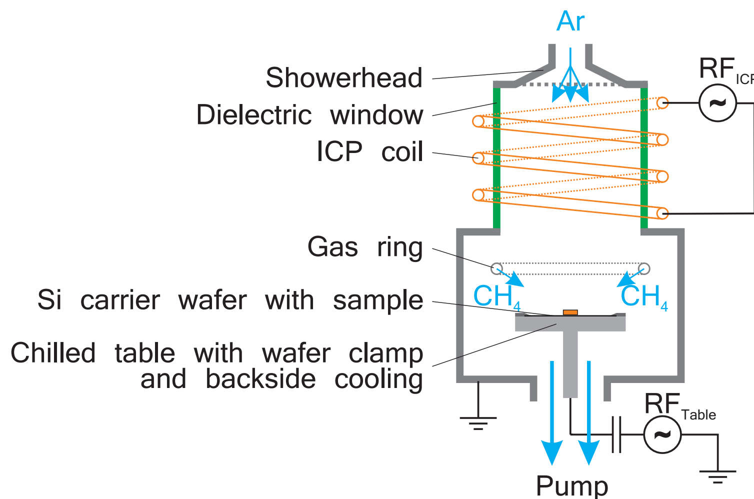

Figure 4.1: Schematic drawing of our ICP tool (dimensions not to scale).

DC bias is crucial in many dry etching applications, since it provides directionality – and thus anisotropy – to the etching process. In the particular case of etching CdHgTe/HgTe, it is equally important that the ion energy does not exceed the threshold for inducing lateral damage to the crystal. The latter is known to occur for ion energies exceeding approximately 100 eV [41]. The process parameters for our ICP etching process are adjusted so as to yield a DC bias of 20 to 30 V. The possibility to separately tune and control the plasma density and the DC bias is the main advantage of ICP tools over other tools used for reactive ion etching (such as the parallel-plate reactive ion etching (RIE) system) [65].

ICP etching of HgCdTe has been intensively studied in the past and details of the etching mechanisms have been determined for a wide selection of gas compositions (see e. g. References [66, 67, 68, 69, 70]). In the case of a CH_4/Ar gas mixture, the etching most likely proceeds via two processes. First, CH_3, CH_3^+, and H radicals generated through dissociation of CH_4 react with Hg, Cd, and Te to form volatile compounds [67, 69]. The rate limiting step of this chemical etching is removal of Cd [69, 70]. Second, the low-energy Ar ions physically remove CdHgTe constituents and the polymer film which is continuously deposited as a byproduct of CH_4 dissociation. The latter is very important, since the undesired polymer film would otherwise block the chemical etching process [67]. A certain amount of Hg may spontaneously leave the surface [67]. This process is capable of etching $Cd_xHg_{1-x}Te$ for all values of x and is thus suitable for etching CdHgTe/HgTe heterostructures.

All of the results in this thesis were obtained with the following process parameters provided by Oxford instruments. Very similar processes have been used in References [71, 72, 73] for etching HgCdTe. The process gases Ar and CH_4 are provided in a gas flow ratio of 20 to 1 (20 sccm Ar and 1 sccm CH_4) while the chamber pressure is set to 13 mbar. The RF power provided to the coil is 1000 W and the power provided to the sample table 15 W, resulting in a usual DC bias between 20 and 30 V, but not exceeding 35 V. The samples are glued to a Si carrier wafer with a thermoplastic mounting adhesive (Crystalbond 509, Aremco Products Inc., Valley Cottage (NY), US) to improve thermal coupling. The temperature of the sample table onto which the Si carrier wafer is clamped is kept at 0 °C.

4.2 Performance of the etching process and selection of etch mask

4.2.1 Surface stoichiometry

When introducing a new etching process, it is important to understand changes made to the etched surface. Ideally, the etching process should not alter the surface stoichiometry. Investigation of the etched surface can easily be accomplished by means of XPS (cf. Section 3.2). Figure 4.2 shows XPS spectra of a MBE-grown CdHgTe layer, before and after being exposed to our ICP etching process for 40 s.

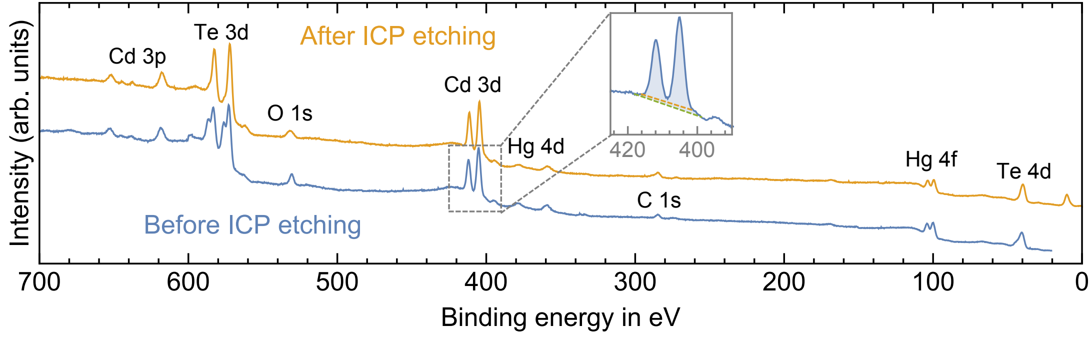

Figure 4.2: XPS spectrum of a CdHgTe layer, either as grown (blue line) or after exposure to a ICP etching process for 40 s (orange line). The most pronounced core level principal peaks are indicated. The inset indicates how to estimate the integrated peak intensity.

Peak	Energy eV	$A_{\mathrm{peak}}/A_{\mathrm{Cd\,3d}} \cdot 100.0$ (before ICP)	$A_{\mathrm{peak}}/A_{\mathrm{Cd\,3d}} \cdot 100.0$ (after ICP)
Cd $3p_{1/2}$	653	9.2 – 12.6	9.9 – 12.2
Cd $3p_{3/2}$	618	23.6 – 25.7	27.0 – 28.4
Te $3d_{5/2}$/Te $3d_{3/2}$	573/584	211.3 – 226.0	190.8 – 200.9
O 1s	531	14.1 – 16.6	12.5 – 13.5
Cd $3d_{5/2}$/Cd $3d_{3/2}$	404/412	(100.0)	(100.0)
Hg $4d_{3/2}$	378	8.1 – 10.9	5.9 – 7.9
Hg $4d_{5/2}$	359	12.3 – 12.7	9.3 – 9.9
C 1s	285	3.9 – 4.6	8.3 – 8.5
Hg $4f_{7/2}$/Hg $4f_{5/2}$	100/104	24.7 – 28.3	17.6 – 20.1
Te 4d	40	26.9 – 28.5	23.8 – 25.9

Table 4.1: Relative peak areas of the core level peaks in Figure 4.2.

In between the growth and the first XPS measurement, the sample was exposed to ambient conditions for several hours to oxidize the surface. After the ICP etching step and prior to the second XPS measurement, the sample was rinsed in acetone, isopropanol, and deionized water. This was necessary to remove the thermoplastic mounting adhesive from the backside of the sample before mounting it in the XPS measurement chamber. The sample was excited with Al K_α X-rays with an energy of 1486.6 eV. The spectra were recorded in an energy range of 0 eV to 700 eV with a step size of 0.25 eV and an integration time of 10 s per data point. One of the spectra (blue) does not extend all the way to 0 eV due to a failure of the high voltage power supply. The energy axis was adjusted, so that the C 1s peak falls onto 284.8 eV. The spectra were normalized to the Cd 3d peak and stacked for clarity.

The spectrum of the untreated CdHgTe surface (blue) is very similar to the ones discussed in detail before (see Figure 3.4). The important result is that the

spectrum acquired after exposing the surface to the ICP etching process (orange) is still very similar to the one of the untreated surface. Qualitatively, one can still identify peaks corresponding to Cd, Hg, and Te. Clearly visible are also the O 1s and the C 1s peaks. There are mainly two minor changes: First, the chemically shifted Te 3d peaks are less pronounced after the ICP etching, indicating a reduction in the amount of Tellurium oxide at the surface. Most likely, the sample was not kept at ambient conditions long enough to allow the formation of a native oxide layer. Second, the relative peak heights are slightly changed. The Hg 4d peaks, for example, appear less pronounced after the ICP etching step than before. This can be quantified by comparing the relative peak areas, $A_{\mathrm{peak}}/A_{\mathrm{Cd\,3d}}$, before and after ICP etching. $A_{\mathrm{Cd\,3d}}$ is the peak area of the (two) Cd 3d peaks, calculated by removing a linear background. This estimated area is shown in light blue in the inset of Figure 4.2. The areas of the other peaks are estimated in the same way. Considering the relative peak amplitude is necessary, since the source and detector settings, as well as the sample positioning, may be slightly different in two consecutive runs, which will affect the absolute peak intensity. Table 4.1 summarizes the results. The values are not given with a standard error, since estimating the subtracted background is very likely the largest error source [56]. The given ranges are the minimum/maximum values obtained by manually varying the linear background. The values scatter considerably, but there are clear trends: Relative to the Cd 3d peak area, the peak areas of all Hg and Te peaks are reduced after ICP etching. This result indicates that the surface has a slightly increased Cd content after ICP etching. This is consistent with literature [70], since the removal of Cd is expected to be the rate-limiting step. The relative peak area of the C 1s peak is increased after ICP etching, which might be related to the use of CH_4 in the etching process. It is not clear, however, whether the post-etch dip in organic solvents may have caused a slightly more pronounced carbon contamination as well.

To sum up, there are only small differences in the surface stoichiometry before and after ICP etching. Main change is a slight increase in the Cd content. Said change is not critical for transport experiments since it will not result in the formation of a conductive layer.

4.2.2 Selection of etch mask

Further tests, e. g. concerning etch rates, as well as the fabrication of devices require the use of a suitable etch mask. The high durability of BaF_2 etch masks in various dry etching procedures (see Reference [52], but also Chapter 3 of this thesis) as well as the fact that they have been successfully employed for HgTe/CdHgTe heterostructures make them favourable to the introduced ICP etching process. The BaF_2 etch masks can be prepared in the same way as it is done for IBE.

To test the durability, a 200 nm thick layer of BaF_2 was deposited on a Si wafer (with native oxide) and exposed to the ICP etching process for 10 min. The thickness reduction of BaF_2 was (61 ± 4) nm, which corresponds to an etch rate of

(102 ± 7) pm/s. As mentioned before, it is possible to reinforce the BaF_2 etch mask with a thin Ti layer with a thickness of 10 to 20 nm. In that case, etch rates are still lower and not even measurable within experimental uncertainty. In any case, etching of a BaF_2 or BaF_2+Ti mask proceeds significantly slower than etching of CdHgTe.

Complete removal of a reinforced BaF_2 layer in water after ICP etching is possible, as was demonstrated already in Section 3.2. There it was also shown (cf. Figure 3.3c) that in combination with ICP etching a pure BaF_2 mask (without Ti reinforcement layer) may be difficult to remove completely in water. After discussing the mechanisms of ICP etching, one can speculate that the formation of residues is caused by polymerization and deposition of CH_4 and related radicals. Physical removal of a polymer layer with accelerated Ar^+ ions is crucial in our ICP process, since the etching of CdHgTe would stop otherwise. However, polymer deposition might occur in the porous structure of the BaF_2 layer, where polymers cannot be removed by (directed) Ar^+ bombardement. A combination of polymers, which are insoluble in water, and BaF_2 would cause the formation of residues. If the mask is "sealed" with a thin Ti layer, this problem can be avoided. Further tests have shown that using a very thick BaF_2 layer can also help to avoid residues. A 300 nm thick BaF_2 layer (without Ti) could be completely removed in water after being exposed to the ICP etching process, while this is not the case for thinner layers ($\lesssim 100$ nm). Since thin BaF_2 layers are beneficial for several reasons (compatibility with thin lift-off masks, absence of sidewalls, smaller thermal load during deposition), the (ICP-etched) transport samples in this thesis were all prepared with thin BaF_2+Ti etch masks.

BaF_2 etch masks can easily be employed for our ICP etching process. There are also disadvantages, though. First of all, the high selectivity favors the formation of hillocks around the mesa, sometimes also referred to as "RIE grass" or simply "micrograss" [63]. It can be caused by deposition of mask material into the undercut of a lift-off mask (cf. Figure 3.1) or during etching by sputtering of mask material. In any case, the mesa edges of samples prepared by ICP etching and a BaF_2-based hard mask often appear rough. SEM images of two different spots on the same sample, Figures 4.3a) and b), illustrate this problem. The sample has been prepared with a BaF_2+Ti etch mask that has been structured using the optical resist AR-N 4340 with a large undercut (on the order of 1 µm). In some places on the sample, cf. a), the mesa step is surrounded by a dense array of hillocks, which make the mesa edge appear very rough. On other places on the same sample, cf. b), this issue is less pronounced and the mesa edge is cleaner. Well visible in both images is a narrow terrace with a width of approximately 100 to 200 nm, surrounding the etch mask. As explained schematically in Figure 3.1, both the terrace and the formation of hillocks may be due to unintended deposition of BaF_2 into the undercut of the lift-off mask. To reduce the formation of hillocks and avoid the terrace, it may be necessary to work with a lift-off mask that has almost vertical sidewalls and only a small undercut. Figure 4.3c) shows a SEM image of a microstructure. For this sample, the BaF_2+Ti etch mask has been structured

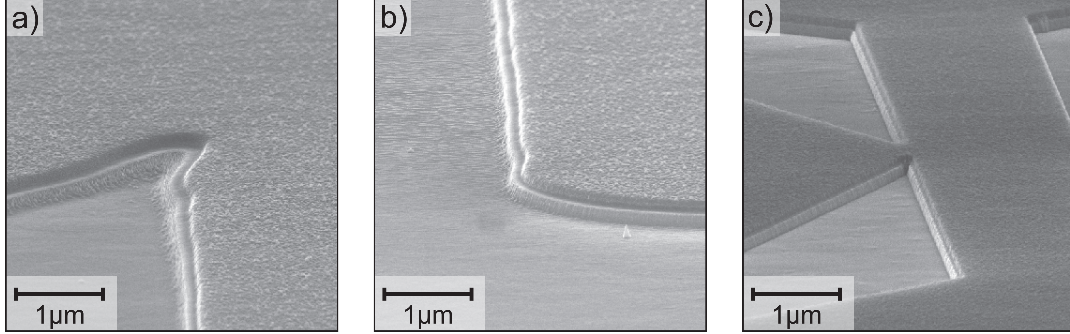

Figure 4.3: Influence of etch masks on CdHgTe mesa edges prepared by ICP etching. a) and b) SEM images of two different positions on a big Hall bar structure after 60 s of ICP etching. The etch mask (100 nm BaF_2 + 20 nm Ti) has been prepared by means of optical lithography using a resist with large undercut (AR-N 4340). c) SEM image of a microstructure after 40 s of ICP etching. The etch mask (100 nm BaF_2 + 10 nm Ti) has been prepared by means of a low-energy EBL process using a resist with small undercut (AR-P 679.03). SEM images are taken with the In-Lens detector at an acceleration voltage of 20 kV, a working distance of 7 mm, and under an angle of approximately 80°. The etch masks have not been removed prior to imaging.

using a thin PMMA lift-off mask with a small undercut. This sample, which is representative of similar microstructures, has clean mesa edges. Narrow corners (center of the image) do not contain hillocks and the etch mask is not surrounded by a terrace. These results confirm that unintended deposition of BaF_2 into the undercut of the lift-off mask may result in rough mesa edges.[1] In contrast, the standard low-energy EBL process used for fabricating micrometer-sized BaF_2 etch masks results in cleaner mesa edges. It should be remarked that SEM images as shown in Figure 4.3 are certainly helpful for understanding possible issues of ICP-etched transport devices. However, roughness on the nanometer scale may not necessarily translate to poor transport properties. A final assessment of the new etching process is thus only meaningful after a careful investigation of the transport results of these devices (see Section 4.3).

A disadvantage is that BaF_2 masks are not suitable for wet etching processes. In principle, dry etching could be followed by a short wet etching step to remove a thin layer of material that is very rough or even damaged by low-energy ion bombardement. This is of course only possible if the same etch mask can be used

[1]Sputtering of mask material is less problematic in our ICP process, which is proven by the absence of hillocks when using a PMMA lift-off mask. There have been experimental results indicating that sputtering of mask material is more pronounced when using BaF_2 without reinforcing Ti. Since this reinforcement layer is in any case necessary for the complete mask removal after etching, this issue was not investigated further.

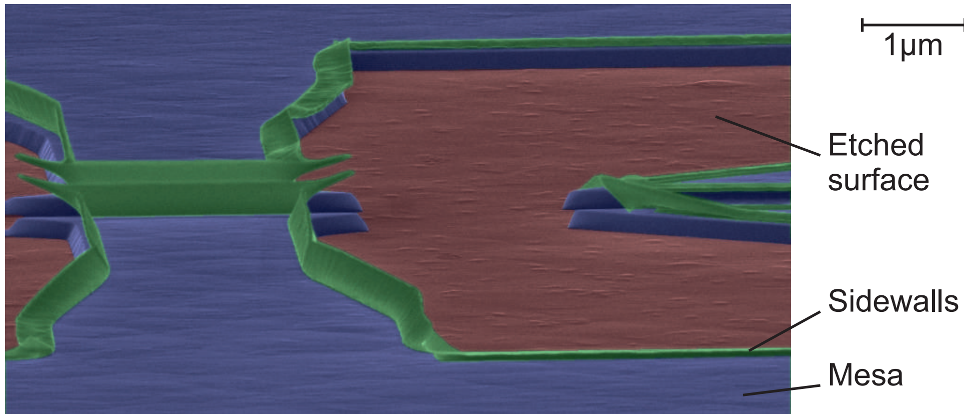

Figure 4.4: SEM image of CdHgTe sample after ICP etching using a PMMA etch mask and stripping in acetone. The image was taken with the In-Lens detector at an acceleration voltage of 20 kV, a working distance of 7 mm, and under an angle of approximately 80°. Coloring was added manually to enhance ease of interpretation.

for both dry and wet etching. BaF_2 can obviously not be used for any water-based wet chemical etching since it will dissolve as well. Furthermore, it was found that BaF_2 is also not suitable for etching in Bromine/ethylene glycol, which is a common alcoholic wet etching solution for CdHgTe [41]. It seems that the porous structure of BaF_2 allows the etchant to attack the underlying material. A detailed discussion of these results, as well as suggestions how to overcome this problem, can be found in Reference [54].

BaF_2 etch masks are of course not the only possible choice for our ICP etching process. Preliminary tests with organic resist masks, which were already established in our group, were not satisfactory, however. The main problem is resist hardening during the etching process, which causes incomplete stripping of the resists, and the formation of sidewalls. Figure 4.4 shows a SEM image of a CdHgTe sample after 60 s of ICP etching using a PMMA etch mask (AR-P 669.06, Allresist GmbH, Strausberg, Germany) with a thickness of approximately 500 nm. The mask has been removed in acetone under ultrasonic excitation (duration 10 min, temperature 50 °C). The SEM image is manually colored to distinguish structures. Etched parts are shown in red and the mesa is shown in blue. The green structure, which extends on top of the mesa edge are resist residues (sidewalls) that could not be removed in the stripping procedure. Removal of these sidewalls may require the use of more aggressive stripping procedures that may deteriorate device quality (cf. Section 2.2). Similar problems occur also with optical resists, such as the AR-N 4340 and the ECI 3012. Details can be found in Reference [64].

On the whole, BaF_2 hard masks, reinforced with a thin Ti layer, can be applied for the introduced HgTe/CdHgTe ICP etching process without further technical developments. At the current stage these hard masks outperform several established

organic resist masks, which suffer from resist hardening and sidewall formation during the etching. If not otherwise mentioned, the ICP-etched samples presented in the following parts of this thesis have been prepared with BaF_2+Ti etch masks. It is important to keep in mind that BaF_2 etch masks, structured with an optical lithography lift-off process, may introduce a considerable edge roughness. Transport experiments are necessary to evaluate whether this might affect the sample quality.

4.2.3 Reproducibility of etch rates

It is important to understand the reproducibility of the results obtained with the new etching process. This concerns run-to-run reproducibility of etch depths as well as the homogeneity of etch depths across a single sample. The latter is crucial for the following tests and should thus be investigated first.

For this experiment, a wafer piece with a MBE-grown CdHgTe layer was first spin-coated with PMMA. Subsequently, one edge was cleaved in order to remove the PMMA bead. Crosses were patterned homogeneously across the sample by means of EBL and used as lift-off mask for a standard BaF_2-Ti etch mask. The sample was then etched for 40 s with our ICP etching process and the mask was stripped prior to measuring the etch depth with a profilometer (Dektak 6M, Veeco Instruments Inc., Tucson, US). The advantage of this procedure is that crosses could be patterned up to the sample's edge without edge bead. Figure 4.5a) shows the etch depth as a function of position on the sample (cf. gray shading, which indicates the sample edges). Results from three rows of crosses, extending from the center of the sample to the sample edges, are shown. The etch depths are very similar in the center of the sample and increase considerably towards the sample edge. For the innermost 2 mm × 2 mm the median etch depth is 113.2 nm with maximum deviations (maximum etch depth vs. minimum etch depth) of 4.5 nm. This is a deviation of only 4 %, indicating a good homogeneity of etch depth across the center of the sample. The dramatic increase of the etch rate towards the sample boundaries might be related to the macroloading effect [74, 75]. This effect describes the dependence of etch rates on the sample areas exposed to the etching process. There, the change in etch rates is related to the varying concentration of radical species at the sample surface. Similarly, the concentration of radicals available to form volatile compounds may be higher at the sample edge and thus cause a higher etch rate. An alternative explanation is related to electrostatics: The potential difference between the plasma and the sample table (usually quantified as DC bias) leads to low-energy ion bombardement of the sample. It is known from similar processes that a higher ion energy increases the etch rate [66, 67]. The electric field which accelerates ions is homogeneous on a flat surface, i. e. in the center of a sample, but may increase considerably at sharp corners (similar to the tip of a lightning rod). Determining the exact mechanism of the etch rate increase at the sample edge remains beyond the scope of this thesis. It is important to note, however, that etch rates should be determined from measurements of the etch depth in the center of the sample. Furthermore, structures which require a

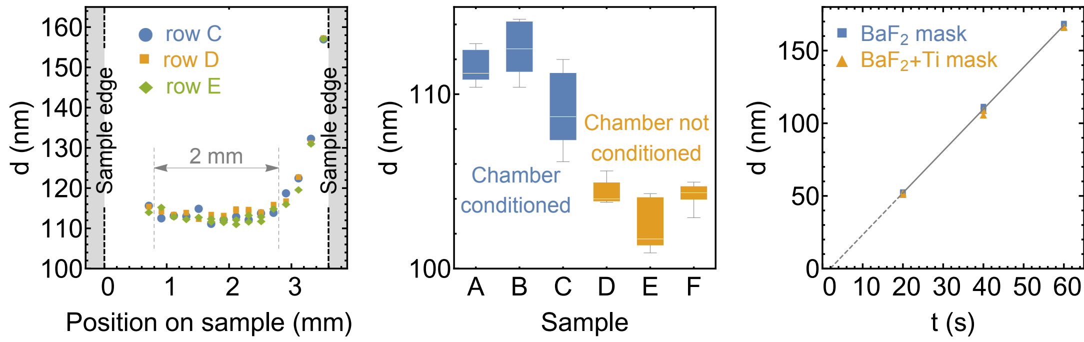

Figure 4.5: Etchrates of the ICP etching process. a) Etch depth in CdHgTe, as a function of lateral position on a sample, after ICP etching for 40 s. b) Etch depths at different positions of CdHgTe samples after ICP etching for 40 s. For different samples (A,B,C,D,E,F) the chamber was prepared differently. c) Etch depth in CdHgTe, as a function of ICP process time, together with a linear fit and extrapolation to zero etch depth.

very accurate etch depth should be placed in the central part of a sample.

The second test concerns the run-to-run reproducibility of etch depths. For this experiment BaF_2+Ti hard masks were patterned on six different CdHgTe samples by means of optical lithography. Since the samples were cleaved manually, edge lengths varied between 2.6 and 3 mm. Prior to etching samples A, B, and C, the chamber was conditioned first (with the silicon carrier wafer inserted). It was cleaned with a high-power oxygen cleaning process (2000 W power to the ICP coil, 100 W power to the sample table, 100 sccm O_2, 50 µbar) and subsequently subjected to the CdHgTe etching process for 10 min. The objective of this procedure is to generate steady conditions, that do not change anymore during etching a sample for a shorter period. Prior to etching sample D, the ICP chamber (with the Si carrier wafer inserted) was only cleaned with the high-power oxygen cleaning process. Samples E and F were etched subsequently, each without further treatment of the ICP chamber. All samples were etched for 40 s and the etch depths measured after stripping the mask. Figure 4.5b) shows the resulting etch depths. The box plots summarize the results of several measurements in the center of a sample. The samples etched in the conditioned chamber were etched slightly deeper than those etched after cleaning the chamber. The maximum deviation of the median values of all samples is 10.9 nm, which corresponds to an etch depth variation of approximately 10 %. With the conditioning, the maximum deviation is only 3.9 nm. These run-to-run deviations in etch depth are sufficiently small for structuring simple HgTe/CdHgTe transport devices, where the main task is achieving a minimum etch depth.

Next, the etch rate of CdHgTe was determined. For this, a total of six samples with either BaF_2 or BaF_2+Ti masks were etched for 20, 40, or 60 s. The etch depths

were determined with the profilometer in the center of the samples. The results are shown in Figure 4.5c), together with a linear fit. The etch rate determined in this way is (2.88 ± 0.03) nm/s. The extrapolation to zero indicates an apparent etch start delay of (1.9 ± 0.4) s. This may be caused by the ignition dynamics of the plasma or the slower etching of a surface film, e. g. due to the native oxide or photoresist residues. The etch rate for MBE-grown HgTe is approximately 6 to 14 nm/s. This rate has a large error bar, since it was deduced indirectly from etching HgTe/CdHgTe heterostructures and assuming a known (and fixed) etch rate for CdHgTe. Etch tests on HgTe layers without a CdHgTe cap layer indicate an etch rate on the order of 14 nm/s. The latter value is also prone to errors due to the combination of a high etch rate and the etch start delay. In any case, etching of HgTe proceeds considerably faster than etching of CdHgTe. Consistent with literature for similar etching processes [70], it can be deduced that removal of Cd is the rate-limiting step.

On the whole our ICP etching process yields very reliable and reproducible results, both across a single sample and from sample to sample. The etch depth variation in the central part of a sample can easily be reduced to approximately 4 %. Reaching a given etch depth with high accuracy is not crucial for the devices presented throughout this thesis, but it may be important for future transport devices. One possible application is etching of HgTe double quantum wells (DQWs), where two HgTe layers are separated by a CdHgTe barrier of only a few nanometers in thickness. In order to separately contact both layers, it will be necessary to etch through only the top layer. The required accuracy is currently not feasible with our wet etching process. Neither can this etching step be done with the high-energy Ar^+ ion milling process, since it leads to n-doping and makes the CdHgTe barrier layer conducting. The new ICP etching process may have the potential to overcome these difficulties. What needs attention for such dedicated device layouts is the increase of the etch rate towards the sample edge.

4.3 Comparison with other etching methods

After understanding basic properties of the new ICP etching process, as well as selecting a suitable etch mask, it is time to discuss transport properties of ICP-etched HgTe devices. To this end the ICP etching has to be incorporated into the standard Hall bar process (cf. Sections 2.2 and 3.3, and Appendix A). This process already includes a BaF_2 hard mask. The IBE step is replaced by ICP etching, all other process parameters can remain unchanged. Samples prepared by this adapted Hall bar process can be compared to samples from the same wafer which have been prepared by the same process, but with IBE etching. To increase the comparability of these sample pairs, they can be fabricated in parallel (so that the etching step is the only difference between both processes). The dry etched sample pairs can be benchmarked to samples from the same wafer, which have been prepared with the wet chemical etching process. The lithography process

for wet etched samples of course differs from the dry-etching based process in several important points, such as the optical photoresist, developer, and stripping procedures. For first tests, it is instructive to work with HgTe 2D EGs, similar to the procedure for testing BaF_2 hard masks (cf. Section 3.3). The following samples are all based on a 9.5 nm thick HgTe layer, sandwiched between 72.5 or 75 nm thick CdHgTe layers. The layer stacks were MBE-grown on a commercial CdTe substrate.

Figure 4.6a) shows the longitudinal resistance as a function of gate voltage of three samples, fabricated from wafer *Q2958* either by means of ICP, IBE, or wet etching. The gate voltages are given with respect to the zero density point. In all three samples, the resistance passes through a pronounced maximum close to zero density. This is the expected behavior, since the Fermi level is tuned through the band gap and conduction is limited to topological surface states. In big Hall bar samples, with dimensions of 200 µm × 600 µm, the edge lengths are on the order of several hundred micrometers. Scattering between counterpropagating edge states leads to a resistance which is much larger than the 12.9 kΩ expected for perfect transmission [5]. The maximum resistance, however, is considerably smaller in the IBE sample than in the ICP and wet etched samples. The same qualitative trend is observed in small Hall bars on the same samples, with dimensions of 10 µm × 30 µm, as shown in Figure 4.6b). In this case, the edge length is much shorter and consequently the maximum resistance remains smaller than in the big Hall bars. Table 4.2 lists the maximum resistance values[2] of the samples fabricated from wafer *Q2958* and *Q2959*. Also samples from wafer *Q2959* show that the maximum resistance in the ICP and wet etched samples is much higher than in the IBE samples. The wet etched samples can be regarded as bench mark, since wet etching is known to preserve the sample quality [46]. The high resistance in these samples indicates that there is an intrinsic scattering mechanism between counterpropagating edge channels, which cannot be avoided. The even higher resistance of the ICP etched samples indicates that the rough mesa edges may introduce a certain amount of additional scattering. On the contrary, the small resistance in the IBE sample can only be explained by n-doping close to the mesa edges. In this case, the Fermi level cannot be tuned precisely to the band gap throughout the whole sample and the maximum resistance remains smaller than in the wet etched samples.

Figures 4.6b) and e) show the total carrier density, obtained from the transverse resistance at a magnetic field of 0.3 T. In overall n-regime ($V_{\mathrm{TG}} - V_{\mathrm{CNP}} > 0$), the curves for all three samples almost coincide and show a linear dependence on gate voltage as expected. The slope in the wet etched sample appears to be slightly higher than in the dry etched samples. Possibly this small difference is due to a slight difference in insulator thickness (the wet etched and the dry etched samples were not processed in parallel). In overall p-regime, these values are not reliable due to

[2]Due to the high sample resistance, the voltage drop over the reference resistor is very small and thus this voltage measurement introduces a large uncertainty.

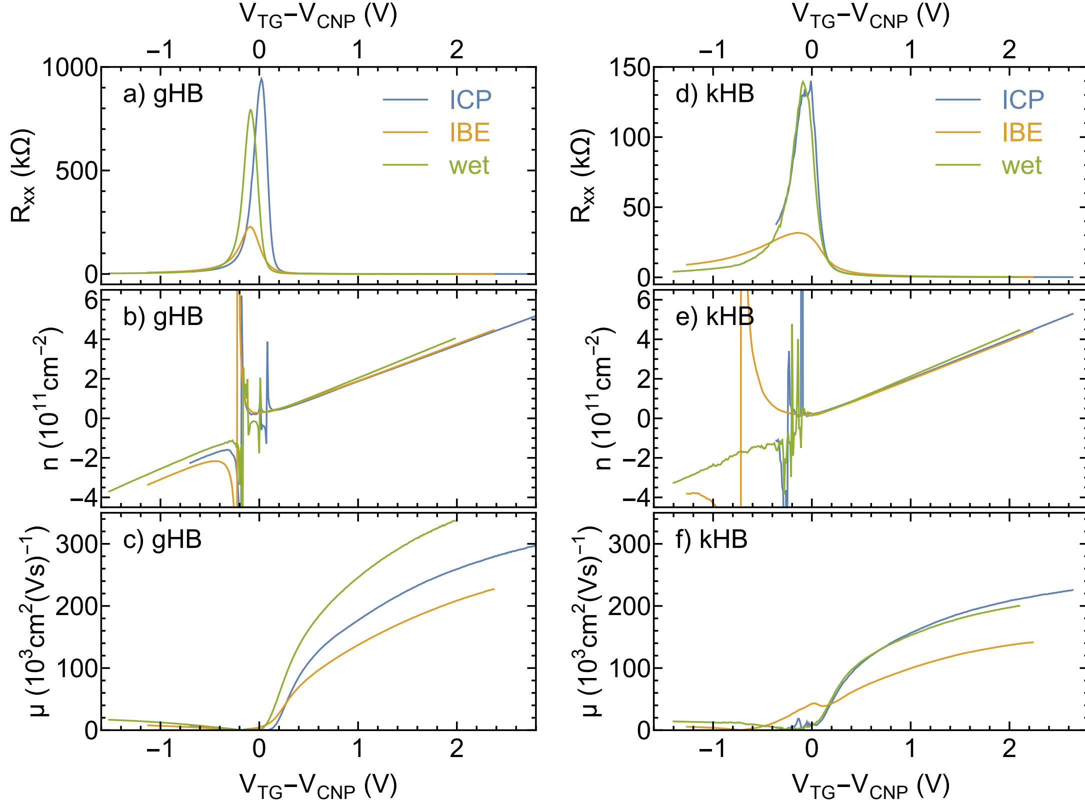

Figure 4.6: Comparison of transport characteristics of samples from wafer *Q2958* prepared with ICP, IBE, or wet etching. a) and d) Longitudinal resistance R_{xx} as a function of top gate voltage V_{TG} with respect to the charge neutrality point V_{CNP}, either for a big Hall bar (gHB, 200 µm × 600 µm) or a small Hall bar (kHB, 10 µm × 30 µm). b) and e) total carrier density n as a function of top gate voltage, estimated from the transverse resistance at a magnetic field of 0.3 T. c) and f) carrier mobility μ as a function of top gate voltage, estimated from the total carrier density and the longitudinal resistance at zero magnetic field. The color code is shown in a) and d). All measurements were done at 4.2 K.

Sample		n_{gnd} (10^{11} cm^{-2})			R_{max} (kΩ)		
		ICP	IBE	wet	ICP	IBE	wet
Q2958	gHB	2.45 - 2.47	2.50 - 2.51	1.63 - 1.70	940 ± 40	227 ± 3	790 ± 50
	kHB	2.38 - 2.44	2.46 - 2.48	1.96 - 1.97	140 ± 20	31.7 ± 0.4	139 ± 2
Q2959	gHB	1.90 - 2.00	1.56 - 1.68	0.59 - 0.63	1230 ± 70	381 ± 7	760 ± 50
	kHB	1.95	1.78 - 1.84	0.76 - 1.02	260 ± 6	64 ± 2	132 ± 5

Table 4.2: Ground density and maximum longitudinal resistance of ICP, IBE, and wet etched samples from wafers *Q2958* and *Q2959*. Each sample contains a big Hall bar (gHB) and a small Hall bar (kHB).

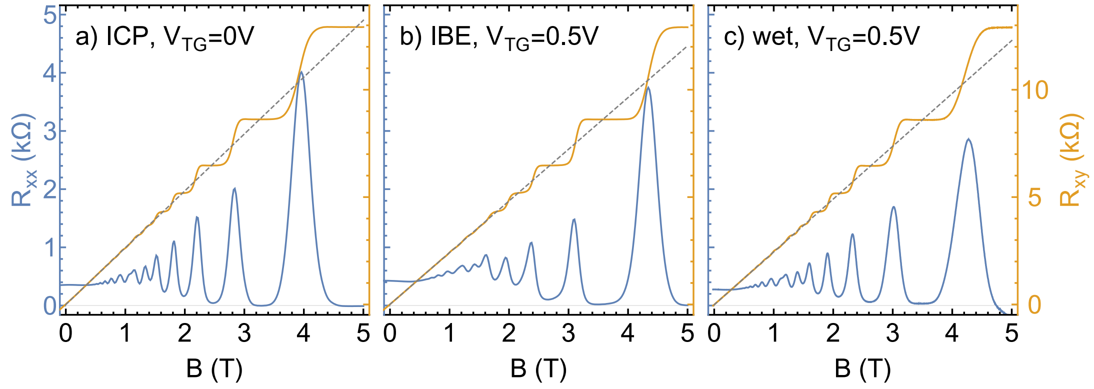

Figure 4.7: Longitudinal resistance R_{xx} and transverse resistance R_{xy} as a function of magnetic field B of samples from wafer *Q2958* prepared with ICP (a), IBE (b), or wet etching (c). These results were obtained on big Hall bar structures and at different top gate voltages as indicated. All measurements were done at 4.2 K.

the influence of the complex valence band structure (cf. Section 12.3.1). Table 4.2 also lists the carrier densities, obtained from Hall measurements done before applying a top gate voltage. The values give the range obtained by measuring the transverse resistance with different contact configurations. As before, these differ by more than the experimental uncertainty. For samples from wafer *Q2958*, the dry etched samples all have ground densities ranging from 2.38 to $2.51 \times 10^{11}\,\text{cm}^{-2}$. The wet etched sample has slightly lower ground densities ranging from 1.63 to $1.97 \times 10^{11}\,\text{cm}^{-2}$. In samples from wafer *Q2959*, the deviations are bigger, ranging from 1.9 to $2.00 \times 10^{11}\,\text{cm}^{-2}$ for the ICP etched sample to only 0.59 to $1.02 \times 10^{11}\,\text{cm}^{-2}$ in the wet etched sample. These results may imply that the lithography process including dry etching causes slightly higher ground densities as compared to the wet etching process. In combination with the results in Section 3.3, these results could indicate that samples with a BaF_2-based etch mask have a slightly higher ground density than those with an ECI etch mask. It is not clear as of now how the different etch masks could introduce a slight density shift. In any case, this small shift would be on the order of normal sample-to-sample variations (cf. discussion in Section 3.3) and is not harmful for most transport experiments.

Figures 4.6c) and f) show the carrier mobility, estimated from the total carrier density and the resistance at zero magnetic field. In all samples (both small and big Hall bars), the mobilities are higher in the ICP and wet etched samples. The same holds true in samples from wafer *Q2959*. The higher resistance maxima in the ICP and wet etched samples (cf. a) and d)) are thus not caused by a degraded sample quality.

Magnetic field dependent measurements do not show significant differences between the differently prepared samples. Figure 4.7 compares the longitudinal and transverse resistances of big Hall bar samples as a function of magnetic field.

At a comparable total carrier density of 2.4 to $2.6 \times 10^{11}\,\mathrm{cm}^{-2}$, all three samples show a pronounced QHE (cf. Section 3.3). Pronounced SdH oscillations set in at magnetic fields lower than 1 T and the longitudinal resistance reaches zero at magnetic fields of approximately 3.5 T. Minima in the longitudinal resistance are accompanied by plateaus in the transverse resistance. At magnetic fields close to 5 T, the longitudinal resistance of the wet etched sample unexpectedly drops below zero. As will be argued in detail in Section 7.3, this is most likely related to issues with the voltage leads and not directly caused by the lithography process.

On the whole, transport properties of samples fabricated by means of ICP etching are comparable to those of wet etched samples. These first results on rather big structures with critical dimensions larger than 10 µm already indicate that ICP etching outperforms IBE as expected. An important result is the high maximum resistance of ICP etched samples when the Fermi level is tuned to the band gap, which is comparable to results from wet etched samples. This is a strong indication that ICP etching does not induce a lateral n-doping like IBE with high-energy Ar^+ ions. Based on these results, it is reasonable to apply ICP etching also to smaller structures with critical dimensions on the order of 1 µm, where IBE is known to massively degrade sample quality [46]. The comparison with wet etched samples indicates that edge transport may be affected by the pronounced mesa edge roughness in ICP etched samples. ICP etching is thus not ideal for investigating the QSH effect. On the other hand, it is a natural choice for HgTe 3D TI microstructures investigated in Chapters 11 and 12.

4.4 Application to microstructures

Since the previous tests were performed on HgTe 2D EG samples, it is instructive to use similar material for a test of micrometer-sized structures fabricated with ICP etching. Sample *QC0336 ch ICP* is based on a HgTe 2D EG with thickness of 9.2 nm and contains two micrometer-sized structures, which are similar to Hall bar structures. They contain separate current leads and voltage probes, so as to perform a 4-terminal measurement of the longitudinal and transverse resistance. Their aspect ratio (length to width) is 5, which differs from typical Hall bar samples. They will be called “channel samples” in the following to indicate this difference. This sample has been prepared by EBL to define a lift-off mask for the BaF_2+Ti hard mask. Etching the mesa was done with ICP etching. The detailed process parameters for ICP-etched microstructures can be found in Appendix A.

Figure 4.8a) shows the longitudinal resistance of a channel on sample *QC0336 ch ICP* with dimensions of $1\,\mu\mathrm{m} \times 5\,\mu\mathrm{m}$ between voltage probes as a function of top gate voltage. Around charge neutrality – determined from the gate dependence of the carrier density in n regime – the resistance passes through a pronounced maximum. The maximum resistance is on the order of 51 kΩ, which is considerably higher than the resistance of 12.9 kΩ expected for edge channel transport in the QSH regime. This resistance can be compared to a similar device prepared by

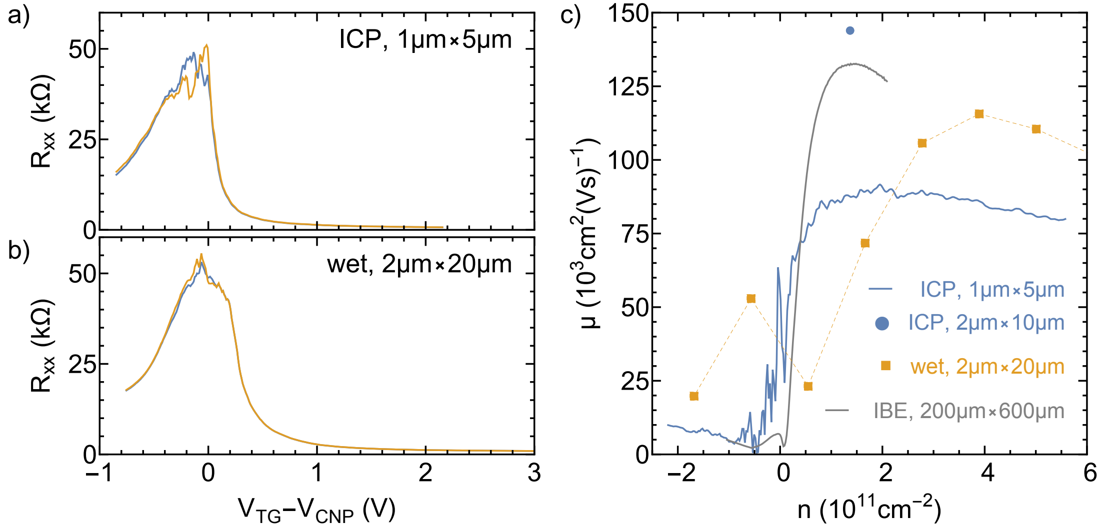

Figure 4.8: Comparison of samples based on wafer *QC0336*, prepared by different lithography processes. a) and b) Longitudinal resistance R_{xx} as a function of the top gate voltage V_{TG} (given w. r. t. the charge neutrality point at V_{CNP}) of a) a 1 µm × 5 µm sized channel structure on sample *QC0336 ch ICP*, b) a 2 µm × 20 µm sized channel structure on sample *QC0336 ch 2*. Blue and orange traces correspond to different contact pairs on the same structure used for the measurement. c) Carrier mobility μ as a function of total carrier density n for samples with different sizes, which have been prepared by different lithography processes (as indicated in the figure).

wet etching. Figure 4.8b) shows the longitudinal resistance of a 2 µm × 20 µm sized channel structure on sample *QC0336 ch 2*, which has been fabricated by wet etching.[3] As for the dry etched sample, the resistance passes through a pronounced maximum around charge neutrality. The maximum resistance is on the order of 55 kΩ. Also the wet etched sample does not reach the resistance expected for perfect transmission. It is important to note, however, that the edge length of the wet etched sample is roughly four times as long as the edge length of the dry etched sample. This implies that edge conduction is affected more heavily by the ICP dry etching process than by the wet etching process, consistent with the results in the previous section.

To evaluate whether ICP etching also affects transport properties in the central part of the microstructures, it is important to consider the carrier mobilities in n-regime (cf. Reference [46]). Figure 4.8c) compares the carrier mobilities for several samples, all based on wafer *QC0336*, as a function of carrier density (obtained

[3]The two samples have different aspect ratios, since they were prepared at different stages of the project. Nevertheless, the layouts and most processing steps (excluding the etching step) are very similar.

from extrapolating the linear density to gate relation in n-regime). The blue line shows data from the ICP etched channel with 1 µm width, cf. a). The blue point shows data from a 2 µm wide channel on the same sample (but without working top gate). The orange squares show data from the wet etched channel with 2 µm width, cf. b). Also shown in gray is data from a big Hall bar sample, prepared by the standard Hall bar process including IBE and a BaF_2 etch mask (cf. Sections 2.2 and 3.3).[4] The 2 µm wide microstructures have maximum mobilities on the order of $140 \times 10^3\,\mathrm{cm^2(Vs)^{-1}}$ (ICP) and $115 \times 10^3\,\mathrm{cm^2(Vs)^{-1}}$ (wet), similar to the value of approximately $130 \times 10^3\,\mathrm{cm^2(Vs)^{-1}}$ found in a big Hall bar. This result shows once more that wet etching preserves sample quality even in very small samples and further indicates that the same is true for ICP etching. The even smaller structure with 1 µm width has a somewhat lower maximum mobility of $90 \times 10^3\,\mathrm{cm^2(Vs)^{-1}}$. It should be noted, though, that this decrease is still considerably smaller than in microstructures prepared by IBE [46].

These somewhat preliminary results show that it is possible to fabricate high-quality, micrometer-sized HgTe transport devices by means of ICP etching. The results also support the hypothesis that dry etching may result in rough mesa edges, thereby causing more backscattering in the edge conduction regime. As discussed before, this may be a limitation for some experiments and a benefit for others.

[4]The microstructures offer a wider density range which is accessible without hysteresis. The reason for this is unclear as of now.

5 Conclusion: A well-controlled, minimally invasive lithography process for HgTe transport devices

The first part of this thesis was concerned with further developing existing lithography processes for HgTe/CdHgTe transport devices. Developments of this kind are crucial for the work in our group, as they are the key to utilizing the full potential of our high-quality MBE-grown HgTe/CdHgTe heterostructures.

In a first step (Chapter 3), BaF_2 was introduced as an etch mask for IBE dry etching to replace the previously used organic resist mask. It was found that BaF_2 layers are easily deposited with standard physical deposition techniques. The layers could easily be structured using existing lift-off processes, including those for micrometer-sized structures. The new etch mask performed well in the existing IBE process with high-energy Ar^+ ions. After etching, the mask can be removed by a very gentle stripping process requiring only deionized water, thus being minimally invasive for the samples. HgTe transport devices fabricated with this new etch mask are comparable to transport devices fabricated with the previously used organic resist masks.

In a second step, a new dry etching process was introduced to replace the previously employed IBE process. This process is based on a high-density Ar/CH_4 plasma, obtained in a commercial ICP tool. It was found that the process parameters supplied by Oxford Instruments yield a reliable and well-controlled etching process with low ion energies. The new etching process could be successfully combined with BaF_2-based etch masks, which greatly simplified process development. Transport devices fabricated with this new etching process indicate that the low ion energy strongly reduces lateral damage as compared to the previously used dry etching process. The ICP etching process is thus also suitable to produce micrometer-sized transport devices.

When choosing between ICP etching and our more established noninvasive etching technique, wet etching, several differences need to be considered: First, the dry etching process is very easy to control and etch depths are very reproducible. This can be very important for applications where reaching an exact etch depth is crucial. For most transport devices discussed in this thesis, this difference is negligible. Second, the dry etching process is highly anisotropic and thus yields a better structural fidelity than the isotropic wet etching process. Structural fidelity is of great importance to transport devices which are used to investigate

size-dependent effects. This advantage was one of the reasons to use dry etching for most devices presented in Part III of this thesis. Third, wet etching is still superior to dry etching in terms of preserving the sample quality at the mesa edge. Several results indicate that the rough mesa edges introduced by ICP etching lead to additional scattering. While clearly detrimental to investigations of the QSH effect, this property of dry-etched samples may prove beneficial for the experiments considered in Part III of this thesis. Note that for the experiments in Part II of this thesis, this difference is not important. There, macroscopic HgTe 3D TI samples are investigated, in which the additional edge roughness is not expected to significantly affect transport properties. To sum up the comparison, there are important advantages for both of our noninvasive etching techniques. It is the task of the experimenter to choose the more appropriate one for the envisioned experiment.

At the end of the part at hand stands an improved lithography process for transport devices ranging from hundreds of micrometers to hundreds of nanometers in size. This process has been used to fabricate several transport devices which are basis for the subsequent parts of the thesis. In order to minimize the risk of collecting data on the basis of systematically biased samples, most of the basic observations have been reproduced and confirmed in wet etched samples.

Part II

Surface states in HgTe 3D TIs

6 Introduction to HgTe-based 3D TIs

6.1 Overview

HgTe is an extremely versatile material system, which combines several beautiful modern-day physics principles in one chemical compound. Depending on layer thickness and applied strain several topological phases can be realized in HgTe, one of which is the 3D TI phase. In recent years, this phase has been studied extensively by our group. Undoubtedly, the most prominent feature of 3D TIs are their two-dimensional Dirac surface states which are protected by topology. The results have unambiguously proven that tensilely strained HgTe layers belong to the class of 3D TI materials. However, some more subtle details could not be resolved in previous measurements or obstructed the understanding of the system.

The current thesis was originally aimed at understanding transport properties of the 2D TSSs in micrometer-sized HgTe samples. Several experimental observations in these microstructures could not be sufficiently explained with the existing model, though. It was thus necessary to take an intermediate step and re-examine general transport properties of HgTe 3D TIs.

This part of the thesis will introduce some of the major obstacles encountered in the past as well as the attempts to develop a refined model of transport in thick HgTe layers. Along the way several intriguing effects were observed which will also be presented.

6.2 Previous work on transport properties of HgTe 3D TIs

The first experimental evidence for the 3D TI nature of tensilely strained HgTe layers came from magnetotransport measurements performed in our group [8]. The observation of a pronounced QHE at high magnetic fields has proven the existence of high-mobility charge carriers with 2D character. Consistent with band structure calculations, those were identified as the TSSs.

The next step was the application of a top gate to change the carrier density in the HgTe layers [24]. It was found that the QHE at high magnetic fields persists up to very high n-type charge carrier densities. This observation conflicts with the occurrence of additional bulk contributions, as commonly seen in other 3D TI

systems at higher charge carrier densities. The absence of a pronounced bulk contribution in HgTe was attributed to the special screening properties of the Dirac-like surface states. In this so-called Dirac screening model, the screening prevents the electric field to penetrate the bulk and change the bulk carrier density.

Further improvements on the device quality were achieved by introducing a thin CdHgTe[1] capping layer to protect the top surface of the HgTe layer [28, 76]. Remarkably, these devices allowed the observation of a pronounced p-type QHE at high magnetic fields. Following the Dirac-screening model it was hypothesized that the unusual electrostatics in HgTe 3D TIs allows to push the Dirac point of the TSSs into the bulk band gap. In that case, the hole branch of the TSSs would give rise to a p-type QHE without being obscured by parallel bulk conductance.

It is important to note, however, that the interpretation of the p-type QHE was a matter of debate as summarized in a concise manner in Reference [76]. The main reason for this uncertainty was the behavior of HgTe samples at low magnetic fields. Only in the n-regime, the Hall resistance was found to depend linearly, with a n-type (positive) slope, on the magnetic field. In p-regime, however, the Hall resistance was found to retain a n-type (positive) slope for low fields, which turns over to a p-type (negative) slope for higher fields. The latter is a clear indication of multi-carrier transport. One of the carrier types was identified with the p-type conduction channel responsible for the QHE, while an additional n-type conduction channel was necessary to explain the strongly nonlinear Hall signal. Strikingly, some samples showed pronounced quantum oscillations in the longitudinal resistance down to very small magnetic fields, indicating an extremely high mobility of the related carriers. The frequency of these oscillations revealed a carrier density of 0.5 to 0.6×10^{11} cm^{-2}, which is sufficient to explain the electron-like nonlinearity in the Hall signal. One suggested explanation was that this parallel n-type conductance channel is in fact (at least) one of the TSSs [76].

One possibility of resolving these puzzling results has been proposed in Reference [77] on the basis of self-consistent k·p-calculations. In this work, the authors suggest that gating a HgTe 3D TI slab does not only alter the occupation of the surface states, in contrast to the Dirac screening picture. In their model the Fermi level shifts significantly and eventually reaches the valence band when gating from n- to p-conductance. The Fermi level should then become pinned at the valence band edge due to the rather high density of states there. This picture implies that the TSSs will always remain n-type, even when gating to an overall p-type carrier density. The hole branch of the TSSs would not contribute to transport. The hole carriers could only be assigned to bulk valence band states in this model. The idea was taken up by another group to explain transport measurements on HgTe 3D TI layers with major focus on the low to intermediate magnetic field regime [25]. However, the experimental observation of a p-type QHE at high fields cannot be explained simply by population of the valence bands with bulk character. The latter can not be the origin of a QHE which occurs only in two-dimensional

[1] As before, CdHgTe is a short notation for $Cd_{0.7}Hg_{0.3}Te$.

systems [8].

An important thought-provoking impulse came from measurements of bulk HgTe layers grown with compressive strain [10]. In this so-called Dirac semimetal phase of HgTe, a pronounced p-type QHE can be observed as well. Self-consistent k·p calculations revealed that this p-type conduction channel can be identified with massive, two-dimensional states which develop at the interface between HgTe and CdHgTe. Even before the field of topological insulators emerged, Volkov and Pankratov suggested the existence of such states at the interface of semiconductors with mutually inverted bands [13]. Consequently, we nowadays refer to these as Volkov-Pankratov states (VPSs). Furthermore, a study on HgTe 3D TIs by means of RF compressibility measurements speculated that a sufficiently high gate potential can induce n-type VPSs [78].

At this point it is necessary to already anticipate some of the results of this thesis, which are included also in References [79] and [80]. By further improving device quality, optimizing measurements and analysis procedures, as well as re-examination of old transport data we have been able to develop a concise model for transport in HgTe 3D TIs in all density regimes commonly accessible in the experiment. Notably, we are now able to experimentally distinguish all conduction channels contributing to transport and relate them to band structure calculations, which correctly consider the electrostatics in the HgTe slab. In fact, it turns out that p-type VPSs readily form also in HgTe 3D TI layers when applying a sufficiently strong top gate potential. This in turn can explain the p-type QHE without having to invoke (nonlocalized) bulk states. References [79] and [80] focus on a description of band structure calculations including electrostatics, and how to relate these to the measurement results. The thesis at hand will add details on the technical developments leading to the recent progress (Chapter 7), the manipulation of TSSs on both surfaces of the HgTe slab (Chapter 8), and the interplay of LLs of different origin in HgTe 3D TIs (Chapter 9).

7 Solving known issues of HgTe 3D TI measurements

Before discussing in more detail the physics of surface state transport in HgTe, it is important to understand some of the more technical obstacles encountered in the past. This is essential to identify possible artifacts in measurements and hence avoid misinterpretation of results.

7.1 Improving general device quality by introducing thick capping layers

One crucial prerequisite for the experiments described in the following is the availability of samples of exceptionally high quality. To achieve this quality, all of the samples which appear in this thesis are equipped with a protective CdHgTe capping layer as well as a CdHgTe buffer layer between the CdTe substrate and the HgTe layer [76].

In Reference [81] it has been shown consistently that thicker capping (and buffer) layers further improve the quality of thin HgTe QWs. It seems plausible that the same is true for thicker HgTe layers. A – somewhat ad hoc – investigation of the relation between cap layer thickness d_{cap} and averaged mobility μ_{av} is shown in Figure 7.1a). The figure includes a collection of transport properties of bulk HgTe layers with tensile strain and CdHgTe bottom and top barrier layers grown in our group in the period from January 2012 to January 2020. Only samples are considered for which a mobility at densities between 2 and $8 \times 10^{11}\,\mathrm{cm}^{-2}$ was provided in our sample database. The wafers which appear throughout the thesis are labeled in the plot. While there is no simple proportionality between cap layer thickness and mobility, it is still observed that most samples with high mobility ($\mu_{\mathrm{av}} > 400 \times 10^{3}\,\mathrm{cm}^{2}(\mathrm{Vs})^{-1}$) have a cap layer thickness of 30 nm or more. Most samples with lower mobility are found to have a thinner cap layer as well. Figure 7.1b) shows the total carrier densities n_{tot} at which the results shown in a) were obtained. This plot is relevant since mobility is generally carrier density dependent (cf. Figure 3.6c) for an example). It becomes clear that high (and low) mobilities can be observed at any carrier density, with some of the highest mobilities obtained at smaller carrier densities of 2 to $4 \times 10^{11}\,\mathrm{cm}^{-2}$. Differences in growth quality over time as well as changes in the lithographic processes can not be accounted for in this analysis. A careful study would have to include a series of

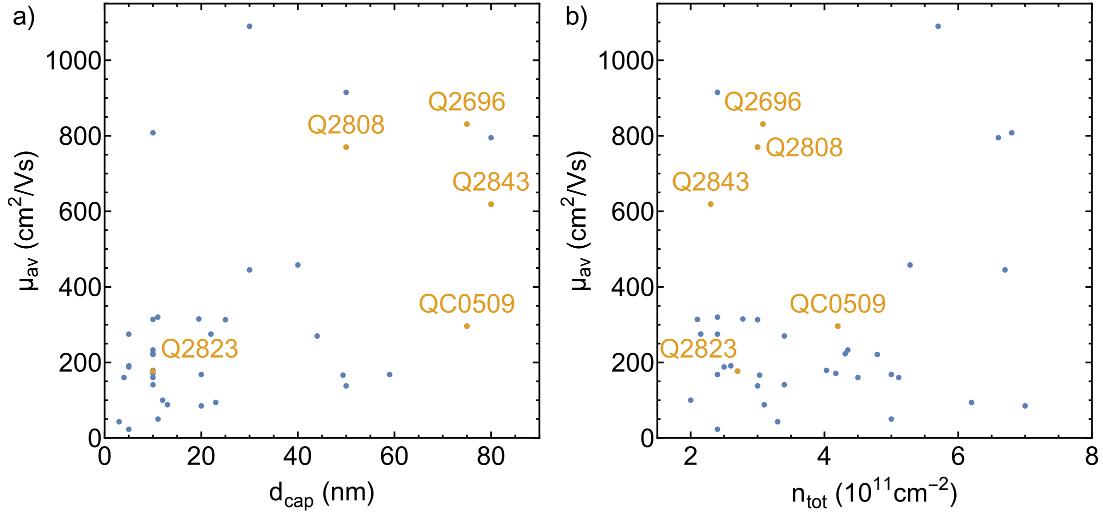

Figure 7.1: Comparison of cap layer thickness, carrier density and carrier mobility for HgTe 3D TI samples. a) Hall mobility μ_{av} plotted as a function of cap layer thickness d_{cap} obtained on tensilely strained HgTe layers with thicknesses of 57 to 111 nm. b) Same mobility data as in a), as a function of carrier density at which the values were obtained. Some wafers used in this thesis are labeled with their wafer number.

HgTe layers, which are grown subsequently and differ only in the capping layer thickness. Samples made from these wafers should be fabricated both with and without top gate electrodes to eliminate differences due to (unintended) ground density shifts. Together with previous investigations, the considerations above still provide a strong motivation to use capping layers with thicknesses of 30 nm or more when possible.

However, the 3D TI phase can only be realized when applying tensile strain. In practice this is achieved by epitaxial growth onto a substrate with slight lattice mismatch, in our case usually CdTe. Once the epitaxial layer reaches a certain critical thickness, strain is released via the creation of different types of lattice defects [12]. Not only does this introduce scattering centers and reduce layer quality, but, even worse, the band structure will change to that of a relaxed layer. For growth on CdTe the lattice mismatch is on the order of 0.3 %, resulting in a critical HgTe layer thickness of 155 nm [20, 21]. For CdHgTe layers on CdTe the lattice mismatch is smaller. This results in larger critical thicknesses of 250 nm on virtual substrates (a thick CdTe buffer grown on a GaAs wafer) to 850 nm on commercial CdTe substrates [20]. For a typical HgTe layer thickness of 70 nm, CdHgTe buffer and top cap layers on the order of 75 nm are possible without strain relaxation [20]. Many of the samples mentioned in this thesis are not far from these values and indeed among the 3D TI layers with highest mobility obtained by our group (cf. Figure 7.1).

So far, the “sample quality” was implicitly defined as the (average) carrier

Stack	ϵ	d in nm	Gate action in 10^{11}/Vcm^2
CdHgTe capping layer	12.7	50	14.0
SiO_2/Si_3N_4 superlattice	5.1	110	2.6
HfOx	25	15	92.1
CdHgTe and SiO_2/Si_3N_4	–	160	2.2
CdHgTe and HfOx	–	125	12.2

Table 7.1: Summary of values for estimating the gate action in our devices, considering a layer thickness d and relative permittivity ϵ of the dielectric.

mobility. For a final device, however, other sample characteristics can be equally important as well. For most of the experiments presented in this thesis, it was crucial to tune the charge carrier density by means of electrostatic gating with a top gate electrode. The gate electrode is separated from the active layer by both the gate insulator and the capping layer, so that both have an influence on the gate performance. From a simple plate capacitor model one can estimate the gate action (i. e. shift of carrier density Δn divided by gate voltage difference ΔV) as

$$\frac{\Delta n}{\Delta V} = \frac{\epsilon_0}{e_0}\left(\frac{d_{\mathrm{CMT}}}{\epsilon_{\mathrm{CMT}}} + \frac{d_{\mathrm{ins}}}{\epsilon_{\mathrm{ins}}}\right)^{-1}, \tag{7.1}$$

where d_{CMT} and d_{ins} are the thickness of the CdHgTe capping layer and the insulator layer, respectively, and ϵ_{CMT} and ϵ_{ins} are the corresponding relative permittivities. Some exemplary values for the gate action are summarized in Table 7.1. Values for the relative permittivities are taken from References [61, 82]. The relative influence of the capping layer is very different for different gate insulator stacks. In the case of the SiO_2/Si_3N_4 superlattice a thick cap layer reduces the gate action from 2.6 to $2.2 \times 10^{11}\,\mathrm{V}^{-1}\mathrm{cm}^{-2}$ as compared to the case without cap layer. In the case of the HfOx gate insulator the gate action is reduced by almost an order of magnitude from 92.1 to $12.2 \times 10^{11}\,\mathrm{V}^{-1}\mathrm{cm}^{-2}$. This means that changing the carrier density by a given value requires a much higher gate voltage applied to the top gate electrode in a sample with thick capping layer. Furthermore, introducing a thick capping layer usually restricts the accessible carrier density range substantially due to the effect of gate hysteresis [61, 76]: When increasing the top gate voltage, the carrier density in the HgTe layer itself changes only up to a certain value. Further increasing the top gate voltage leads to tunneling of charge carriers to trap states, which exist at the semiconductor-insulator interface or in the insulator itself. These charges counteract the effect of the gate electrode, so that further increasing the gate voltage does not increase the charge carrier density in the HgTe layer. While this effect can improve the device performance by smoothing the potential landscape [62], it also restricts the accessible carrier density range.

The apparent disadvantage of a lower gate action can also turn out to be an advantage for some experiments. In the case of microstructures which were also

investigated by means of current heating, a small gate action is beneficial, since it helps to avoid artifacts due to the so-called self-gating effect. For these devices, the use of a thick capping layer may be crucial.

On the whole, the cap layer thickness has to be adjusted to the actual experimental requirements. For most of the experiments discussed in the thesis at hand, the disadvantage of a lower gate range was acceptable as compared to lower mobility and higher self-gating effects. Hence, most devices are made out of layer stacks with thick capping layers.

7.2 Avoiding destructive lithography processes

Another crucial improvement is the use of minimally invasive lithographic processes. One has to take special care when structuring HgTe layers as discussed in detail in Reference [46] and in Section 4.3 of this thesis. A lot of HgTe 3D TI devices from our group have been structured by means of IBE with high-energy Ar^+ ions so far. Nowadays it is known that this IBE process introduces n-type doping and laterally degrades the crystal quality within several µm from the mesa edge. In order to properly assess old data, it is worth to briefly summarize possible fingerprints of this effect in HgTe 3D TI transport data.

The first of these artifacts is observed in QHE measurements in arbitrary sized HgTe 3D TI samples. Differing from the expectation, one often – but not always – observes that the transversal resistance R_{xy} does not quantize to the expected plateau values. This is often accompanied by the longitudinal resistance of the samples not going to zero (cf. Reference [76] and Figure 7.2a) of the thesis at hand). A commonly accepted explanation for this effect was conduction through the side surfaces of the 3D TI slab, which are parallel to the magnetic field and thus in principle still conducting at high fields [8, 25]. This additional conduction channel would increase the current through the sample, while the measured Hall voltage would stay roughly constant, resulting in a shift of the plateaus to lower values. The additional conduction channel would also – somewhat counterintuitively – increase the longitudinal (4-point) resistance, since it allows for backscattering of edge channels.

This hypothesis can be examined by fabricating a pair of samples from the same wafer but with different etching techniques. One such sample pair has been prepared from wafer *Q2843*, featuring a 70 nm thick HgTe layer sandwiched between 80 nm thick buffer and cap layers. The layers have been grown on a relaxed virtual CdTe substrate on top of a doped GaAs wafer, which can be used as a back gate. However, for the measurements discussed here, the back gate is grounded.[1] Etching the mesa was done either with the IBE (sample *Q2843 HB IBE*) or the ICP etching (sample *Q2843 HB ICP*) process. All other steps were

[1] We will return to another sample from this wafer in Section 8.2, where the back gate is extensively used.

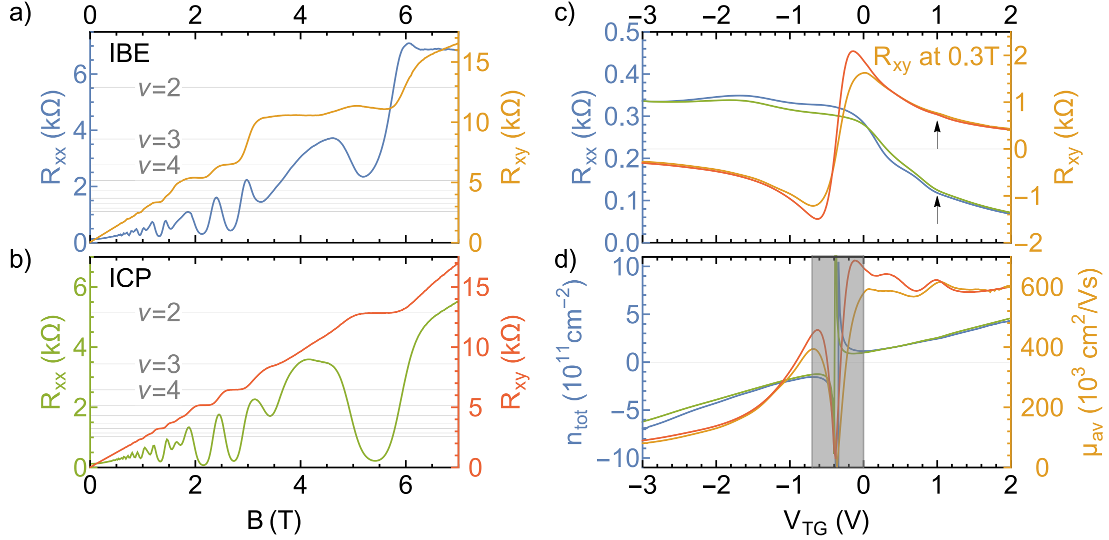

Figure 7.2: Magnetotransport on two samples fabricated from wafer *Q2843* measured at $T = 1.8\,\mathrm{K}$. a) and b) show longitudinal resistance R_{xx} and transverse resistance R_{xy} as a function of magnetic field B for sample *Q2843 HB IBE* and sample *Q2843 HB ICP*, both at a top gate voltage $V_{\mathrm{TG}} = 1\,\mathrm{V}$. c) shows $R_{\mathrm{xx}}(B = 0\,\mathrm{T})$ and $R_{\mathrm{xy}}(B = 0.3\,\mathrm{T})$ as a function of V_{TG} for both samples. The color code corresponds to Figures a) and b). The arrows mark the gate voltage of the traces shown in a) and b). d) shows the (total) carrier density n_{tot} and average Hall mobility μ_{av}, which were calculated from the data in c). The shaded area marks the region where values are not reliable due to the low total carrier density.

virtually identical and also done in parallel wherever possible, so as to minimize random deviations in the lithographic process.

Figures 7.2a) and b) show magnetotransport results of the two samples for a top gate voltage of $V_{\mathrm{TG}} = 1\,\mathrm{V}$ obtained at a temperature of 1.8 K. Both samples show a pronounced QHE with strong oscillations in the longitudinal resistance R_{xx} and clear steps in the Hall resistance R_{xy}. However, in sample *Q2843 HB IBE*, the minima in the longitudinal resistance do not decrease as much as in sample *Q2843 HB ICP*. Furthermore, in sample *Q2843 HB ICP* the Hall resistance shows plateaus at exactly the expected values (thin gray gridlines). In sample *Q2843 HB IBE*, on the contrary, there appears a distorted plateau situated between the expected resistance values for $\nu = 2$ and 3 filling factors.

These differences are surprising, since other sample characteristics are very similar. Figure 7.2c) compares the longitudinal resistances at zero magnetic field and the Hall resistances at a magnetic field of $B_1 = 0.3\,\mathrm{T}$ for both samples. Both curves almost fall on top of each other. The main difference is that the Hall resistance trace of the ICP-etched sample displays a steeper step around the sign reversal (i. e. at low carrier density). To have a more quantitative comparison, the

data from c) can be used to estimate for all gate voltages the total carrier density as

$$n_{\mathrm{tot}}(V_{\mathrm{TG}}) = \frac{B_1}{eR_{\mathrm{xy}}(V_{\mathrm{TG}}, B_1)}, \tag{7.2}$$

where e is the electron charge, and the Hall mobility as

$$\mu_{\mathrm{av}}(V_{\mathrm{TG}}) = \frac{1}{3}\frac{R_{\mathrm{xy}}(V_{\mathrm{TG}}, B_1)}{B_1 \cdot R_{\mathrm{xx}}(V_{\mathrm{TG}}, 0\,\mathrm{T})}, \tag{7.3}$$

where the factor of 1/3 accounts for the aspect ratio of the device. Equations 7.2 and 7.3 are the same as for evaluating Hall measurements in 2D metals (cf. Equations 3.1 and 3.2). The resulting mobility values are thus average values. The result is shown in Figure 7.2d). This simple estimation does not give reliable results for very low densities (the region which is shaded with gray). For high positive and negative gate voltages the relation between carrier density and gate voltage for both samples is almost linear, as expected. Especially in the n-regime the two curves fall on top of each other, meaning that the magnetoresistance traces in a) and b) should be very comparable in carrier density. The Hall mobilities reach values on the order of $600 \times 10^3\,\mathrm{cm^2(Vs)^{-1}}$ in the n-regime ($V_{\mathrm{TG}} > 0\,\mathrm{V}$), which as shown in Figure 7.1 is among the higher values reported for HgTe 3D TIs. In p-regime, the values decrease to values on the order of $85 \times 10^3\,\mathrm{cm^2(Vs)^{-1}}$, which is almost a factor of seven lower than for comparable n-densities. These values are quantitatively comparable for both samples.

It seems that the two different etching methods result in a similar behavior in low magnetic fields, where the whole plane of the sample conducts. Strong deviations occur at high magnetic fields, where edge channel conduction dominates. Other samples, prepared by ICP etching (cf. Chapter 8) also show proper quantization and vanishing 4-point resistance. The deviations from the expected QHE behavior in samples prepared by the more invasive etching method contradicts the side surface TSS as mechanism for these deviations. It seems more likely that unintentional damage at the mesa edge induced by the etching method is responsible for the nonvanishing 4-point resistance and deviation from the expected QHE plateau values.

Further support for this explanation is found in HgTe 3D TI microstructures, which show another distinct artifact. This can be demonstrated with samples *Q2696 ch 1* and *Q2696 ch 2*. Wafer *Q2696* includes a 73 nm thick HgTe layer, sandwiched between 75 nm thick buffer and cap layers, grown on a CdTe substrate. The samples contain several channel structures with widths $W = 16\,\mu\mathrm{m}, 8\,\mu\mathrm{m}, 4\,\mu\mathrm{m}, 2\,\mu\mathrm{m}$ and an aspect ratio of $W : L = 1 : 10$ between voltage probes. All channels allow for a 4-point measurement of the longitudinal resistance, but only the 16 µm channel is equipped with voltage probes to measure Hall voltages. Optical microscope images of one sample are shown in Figure 7.3. The important difference is that sample *Q2696 ch 2* has been structured by means of IBE, while sample *Q2696 ch 1* was structured by the standard wet etching process. Another difference is that sample

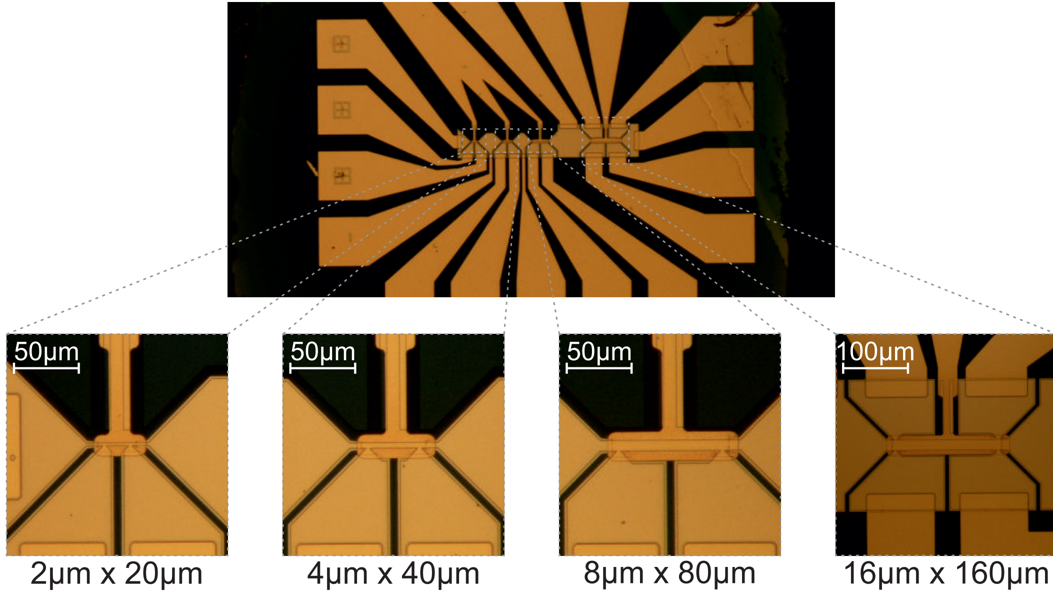

Figure 7.3: Optical microscope images of sample *Q2696 ch 2*. The actual channel structures are enlarged to resolve more details. The dimensions of the channels (width × length) are indicated and refer to the parts between voltage probes.

Q2696 ch 1 is equipped with the HfOx gate insulator, while sample *Q2696 ch 2* is equipped with the SiO_2/Si_3N_4 insulator. The samples were not processed in parallel, but independently. The 2 µm wide channel on sample *Q2696 ch 1* could not be measured due to a short between the top gate and one of the voltage leads.

Figure 7.4a) shows the longitudinal resistance R_{xx} of several channels on sample *Q2696 ch 2* as a function of top gate voltage. The blue curve shows the result from the 16 µm wide channel. It shows a low resistance for high gate voltages, passes through a sharp maximum of 1.3 kΩ at 0.55 V and then decreases for lower gate voltages. Measurements in this channel at small magnetic fields indicate that the gate voltage of zero total charge is close to 0 V.[2] Several changes appear for smaller channel widths. First, the peak in the longitudinal resistance moves towards lower gate voltages (−0.6 V for 8 µm, −1.5 V for 4 µm, and not observable in the hysteresis-free range for 2 µm). Likewise, the gate voltage of zero total density is shifted to lower gate voltages (0.05 V for 8 µm, −0.85 V for 4 µm, and not observable in the hysteresis-free range for 2 µm, not shown). Second, the maximum resistance increases considerably when going to smaller channel widths, even though the aspect ratio is similar. The third change is more visible when normalizing and shifting the resistance with respect to the peak position. Figure 7.4b) shows

[2]Note that the point of zero charge carrier density is estimated from the maximum longitudinal resistance at a small perpendicular magnetic field, cf. Section 8.2. For the narrow channels this is necessary since only the longitudinal resistance is measured. For the 16 µm channel the low-field Hall data gives comparable results.

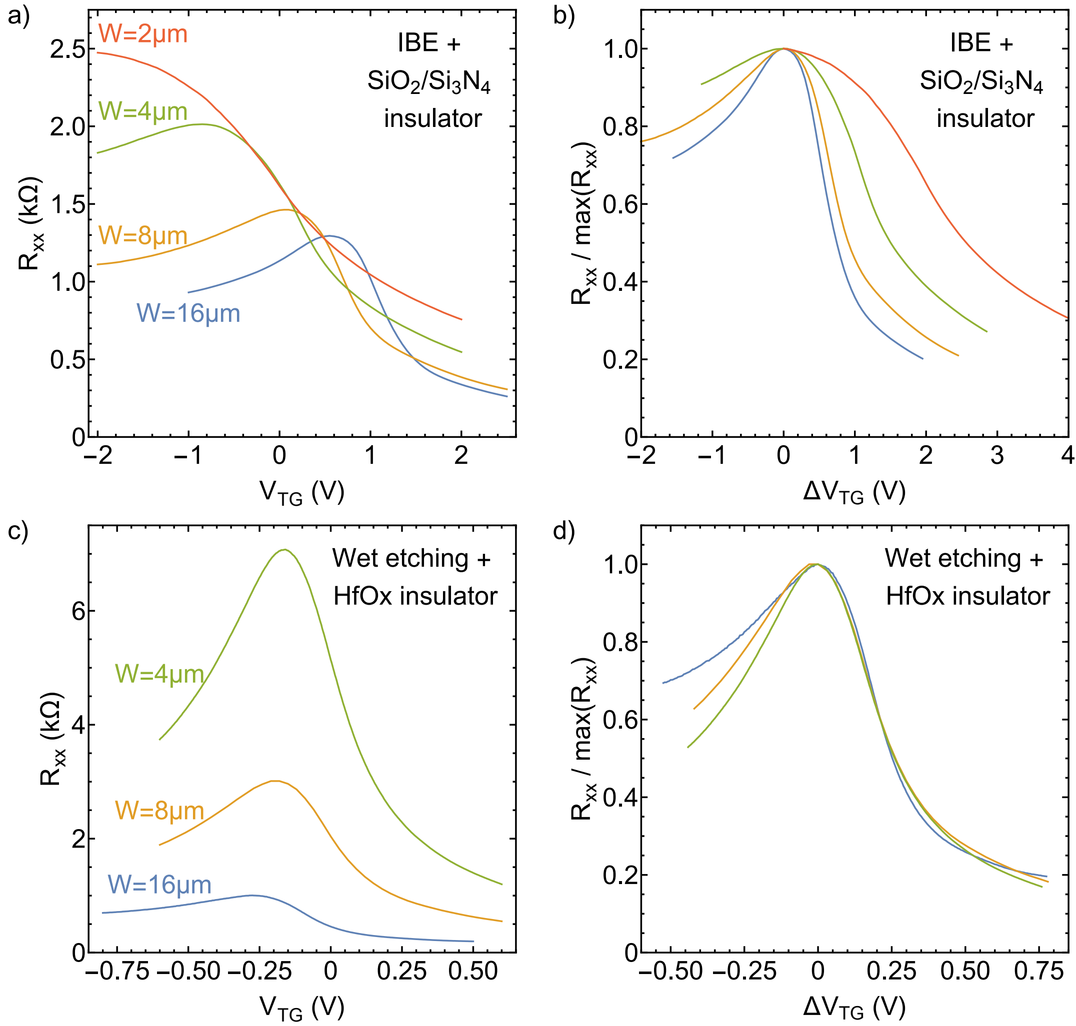

Figure 7.4: Comparison of samples *Q2696 ch 1* and *Q2696 ch 2*. a) Longitudinal resistance R_{xx} as a function of top gate voltage V_{TG} for channels on sample *Q2696 ch 2* with different widths W. b) Same data, but with R_{xx} normalized to the maximum resistance as a function of gate voltage, relative to the maximum position $\Delta V_{\mathrm{TG}} = V_{\mathrm{TG}} - V_{\mathrm{TG,\,max}(R_{\mathrm{xx}})}$. The color code corresponds to the color code in a). c) Longitudinal resistance R_{xx} as a function of top gate voltage V_{TG} for channels on sample *Q2696 ch 1* with different widths W. d) Same data, but normalized as explained in b). All measurements were done at $T = 1.4\,\mathrm{K}$.

for all channels the normalized resistance $R_{xx}/\max(R_{xx})$, which is shifted so that the maximum values coincide at $\Delta V_{TG} = 0\,V$. Plotting the data in this way demonstrates a significant broadening of the resistance peak which occurs when decreasing the channel width.

These changes are likely caused by unintentional doping of the layer stack close to the mesa edge. This effect becomes more dominant at smaller sample sizes. First of all, the observed overall shift in the ground density (seen as a shift of the peak position to more negative gate voltages) is consistent with an overall n-doping. Second, doping will not only take place in the HgTe layer itself, but also in the buffer and cap layers. It seems that the doped cap layer can partially screen the electric field from the top gate, thereby reducing the gate action. This is seen as a broadening of the resistance peak at low carrier densities. Third, the overall resistance increase can be understood from lowering the mobility due to crystal defects introduced by unintentional doping. This point is more difficult to evaluate, though, since additional doping can heavily change the electrostatics in the slab and may thereby also provide a possibility to decrease the resistance as observed in HgTe QWs (cf. Section 4.3).

A direct comparison with sample *Q2696 ch 1*, which should not display changes due to unintentional doping, can help to check these hypotheses. Figure 7.4c) shows the longitudinal resistance as a function of gate voltage for three channels with differing width. There is also an overall increase in resistance when going to smaller channel widths. The peak positions, however, hardly shift in gate voltage. The small shift observed when going from the 16 μm wide channel to the smaller ones might be due to the fact that it has been measured in a different cooldown cycle. Figure 7.4d) shows the gate dependent sample resistances, normalized and shifted as in b). In this case, the curves are almost identical for positive ΔV_{TG} and still very similar for negative ΔV_{TG}. The peak widths become slightly narrower when going to smaller channel widths.

These differences proof that an etching method, which does not induce doping of the mesa edges allows to preserve sample properties. Neither does the gateability suffer, nor does the ground density shift. The remaining width-dependent change is a dramatic increase in resistance, which is even stronger in sample *Q2696 ch 1* than in sample *Q2696 ch 2*. There are several possible explanations for this observation, which might even coexist and amplify each other. One important point is the outstandingly high mobility of wafer *Q2696*. It is expected (and will be discussed in more detail in Chapter 11) that micrometer-sized channels display a characteristic increase in resistance due to scattering of charge carriers at the boundaries of the channel [39]. Furthermore, the very high sample quality may increase the impact of single impurities in the channel. While in big samples (i. e. with typical dimensions much larger than the impurity mean free path) resistance is an averaged transport quantity, a narrow channel can dramatically change its resistance due to even a single impurity. Lastly, the effective width of the channels that can actually participate in transport is not known for sure. The effect of the isotropic etching procedure was considered when making the sample layout for wet etching. Optical

microscope images suggest, however, that the true aspect ratios are rather 11.5, 10.9, and 10.3 for the nominally 4 µm, 8 µm, and 16 µm wide channels, respectively. It is also not completely clear if the top gate electrode, which is wrapped around the mesa, may have a negative impact on transport close to the mesa edge. While it is difficult at this point to unambiguously quantify each of the described effects, one may note that an increase in resistance is not surprising, but rather expected. Part III contains data from other sets of HgTe microstructures, whose properties are fully compatible with the interpretation given here.

On the whole, it seems very likely that artifacts previously observed in both macroscopic HgTe Hall bars as well as, more recently, in microstructures originate from the well-known problem of unintentional doping of mesa edges. The results in this thesis are thus mostly based on samples which have been fabricated by ICP or wet etching to avoid these issues.

7.3 Problems with contacting devices in magnetic fields

Another technical problem related to HgTe-based layer systems is the difficulty to reliably contact devices in high magnetic fields. The reason for this is partially related to the device design. Figure 7.5 shows optical images of two samples, *Q2696 HB ICP* and *Q2843 HB ICP 2*, which are examples of the two standard designs for optical Hall bar structures. Both contain parts which are covered with the top gate electrode and define the actual device that shall be investigated by means of transport experiments. Ohmic contacts to the HgTe layer are realized with AuGe/Au pads. In between there are regions which are neither covered by the top gate nor the contacting metal layer, called “ungated regions” henceforth. In Figure 7.5 examples of those regions are highlighted by red circles. The advantage of this procedure is the possibility to encapsulate and thus protect the etched mesa below the insulator material before proceeding with other lithography steps (cf. Appendix A). It has been shown already in [42] that the ungated regions can create measurement artifacts in HgTe 2D EGs when the carrier density is very low. The same effect may also be of importance in HgTe 3D TI samples.

A more detailed view of one contact lead is depicted in the inset to Figure 7.6a). The lead contains three distinct areas: One in which the mesa is covered by the top gate electrode, one which is covered by the ohmic contact metal (AuGe), and one which is not covered by any of these. In high magnetic fields, when the sample is in the edge channel regime, there will be a different number of propagating edge channels in each of these regions. For simplicity the AuGe contacts can be considered ideal in the sense that they are reflectionless [60]. Since the as-grown HgTe layers are close to intrinsic, the ungated regions can easily have a smaller total carrier concentration than the gated regions at high gate voltages. In other words, the number of occupied edge channels is lower in the ungated regions.

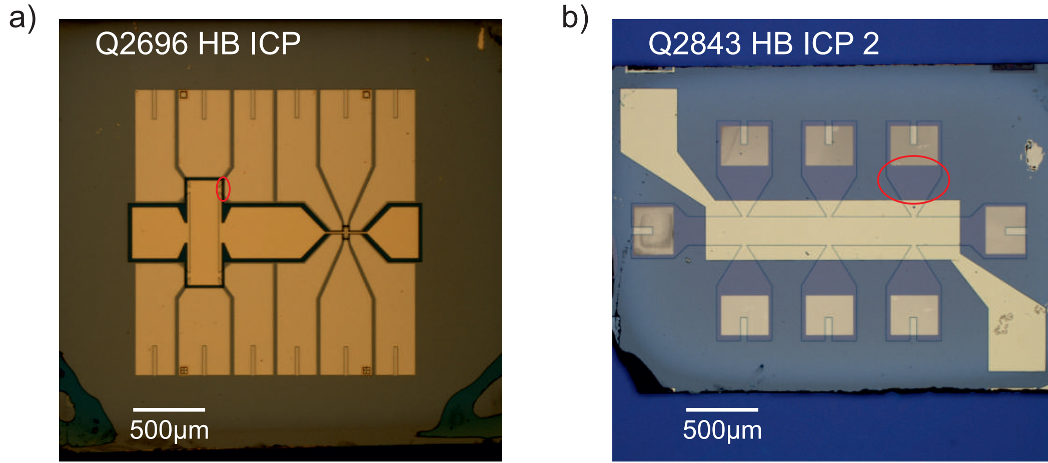

Figure 7.5: Ungated regions in the standard designs for optical Hall bar structures. a) Shows an optical image of sample *Q2696 HB ICP*, while b) shows an optical image of sample *Q2843 HB ICP 2*. The red circles highlight exemplary ungated regions, which are neither covered by the top gate electrode nor the AuGe/Au contact layer.

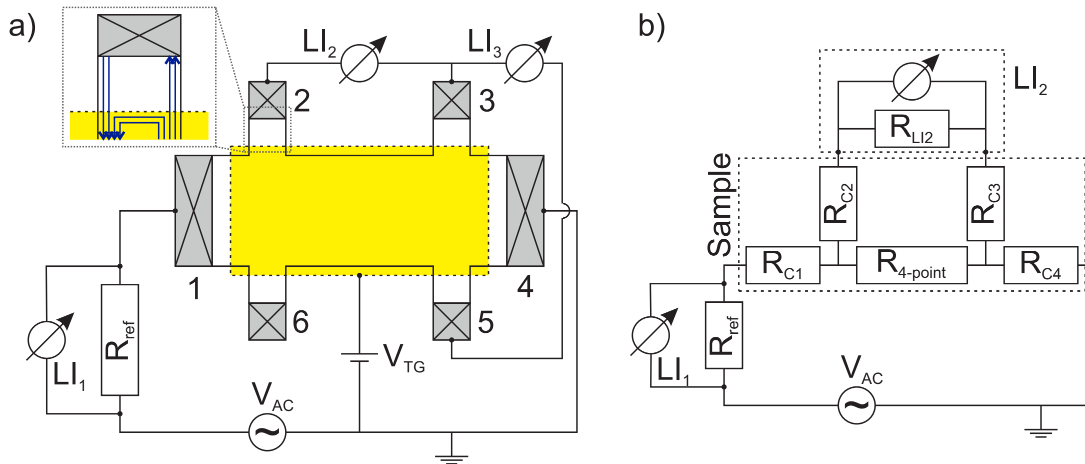

Figure 7.6: Measurement scheme and circuit schematics in standard Hall bars. a) Standard measurement scheme for Hall bars, including current contacts (1, 4), voltage probes (2, 3, 5, 6), and a top gate electrode at potential V_{TG}. An AC excitation voltage V_{AC} is applied over the sample and a known reference resistor R_{ref}. Voltage drops are measured with Lock-In amplifiers LI1, LI2, and LI3. Inset: Zoom onto one contact, including a sketch of the propagating edge channels in the QHE regime. b) Simplified circuit diagram of the measurement, including the input impedance of LI2, R_{LI2}, and the resistances of ungated contact regions, $R_{\mathrm{C1}}, R_{\mathrm{C2}}, R_{\mathrm{C3}}, R_{\mathrm{C4}}$.

This situation is reminiscent of experiments with QPCs [83] in GaAs/AlGaAs 2D EGs, which have been used as current injectors or voltage probes to measure SdH oscillations in high magnetic fields. It was found that depleting the QPC leads to selective coupling between LLs in the bulk of the sample and the contacts, which results in a difference in occupation for different edge channels. SdH oscillations could be suppressed by adjusting the QPC settings in these experiments. The difference in occupation can sustain as long as there are no scatterers, which equilibrate the edge channels [84]. This implies that high-quality samples are more prone to display artifacts due to unequilibrated edges channels.

An additional problem is the strong magnetoresistance observed in HgTe 3D TI samples close to charge neutrality. Figure 7.6b) shows a simplified circuit diagram of the 4-terminal measurement shown in a), which explicitly includes resistances to account for ungated regions in the current leads (R_{C1} and R_{C2}) and two voltage leads (R_{C3} and R_{C4}). In an idealized situation, the voltage leads do not carry current, so that the measurement yields the 4-terminal resistance $R_{\text{4-point}}$ of the sample. However, once the resistance of the voltage leads is comparable to the input impedance of the Lock-In amplifiers (10 MΩ for the SR124 [85], which is used for most measurements in this thesis), the total potential differences will partially drop there. What is measured may thus be only a small fraction of the actual signal. In addition, the excitation current drops significantly once the current leads present a high series resistance. (Note that the excitation voltage, not current, is kept constant in the experiments in this thesis.) In this situation the measurements are much more sensitive to uncertainties like constant offsets of the Lock-in amplifiers and noise. In brief, the magnetic field-induced high resistivity of current and voltage leads resembles a transition to fully insulating leads. In this extreme situation, one would obviously not be able to perform any kind of resistance measurement.

The problems related to ungated regions can be demonstrated in HgTe samples grown on conducting substrates [21]. The substrate can be contacted and used as global back gate [86], which allows to change the carrier density in current and voltage leads. Sample *Q2843 HB ICP 2* is equipped with such a back gate. The lithographically defined top gate on this sample does not fully cover the contact leads (cf. Figure 7.5). Figure 7.7a) shows the longitudinal, R_{xx}, and transverse resistance, R_{xy}, as a function of the magnetic field B, for different values of the back gate voltage V_{BG}. These measurements were done with a top gate voltage of $V_{\mathrm{TG}} = 0.2\,\mathrm{V}$ and at a base temperature of 150 mK. For a high positive back gate voltage of $V_{\mathrm{BG}} = 10\,\mathrm{V}$, the measurement shows a typical QHE as described before. There is a slight deviation of R_{xy} from the expected values, which is on the order of 2 % at 4.5 T and thus slightly higher than the experimental uncertainty of $\approx 1.4\,\%$. (Since this measurement was not optimized for an absolute resistance measurement, this deviation should not be over-interpreted, though.) At $V_{\mathrm{BG}} = 0\,\mathrm{V}$, a clear QHE can be observed only up to $\approx 2.5\,\mathrm{T}$. For higher fields, the measured R_{xx} and R_{xy} drop to negative values and show strong fluctuations. At $V_{\mathrm{BG}} = -10\,\mathrm{V}$, there are no strong fluctuations, R_{xx} remains positive, and R_{xy} increases mostly

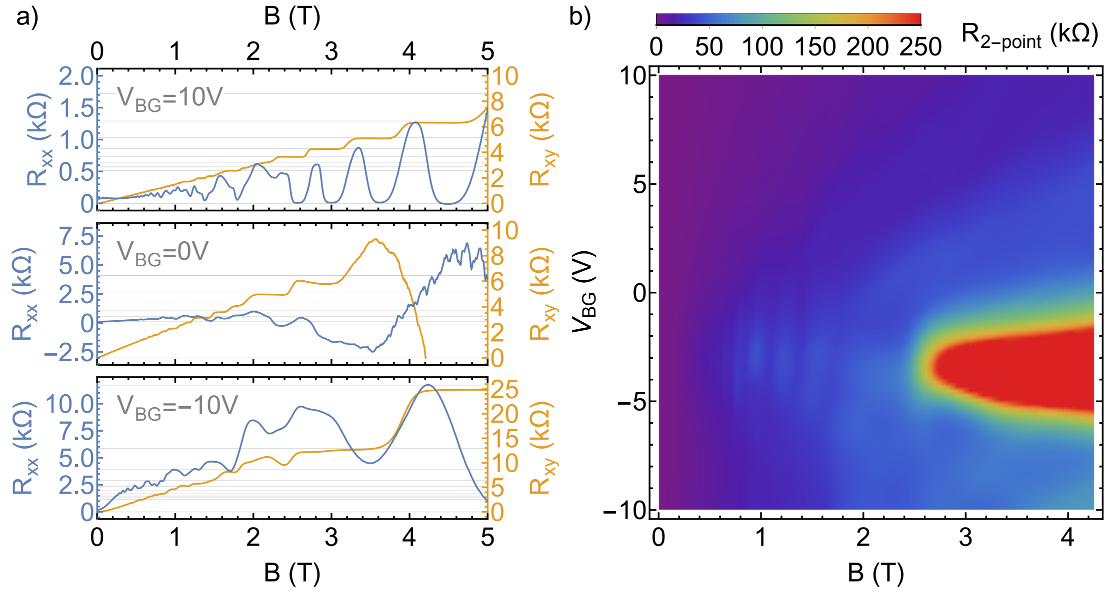

Figure 7.7: Effect of back gate voltage V_{BG} on measurements of the QHE in sample *Q2843 HB ICP 2*. a) Longitudinal, R_{xx}, and transverse resistance, R_{xy}, as a function of magnetic field, B, for different values of V_{BG} as indicated. b) Two-point resistance $R_{\text{2-point}}$ as a function of V_{BG} and B as color code. All measurements were done at a top gate voltage of $V_{\mathrm{TG}} = 0.2\,\mathrm{V}$ and a temperature of 150 mK.

monotonically with B.

These results can be linked to the preceding discussion by considering the two-terminal resistance $R_{\text{2-point}}$ (i. e. the resistance between contacts 1 and 4 in Figure 7.5a)) of the sample. This resistance includes the resistance of the ungated regions in the current leads. Figure 7.7b) shows the two-terminal resistance of sample *Q2843 HB ICP 2* for a wide selection of parameters. Note that this measurement was done in a separate measurement, with a slightly reduced range of B as compared to a). As a general trend, $R_{\text{2-point}}$ increases with B, albeit with a strongly V_{BG}-dependent slope. For $B = 4.26\,\mathrm{T}$, $R_{\text{2-point}}$ reaches a pronounced maximum at $V_{\mathrm{BG}} = -4.4\,\mathrm{V}$ and decreases rapidly for higher and lower back gate voltages. Even without a detailed understanding of the interplay of top gate and back gate (cf. Section 8.2) it is reasonable to interpret the peak in $R_{\text{2-point}}$ as a (total) carrier density minimum. The small-field Hall slopes in Figure 7.7a) show that the total density in the gated region decreases with V_{BG}, but remains n-type in the investigated parameter range. The total carrier density minimum can thus be assigned to the ungated regions. A small total carrier density in the leads causes pronounced artifacts in the QHE measurements even at small magnetic fields, which level off as V_{BG} is driven away from this minimum. For the measurements in a) without artifacts, the two-terminal resistance is well below 50 kΩ ($V_{\mathrm{BG}} = 10\,\mathrm{V}$) and 80 kΩ ($V_{\mathrm{BG}} = -10\,\mathrm{V}$). For the measurement at $V_{\mathrm{BG}} = 0\,\mathrm{V}$, which displays

strong artifacts, $R_{2\text{-point}}$ reaches $100\,\mathrm{k\Omega}$ at $2.7\,\mathrm{T}$ and approaches $1\,\mathrm{M\Omega}$ at $5\,\mathrm{T}$.[3] These results indicate that problems related to the contacts can indeed be switched on and off in the same device by changing the carrier density in the ungated leads.

In addition to including a back gate, there are other possibilities to change the carrier density in areas not covered by the top gate. One possibility is in-situ illumination with an LED. This procedure was tested on sample *Q2696 HB ICP*. It reduced the pronounced measurement artifacts. The induced changes were not very reproducible, however. More promising is the use of modulation doping layers [87] which induce a constant density shift. This approach allows for high quality QHE measurements in HgTe 3D TI devices up to high magnetic fields (cf. Section 8.2 of this thesis and Reference [79]). It is also possible to avoid ungated regions by making the top gate electrode overlap the metallized part of the ohmic contacts. This approach has been applied to HgTe microstructures in the past [42] as well as to some micrometer-sized devices in this thesis. A systematic investigation and description can be found in Reference [88].

[3] These values have to be understood as estimates, since the reference resistance used in this measurement was $R_{\mathrm{ref}} = 9.998\,\mathrm{k\Omega}$. Absolute and relative uncertainties in the measurement of small voltages over R_{ref} can cause huge uncertainties regarding the absolute values of $R_{2\text{-point}}$. However, the qualitative behavior is correct.

8 Identification and manipulation of topological and trivial surface states in HgTe 3D TIs

The previous chapter has detailed the modifications needed to obtain high-quality measurements of HgTe 3D TI layers. It is now time to turn to improvements in understanding this system, which is one of the main goals of this thesis. This chapter will first introduce measurements on a pristine HgTe sample, which is similar in principle to samples that have been discussed in literature before. The main differences are the use of low-damage lithography and the understanding of possible measurement artifacts. This step is necessary to make a connection to previous work. The following section focuses on reproducible manipulation of the bottom TSS, which has not been achieved with a comparable level of detail and understanding before. The third section connects the experimental findings to more recent developments in modeling the band structure of HgTe 3D TIs, with a particular focus on the different carrier systems contributing to transport.

8.1 Experimental identification of surface states of pristine HgTe layers in low magnetic fields

Sample *Q2696 HB ICP* can be used to understand properties of a pristine, high-mobility 3D TI layer, including the already discussed contact problems in magnetic fields. In the following, only data from the big Hall bar (dimensions $200\,\mu\mathrm{m} \times 600\,\mu\mathrm{m}$) will be discussed. The overall sample properties are introduced by considering gate voltage dependent measurements. Figure 8.1a) shows the longitudinal resistance R_{xx} as a function of top gate voltage V_{TG} without magnetic field and with a small perpendicular magnetic field of $B = 0.3\,\mathrm{T}$. Also included is the transverse resistance R_{xy} with the magnetic field of 0.3 T. The zero-field resistance shows an overall increase when gating from positive to negative gate voltages. At $V_{\mathrm{TG}} = 0.2\,\mathrm{V}$ the resistance includes a sharp peak. The longitudinal resistance becomes much larger upon application of a small magnetic field, i. e. the sample shows a strong magnetoresistance. A very pronounced peak is observed at $V_{\mathrm{TG}} = -0.7\,\mathrm{V}$, with the maximum resistance value being roughly 90 times higher than without magnetic field. The transverse resistance shows positive values for top gate voltages $V_{\mathrm{TG}} > 0.9\,\mathrm{V}$, indicating overall n-type transport. For

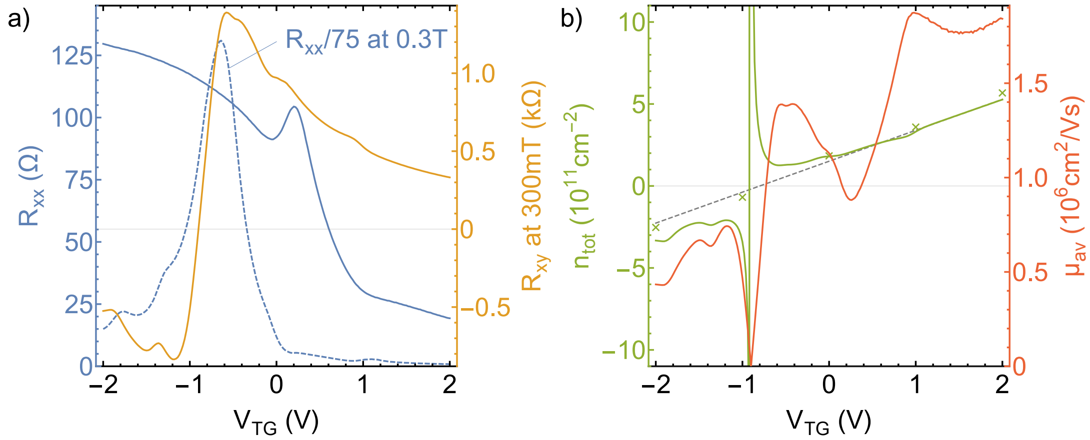

Figure 8.1: Basic characterization of sample *Q2696 HB ICP* at $T = 30\,\mathrm{mK}$. a) Longitudinal resistance R_{xx} at $B = 0\,\mathrm{T}$ (solid blue line) and $B = 0.3\,\mathrm{T}$ (dashed blue line), and transverse resistance R_{xy} at $B = 0.3\,\mathrm{T}$ (orange line), as a function of top gate voltage V_{TG}. R_{xx} at 0.3 T has been divided by 75 to fit the same scale. b) Total density n_{tot} (green line) and averaged mobility μ_{av} (red line) as a function of gate voltage, obtained from the data in a). Green crosses mark densities obtained from fitting magnetic field sweeps as shown in Figure 8.2a) through c). The gray dashed line is a fit to the green line in the range V_{TG} =1 V to 2 V.

$V_{TG} < 0.9\,\mathrm{V}$ the value is negative, indicating overall p-type transport. Thus, the point of sign reversal is close to, but not exactly at, the maximum longitudinal resistance position with finite magnetic field.

Figure 8.1b) compares the total carrier density n_{tot} and Drude mobilities μ_{av}, obtained from the data in a) via Equations 7.2 and 7.3. The density variation is linear with gate voltage for overall n-densities. The divergence for small total densities is an artifact caused by division by zero. Extrapolating the gate action to p-regime (gray dashed line) shows a small deviation between expected and measured values. A more accurate carrier density estimate is achieved by fitting the transverse resistance for a range of magnetic field values. The chosen magnetic field range for the linear fitting procedure is $B = 0.2\,\mathrm{T}$ to 1 T in this case. The results for a selection of gate voltages are shown in figure 8.1b) as crosses. The more elaborate approach yields a linear relationship between density and gate voltage as expected. This shows that the apparent deviation seen in the simple analysis is due to including only one data point for R_{xy} for estimating the slope. The mobility is very high on n-side, reaching $1.9 \times 10^6\,\mathrm{cm}^2(\mathrm{Vs})^{-1}$ at $V_{TG} = 1\,\mathrm{V}$. It decreases towards $V_{TG} = 0\,\mathrm{V}$ and rises again for negative gate voltages. Due to the aforementioned shortcomings of this analysis, the values for negative gate voltages might not be reliable, though.

These results for the gate-dependent resistances are quite puzzling. In usual

semiconductor devices, one expects to observe a maximum in longitudinal resistance at the smallest total carrier density. The 3D TI sample, in contrast, shows only a minor resistance peak at a clearly nonzero total carrier density. The actual zero-density point is almost featureless. Instead, the resistance further increases when moving away from the zero-density point towards more negative gate voltages. Clearly, a more dedicated analysis of this sample is needed.

One way to obtain more information is a careful analysis of transport properties in quantizing magnetic fields. Figures 8.2a) through c) show the longitudinal and transverse resistance as a function of perpendicular magnetic field for several top gate voltages. For all gate voltages, the longitudinal resistance shows pronounced quantum oscillations, while the transverse resistance develops in a step-like fashion as expected for the QHE. As mentioned in Section 7.3, this sample is prone to show contact problems in high magnetic field due to low-density ungated regions. Indeed, the longitudinal resistance shows features which may be attributed to a nonideal voltage probe. An example is the "plateau" in the longitudinal resistance in the field range of 2.6 to 4.6 T in b). Since the transverse resistance is quantized in this field range, one would actually expect the 4-point longitudinal resistance to be zero.[1] The following considerations are thus based on the transverse resistance, which contains a similar amount of information as the longitudinal resistance. Transitions between plateaus occur whenever the Fermi energy passes through a LL, either due to varying the charge density in the system or the applied magnetic field. These transitions are easy to identify in the derivative of the transverse resistance, either with respect to magnetic field or gate voltage.[2] The latter is chosen, since the gate voltage is varied quasi-continuously in the measurement.

Figure 8.2d) shows the negative derivative of R_{xy} with respect to gate voltage for a fine grid of magnetic field and top gate voltage values. The color code starts at zero, since negative values are merely artifacts due to the sign reversal of the transverse resistance (cf. $V_{\mathrm{TG}} = -1.2\,\mathrm{V}$ to $-0.6\,\mathrm{V}$). This kind of plot is known as LL fan chart, since the purpose is to visualize the LL dispersion. Small numbers indicate for selected points the LL filling factor obtained from R_{xy}. The low-field LL fan chart for sample *Q2696 HB ICP* is rather complex and needs to be divided into several regions for interpretation. The region enclosed by dashed gray lines ($0\,\mathrm{V} < V_{\mathrm{TG}} < 0.8\,\mathrm{V}$) is a convenient starting point. Here one can observe mostly one pronounced set of LLs, which is strongly top gate dependent. Since LLs in this fan move to higher fields when increasing the electron concentration (i. e. when increasing the gate voltage), it corresponds to n-type carriers. This is also consistent with the filling factors, which decrease towards higher magnetic field values (e. g. transitions $6 \rightarrow 5$, $8 \rightarrow 7$, and $10 \rightarrow 9$). At certain values of the

[1] Strictly speaking, this is only true since at $V_{\mathrm{TG}} = 0\,\mathrm{V}$ only electron states contribute to transport. If both electrons and holes contribute, the expectation is in general different, cf. Section 9.3.

[2] A more common approach is to work with the derivative of $\sigma_{\mathrm{xy}} = R_{\mathrm{xy}} / \left(R_{\mathrm{xy}}^2 + \rho_{\mathrm{xx}}^2\right)$, since it avoids the discontinuity around the charge neutrality point. Here, however, the results for ρ_{xx} are not reliable.

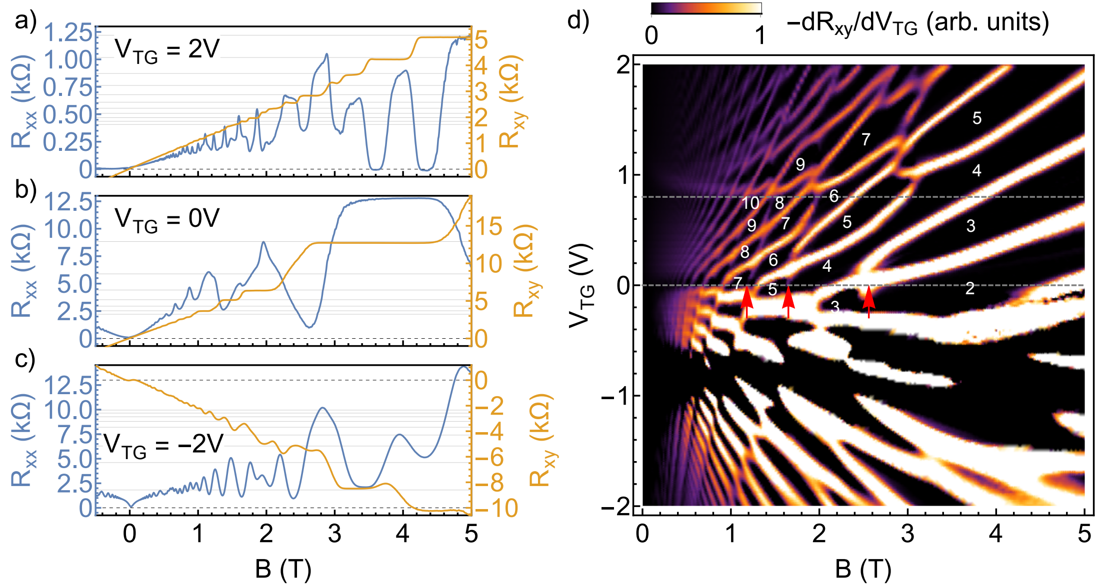

Figure 8.2: Magnetic field sweeps and LL Fan chart for sample *Q2696 HB ICP* at $T = 30\,\text{mK}$. a), b), c) Longitudinal resistance R_{xx} and transverse resistance R_{xy} as a function of magnetic field B for different top gate voltages V_{TG}. Dashed gray lines mark $R_{\text{xx}} = 0$ and $R_{\text{xy}} = 0$, while solid gray lines indicate expected plateau values for the QHE. d) LL Fan chart, obtained by plotting $-dR_{\text{xy}}/dV_{\text{TG}}$ in a color code as a function of magnetic field and top gate voltage. Numbers denote LL filling factors obtained from R_{xy}. Arrows and lines are explained in the text.

magnetic field, this fan is intersected by a second, much less pronounced fan with a weaker top gate dependence (cf. red arrows). The gate dependence, together with filling factor transitions, reveals that this fan also corresponds to n-type carriers. Previous works on HgTe 3D TIs have shown that transport in the overall n-regime is dominated by the TSSs [24, 25, 89]. Hence, the two n-type carrier systems observed here can be attributed to the TSSs. The top gate dependence indicates that the more pronounced fan corresponds to the top TSS. It partially screens the electric field induced by the top gate. This screening and the larger separation from the gate result in a weaker gate dependence of the bottom TSS.

It is also possible to check that only the two TSSs contribute to transport in the gate voltage window of 0 to 0.8 V. Figure 8.3a) shows a zoom of the fan chart. Green and red lines indicate approximate positions of LLs associated with the top and bottom TSS, respectively. The two sets of lines display crossings at a constant top gate voltage of $V_{\text{TG}} = 0.5\,\text{V}$ (cf. gray dashed line). The crossings of LLs show that the periodicity of the two LL fans is equal at $V_{\text{TG}} = 0.5\,\text{V}$. In other words, the two TSSs should have roughly the same occupation number here. Figure 8.3b) shows a high-resolution measurement of the transverse resistance as a function of magnetic field at this gate voltage. Up to $B \approx 1.5\,\text{T}$ the LL filling

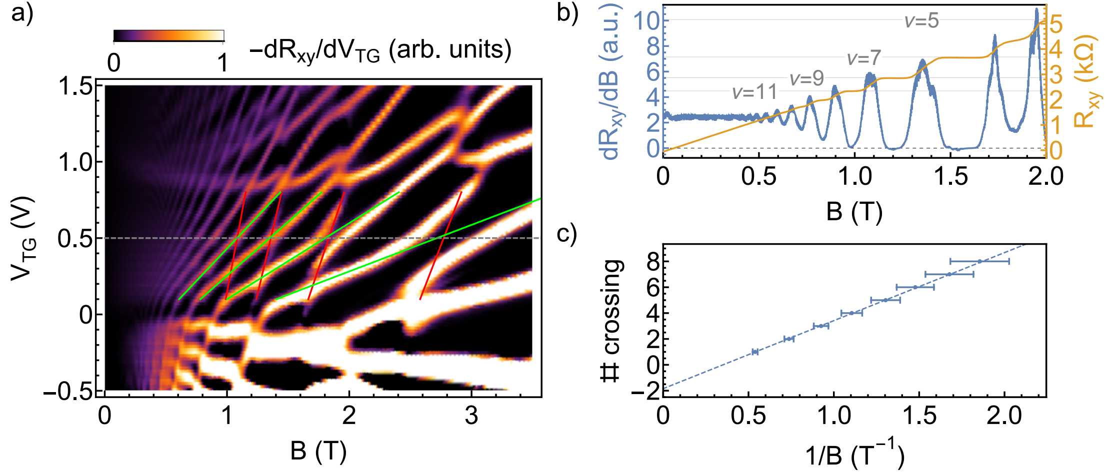

Figure 8.3: Equal density line of TSSs in sample *Q2696 HB ICP*. a) Zoom of the data in Figure 8.2d). Green (red) lines indicate the approximate positions of top (bottom) TSS LLs. b) Transverse resistance R_{xy} and dR_{xy}/dB as a function of magnetic field B at a top gate voltage of $V_{TG} = 0.5\,\mathrm{V}$, cf. dashed line in a). Gray lines indicate LL filling factors. c) Plot of integer numbers associated with maxima in dR_{xy}/dB versus corresponding $1/B$ positions. The dashed line is a linear fit.

factors change in steps of two and display only odd values. This is the expected and previously described [24] behavior for the situation of degenerate TSSs. The carrier density of the TSSs at this gate voltage can be evaluated quantitatively. A set of LL transitions associated with a carrier density n are periodic in $1/B$ with a spacing of [60]

$$\Delta\left(\frac{1}{B}\right) = \frac{e}{h}\frac{g}{n}, \tag{8.1}$$

where e is the electron charge, h Planck's constant, and g the spin- and valley degeneracy factors ($g = 1$ for TSSs in HgTe [24]). A plot of the LL transitions in b) versus $1/B$ is shown in Figure 8.3c). A linear fit to the data provides a slope of $(5.260 \pm 0.051)\,1/\mathrm{T}^{-1}$, corresponding to a carrier density of $(1.27 \pm 0.02) \times 10^{11}\,\mathrm{cm}^{-2}$ per TSS. The total density in the TSSs is thus $(2.54 \pm 0.04) \times 10^{11}\,\mathrm{cm}^{-2}$. This value agrees within uncertainties with the value of $(2.55 \pm 0.03) \times 10^{11}\,\mathrm{cm}^{-2}$ obtained from a linear fit to the low-field R_{xy} slope. These results proof that at a gate voltage of 0.5 V the only mobile carriers originate from the TSSs, consistent with the findings in [24].

The LLs related to the top TSS are so pronounced in Figure 8.2d), that they can be traced continuously to regions of higher and lower gate voltage. At high n-densities ($V_{TG} > 0.8\,\mathrm{V}$) they are superimposed onto another set of LLs. At lower gate voltages ($V_{TG} < 0\,\mathrm{V}$), and eventually reaching overall p-conductance, they become superimposed onto a set of LLs, which can be interpreted as a p-type LL fan. An important observation in these regions (high overall n- and p-densities) is

the change in gate dependence of the top surface. E. g. at $V_{TG} = 0\,V$, the slope of the TSS LLs with respect to gate voltage changes. In this case, the density change of the top TSS with gate voltage becomes weaker for $V_{TG} < 0\,V$. The same is true for $V_{TG} > 0.8\,V$. In the gate voltage range of 0 V to 0.8 V, the top TSS carrier density displays the strongest dependence on top gate voltage. The additional features seen at high and low gate voltages appear to partially screen the electric field applied by the top gate.

Since these features appear simultaneously with the TSSs, they are likely of a different origin. As explained in Chapter 6, it was suggested before that bands derived from the bulk band structure can contribute to transport [10, 25, 89]. The electrostatic potential induced by the top gate can give rise to the formation of massive p-type VPSs as in compressively strained HgTe layers [10]. Likewise, conduction band states may contribute to transport at high n-densities [25, 78, 79, 89]. This model implies a small gate range for sample *Q2696 HB ICP*, cf. gray lines in Figure 8.2d), in which only TSSs are populated. Outside this range the TSSs are superimposed with additional states. Tentatively, the additional p-states will be assigned to VPS from now on, while the additional n-states will be assigned to conduction band states. A more detailed and rigorous justification for this assignment will follow.

The superposition of a n-type carrier system (TSS) and a p-type carrier system (VPS) can explain the nonlinearity in transverse resistance that has been observed frequently in HgTe 3D TI samples in p-regime [25, 76, 89]. This effect has also been observed in sample *Q2696 HB ICP*, cf. Figure 8.2c). The high-mobility TSSs dominate at low magnetic fields, providing an electron-type sign of the Hall voltage, while at higher fields the total carrier density dominates, providing a hole-type sign of the Hall voltage. The superposition of different carrier systems also provides a qualitative explanation for the puzzling zero-field resistance as a function of gate voltage observed in this sample, cf. Figure 8.1a). When decreasing the gate voltage, the high-mobility TSSs are depleted and the resistance increases. Once the gate voltage is sufficient to populate additional bands, those will partially screen the electric field from the top gate. In addition, they screen charged impurities and thereby reduce the scattering of high-mobility carriers with impurities [90]. Hence, the resistance decreases. Upon further lowering the gate voltage, the continuing depletion of the TSS increases the resistance, albeit at a slower pace. A more quantitative discussion of this effect will follow in Section 8.2.1.

On the whole, the high-quality sample *Q2696 HB ICP* displays several features, which seem counterintuitive at first. However, these features can easily be explained within a revised model that includes the TSSs and in addition massive states which are linked to the bulk band structure of tensilely strained HgTe. There are two ways to proceed from here. From an experimental perspective, it is necessary to consider more high-quality samples, which do not suffer from the contact issues discussed in the chapter above. Ideally, these experiments should include a dedicated manipulation of both TSSs to confirm the postulated assignment of LLs and disentangle the contributions from additional states. This approach will be

the topic of the next section. From a theoretical point of view, a confirmation of the qualitative description with well-established band structure calculations seems necessary. A brief summary of this approach will be given in Section 8.3.

8.2 Manipulating both topological surface states

From a technological point of view, there are two ready-to-use possibilities to modify the bottom TSS contribution to transport: Either by introducing a modulation doping layer below the HgTe layer (static manipulation) or by using a conducting substrate as back gate. Both approaches have been in use in our group for HgTe-based 2D EGs [20, 81]. The modulation doping approach has been introduced in close collaboration with D. Mahler, who presented some of the data in his thesis to differentiate the different transport channels included in the revised HgTe 3D TI model [79]. For the sake of completeness, there will be some overlap and repetitions. The backgating approach has also been used for manipulating HgTe-based 3D TI layers before, albeit with somewhat unclear results [76]. The focus in the previous work was placed on the medium to high magnetic field regime ($B > 6\,\mathrm{T}$) and on overall n-densities. However, the focus in the thesis at hand will be placed on the low magnetic field behavior and extended to both n- and p-regime.

8.2.1 Introducing a modulation doping layer

Figure 8.4a) shows the layer stack of wafer *QC0502*, as grown by MBE. It is a typical example of layer stacks including a CdHgTe:I modulation doping layer. Due to the band offset the I donor electrons move to the HgTe layer. The remaining positively charged donors keep electrons close to the CdHgTe/HgTe interface and thus lead to an increased n-density at the bottom side of the HgTe layer [91].

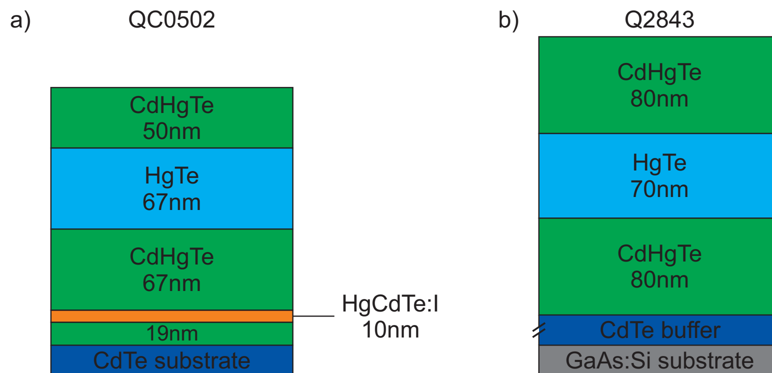

Figure 8.4: Exemplary layer stacks of wafers *QC0502* and *Q2843*, including a $\approx 70\,\mathrm{nm}$ thick HgTe layer and either a CdHgTe:I modulation doping layer, a), or a conducting GaAs:Si substrate which can be used as a back gate, b).

This is reminiscent of the effect of a gate electrode, with the main difference that modulation doping induces a static density shift which can not be changed in situ. The advantage over other doping techniques is the spatial separation of the active layer and charged donors, which leads to a potentially high carrier mobility [91].

Magnetotransport and Landau levels of a modulation doped sample

Sample *QC0502 HB ICP*, based on wafer *QC0502*, contains a Hall bar with dimensions 200 µm × 600 µm. It has been structured by means of ICP etching and contains a top gate layer stack. Figure 8.5a) shows the top gate dependence of the longitudinal resistance at magnetic fields $B = 0\,\mathrm{T}$ and 300 mT, together with the transverse resistance at 300 mT and 600 mT. The zero-field resistance displays a pronounced maximum at $V_{\mathrm{TG}} = -2.5\,\mathrm{V}$ and a smaller, but also well-resolved, peak at $-1.5\,\mathrm{V}$. This second peak is accompanied by the onset of a very pronounced magnetoresistance for $V_{\mathrm{TG}} < -1.6\,\mathrm{V}$. The low-field longitudinal resistance shows a pronounced peak at $V_{\mathrm{TG}} = -2.9\,\mathrm{V}$, which is close to the point of sign reversal of the transverse resistance ($-3.1\,\mathrm{V}$). It is interesting to note that these results are very similar to the ones obtained for the undoped sample *Q2696 HB ICP* (cf. Figure 8.1). The onset of strong magnetoresistance presumably marks the gate voltage at which additional p-type carriers are introduced. The large p-type carrier density screens impurities and increases the mobility of the TSSs at zero magnetic field. Figure 8.5b) shows the total carrier density n_{tot} and Drude carrier

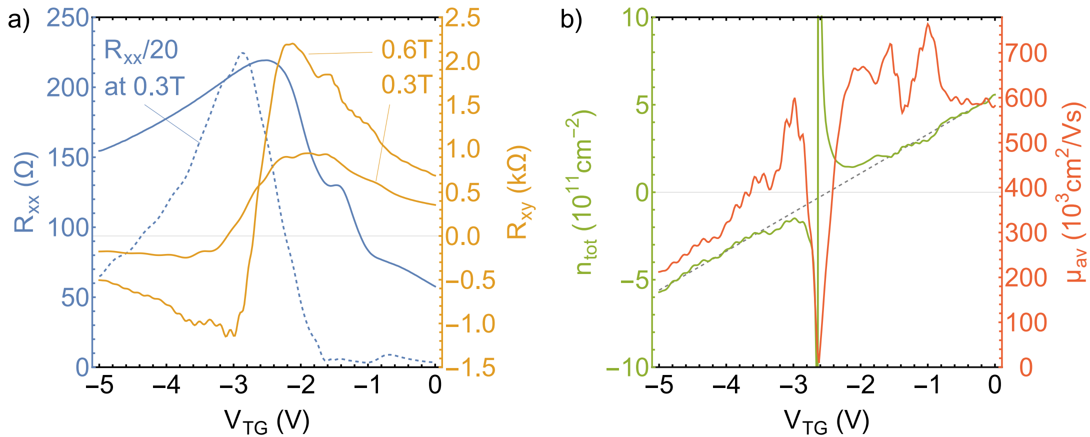

Figure 8.5: Basic characterization of sample *QC0502 HB ICP* at $T = 30\,\mathrm{mK}$. a) Longitudinal resistance R_{xx} at $B = 0\,\mathrm{T}$ (solid blue line) and 300 mT (dashed blue line), and transverse resistance R_{xy} at 300 mT and 600 mT (orange lines), as a function of top gate voltage V_{TG}. R_{xx} at a small magnetic field is divided by 20 to fit the same scale. b) Total density n_{tot} (green line) and averaged mobility μ_{av} (red line) as a function of gate voltage, obtained from the data in a). The gray dashed line is a linear fit to the green curve, excluding $V_{\mathrm{TG}} = -3$ to $-2\,\mathrm{V}$.

mobility μ_{av}, obtained from gate-dependent measurements at $B = 0\,\mathrm{T}$, $300\,\mathrm{mT}$, and $600\,\mathrm{mT}$. The carrier density develops linearly with gate voltage as expected, except for the narrow region around zero density, where this analysis is not reliable. The averaged carrier mobility is on the order of $600 \times 10^3\,\mathrm{cm}^2(\mathrm{Vs})^{-1}$ on n-side and decreases approximately by a factor of three towards most negative gate voltages. These values indicate a very high sample quality.

As for sample *Q2696 HB ICP*, it is instructive to consider a LL fan chart. The longitudinal and transverse resistance of sample *QC0502 HB ICP* have been measured for a fine grid of top gate and magnetic field values. The step size for magnetic field values B was very small at low magnetic fields and gradually increased towards higher fields to capture the $1/B$ dependence of quantum oscillations. Figure 8.6a) shows the longitudinal resistance in a logarithmic color code as a function of both top gate voltage and magnetic field. (Note that the high sample quality and the absence of contact issues allow the direct observation of LLs as maxima in the resistance. The fan chart of sample *QC0502 HB ICP* is not based on a derivative of measured values, in contrast to the fan chart of sample *Q2696 HB ICP*.) For comparison, a trace of this data at a constant top gate voltage of $V_{\mathrm{TG}} = -1.1\,\mathrm{V}$ is shown in Figure b). As expected, the longitudinal resistance displays pronounced SdH oscillations and decreases to zero in between maxima. The transverse resistance develops in a step-like fashion with plateau values corresponding to the expected values. The transitions between LLs are equally well resolved in the 2D plot in Figure a). In resemblance of sample *Q2696 HB ICP*, there is a gate voltage window, where mainly two sets of LLs are observed ($-1.7\,\mathrm{V} < V_{\mathrm{TG}} < -1.0\,\mathrm{V}$). Both sets are equally well resolved here and can be attributed to the TSSs. Different from the previous sample these sets can both be traced over a wide range of gate voltages. As before, the slope of LLs with gate voltage is not constant, but changes when additional features appear.

For lower gate voltages ($V_{\mathrm{TG}} < -1.7\,\mathrm{V}$), an additional LL fan is observed, which has p-type character. This clarifies the situation in sample *Q2696 HB ICP*, where the p-regime could not be analyzed in detail. The details of this p-type fan can be understood by considering traces, for example at a constant magnetic field of $B = 3.9\,\mathrm{T}$ as shown in Figure d). In the two-carrier regime ($V_{\mathrm{TG}} \lesssim 1.7\,\mathrm{V}$) this trace shows pronounced SdH oscillations in the longitudinal resistance, which make up the p-type fan. At the same time, the transverse resistance is properly quantized, yielding a well-resolved p-type QHE. The main difference to the n-type QHE in the same sample is that the filling factor changes in steps of two. A magnetic field-dependent trace taken at overall p-densities ($V_{\mathrm{TG}} = -4.4\,\mathrm{V}$), shown in Figure c), also displays the pronounced SdH oscillations. This trace shows, however, that the evolution of the transverse resistance is rather complex. For magnetic fields smaller than $B \approx 3\,\mathrm{T}$ it shows an oscillatory behavior. For higher magnetic fields the filling factors change in steps of two, comparable to the situation seen in trace d). Combining these information with the overall appearance of the LL fan suggests that the the p-type QHE is actually a superposition of several fans. The LLs originating from p-carriers seem to be doubly degenerate, which would

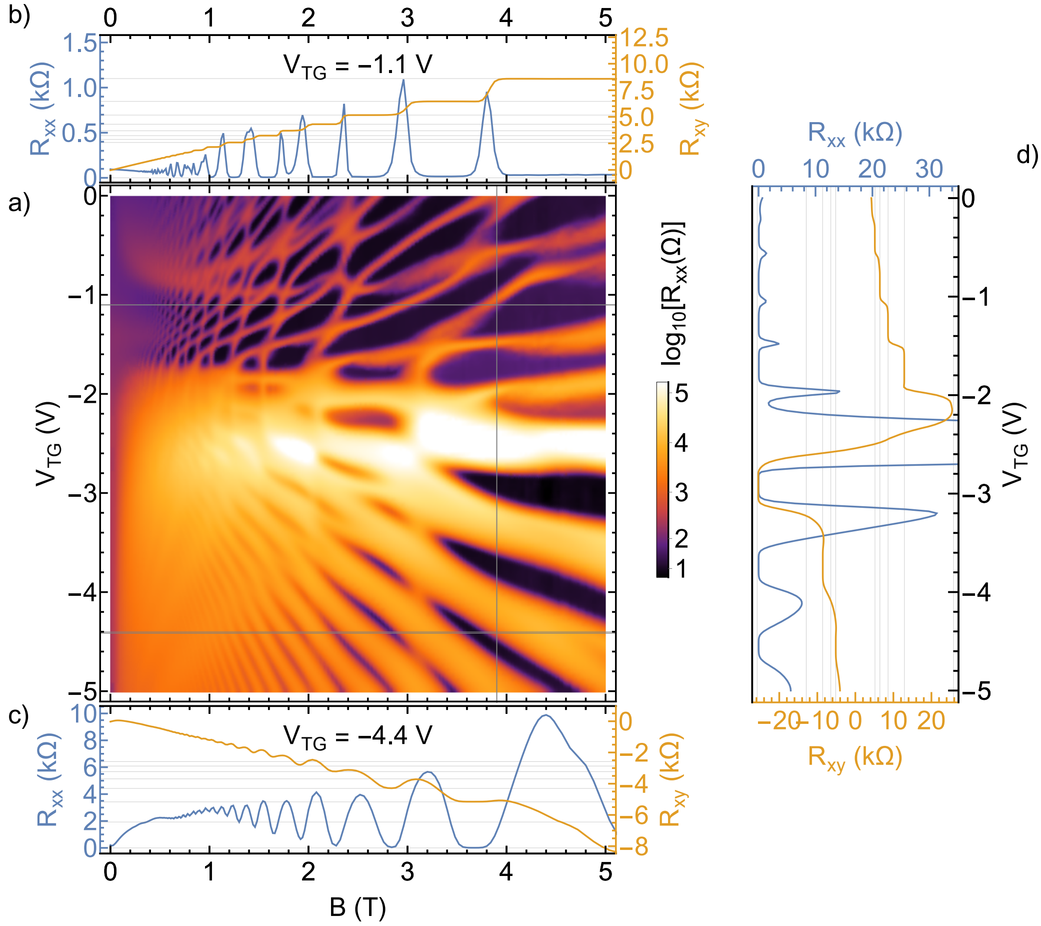

Figure 8.6: Fan chart measurement of sample *QC0502 HB ICP* at $T = 30\,\mathrm{mK}$. a) Longitudinal resistance R_{xx} as a function of magnetic field B and top gate voltage V_{TG}, displayed in a logarithmic color scale. Thin gray lines indicate positions of traces in Figures b), c), and d), extracted from the same measurement.

explain the filling factor changes in steps of two. A more detailed deconvolution of such a fan chart in its entirety will follow in Section 9.2. First, a more rigorous approach to obtain quantitative information from fan charts will be introduced.

Quantitative analysis with fast Fourier transformations

The high quality of sample *QC0502 HB ICP* allows for an automated method to disentangle different transport channels. This approach uses a fast Fourier transformation (FFT) to obtain carrier densities from the $1/B$ periodicity of SdH oscillations. A manual analysis of SdH oscillations to determine carrier densities has been applied to sample *Q2696 HB ICP* in this thesis and in previous works on HgTe 3D TIs [24, 76]. The manual analysis is difficult to apply when several sets of LLs are superimposed. The main problem is then to correctly bunch the

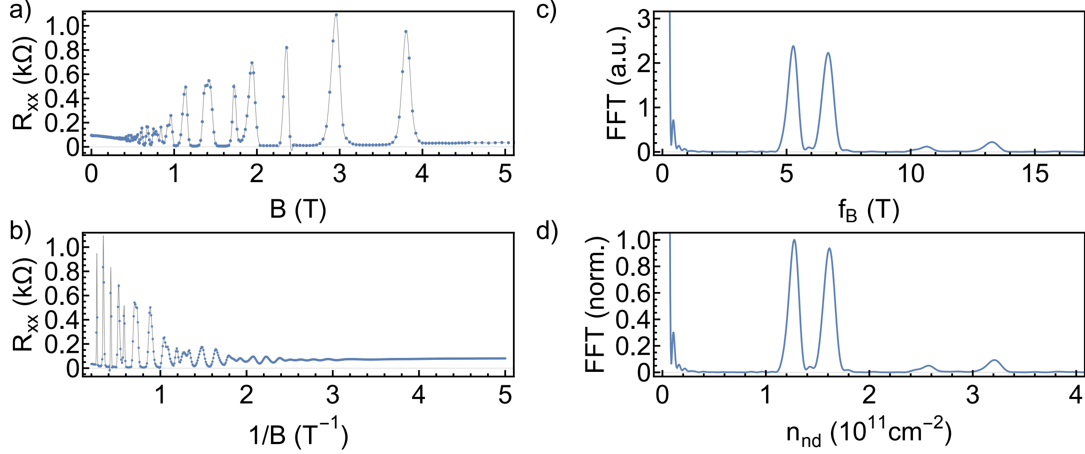

Figure 8.7: Illustration of the FFT approach to determine carrier densities in sample *QC0502 HB ICP*. a) Longitudinal resistance R_{xx} as a function of magnetic field B at $V_{\mathrm{TG}} = -1.1\,\mathrm{V}$. Blue are data points, gray is an interpolation function. b) Data points which are equidistant in $1/B$ are generated from the interpolation function. c) FFT spectrum of the data in a). d) Spectrum with frequency axis converted to density axis. The amplitudes have been normalized to the highest peak for $n_{\mathrm{nd}} > 0.2 \times 10^{11}\,\mathrm{cm}^{-2}$.

corresponding sets of LL transitions. In such a situation the FFT analysis can help to sort the data. In addition, the FFT approach is highly automatized and can be applied to large datasets. Application of the FFT approach to transport data obtained on HgTe 3D TI layers has also been reported elsewhere, e. g. in the supplementary material of [28]. A detailed description, together with a proof for the excellent reproducibility of the results has been given in [79]. A brief outline is given in the following and illustrated in Figure 8.7. All FFT analyses in this thesis were performed with built-in functions of the program Mathematica 12.0 [92], using standard techniques like zero-padding and windowing with a Hann window. The starting point is the longitudinal resistance as a function of magnetic field, e. g. at $V_{\mathrm{TG}} = -1.1\,\mathrm{V}$ in Figure 8.6a). The data points are first interpolated, cf. Figure 8.7a), to generate a set of points which are equidistant in $1/B$, cf. b). For this step it is crucial to measure R_{xx} on a fine grid of B values. The FFT of this data provides a spectrum of the individual frequencies f_B of SdH oscillations in $1/B$, as seen in c). A direct consequence of the nonsinusoidal character of the input data is the occurrence of higher harmonics, in this case at double the frequency. Finally, the spectrum can be normalized and the frequencies can be related to carrier densities by the relation $n_{\mathrm{nd}} = \frac{e}{h} f_B$. (The subscript “nd” denotes that this relation implicitly assumes a nondegenerate carrier system.) The result, as shown in d), is a spectrum of individual carrier densities at a given gate voltage. Repeating this analysis for a dense number of gate values allows to trace the

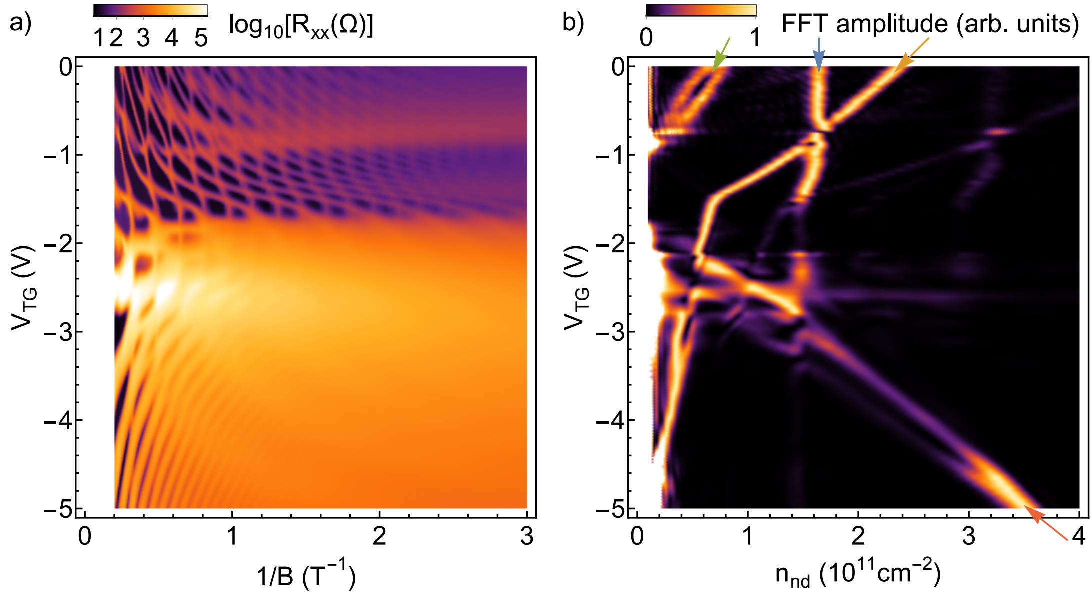

Figure 8.8: FFT analysis covering the full gate range in sample *QC0502 HB ICP*. a) Longitudinal resistance R_{xx} as a function of inverse magnetic field $1/B$ and top gate voltage V_{TG}, displayed in a logarithmic color scale. (Same data as in Figure 8.6a). b) Normalized FFT amplitude as a function of (nondegenerate) carrier density n_{nd} and top gate voltage, displayed in a linear color scale.

density change in individual conduction channels as a function of total density. This approach has been widely used for disentangling transport channels in DQW structures, e. g. to investigate the effect of negative compressibility [93, 94].

It is straightforward to apply this analysis procedure to the LL fan chart data for sample *QC0502 HB ICP*. Figure 8.8a) shows the same data as Figure 8.6a), but with the x-axis converted to $1/B$. This way of plotting clearly shows that the LL fans identified previously are periodic in $1/B$ for small values of B. Figure 8.8b) shows the result of the FFT analysis for all gate voltages and magnetic field values in the range 0.2 to 5 T. The x-axis is rescaled to carrier densities n_{nd} and the FFT amplitude is normalized with respect to the maximum amplitude for $n_{\mathrm{nd}} > 0.25 \times 10^{11}\,\mathrm{cm}^{-2}$. Four distinct lines are visible in the FFT spectrum. Most pronounced are two n-type carrier densities, which can be attributed to the TSSs. Those are the only densities visible for $V_{\mathrm{TG}} = -1.8\,\mathrm{V}$ to $-1\,\mathrm{V}$. From the different gate dependencies it can be deduced that the line which starts at a density of $2.4 \times 10^{11}\,\mathrm{cm}^{-2}$ ($V_{\mathrm{TG}} = 0\,\mathrm{V}$, cf. orange arrow) corresponds to the top TSS. It is strongly top gate dependent down to $V_{\mathrm{TG}} = -1.5\,\mathrm{V}$, kinks at this gate voltage, and continues with a smaller gate dependence to a density below $0.2 \times 10^{11}\,\mathrm{cm}^{-2}$ at $V_{\mathrm{TG}} = -5\,\mathrm{V}$. The other n-density (cf. blue arrow) shows only a small gate dependence in the window $V_{\mathrm{TG}} = -1.6$ to $-1\,\mathrm{V}$. Quantitatively, it changes from $1.6 \times 10^{11}\,\mathrm{cm}^{-2}$ at $V_{\mathrm{TG}} = 0\,\mathrm{V}$ to $1.4 \times 10^{11}\,\mathrm{cm}^{-2}$ at $V_{\mathrm{TG}} = -5\,\mathrm{V}$.

Both LL frequencies have higher harmonics at twice the fundamental frequency, creating faint additional lines. The other prominent line in the range $V_{\mathrm{TG}} = -1$ to 0 V (cf. green arrow) is likely related to bulk carriers as mentioned in Section 8.1. In the FFT, this feature appears to be splitted, pointing towards a twofold spin degeneracy which would be expected for bulk conduction bands in HgTe. The prominent p-type feature which is clearly visible in the gate range $V_{\mathrm{TG}} = -5$ to -2 V (cf. red arrow) corresponds to p-type carriers, the aforementioned VPSs. The line corresponding to p-type carriers appears to be splitted. However, the carrier difference between the two lines is exactly the same as the carrier density of the top TSS. It is thus likely that the faint line is simply the difference of fundamental frequencies. These kind of sum frequencies are common in FFT analyses of SdH oscillations and usually attributed to the oscillatory chemical potential (see e. g. Reference [95]).

Figure 8.9a) summarizes the individual carrier densities obtained by FFT with the assignment explained above. It includes the contributions from top and bottom TSS (n_{TS} and n_{BS}) as well as additional n-type and p-type carriers (n_{nb} and n_{pb}), which are likely related to bulk-derived states. These densities can be compared to the total density n_{tot} that was obtained by linearly fitting the experimental results (cf. Figure 8.5b). In principle, the sum of all individual densities should be equal to n_{tot}. This is indeed the case when considering a double degeneracy of p-states. As discussed above, this double degeneracy is consistent with the evolution of LL filling factors in steps of two. The agreement between the FFT results and the directly obtained density values is an important consistency check for this approach. The main deviations are found close to band edges ($V_{\mathrm{TG}} \approx -1.6$ V and -1 V, cf. grid lines) – an outcome to be expected since for very small carrier densities, LLs only occur for small magnetic fields where they cannot be resolved clearly.

Modelling the zero-field longitudinal resistance

It is now possible to make use of the quantitative FFT results to model the low-magnetic field transport in the HgTe 3D TI system. As a simplification it can be assumed that each carrier species with density n_i and charge $q_i e$ has an average mobility μ_i. With the knowledge of n_i and μ_i, the elements of the conductivity tensor as a function of magnetic field B can be calculated in a simple multi-carrier model as [12]

$$\sigma_{\mathrm{xx}} = \sigma_{yy} = \sum_i \frac{n_i e \mu_i}{1 + \mu_i^2 B^2}, \quad \text{and} \tag{8.2}$$

$$\sigma_{\mathrm{xy}} = -\sigma_{yx} = \sum_i q_i \frac{n_i e \mu_i^2 B}{1 + \mu_i^2 B^2}. \tag{8.3}$$

The transport coefficients are then found as [12]

$$R_{xy} = \frac{\sigma_{xy}}{\sigma_{xx}^2 + \sigma_{xy}^2}, \quad \text{and} \tag{8.4}$$

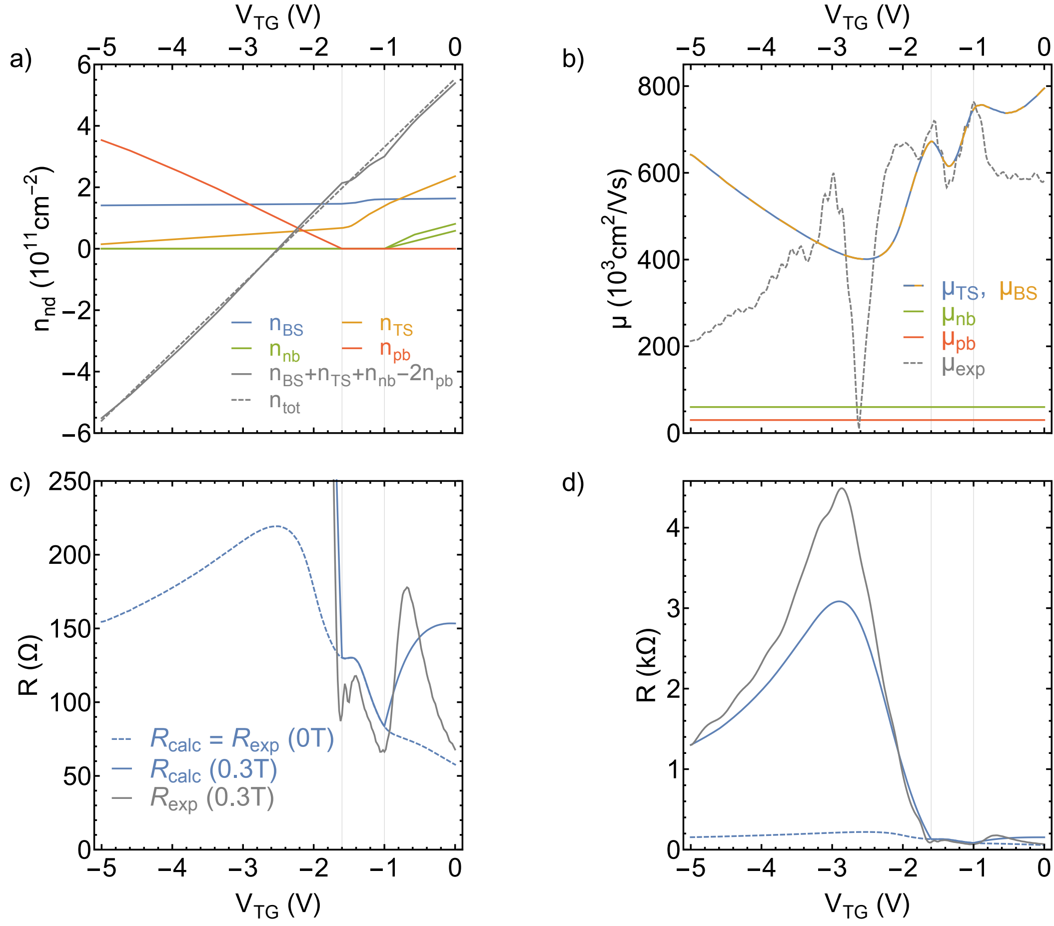

Figure 8.9: Summary of FFT results and comparison to low-magnetic field data. a) Individual carrier densities as obtained by performing an FFT analysis over the full gate range as shown in Figure 8.8b). The color code shows the assignment to top and bottom TSS (n_{TS} and n_{BS}), n-type and p-type bulk carriers (n_{nb} and n_{pb}). Shown in gray is the sum of all densities, considering a twofold degeneracy of p-states. The dashed line is the experimentally observed total density n_{tot}. b) Individual carrier mobilities, estimated from the experimental gatesweep and carrier densities as shown in a). For details, see text. c) Experimentally obtained and calculated longitudinal resistances (R_{exp} and R_{calc}) at $B = 0\,\mathrm{T}$ and $B = 0.3\,\mathrm{T}$. The curves at $B = 0\,\mathrm{T}$ coincide by construction (cf. text). d) Same as in c), but for a wider range of resistance values.

$$\rho_{xx} = \frac{\sigma_{xx}}{\sigma_{xx}^2 + \sigma_{xy}^2}. \tag{8.5}$$

Since the values of n_i are known from the FFT analysis, the remaining task is to find estimates for the mobilities μ_i. The usual approach would require a multi-carrier fit. In practice, however, multi-carrier fits with several different species do not necessarily give robust results [12]. From a principal point of view the main problem is the validity of Equations 8.2 and 8.3. One approximation is that each carrier species has one discrete density and mobility which are furthermore independent of magnetic field. In reality this is not necessarily the case. Moreover, these equations do not consider any effects going beyond the classical description like SdH oscillations or weak (anti-) localization. From a more practical point of view, the large number of fit parameters makes the results strongly dependent on details like starting parameters or the considered field range. For these reasons, the mobilities of massive n- and p-states are estimated from simple two-carrier fits (i. e. without distinguishing the two TSSs) to be on the order of $\mu_{\text{nb}} \approx 60 \times 10^3\,\text{cm}^2(\text{Vs})^{-1}$ and $\mu_{\text{pb}} \approx 30 \times 10^3\,\text{cm}^2(\text{Vs})^{-1}$, respectively. When assuming the latter values to be fixed, the TSS mobilities $\mu_{\text{TS}} = \mu_{\text{BS}}$ can be calculated from $R_{\text{xx}}(B = 0\,\text{T})$. The results are shown in Figure 8.9b). As expected, the TSS mobilities are strongly density-dependent. When these are the only conduction channels, the mobility reaches a local minimum at $V_{\text{TG}} \approx -1.3\,\text{V}$. Around this gate voltage the TSS mobilities are of course comparable to the average Drude mobility μ_{exp}, which is also shown for comparison (cf. Figure 8.5b)). Once additional bands start to become populated, the TSS mobility considerably increases. This can be attributed to enhanced screening of charged impurities, which is one of the dominant scattering mechanisms in HgTe at low temperatures [96]. For higher n-densities, the TSS mobilities hardly change, while for p-densities they decrease again. One has to keep in mind that the individual carrier mobilities – in contrast to the carrier densities obtained from the FFT analysis – are only estimates.

With these estimates and Equations 8.2 through 8.5, it is possible to calculate the low-magnetic field resistance. Figures 8.9c) and d) show both the measured and calculated longitudinal resistances at $B = 0.3\,\text{T}$ and the resistance at zero field (dashed). There is a reasonably good quantitative agreement between the measured and calculated values. Qualitatively, there is only a weak magnetoresistance when only TSS are populated. This is comparable to the situation of a classical 2D EG, which should not show any magnetoresistance at low fields [12]. In a restricted system the Hall voltage exactly equals the Lorentz force, so that the charge carriers are not deflected from their zero-field trajectory and do not experience additional resistance. Once other carriers (with differing mobilities) are introduced, a pronounced magnetoresistance occurs. In the classical description, the Hall voltage cannot completely compensate the Lorentz force anymore, so that carriers will follow bent trajectories and thus experience a higher total resistance. This is observable for additional n-type carriers, but even more pronounced for additional p-type carriers. Notably, the maximum in resistance is found at $V_{\text{TG}} = -2.9\,\text{V}$, which is close to the charge neutrality point. From Equations 8.2 through 8.5

follows that in the limit of high magnetic fields the maximum resistance occurs at the charge neutrality point, where the Hall voltage is nearly zero. The Lorentz force is not compensated at all and the resistance increases indefinitely. (In practice this usually cannot be observed due to the onset of other effects like SdH oscillations, which go beyond the classical description.) This explanation for the gate-dependence of the resistance is fully consistent with previous explanations [25, 89].

The good qualitative and in parts quantitative agreement between the measured and calculated resistances in small magnetic fields show the validity of the carrier mobility estimates. These estimates depend on a good knowledge of the carrier densities, which was obtained from the FFT analysis. The approach outlined here may be a useful starting point when a more detailed deconvolution of transport channels is necessary.

Reproducibility of the modulation doping approach

To demonstrate the reproducibility of the modulation doping approach another sample is taken into consideration. *QC0501 HB ICP* has a very similar layer stack as sample *QC0502 HB ICP*, but with a higher level of I-doping in the modulation doping layer. Note that when measuring sample *QC0501 HB ICP*, one contact in the cryostat failed. The current was thus send from contact 6 to 4, and the longitudinal and transverse voltages measured between 2 and 3, and 3 and 5, respectively (cf. Figure 7.6a) for a definition of contacts). The longitudinal resistance as a function of magnetic field and gate voltage is shown in Figure 8.10a). As in sample *QC0502* one can distinguish several intersecting LL fans, mainly the top TSS (strongly gate dependent n-type fan), the bottom surface (nearly gate independent fan) and the p-type fan. It is of course possible to apply the same FFT analysis as discussed before also to this sample. The results are shown in Figure 8.10b). For the FFTs, resistance data in the range 0.2 to 5 T were considered. The lower resolution of the measurements in B leads to a less clearly resolved spectral decomposition. The main features can still be identified, however. The bottom TSS (cf. blue arrow) has a nearly constant carrier density of $\approx 1.9 \times 10^{11}\,\mathrm{cm}^{-2}$ over the full gate range. The top TSS (cf. orange arrow) is strongly top gate dependent down to $V_{\mathrm{TG}} \approx -1.8\,\mathrm{V}$ and becomes less gate dependent when hole states are populated. The aforementioned additional n-and p-type carriers are also resolved for a range of gate voltages (cf. green and red arrows, respectively). The main difference to sample *QC0502 HB ICP* is of quantitative nature. The bottom TSS has a considerably higher carrier density due to the higher level of I-doping. The increase on the order of 0.3 to $0.4 \times 10^{11}\,\mathrm{cm}^{-2}$ is sufficient to decrease the region in which solely TSSs are populated to a small voltage window around $-1.8\,\mathrm{V}$. On the other hand, the higher carrier density also allows to directly observe the bottom TSS up to high fields. This will be discussed in more detail in Section 9.2.

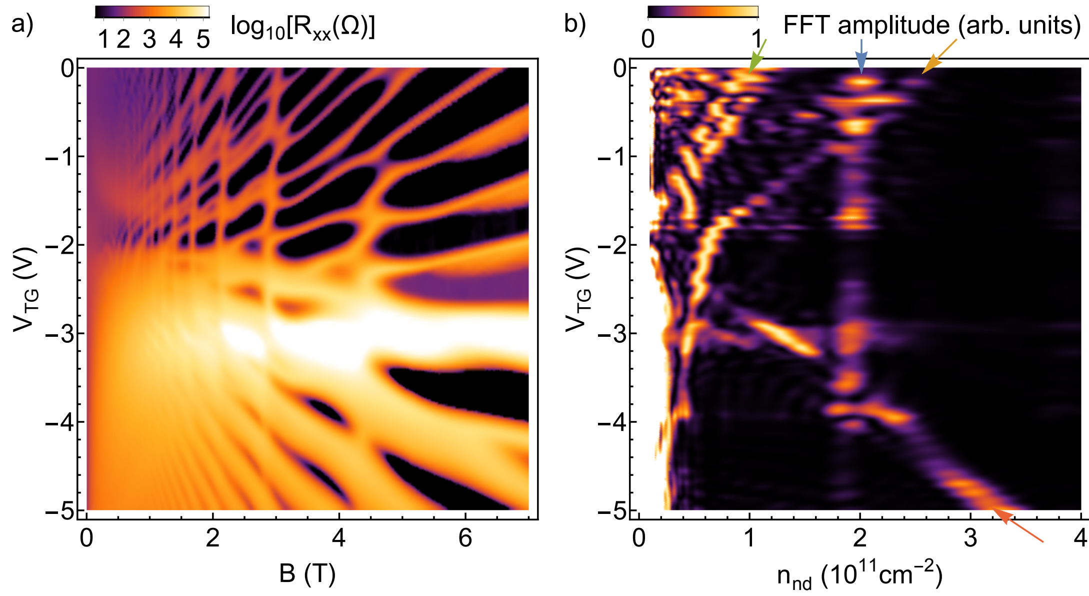

Figure 8.10: LL fan chart and FFT analysis of sample *QC0501 HB ICP*. a) Longitudinal resistance R_{xx} as a function of magnetic field B and top gate voltage V_{TG} at 30 mK, displayed in a logarithmic color scale. b) Normalized FFT amplitude as a function of carrier density n_{nd} and top gate voltage, displayed in a linear color scale.

Summary

On the whole it could be shown that modulation doping is suitable for controlling the density of the bottom TSS in the HgTe 3D TI system. Without modulation doping the carrier density is restricted to values on the order of $1 \times 10^{11}\,\mathrm{cm}^{-2}$ and can be influenced only slightly with the common top gate approach (cf. sample *Q2696 HB ICP*, Section 8.1). With modulation doping, in contrast, densities of $1.9 \times 10^{11}\,\mathrm{cm}^{-2}$ (cf. sample *QC0501 HB ICP*) and intermediate values (cf. sample *QC0502 HB ICP*) can be achieved easily. In these samples it is possible to directly observe the bottom TSS, even at low fields and in the presence of other conduction channels. Furthermore, the high quality of the samples permits the use of an FFT-based analysis. Being able to distinguish conduction channels facilitates quantitative estimates of carrier mobilities and thus prediction of transport parameters over a wide range of gate voltages. This kind of information helps to understand details of the gate-dependent resistance like multiple peaks at zero-B as well the magnetoresistance at small magnetic fields.

8.2.2 Introducing a back gate

Modulation doping is a good method to induce a static change of the density of the bottom TSS when growing the HgTe 3D TI layer. It is desirable, however,

to introduce a back gate, which allows the experimenter to change the density of the bottom TSS during the experiment. One possibility to achieve this is growing the HgTe/CdHgTe heterostructures on a virtual CdTe substrate as shown in Figures 8.4b) and 8.11c) for wafer *Q2843*. A conducting GaAs wafer serves as a substrate and a CdTe layer is grown on top, sufficiently thick to relax completely and restore the lattice constant of CdTe [20]. The usual layer stack – consisting of a CdHgTe barrier, the HgTe layer, and the CdHgTe cap layer – is then epitaxially grown on top and fully strained. Transport devices can be fabricated with the usual lithographic techniques, including a top gate stack. The doped GaAs substrate can be electrically contacted at the backside with conducting glue and used as back gate. The thick CdTe buffer and CdHgTe barrier layers act as dielectric. In the following, the back gate voltage will be denoted V_{BG}.

Figure 8.11 summarizes some basic characteristics of sample *Q2843 HB ICP 2*, a 200 µm × 600 µm big Hall bar sample with both a top and back gate, fabricated with the ICP etching process. (Note that differing from the samples shown before the top gate stack was fabricated with a thin HfOx layer as dielectric, so that the top gate action is enhanced considerably.) Figure a) shows the longitudinal resistance as a function of top gate voltage at two back gate voltages of 10 V and −10 V, respectively. In both cases, one can identify a pronounced maximum in the resistance, which is shifted about 0.12 V by changing the back gate voltage. The main difference is an overall higher resistance for the negative back gate voltage. The longitudinal resistance in a small magnetic field of $B = 0.3\,\mathrm{T}$, as shown in Figure b), also displays a very pronounced peak for both back gate voltages. A comparison with the transverse resistance (dashed lines) indicates that the peak positions correspond to the region of lowest total density. The gate voltage difference between the peak positions is enhanced to about 0.35 V. These data proof that the back gate is working in principle and can be used, similar to the top gate, to shift the overall carrier density in the HgTe layer. The gate action is of course much reduced in comparison to the top gate, since the dielectric layer between the GaAs substrate and the HgTe layer is so thick. In more quantitative terms, the ratio of the gate actions for top and back gate can be estimated from magnetic field sweeps to be on the order of 35 to 39. Figure 8.11c) shows an exemplary magnetic field sweep for a gate setting of $(V_{\mathrm{TG}}, V_{\mathrm{BG}}) = (-0.2\,\mathrm{V}, 10\,\mathrm{V})$. As in other high-quality samples shown before, the longitudinal resistance shows pronounced SdH oscillations with the resistance dropping to zero in between maxima. The transverse resistance shows quantized values which are compatible with the expected values (cf. dashed lines) within experimental uncertainties. Around a magnetic field of 10.5 T the sample seemingly undergoes a transition to a highly resistive state. From the low-magnetic field regime one can infer a total n-type carrier concentration of $n_{\mathrm{tot}} = 2.0 \times 10^{11}\,\mathrm{cm}^{-2}$ and an averaged Drude mobility of $\mu_{\mathrm{av}} = 570 \times 10^{3}\,\mathrm{cm}^{2}(\mathrm{Vs})^{-1}$, indicating a high sample quality.

In order to better understand the influence of top and back gate, it is instructive to consider LL fan chart measurements and corresponding FFT analyses as before. The left column of Figure 8.12 compares fan chart measurements in dependence

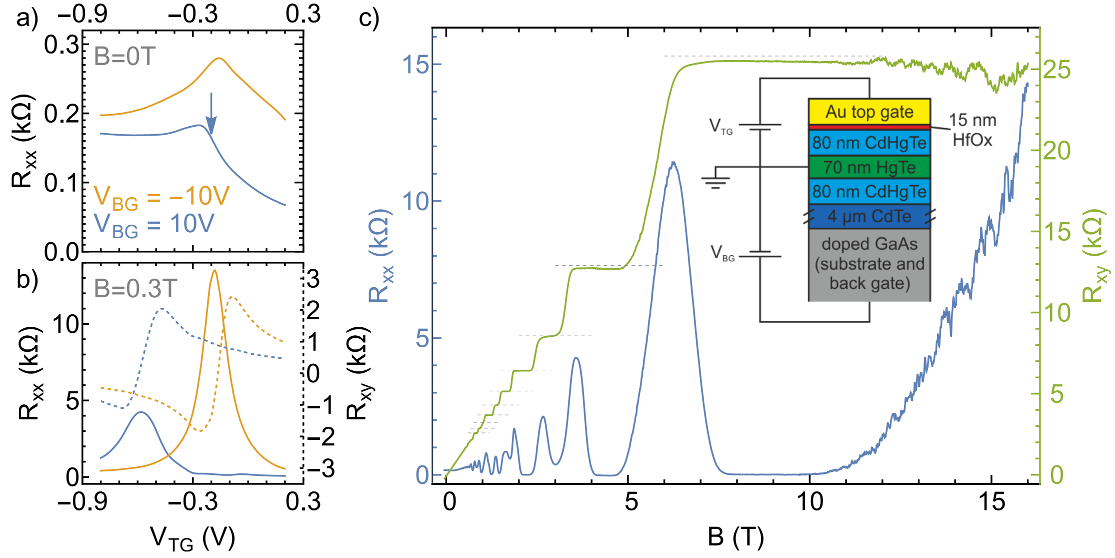

Figure 8.11: Basic characterization of sample *Q2843 HB ICP 2* at 150 mK. a) Longitudinal resistance R_{xx} as a function of top gate voltage V_{TG} at different back gate voltages V_{BG} at zero magnetic field. b) Longitudinal and transverse (R_{xy}, dashed) resistance as a function of top gate voltage at different back gate voltages at a magnetic field of 0.3 T. c) Longitudinal and transverse resistance as a function of magnetic field B for a gate setting of $(V_{TG}, V_{BG}) = (-0.2\,\mathrm{V}, 10\,\mathrm{V})$, cf. arrow in a). Inset: Layer stack for this sample, including the MBE-grown heterostructures, the lithographically defined top gate stack, and the applied gate voltages.

of magnetic field and either top gate voltage (Figures a) and c)) or back gate voltage (Figures e) and g)). Here the plotted quantity is the derivative of the Hall conductivity σ_{xy} with respect to gate voltage.[3] The right column shows the FFT analyses of the longitudinal resistance in the magnetic field range of 0.2 to 3 T.

In Figure a) (V_{TG} varied, $V_{BG} = 10\,\mathrm{V}$), one can immediately recognize the similarity to data obtained on the modulation-doped sample *QC0502 HB ICP* (Figure 8.6). Over a certain range of gate voltages ($-0.29\,\mathrm{V} < V_{TG} < -0.05\,\mathrm{V}$), only the n-type TSSs are present. These also appear in the corresponding FFT analysis, shown in Figure b). From the gate dependence, one can again distinguish the bottom TSS (marked with a blue arrow) and the top TSS (orange arrow). For positive top gate voltages, one can again distinguish additional n-type bulk states, which appear as a pronounced set of LLs in the fan chart, but also in the FFT

[3] Despite the high sample quality, it is necessary to work with a derivative here. For certain back gate settings the already described contact problems occur (cf. Section 7.3), making it difficult to distinguish more subtle features in the longitudinal resistance from artifacts. Additionally, for certain gate voltages there is a large number of LLs contributing to the fan chart, making it again difficult to distinguish features without the aid of a derivative signal.

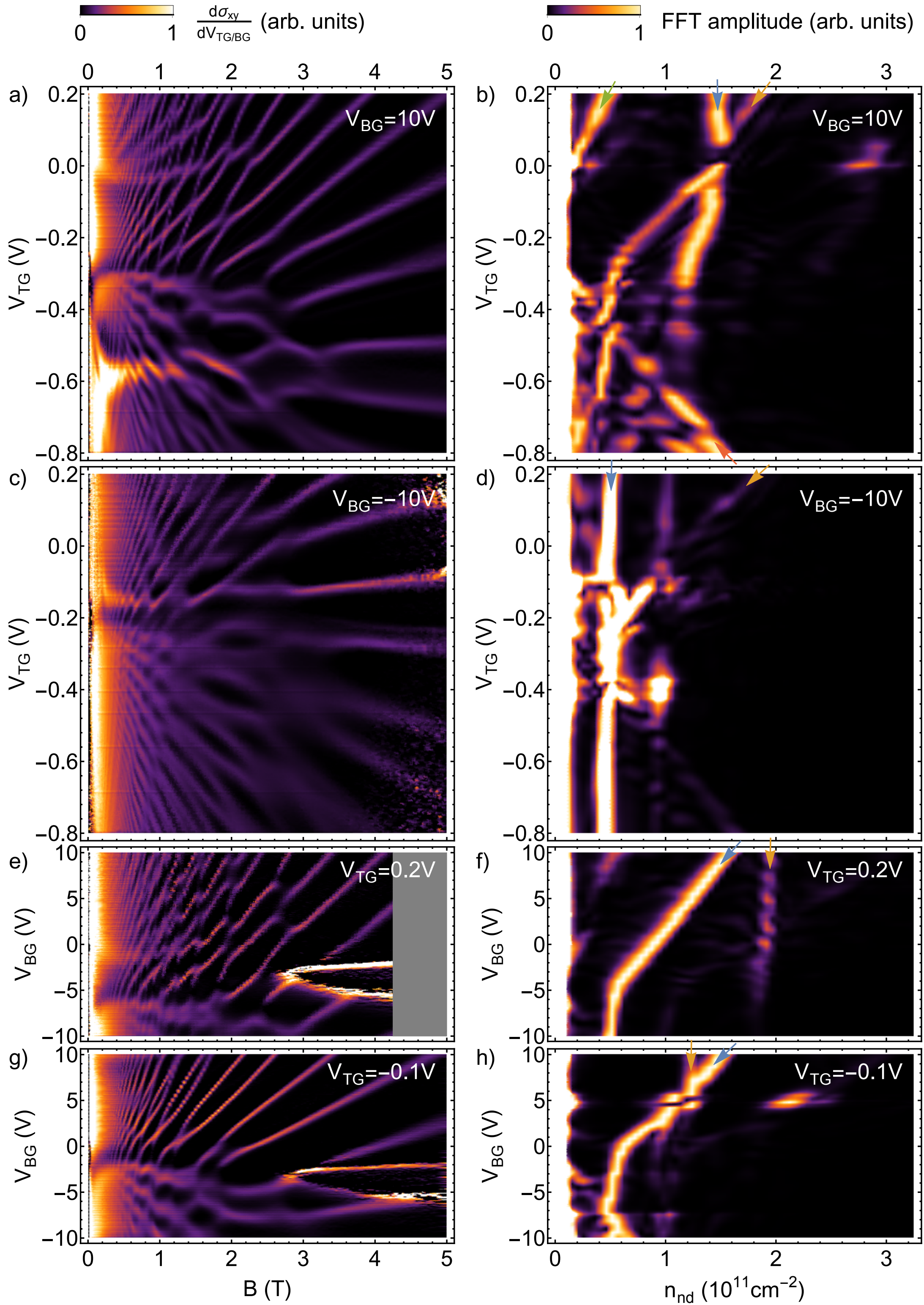

Figure 8.12: LL fan chart measurements of sample *Q2843 HB ICP 2* for different top gate/back gate settings. Left column: Derivative of Hall conductivity σ_{xy} with respect to the varied gate voltage as a function of gate voltage and magnetic field. In a) and c), the top gate voltage and in e) and g) the back gate voltage is varied. Right column: FFT analyses corresponding to the fan charts shown on the left.

analysis (green arrow). For gate voltages more negative than $-0.29\,\mathrm{V} < V_{\mathrm{TG}}$, a pronounced p-type LL fan appears (red arrow) and the top TSS carrier density becomes pinned to $\approx 0.5 \times 10^{11}\,\mathrm{cm}^{-2}$. At a back gate voltage of $V_{\mathrm{BG}} = -10\,\mathrm{V}$, the LL fan chart, Figure c), becomes more difficult to analyze. In the FFT analysis one can identify a pronounced carrier density around $0.5 \times 10^{11}\,\mathrm{cm}^{-2}$, which does not depend on the top gate voltage and can thus be attributed to the bottom TSS (blue arrow). The top TSS is still visible (orange arrow), albeit not as pronounced as the bottom TSS. Additional n- and p-states are not resolved in this measurement.

By making use of back gate-dependent fan chart measurements, one can reverse the role of the TSSs. Figure e) shows the LL fan chart in dependence of back gate voltage for a fixed top gate voltage of $V_{\mathrm{TG}} = 0.2\,\mathrm{V}$. The overall picture, despite some artifacts at higher fields, is remarkably similar to Figure a). The corresponding FFT analysis (Figure f)) reveals that the TSS carrier density which has been weakly top gate dependent in b) is, in turn, strongly back gate dependent (blue arrow) and vice versa (orange arrow). The same holds when setting the top gate voltage to $V_{\mathrm{TG}} = -0.1\,\mathrm{V}$ as in Figure g). Here one finds a wide back gate window where predominantly TSSs are found before additional p-states set in at $V_{\mathrm{BG}} \approx -1.0\,\mathrm{V}$. (The low gate action of the back gate is not sufficient to also induce the onset of additional n-states in this measurement.) A comparison between Figures f) and h) shows that the back gate dependence of the bottom TSS is hardly affected by changing the top gate voltage as expected.

On the whole, these results demonstrate that it is indeed possible to use the suggested back gate approach to deliberately tune the density of the bottom TSS. The FFT approach introduced previously proofed helpful for understanding the gating behavior and disentangling the different conduction channels. Importantly, the tentative assignment of LLs to top and bottom TSSs has been confirmed unambiguously with top and back gate dependent measurements. In Sections 9.1, the combination of top and back gates will be of great use in finding indications for interactions between TSSs from top and bottom surface.

8.3 Comparison of experimental data with k·p calculations including electrostatics

In the previous sections it was shown that improved experimental approaches as well as more refined data analysis approaches have made it possible to experimentally disentangle and individually manipulate different transport channels in the HgTe 3D TI system. One may ask now “what is the actual origin of these individual transport channels?” To this end my colleagues and I have compared experimental results to band structures from k·p theory. The band structures were calculated with the program *kdotpy*.[4] The main results have been included already in Reference [80]

[4] *kdotpy* is a Python program developed mainly by Dr. W. Beugeling and F. Bayer, which is based on earlier efforts by Dr. A. Pfeuffer-Jeschke and Dr. E. G. Novik [97, 98] and by Dr. J.

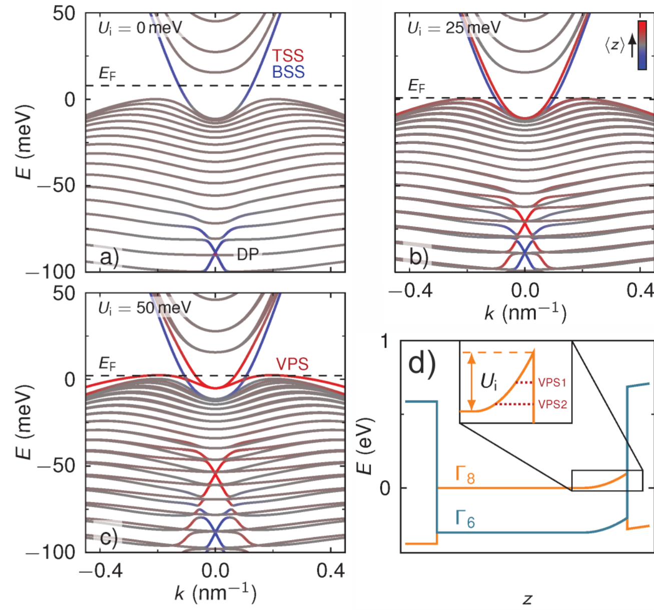

Figure 8.13: k·p band structure calculations for a 60 nm thick tensilely strained HgTe layer. a) Doubly degenerate band structure without electrostatic potential. The topological surface states on the top and bottom surfaces (TSS and BSS), the Dirac point (DP), and the Fermi level (dashed line) are indicated. b) and c) band structures with nonzero potential strength U_i. Volkov-Pankratov states are marked as VPS. The inset in b) illustrates the color code: states localized close to the top (bottom) surface are shown in red (blue), other states in gray. d) Band edge diagram of the Γ_6 and Γ_8 bands, which are shifted by the potential $U(z)$. The inset defines U_i and sketches the confined VPS. All figures were adapted from figures prepared by Dr. W. Beugeling for Reference [80].

and in more detail in Reference [79].

The k·p calculations shown here use a basis of 8 orbitals and consider a semi-infinite HgTe layer, confined in the growth direction z [24, 97, 98]. Bulk and surface states are identified by considering the expectation value $\langle z \rangle$ of wave functions.

Figure 8.13a) shows the band structure of a 60 nm thick HgTe layer with CdTe lattice constant. Since no external gate potential is applied all bands are doubly degenerate, including the TSSs (marked in red and blue). A bulk band gap is opened between the heavy Γ_8 valence and light Γ_8 conduction bands (marked in gray) due to tensile strain. Hybridization between Γ_6 and Γ_8 bands causes the indirect band gap, since the valence band maxima appear at nonzero k values. The resulting peculiar valence band shape, often called "camel back", gives rise to a

Böttcher. See also Reference [99].

very large density of states (DOS). The Dirac point of the TSSs is buried deep in the valence band, roughly 90 meV below the valence band maximum. In intrinsic samples the Fermi level E_f is situated in the bulk band gap, so that only the TSSs contribute to transport.

By making use of a gate electrode, the carrier density in HgTe layers can be changed. From the experiments using both top and back gates it is known that changing a gate potential will mainly influence the TSS which is close to the corresponding gate electrode (cf. Section 8.2). This can be incorporated in the calculations by assuming that a change in charge density is restricted to a thin layer close to the HgTe/CdHgTe interface. The corresponding electrostatic potential inside the HgTe layer can be found by solving the Poisson equation. The result is schematically sketched as a band alignment diagram in Figure 8.13d). From now on, the strength of the gate influence will be expressed in terms of the maximum potential shift U_i. By construction, this potential shift has the most pronounced influence on the corresponding TSS. Figure 8.13b) shows the band structure for a potential shift of $U_i = 25\,\mathrm{meV}$, corresponding to applying a negative top gate voltage. The Dirac point of the top TSS shifts to higher energies and the degeneracy of the TSSs is lifted. At the same time, the large DOS at the camel back pins the Fermi level.

At still higher potentials, cf. Figure 8.13c), a new hole state appears which is also localized at the top surface. The sudden appearance of this state is due to the confinement energy in the potential well created by U_i. It can be identified as the first of a series of VPSs [13], similar to the situation in compressively strained HgTe layers [10]. The VPS shares many characteristics with the bulk valence bands, including the energy maximum at nonzero k and the large DOS, so that the Fermi level is pinned to this state from now on. The crucial difference to the 3D bulk bands is that the new state is confined close to the surface and has 2D character. As a consequence it can give rise to a p-type QHE in high magnetic fields. Importantly, this would not be the case for closely spaced bulk valence bands [24] which retain their 3D character. This argument may be challenged in the case of a 60 nm thick HgTe layer, in which the bulk bands still show a considerable size quantization (cf. Figure 8.13a). In Reference [10], however, a p-type QHE was also reported for compressively strained HgTe layers with a thickness of 120 nm, in which size quantization is negligible. In this case the observation of a 2D transport effect can only be explained by the occurrence of gate-induced 2D states. It is likely that the same is true for tensilely strained HgTe layers. A rigorous experimental proof that the p-type QHE in HgTe 3D TIs is caused by 2D states localized at surfaces rather than bulk bands can be found in Section 9.1.

The appearance of p-type VPSs in the overall p-regime is a natural consequence of applying a nonzero electrostatic potential. The same is not necessarily true for additional n-type states, which contribute a n-type QHE to the LL fan chart in our 3D TI samples. The reason for this asymmetry is the very different effective mass for conduction and valence bands. In the textbook example of an electron in a square quantum well, the confinement energy E_c scales inversely proportional

to the effective mass, $E_c \propto m_{\text{eff}}^{-1}$ [100]. One can now extract effective masses from the band structure without potentials, Figure 8.13a), to get order-of-magnitude estimates. This analysis shows that the effective mass of the conduction bands is roughly 2 (at $k \approx 0\,\text{nm}^{-1}$) to 10 (at $k \approx 0.1\,\text{nm}^{-1}$) times smaller than the effective mass at the valence band maximum. This implies that the minimal positive gate voltage required to induce n-type VPSs is approximately 2 to 10 times larger than a negative gate voltage required to induce p-type VPSs. (For this order-of-magnitude estimate it may be neglected that the actual potential (cf. Figure 8.13d) differs of course from the textbook example.) To understand the consequence of this difference, let us assume now that the Fermi level is initially situated in the bulk band gap. When applying more negative gate voltages, the Fermi level shifts to the valence band and is pinned there, and eventually p-type VPSs appear which lift the Fermi level from the bulk valence bands. Likewise, when applying more positive gate voltages, the Fermi level shifts to the conduction band (albeit without a strong pinning effect there), and then a large additional gate voltage change is required to induce n-type VPSs. This should have been observable in some way in the experimental results, which is not the case. However, the effect of size quantization leads to a much larger subband separation in the conduction band than in the valence band. (Again, the difference in effective mass causes this difference.) It is thus more likely that the additional n-type QHE is simply contributed by additional conduction band states, which has been suggested before (e. g. in References [25, 89]). Further experimental evidence for this hypothesis can be found in Section 9.1.

The latter assumption may appear contradictory to a previous study from our group [24] in which it was argued that only TSSs contribute to the n-type QHE in HgTe 3D TIs. This conclusion was mainly based on two arguments: First, if 3D bulk states interfere, it is not possible to observe a clear QHE from the 2D TSSs. Second, LL transitions at high magnetic fields ($B \gtrsim 4\,\text{T}$) are compatible with superimposed QHEs from only two 2D carrier systems. The first argument is valid of course and was also used in this thesis to argue for the existence of 2D p-type VPSs. However, the subband splitting in the conduction band of even a 80 nm thick HgTe layer is still on the order of 7 meV, corresponding to a thermal energy of $\approx 80\,\text{K}$. (For the valence band, the subband splitting is only on the order of 2 meV, or $\approx 23\,\text{K}$.) It seems very likely that the conduction band states appear as 2D states in transport experiments at temperatures of 4.2 K or below. In other words: Gating the Fermi level into the conduction band is not equal to populating a 3D carrier system; at least not in a HgTe slab thinner than 80 nm at low temperatures. The second argument is also valid, but based on the resolution of the data in Reference [24] it can also not be excluded that three carrier systems contribute to the overall n-type LL fan chart. This is especially true when considering that the conduction band states contribute with a much smaller carrier density than the TSSs (cf. FFT analysis in Figure 8.8). This implies that a LL fan originating from the conduction band can only be observed at small magnetic fields, before the quantum limit is reached. A more elaborate discussion on this topic will follow in

Section 9.2. On the whole, the findings in Reference [24] may also be interpreted under the assumption that normal conduction band states contribute to transport at high n-densities. In any case, it is clear that in n-regime the high-mobility TSSs will dominate the transport properties of the system.

In the subsequent parts of this thesis, the interpretation of HgTe 3D TI transport data will be based on the model described above, which is briefly summarized here for convenience. This model includes four distinct transport regimes, sorted from high overall n-densities to high overall p-densities:

1. Top and bottom TSSs as well as conduction band states are occupied when the Fermi level is situated in the conduction band. The TSSs dominate transport properties under these circumstances.

2. Only TSSs contribute to transport when the Fermi level is situated in the bulk band gap.

3. The Fermi level can be tuned close to, or into, the camel back - shaped valence band and is pinned there. High-mobility TSS electrons and low-mobility bulk holes coexist.

4. Under the influence of a stronger negative gate potential two-dimensional p-type VPSs may form and further pin the Fermi level. High-mobility TSS electrons and medium-mobility VPS holes coexist and give rise to pronounced multi-carrier transport signatures.

This model will be important to disentangle the interplay of LLs originating from different carrier systems (next chapter) and to understand temperature-dependent transport in HgTe microstructures (Section 12.2).

9 Interplay of Landau levels in high-quality HgTe 3D TIs

The previous chapter has been devoted to identifying and manipulating the different surface states in high-quality HgTe 3D TI devices. The following chapter applies the new techniques and findings to investigate and interpret new transport effects in macroscopic HgTe 3D TI samples.

9.1 Mutual screening and avoided crossings of Landau levels

As shown in Section 8.2, it is possible to combine top and back gates in order to tune the carrier densities of top and bottom TSS separately. To demonstrate this, one gate voltage was kept constant, while the other gate voltage and the magnetic field were varied. However, it is of course also possible to obtain the evolution of LLs when both gate voltages are varied at a constant magnetic field.

Figure 9.1a) shows the longitudinal resistance of sample *Q2843 HB ICP 2* as a function of both top and back gate voltage at a fixed magnetic field of 0.75 T. The chosen aspect ratio ensures that both x- and y-axis show approximately the same

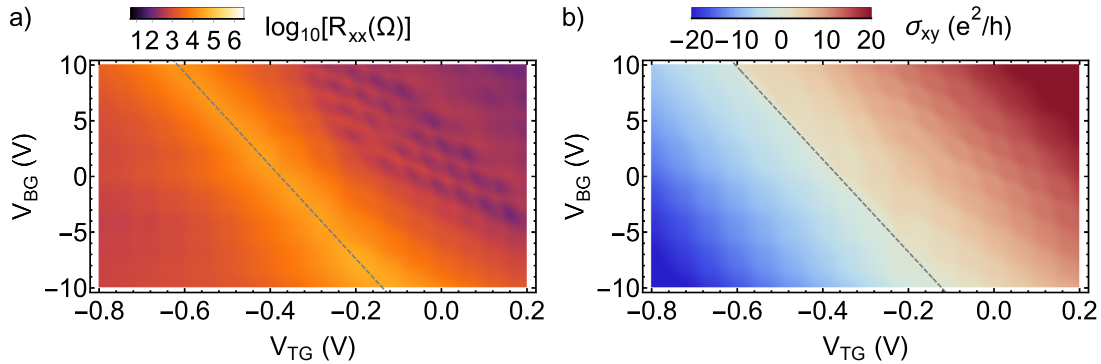

Figure 9.1: Top gate – back gate map of sample *Q2843 HB ICP 2*, obtained at a magnetic field of 0.75 T. a) Longitudinal resistance R_{xx} as a function of top gate voltage V_{TG} and back gate voltage V_{BG}, displayed in a logarithmic color scale. b) Hall conductivity σ_{xy} as a function of top gate and back gate voltage. Gray dashed lines indicate approximate lines of maximum R_{xx} and zero σ_{xy}, respectively.

change in carrier density, despite the difference in gate actions. The longitudinal resistance shows several features. The first feature is the line of maximum resistance, which runs in a 45° angle with respect to the axes (gray dashed lines). A comparison with the Hall conductivity, which is shown in Figure 9.1b) indicates that maxima in resistance appear along the line of minimal total density. The equal-density lines thus run from the left upper corner (high V_{BG}, low V_{TG}) to the right lower corner (low V_{BG}, high V_{TG}). The maximum change in density is obtained perpendicular to this. The second feature is a skewed checkerboard pattern in the resistance for overall n-densities (i. e. high V_{BG}, high V_{TG}). A brief comparison with the LL fan charts shown in Figure 8.12 indicates that this is the region, where the Fermi level is situated within the bulk gap and only the TSSs are occupied. The checkerboard pattern is thus related to the LLs of the TSSs. It is also visible as a step-like evolution of the Hall conductivity (Figure 9.1b)). Less resolved features are a faint (and apparently nonskewed) checkerboard pattern for overall p-densities as well as a rise in resistance for the highest overall n-densities. These features are most likely related to massive VPSs and conduction band states.

The visibility of LLs can be enhanced by plotting the derivative of the Hall conductivity with respect to both gate voltages. It is practical to calculate the norm of the weighted gradient, defined as

$$\nabla_{\mathrm{weighted}}\sigma_{xy} = \left(\frac{\partial\sigma_{xy}}{\partial V_{\mathrm{TG}}} \cdot \frac{1}{\mathrm{GA}_{\mathrm{TG}}}, \frac{\partial\sigma_{xy}}{\partial V_{\mathrm{BG}}} \cdot \frac{1}{\mathrm{GA}_{\mathrm{BG}}}\right), \tag{9.1}$$

where $\mathrm{GA}_{\mathrm{TG}}$ ($\mathrm{GA}_{\mathrm{BG}}$) denote the gate action, i. e. carrier density shift vs. applied gate voltage, of the top gate (back gate). Equation 9.1 is equivalent to calculating the gradient of the conductivity with respect to the total charge carrier density. The weighting is necessary, since the gate actions for top and back gate differ by a factor of approximately 40.

Figure 9.2a) shows this weighted gradient applied to the data in Figure 9.1b). (Note that a part of the p-regime has been cut off in favor of a more detailed view of the remaining parameter range.) LLs are very clearly resolved over the entire gate voltage range. The area enclosed in white dashed lines roughly corresponds to the bulk band gap, in which only LLs from the TSSs are occupied. A comparison with σ_{xy} shows that these LLs are nondegenerate (cf. exemplary traces in Figure 9.2b) and c) and white numbers indicating quantum Hall indices). One set of LLs is mostly dependent on the top gate (vertical lines), while the other is mostly dependent on the back gate (horizontal lines). This allows to identify them as top and bottom TSSs, respectively. However, both sets of LLs depend weakly on the other gate as well, leading to a skewed checkerboard pattern. An interesting result can be observed when looking at the line of equal density of top and bottom TSSs (cf. green arrows). Here, the checkerboard pattern is distorted by an apparent anticrossing of LLs with the same index, resulting in ring-like patterns. In the most basic model for Dirac-like surface states, one would expect that σ_{xy} shows odd plateau values $\nu = 7, 9, 11, 13, 15$ along this line. However, an even integer or odd integer sequence of Hall plateaus is only observable when the LL index of the

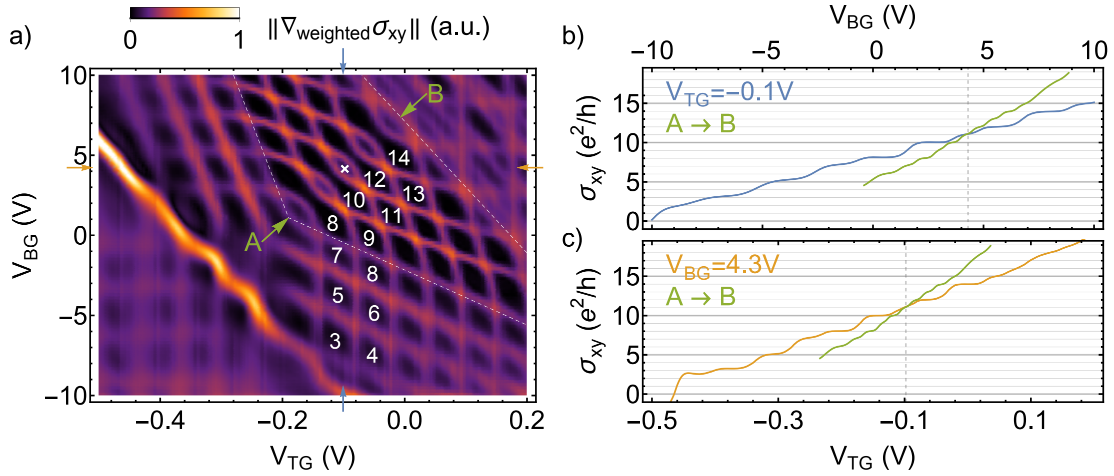

Figure 9.2: Landau levels and filling factors of sample *Q2843 HB ICP 2* at a magnetic field of 0.75 T. a) Norm of the weighted gradient of σ_{xy} with respect to top and back gate voltage, respectively. Integer numbers indicate quantum Hall indices. Arrows refer to traces of σ_{xy} in b) and c). b) σ_{xy} as a function of back gate voltage, at $V_{TG} = -0.065\,V$. c) σ_{xy} as a function of top gate voltage, at $V_{BG} = 4\,V$. The dashed lines indicate the crossing point of both traces, marked with a cross in a).

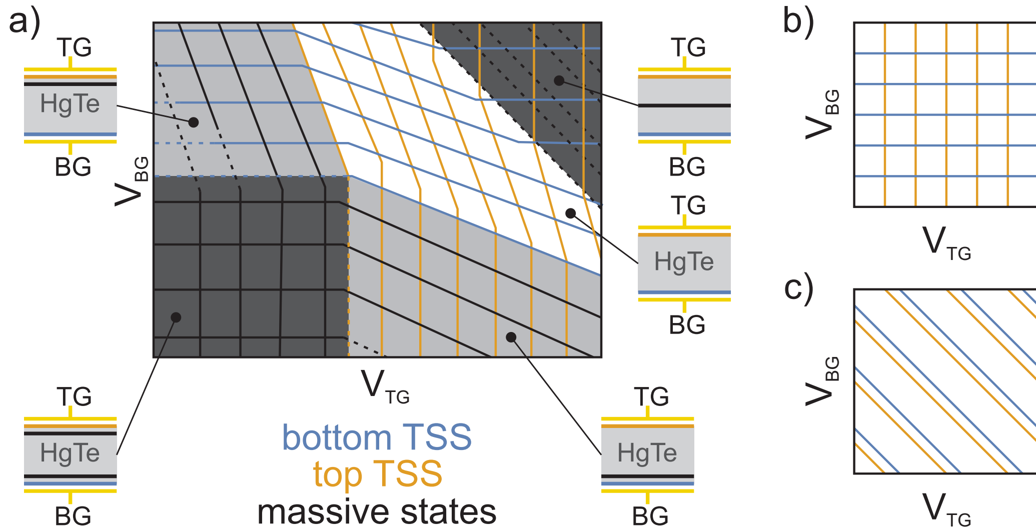

Figure 9.3: Sketch of the gate dependence of LLs. a) LL scheme based on the measurement shown in Figure 9.2a). Colored lines represent LLs from top and bottom TSSs and black lines represent LLs from massive states. Dashed lines indicate LLs which are not well resolved. Gray shading refers to different screening regimes, which are schematically explained with the insets. b) and c) Expected LL evolution with top and back gate for the case of perfect screening (b) and without screening (c).

top and bottom surface differ by either $\Delta\nu = 1$ or $\Delta\nu = 2$, respectively. In the equal density regime the observed anti-crossing gives rise to a complete integer sequence of QH plateaus, cf. green traces in b) and c).

When moving away from the bulk band gap, towards more p-type densities, another set of LLs appears, which is doubly degenerate (cf. transitions $7 \rightarrow 5 \rightarrow 3$ and $8 \rightarrow 6 \rightarrow 4$). These LLs can be assigned to massive p-type VPSs. The massive p-states are affected by both gates, just like the TSSs in the band gap. The latter, however, stop depending on both gate voltages once the massive states are occupied, indicating a change in screening behavior. The LLs from massive p-states can be traced to the regime of highest overall p-densities (low V_{BG}, low V_{TG}), where they form a regular checkerboard pattern. When moving to the opposite extreme, towards high n-densities, a similar effect can be observed. Additional LLs appear which are less clearly resolved. They run parallel to the equal-density contours. As before, the onset of additional states changes the screening behavior, so that LLs of the TSSs seize to depend on both gates here.

Figure 9.3a) is an attempt to qualitatively summarize and explain the LLs found in Figure 9.2a). LLs from top and bottom TSS are depicted in blue and orange, and massive states (p-type or n-type) in black. Insets display a schematic of the layer stack, indicating the contributing states as well as both gates. Let us consider first the area with white shading, corresponding to the bulk gap where only TSSs contribute to transport, cf. white dashed lines in Figure 9.2a). Both TSSs are affected by both gates, albeit with a different gate action. The reason is the finite DOS of the TSSs, which results in imperfect screening of the externally applied electric field [24, 76, 79, 89, 101]. Figure 9.3b) shows the expected LL pattern in the case of perfect screening, where the TSSs are only affected by the nearby gate. Figure 9.3c) shows the opposite extreme, where no screening applies and both TSSs are equally affected by both gates. The situation found in the experiment is in between these two extremes. Now let us consider the areas with light gray shading in Figure 9.3a). Here the gate voltage applied to either the top or back gate is sufficiently high to induce the formation of massive p-type VPSs. These massive states have a large DOS and can effectively screen the electric field of the nearby gate electrode. The states themselves, however, are still affected by both gates. This changes in the p-regime with dark gray shading. Here the electric field applied with the gate electrode is screened on both sides of the HgTe slab, so that all populated states are only affected by the nearby gate electrode. The result is a regular checkerboard pattern, as explained in Figure b). In the high n-regime with dark gray shading, the situation is slightly different. Here, additional n-type states screen the electric field of the gate electrodes, so that a regular checkerboard pattern for the TSSs appears. However, the massive states themselves are affected equally by both gates, as explained in Figure c). This indicates that the massive n-type states are not localized at a surface, but rather found in the bulk of the HgTe slab. This observation is consistent with the hypothesis that massive n-type states are in fact conduction band states rather than VPSs (cf. Section 8.3). On the whole, a qualitative model based on changes in the screening behavior of the

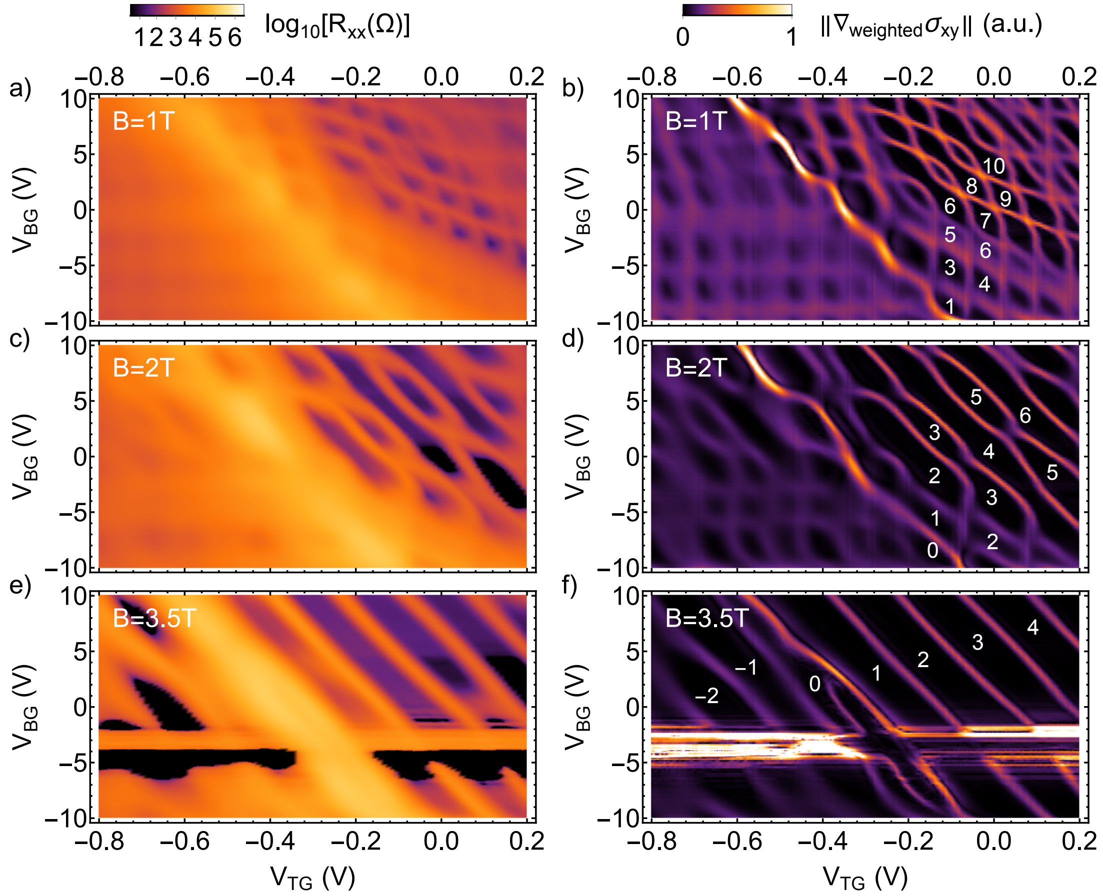

Figure 9.4: Top gate – back gate maps of sample *Q2843 HB ICP 2* at magnetic fields of 1 T, 2 T, and 3.5 T. a), c), and e) Longitudinal resistance R_{xx} as a function of top gate voltage V_{TG} and back gate voltage V_{BG}, displayed in a logarithmic color scale. b), d), and f) Norm of the weighted gradient of σ_{xy} with respect to top and back gate voltage. Integer numbers indicate the quantum Hall indices.

system seems sufficient to explain the overall structure of the top gate – back gate map.

The next logical step is to increase the magnetic field and investigate the changes in the top gate – back gate map. Figure 9.4a) shows the longitudinal resistance as a function of top and back gate voltage at a magnetic field of 1 T. The gradient of σ_{xy} is shown in Figure b). The overall behavior of this top gate – back gate map is still very similar to the one discussed before (cf. Figure 9.2). Crucial features like the anticrossing of LLs with the same index are preserved. The main differences are lower filling factors and, related to this, a wider LL separation. Several noticable changes are observed when increasing the magnetic field to 2 T as shown in Figures c) and d). First, the degeneracy of LLs is lifted, which is the expected behavior due to the Zeeman splitting. Second, in the n-regime several LLs seem to “merge” and

evolve from the checkerboard-like pattern towards a pattern reflecting the total charge in the system. Third, the longitudinal resistance drops below zero, cf. black areas in c), indicating the onset of contact issues (cf. Section 7.3). When increasing the magnetic field to 3.5 T as shown in Figures e) and f), these contact issues become more pronounced, especially in the back gate range of −7 to −1 V. In the remaining parameter range, the LLs have arranged in a very regular pattern which is highly reminiscent of the sketch in Figure 9.3c). The evolution of LLs is now determined by the total charge concentration in the system. The transition to this regime is interesting in itself and will be discussed in more detail in Section 9.2.

It is now time to set the top gate – back gate behavior of HgTe 3D TIs into the context of previous experiments employing dual-gated 3D TI films. Most closely related to the work at hand is Chapter 5 of Reference [76]. There a 75 nm thick HgTe layer, quite similar to the one discussed here, has been measured using both a top and back gate. The main differences are the much thinner top cap layer as well as the employed etching technique (IBE). As a result the overall sample quality was lower and higher magnetic fields needed to be employed to resolve LLs in the measurements. As expected, the results still share a lot of similarities with the ones reported here. For example, in Figure 5.4 of Reference [76], two sets of LLs can be distinguished, one of which is affected only by the top gate and one which is affected by both gates. These results have been interpreted under the assumption that only TSSs contribute to transport. Hence the apparent asymmetry in gating behavior was not easy to understand and seemed to imply that the top gate induces a higher density change in the bottom TSS than the top TSS. With the recent progress in understanding HgTe 3D TIs – especially the screening picture in Figure 9.3a) – it is now clear that in Reference [76] both TSSs and bulk bands have contributed to transport. The exclusively top gate dependent set of LLs can be attributed to the top TSS, while the top and back gate dependent set can be attributed to conduction band states. Measurements in Reference [76] at higher magnetic fields also show a transition to a unified LL sequence, which only reflects the total density in the system and not the individual densities. On the whole, the results presented in the thesis at hand are fully consistent with previous top gate – back gate dependent measurements on HgTe 3D TIs. The main improvement is the higher resolution, which allows for a more detailed understanding of the interplay of several overlapping bands.

There has also been a number of studies exploring a dual-gate configuration on other 3D TI materials. Studies with the bulk-insulating TI $BiSbTeSe_2$ also observed a clear QHE from both topological surface states. References [102] and [103] discuss the conductivity of $BiSbTeSe_2$ flakes at high magnetic fields, as a function of both top and back gate. They found that the two sets of TSS LLs form a slightly distorted checkerboard pattern, very similar to the one observed here in HgTe samples (cf. Figure 9.2). One important difference to the HgTe results is that in $BiSbTeSe_2$ the Dirac points are accessible by electrostatic gating so that the top gate – back gate maps obtained on these samples contain also the hole part of the Dirac spectra. It is thus possible to investigate the situation of

counterpropagating TSS edge modes and the interaction between these [102, 103]. In HgTe, the situation of counterpropagating edge modes can also be investigated, but here the modes have a different origin (cf. Section 9.2).

Another important difference is that in thick $BiSbTeSe_2$ flakes investigated in [102, 103], the LLs in the top and bottom TSS are completely independent of each other and no anticrossings are observed. Upon decreasing the $BiSbTeSe_2$ flake thickness, hybridization of TSSs leads to a noticable splitting of the $N = 0$ LL [104] and the resulting top gate – back gate map displays a feature similar to the anticrossing seen in HgTe. The critical thickness for this splitting to occur is on the order of 16 nm [104] – much less than the thickness of the investigated HgTe layers. Given the larger bulk band gap in $BiSbTeSe_2$ of ≈ 300 meV [105] as compared to the bulk band gap of ≈ 20 meV in HgTe, the wave functions of the TSSs are more confined in $BiSbTeSe_2$. The critical thickness for the 3D to 2D transition is on the order of 5 nm for Bi_2Se_3 [106], which is considerably thinner than the 16 nm at which signs of intersurface coupling are observed in the top gate / back gate map [104]. It thus seems plausible that in HgTe, where the 3D to 2D transition occurs at a thickness of ≈ 40 nm [24], signs of a weak intersurface coupling may be observed also in 70 nm thick layers. This tentative conclusion should be carefully checked in future studies. Similar to [104] one could vary the thickness of the HgTe layer in high-quality stacks, which include both a top and back gate, in order to check the thickness-dependence of anticrossings of LLs. This line of research is interesting for several reasons. 1) The 2D surface states in 3D TIs, which are by construction in close proximity to each other, are reminiscent of two parallel 2D EGs as investigated in DQW structures. Similar to DQWs, one may expect to observe new phenomena such as exciton condensation [107, 108]. 2) One of the still open questions in 3D TI research concerns the role of side surfaces in 3D TI transport measurements. Although speculative, one may consider that the coupling of LLs from the two TSSs is mediated via the side surfaces and thus found in comparably thick layers without a noticeable hybridization gap.

On the whole, exploring HgTe 3D TIs via a combined top gate – back gate approach proofs extremely valuable in disentangling transport channels and LLs in small magnetic fields. The observations are fully consistent with previous work on dual-gated 3D TIs, including the apparent coupling of TSSs. A simple screening picture suffices to explain the behavior of massive and massless surface states in small magnetic fields, while for higher magnetic fields a more complicated intermixing of LLs is observed. This regime will be investigated in more detail in the next section.

9.2 Evolution of Landau levels in high magnetic fields

In the previous sections, transport properties of HgTe 3D TI layers were discussed in detail mostly for magnetic fields of less than $\approx 5\,\mathrm{T}$. It has been shown that LLs appear mostly periodic in $1/B$, facilitating the assignment of LLs to individual transport channels. In high magnetic fields, however, a rather different behavior is observed as described below. This part of the thesis is based on close collaborations with Dr. L.-X. Wang and Dr. W. Beugeling.

Two previously mentioned samples provide good examples of the behavior of high-mobility HgTe 3D TI layers in high magnetic fields. Figure 9.5 shows LL fan charts for samples *QC0501 HB ICP* and *Q2843 HB ICP 2*. Here the focus is on the high magnetic field regime up to 16 T. For sample *Q2843 HB ICP 2* the back gate voltage is set to 10 V to avoid contact issues. As discussed in Sections 8.2.1 and 8.2.2 both samples show a superposition of several LL fans in small magnetic fields ($B \lesssim 5\,\mathrm{T}$), corresponding to the occupied bands at a given gate voltage. The high-field regime shows a qualitatively different behavior. Here the superposition of different LL fans seemingly undergoes a transition to a single LL fan. As can be deduced from the quantum Hall indices, the LLs are nondegenerate in high

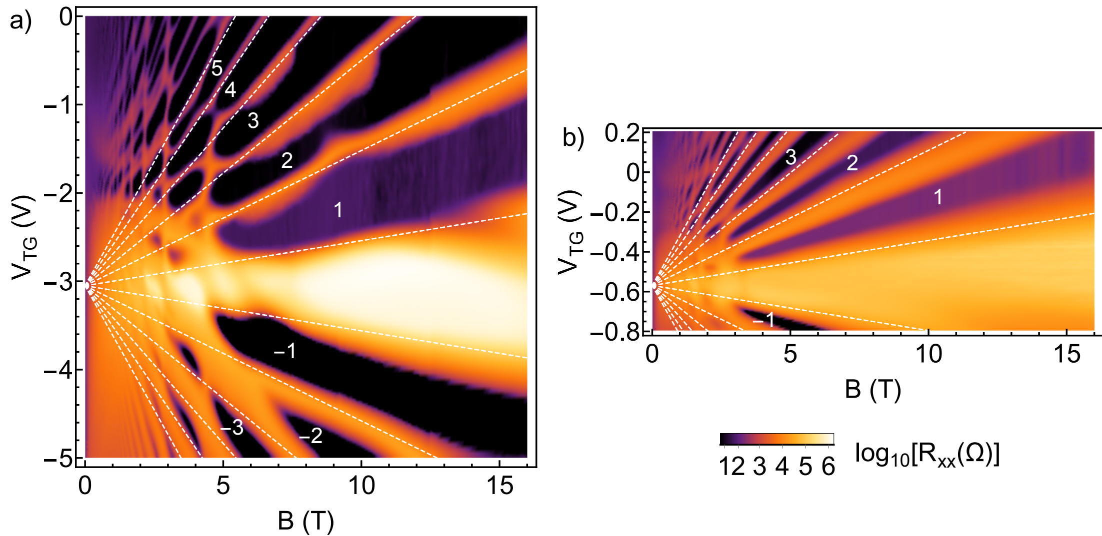

Figure 9.5: Two representative LL fan charts at high magnetic fields. a) and b) Longitudinal resistance R_{xx} of samples *QC0501 HB ICP* (a) and *Q2843 HB ICP 2* (b) as a function of magnetic field B and top gate voltage V_{TG}. Same data as shown in Figures 8.10a) and 8.12a). The same logarithmic color scheme is used in both figures and the gate voltage axes have been scaled according to total carrier density change. Dashed white lines indicate a LL fan reflecting the total carrier density, and white numbers denote total filling factors.

magnetic fields. For sample *QC0501 HB ICP* the transition to a single fan occurs for magnetic fields $B \gtrapprox 5\,\mathrm{T}$ while for sample *Q2843 HB ICP 2* it occurs at slightly lower fields of $B \gtrapprox 3\,\mathrm{T}$.

Using the total charge carrier density n_{tot}, one can calculate a LL fan chart for a free electron gas (i. e. with parabolic dispersion relation) according to [60]

$$B_{\mathrm{LL}} = \frac{n_{\mathrm{tot}} h}{e} \left(n_{\mathrm{LL}} + \frac{1}{2} \right)^{-1}, \tag{9.2}$$

where B_{LL} is the magnetic field, at which a LL of index $n_{\mathrm{LL}} \in \mathbb{Z}$ is crossed, e is the electron charge, and h the Planck constant. The results of this calculation are shown as white dashed lines in Figure 9.5. The single carrier fan chart describes the high field regime quite well. The reason is the strongly oscillating DOS in strong magnetic fields, where the LL separation in energy becomes comparable to or larger than the LL broadening. This has pronounced implications on screening and charge distribution. At sufficiently high magnetic fields, the resulting LL fan does not reflect the individual band contributions, but rather the overall carrier density in the system [25, 89, 109].

In the intermediate field regime, the evolution of LLs with magnetic field and gate voltages can be quite complicated. In order to sort LLs, it is instructive to consider a simplified toy model similar to the one developed in Reference [89]. This model includes three steps for each gate voltage:

- Extracting the carrier densities of individual transport channels from the data.
- Calculating the LL dispersion and the corresponding total density vs. energy and magnetic field. The band edges are shifted, so that the experimentally observed carrier densities are recovered at $B = 0\,\mathrm{T}$.
- Finding the electrochemical potential $\mu(B)$ from the requirement that the total carrier density has a constant value at a given gate voltage.

The crossings of the electrochemical potential with LLs can then be collected for all gate voltages and a plot of LLs vs. gate voltage and magnetic field constructed. The latter corresponds to the experimentally observed LL fan. The major difference to the model developed in [89] is that the low-field carrier densities are extracted from the experiment and not obtained from an effective capacitor model.

A minimal model includes three bands: Massive p-VPS and n-bulk states (modeled as parabolic bands), and TSSs (modeled as idealized Dirac bands with linear dispersion). The band offsets are determined so that at zero energy and magnetic field, the carrier densities correspond to the experimental values:

$$E_{m,0} = -\frac{\hbar^2 \pi n_m}{2 m_m} \quad \text{for massive states} \tag{9.3}$$

$$E_{\mathrm{TSS},0} = -\hbar v_F \sqrt{4\pi n_{\mathrm{TSS}}} \quad \text{for TSSs} \tag{9.4}$$

Carrier type	eff. mass	Fermi velocity	g-factor	σ_0
TSS	–	5×10^5 m/s	–	1 meV
p-type VPS	0.2 m$_0$	–	6	1 meV
cond. band	0.1 m$_0$	–	15	1 meV

Table 9.1: Parameters used for modelling the LL fan charts as explained in the text and shown in Figure 9.6. m_0 denotes the electron rest mass.

where n_m and n_{tss} are the densities of massive and topological surface states, respectively, m_m is the effective mass of massive states (defined here as positive for electrons and negative for holes), and v_F the Fermi velocity of TSSs. The LL dispersions are given by [8, 60]

$$E_m(B, N, \pm) = E_{m,0} + \left(N + \frac{1}{2}\right)\frac{\hbar eB}{m_m} \pm \frac{g_m^* \mu_B}{2} B \quad \text{for massive states} \tag{9.5}$$

$$E_{\text{TSS}}(B, N) = E_{\text{TSS},0} + \sqrt{2e\hbar v_F^2 BN + (g_{\text{TSS}}^* \mu_B B)^2} \quad \text{for TSSs,} \tag{9.6}$$

where $N = 0, 1, 2, 3, ...$ is the LL index, μ_B the Bohr magneton, and g_m^* and g_{TSS}^* the Landé g-factors for massive and topological surface states, respectively. $\pm$ refers to spin-up and -down subbands. The total DOS of the system, assuming each LL is broadened with a Gaussian shape, is given by

$$D(E) = \frac{eB}{h\sigma\sqrt{2\pi}} \sum_s C_s \cdot \exp\left(-\frac{(E - E_s)^2}{2\sigma^2}\right), \tag{9.7}$$

where $\sigma = \sigma_0\sqrt{B/B_0}$ with $B_0 = 1\,\text{T}$ defines the broadening of LLs [98] and the sum runs over all LLs s at energy E_s, including those from massive as well as topological surface states. $C_s = 1$ for all LLs except the $N = 0$ LL for the TSSs, where it takes $C_s = 1/2$, reflecting the half-filled character of that LL. Numerical integration of Equation 9.7 with respect to energy relates a change in energy to a change in total carrier density of the system. From a practical point of view, however, it is helpful to distinguish the individual DOS contributions of n-type and p-type states, integrate those to find the individual density contributions, and sum them to find the total carrier density at a given energy:

$$n_{\text{tot}} = \int_{-\infty}^{E} D_{\text{n-type}}(E')dE' + \int_{+\infty}^{E} D_{\text{p-type}}(E')dE', \tag{9.8}$$

where D_{i} refers to the part of Equation 9.7, which includes only LLs from n-type bands (i. e. TSSs and n-bulk states) or p-type bands (p-VPS).

Figure 9.6 shows the result of the toy modelling approach described so far. The parameters used for this calculation are summarized in Table 9.1. (These values are chosen so as to qualitatively reproduce the experimental results. The Zeeman splitting of the TSSs does not qualitatively change the results and is

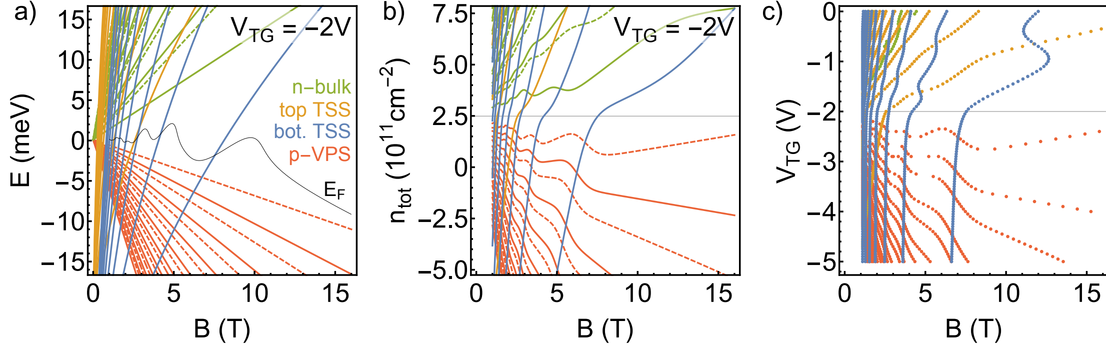

Figure 9.6: Toy model calculation of a LL fan chart for sample *QC0501 HB ICP*. a) LL dispersion with energy E and magnetic field B for the density arrangement at a top gate voltage of $V_{\mathrm{TG}} = -2\,\mathrm{V}$. b) LL dispersion with total density n_{tot} and magnetic field B for $V_{\mathrm{TG}} = -2\,\mathrm{V}$. c) LL dispersion with gate voltage.

neglected.) As an example, consider the density arrangement at a gate voltage of $V_{\mathrm{TG}} = -2\,\mathrm{V}$. First, the corresponding LL fan in energy E is calculated as a function of magnetic field B, based on Equations 9.3 and 9.4 for the band offsets and Equations 9.5 and 9.6 for the LL dispersion. The result is shown in Figure 9.6a). The corresponding total carrier density at each point in the (E, B) parameter space is calculated with Equation 9.8. The evolution of the electrochemical potential μ is then found from the requirement that the total carrier density has to be constant. It displays a strongly oscillatory behavior once the energy separation becomes larger than the broadening of LLs. For instructive purposes, one can also plot the LL fan not as a function of E, but n_{tot}, as shown in Figure 9.6b). Now the LLs display an oscillatory behavior, similar to the experimental results (cf. Figures 8.6 and 8.10). The experimentally relevant trace, however, is at the total density found at $-2\,\mathrm{V}$ gate voltage (black line). After repeating the same procedure for all gate voltages one can collect the position of LLs and plot them versus gate voltage and magnetic field, as shown in Figure 9.6c). Similar to the experiment, the fan chart is quite complicated at low fields ($B \leq 5\,\mathrm{T}$). LLs are not straight, but display wiggles when other LLs come close in energy. At higher magnetic fields, the LLs rearrange and eventually represent the total density of the system. Two points should be emphasized here which will facilitate the understanding of results in the present thesis and previous work:

- Straight lines in the experimental fan chart might actually be the result of reorganization of several LLs with different origin. Especially the LLs originating from p-VPS bands may falsely be attributed to an n-type band. The assignment of quantum Hall indices to filling factors crucially depends on this effect.

- In the overall n-regime, the LL fan is mostly dominated by the TSSs. n-bulk

states are also visible, but heavily distorted. Due to their small overall density, these bands are not contributing at all for higher magnetic fields ($B \geq 5\,\mathrm{T}$). This might explain why they were not observed at all in Reference [24].

One obvious discrepancy between the model and the experimental result, Figure 9.5a, is the appearance of the $N = 1$ LL from the bottom TSS at approximately 7 T. Also the switching between LLs from top and bottom TSS at higher fields is not experimentally observed. One reason might be an enhanced charge transfer at higher fields, similar to the one observed in [110] in a bilayer 2D EG sample. In this scenario, all charge carriers would be transferred to the band with higher density, in order to minimize the overall energy. It could explain why in the experiment the system shows only small deviations from a single band system even at fields where this is not yet the case in the simulation.

On the whole, the simple toy model is sufficient to provide a qualitative understanding of the experimental results. It is of course far from a quantitative match. A better fit would certainly require a computationally heavy approach based on a fully self-consistent k·p calculation, which is far beyond the scope of this work.

9.3 Coexistence of topological surface states and Volkov-Pankratov states

As shown in the previous section, the interplay of several LL fans can give rise to rather complex LL sequences. It is instructive, however, to assign LLs to specific subbands. In the following, this assignment is crucial in order to understand the situation in which counterpropagating LLs originating from electron and hole subbands occur at the same time. This part of the thesis is based on fruitful discussions with Dr. L.-X. Wang who recognized that the situation of counterpropagating edge states in our samples is not as simple as one might think at first glance.

Figure 9.7a) shows the LL dispersion of sample *QC0501 HB ICP* (same measurement as in Figures 8.10 and 9.5). The focus shall be on the regime of small total density and intermediate magnetic fields, where the resistance is large. LLs are thus better resolved in the longitudinal conductivity, which is the plotted quantity here (instead of the resistance as before). Quantum Hall indices are indicated. A tentative assignment of LLs to the individual subbands is shown in Figure 9.7b). It is based on the modelling described before (cf. Figure 9.6) and considers the top TSS, bottom TSS, and spin-resolved p-VPS. Especially the LLs originating from p-VPSs differ considerably from a simple, single fan. An “accidental” degeneracy of states with different spin and LL index can be misleading when interpreting the fan chart. By comparison with a) and the assignment of LLs it is possible to find the individual filling numbers $\nu_{\mathrm{top\,TSS}}$, $\nu_{\mathrm{bot.\,TSS}}$, and $\nu_{\mathrm{p\text{-}VPS}}$, respectively. Note that the total filling factor is given by

$$\nu = +\nu_{\mathrm{top\,TSS}} + \nu_{\mathrm{bot.\,TSS}} + 1 - \nu_{\mathrm{p\text{-}VPS}}, \tag{9.9}$$

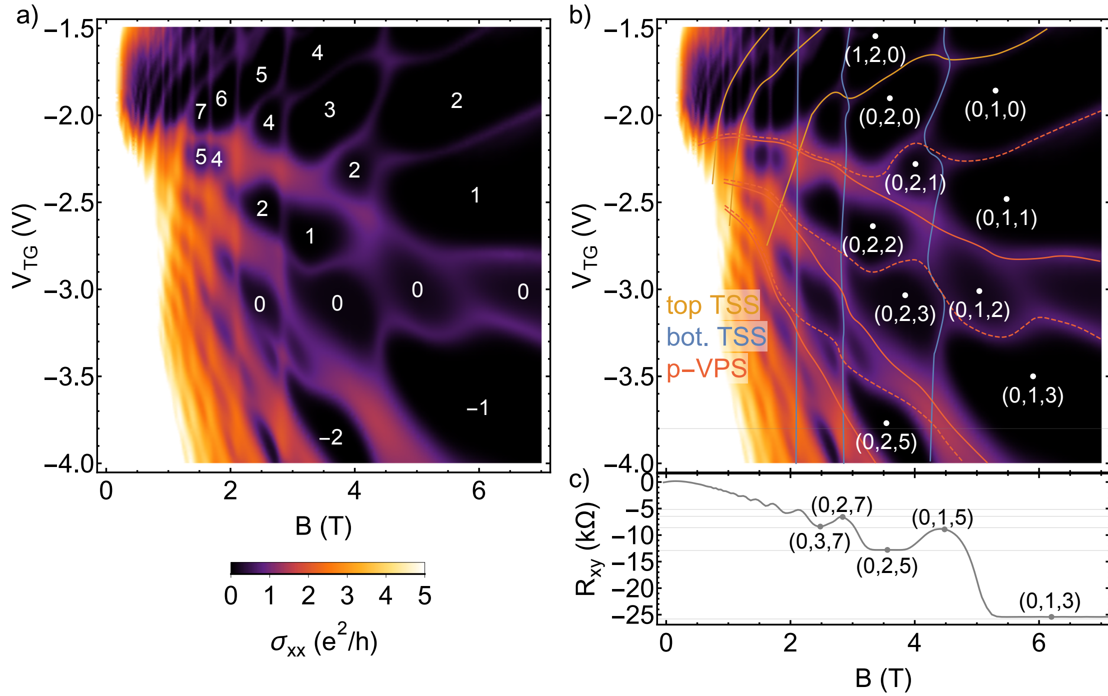

Figure 9.7: Re-entrance of QHE plateaus in sample *QC0501 HB ICP*. a) and b) Longitudinal conductivity σ_{xx} as a function of top gate voltage V_{TG} and magnetic field B. Numbers in a) indicate quantum Hall indices, numbers in b) indicate individual filling factors for each band in the form $(\nu_{\text{top TSS}}, \nu_{\text{bot. TSS}}, \nu_{\text{p-VPS}})$. Colored lines are suggested LL dispersions. c) Transverse resistance R_{xy} as a function of magnetic field at $V_{\mathrm{TG}} = -3.8\,\mathrm{V}$, cf. gray line in b).

due to the half-filled LLs typical for Dirac systems. The crossing of LLs with different character gives rise to a peculiar effect: The “re-entrance” of LLs. This can be seen in Figure 9.7c), which shows a transverse resistance trace at a top gate voltage of $-3.8\,\mathrm{V}$. Since the overall carrier density here is p-type, the transverse resistance should decrease (in a step-like fashion) with increasing magnetic field. This occurs in a strongly nonmonotonic fashion, however. For fields higher than $\approx 2\,\mathrm{T}$ the transverse resistance clearly decreases in steps of two (cf. transitions $(0, 2, 7) \rightarrow (0, 2, 5)$ and $(0, 1, 5) \rightarrow (0, 1, 3)$), reflecting the accidental degeneracy of p-VPS states. On the contrary, the transverse resistance increases in steps of one whenever a LL of the bottom TSS is crossed (cf. transitions $(0, 3, 7) \rightarrow (0, 2, 7)$ and $(0, 2, 5) \rightarrow (0, 1, 5)$). A similar observation has been made in HgMnTe layers of comparable thickness [88]. On the whole, it seems that the total filling factors are simply given by the sum of individual filling factors, as indicated by Equation 9.9. This seems reminiscent of superimposed n-type LLs [8, 24, 25, 89], for which the quantum Hall indices can be found by adding up the individual contributions.

However, the situation of counterpropagating edge states is quite different from

the situation of copropagating edge states. To understand this, one must consider the Landauer-Büttiker type description of transport in the quantum Hall regime (see e. g. [60] for an instructive introduction), which is based on transmission probabilities between voltage probes. Scattering between copropagating states can not change the transmission probability due to the lack of a reverse-propagating channel [60]. The number of copropagating quantum Hall edge channels can thus be added to give a total transmission probability. In contrast, the authors of Reference [103] pointed out that the scattering between counterpropagating states can have a strong influence on transmission probabilities. To see this, consider the Landauer-Büttiker description of transport in a 6-terminal Hall bar device. The current flowing into (positive sign) or out of (negative sign) terminal p is given by

$$I_p = \sum_q G_{pq}(V_p - V_q), \tag{9.10}$$

where G_{pq} denotes the conductance from terminal p to q, and V_p and V_q the potentials of those terminals. For edge-channel transport, the conductance is

$$G_{pq} = G_0 n_i \tau_i, \quad \text{with} \quad G_0 = \frac{e^2}{h} \tag{9.11}$$

where n_i denotes the number of edge states and τ_i their transmission probability. In the following, the index $i = f, b$ will denote whether the considered edge channels are forward moving ($i = f$) or backwards moving ($i = b$). The τ_i are taken as constants, implicitly neglecting that τ_i can in general differ for individual edge states and terminal configurations. In the QHE regime all conductance coefficients are zero, unless $q - 1 < p < q + 1$ (i. e. only adjacent terminals are connected). Combining Equations 9.10 and 9.11 then gives

$$(I_1 \quad I_2 \quad I_3 \quad I_4 \quad I_5 \quad I_6)^\intercal = G_0 M \cdot (V_1 \quad V_2 \quad V_3 \quad V_4 \quad V_5 \quad V_6)^\intercal \tag{9.12}$$

with

$$M = \begin{bmatrix} -n_f\tau_f - n_b\tau_b & n_f\tau_f & 0 & 0 & 0 & n_b\tau_b \\ n_b\tau_b & -n_f\tau_f - n_b\tau_b & n_f\tau_f & 0 & 0 & 0 \\ 0 & n_b\tau_b & -n_f\tau_f - n_b\tau_b & n_f\tau_f & 0 & 0 \\ 0 & 0 & n_b\tau_b & -n_f\tau_f - n_b\tau_b & n_f\tau_f & 0 \\ 0 & 0 & 0 & n_b\tau_b & -n_f\tau_f - n_b\tau_b & n_f\tau_f \\ n_f\tau_f & 0 & 0 & 0 & n_b\tau_b & -n_f\tau_f - n_b\tau_b \end{bmatrix}$$

In the experiment current is flowing only from contact 6 to 4, so that $I_6 = -I$, $I_4 = I$, and $I_{i \neq 6,4} = 0$ (cf. Figure 7.6 for a definition of contact numbers and note the nonstandard measurement configuration for sample *QC0501 HB ICP*). The set of Equations 9.12 can then be solved to obtain the 4-point resistivities

$$\begin{aligned} R_{\mathrm{xx}} &= \frac{V_2 - V_3}{I} = \frac{(n_b\tau_b)^2 n_f\tau_f}{(n_b\tau_b)^4 + (n_b n_f \tau_b \tau_f)^2 + (n_f\tau_f)^4} G_0^{-1} \\ R_{\mathrm{xy}} &= \frac{V_5 - V_3}{I} = \frac{-(n_b\tau_b)^3 + (n_b\tau_b)^2 n_f\tau_f + (n_f\tau_f)^3}{(n_b\tau_b)^4 + (n_b n_f \tau_b \tau_f)^2 + (n_f\tau_f)^4} G_0^{-1} \end{aligned} \tag{9.13}$$

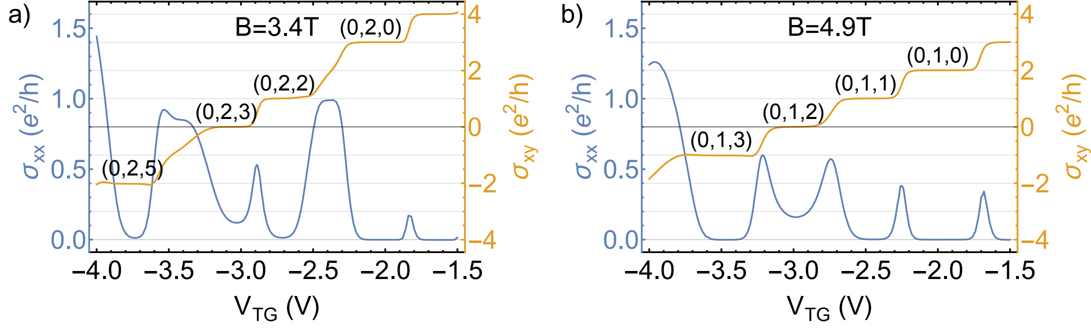

Figure 9.8: Longitudinal and Hall conductivity as a function of top gate voltage in sample *QC0501 HB ICP*. a) At a magnetic field of 3.4 T. b) at a magnetic field of 4.9 T.

and from these the conductivities

$$\sigma_{\text{xx}} = \frac{R_{\text{xx}}}{R_{\text{xx}}^2 + R_{\text{xy}}^2} \quad \text{and} \quad \sigma_{\text{xy}} = \frac{R_{\text{xy}}}{R_{\text{xx}}^2 + R_{\text{xy}}^2}. \tag{9.14}$$

One can now compare the results obtained via Equations 9.13 and 9.14 with the experimental results. Exemplary traces of σ_{xx} and σ_{xy} as a function of gate voltage are plotted in Figure 9.8 for fixed magnetic fields of 3.4 T and 4.9 T. The filling levels for different bands are indicated as well (cf. Figure 9.7b). First, consider the situation of copropagating edge states at $(B, V_{\text{TG}}) = (3.4\,\text{T}, -2.1\,\text{V})$ with filling numbers $(0, 2, 0)$. "Forward"-moving edge states will from now on be associated with n-type bands, so that in this case $n_f = 3$ and $n_b = 0$. When assuming perfect transmission ($\tau_f = \tau_b = 1$), the calculated conductivities are $(\sigma_{\text{xx}}, \sigma_{\text{xy}}) = (0, 3)G_0$, consistent with the experimental values. Second, consider the situation of an unbalanced number of counterpropagating edge states at $(B, V_{\text{TG}}) = (3.4\,\text{T}, -2.7\,\text{V})$ with filling numbers $(0, 2, 2)$. When assuming perfect transmission with $n_f = 3$ and $n_b = 2$, the calculated conductivities are $(\sigma_{\text{xx}}, \sigma_{\text{xy}}) \approx (1.44, 3.73)G_0$, which is very different from the experimentally observed values $(\sigma_{\text{xx}}, \sigma_{\text{xy}}) \approx (0.01, 1.01)G_0$. The corresponding transmission probabilities can be estimated by comparing the experimental results and Equations 9.13 and 9.14. For the case of $n_f = 3$ and $n_b = 2$, one finds $\tau_f \approx 0.34$ and $\tau_b \approx 0.06$. These values are significantly smaller than one, indicating a strong effect of scattering in between counterpropagating edge channels. The system behaves as if there were $n_f\tau_f = 1.01 \approx 1$ forward moving and $n_b\tau_b = 0.12 \approx 0$ backward moving states contributing to transport. That is to say, the system behaves as if an equal amount of forward and backward moving states are cancelling each other out. The transport properties of the system as a whole are defined only by the difference between the two, i. e. the net number of states $n_f - n_b$. The same reasoning can be applied to other (unbalanced) filling factor configurations indicated in Figure 9.8. Third, consider the case of a balanced number of counterpropagating edge states, for example at $(B, V_{\text{TG}}) = (3.4\,\text{T}, -3.1\,\text{V})$ with filling numbers $(0, 2, 3)$. The calculated conductivities for

$n_f = 3$ and $n_b = 3$ are $(\sigma_{\text{xx}}, \sigma_{\text{xy}}) = (4.5, 4.5)G_0$, while the experimental values are $(\sigma_{\text{xx}}, \sigma_{\text{xy}}) \approx (0.15, 0.00)G_0$.[1] The cancellation of forward and backward moving states leads to a large longitudinal and small transverse resistance, resulting in a finite σ_{xx} and vanishing σ_{xy}. On the whole, the experimental results can be well explained by assuming scattering of counterpropagating edge states. This situation is reminiscent of the famous QSH effect [5]. There, the 4-terminal conductance of $2e^2/h$ results from two counterpropagating edge states, which do not scatter due to spin conservation. In big samples, however, scattering can still occur and reduces the 4-terminal conductance significantly [46, 62]. The same reasoning may be applied to edge states in 3D TIs [102, 103].

For the sake of completeness, two important remarks regarding the validity of the preceding discussion are necessary. First, the simple model used to obtain Equations 9.13 and 9.14 does not take into account any properties of a scattering mechanism. Hence, it does not distinguish transmission probabilities for "short" or "long" edges, which may in general be quite different. A more rigorous treatment, including explicitly the spatial variation of scattering probabilities, can be found in Reference [111]. Qualitatively, however, the above consideration is still meaningful, since the experimental results can only be modeled correctly when assuming strong scattering between counterpropagating edge states. Second, a nonstandard measurement configuration was used when measuring sample *QC0501 HB ICP*. However, the same discrepancy between calculated and measured values of σ_{xx} and σ_{xy} (when assuming perfect transmission) is found in sample *QC0502 HB ICP* (cf. Section 8.2.1), which was measured with the standard configuration. The deviation between expected and experimentally observed conductance values is thus not an artifact of the measurement configuration.

On the whole, the situation of counterpropagating edge channels in HgTe 3D TIs may seem simple once the individual LLs are sorted. The total QHE indices are determined by the sum of individual filling factors. A closer inspection shows, however, that this behavior points towards a complex situation, in which individual edge channels can interact and equilibrate in between voltage probes. More dedicated theoretical work may be required to resolve the underlying microscopic mechanism. An important step in this direction can be found in Reference [111].

[1] The reader might be surprised at this point since three forward-moving and three backward-moving edge states with perfect transmission seem to imply $(\sigma_{\text{xx}}, \sigma_{\text{xy}}) = (6, 0)G_0$. This is not the case here due to the nonstandard measurement configuration. .

10 Conclusion: Refined model for surface state transport in HgTe

A short summary of this part of the thesis is in order. The starting question was "How can we understand transport properties of the HgTe 3D TI system over the full density range which is experimentally accessible?"

From the experimental side several steps were taken to improve the device quality and resolution of measurements for a wide range of carrier densities and magnetic fields. It was found that the focus should be placed on samples with thick CdHgTe capping layers, which show high carrier mobilities. Also the etching techniques used to structure samples were shown to play a crucial role in avoiding sample degradation. Especially etching with high-energy Ar^+ ions induces lateral sample degradation, a density shift, and consequently a number of artifacts in measurements. Less invasive etching techniques like wet etching or the newly introduced low-energy inductively coupled plasma etching were found to favor high-resolution measurements also in thick HgTe layers. Furthermore it was shown that ungated regions in the contact leads with low carrier density can introduce pronounced artifacts in the measurements. The use of a (global) back gate or a modulation doping layer to increase the carrier density in the ungated regions was identified as a straightforward solution to this problem.

The extraordinarily high quality of some of the investigated samples allowed to identify several transport channels contributing to transport in the HgTe 3D TI system besides the already known topological surface states. Especially valuable was the use of Fourier transforms to extract the carrier densities of the different subbands on a quantitative basis. Manipulation of all surface states in the HgTe layer by means of modulation doping and backgating helped to assign the individual contributions to the topological surface states as well as massive p-type and n-type states. Based on detailed k·p calculations as well as the mutual screening of individual states it was concluded that the massive p-type states are (trivial) surface states. These so-called Volkov-Pankratov states form due to the electrostatic potential well created at the HgTe/CdHgTe interface by a strong negative gate potential. They are the origin of the pronounced p-type QHE commonly observed in high-quality HgTe layers. If the gate potential is not yet strong enough to induce these surface states, the bulk valence bands may also affect transport properties. The massive n-type states were shown to most likely originate from the bulk conduction band, which is split into well-separated subbands due to size quantization. They are different from n-type Volkov-Pankratov states which could appear at very high n-densities.

With this more detailed understanding of the HgTe 3D TI system it was then possible to investigate the interplay of LLs of different origin. Top gate - back gate maps at low magnetic fields ($B \lesssim 1\,\mathrm{T}$) demonstrated the mutual screening of the different bands. Furthermore, avoided crossings between LLs of the same index from top and bottom TSS were found, which hint at a nonzero interaction between these surface states. Due to the large separation between the two surfaces this finding is surprising and raises further questions as to the nature of this possible interaction. In modulation doped samples it was possible to observe the superposition of a n-type QHE from the bottom TSS and a p-type QHE from Volkov-Pankratov states in an intermediate field range ($2\,\mathrm{T} \lesssim B \lesssim 7\,\mathrm{T}$). It was found that the total QHE indices are given by the sum of individual filling factors. While intuitive at first, this result can only be understood when assuming equilibration of the different edge modes in between voltage probes. Future studies (possibly with a strong theoretical background) should investigate the microscopic origin of this effect. In high magnetic fields ($B \gtrsim 3\,\mathrm{T}$), many HgTe 3D TI samples were found to undergo a transition from a complicated superposition of LLs to a single set of LLs. This transition could be explained qualitatively by considering a simple toy model which allows for a charge transfer between different LLs.

The most important aspect of the revised model for transport in HgTe 3D TIs is that the n-type topological surface states contribute to transport in the full parameter range that is commonly accessible in transport experiments. Only massive p-states (both from the valence band and Volkov-Pankratov states) can alter the transport properties significantly, while additional n-type massive states only contribute minor changes. This model will be of great importance in the next section, which will focus on transport in HgTe microstructures.

Part III

Transport properties of HgTe-based microstructures

11 Fingerprints of ballistic effects in surface state transport

The previous part has been devoted to understanding transport properties of big HgTe 3D TI samples. “Big” in this context means that the device dimensions are larger than all other characteristic length scales of electron transport. These may include the mean free paths for scattering (at impurities, phonons, and other charge carriers), the phase coherence length, and the cyclotron radius. The lithographic techniques presented in Part I enable the fabrication of high-quality HgTe devices, which are considerably smaller than the Hall bar samples mentioned before. The high mobility of surface state electrons should suffice for reaching the regime of ballistic transport, where the electron mean free path is comparable to, or longer, than the device dimensions. This transport regime is commonly achieved in high-mobility 2D EG samples [112]. It is an interesting question whether the Dirac surface state electrons in a 3D TI will behave different than electrons in conventional 2D EGs in this transport regime. One possible method to identify the ballistic regime is to apply small magnetic fields or to change the carrier temperature and analyze the resulting resistance changes. The following part of this thesis discusses results in micrometer-sized HgTe 3D TI samples in which the observation of ballistic effects seems feasible.

11.1 Signatures of ballistic transport in the semiclassical transport picture

In very clean samples at low temperatures the scattering mean free path of electrons l_{mfp} is long. In between scattering events the charge carriers move along straight trajectories, which can become comparable to the typical system size L_{C}.[1] Applying a small magnetic field will alter this situation considerably, because it forces the charge carriers on circular trajectories by virtue of the Lorentz force. These circular trajectories are defined by the cyclotron radius

$$R_{\mathrm{C}} = \frac{\hbar k_F}{eB}, \tag{11.1}$$

[1] This model for transport is often referred to as semiclassical transport picture, since charge carriers are treated like moving objects in classical mechanics. The properties of the charge carriers (i. e. quasiparticles) themselves as well as their behavior in scattering events is derived from quantum mechanics, however.

where $\hbar$ is the reduced Planck constant, k_F the Fermi wave vector, e the elementary charge, and B the applied magnetic field. In big samples, where the transport mean free path is short as compared to the device dimensions ($l_{\mathrm{mfp}} \ll L_{\mathrm{C}}$), the Lorentz force will be counteracted by the Hall voltage and no magnetoresistance is observed. In small samples which are in the ballistic transport regime ($l_{\mathrm{mfp}} \gtrsim L_{\mathrm{C}}$), however, this may be quite different.

One famous example of this are commensurability effects in regular antidot arrays [113]. For these experiments, a periodic pattern of defects ("antidots") with lattice constant a is created in an otherwise defect-free 2D conductor. Pronounced resistance resonances are observed, when the ratio of the cyclotron radius to the antidot lattice constant a allows for stable orbits around one or several antidots [113]. This direct relation between device geometry, Fermi wave vector, and magnetic field has also been observed in the Dirac surface states of HgTe 3D TIs [29]. This experiment demonstrates that a ballistic transport effect known from conventional 2D EGs can equally be observed in high-mobility HgTe samples.

Another example of magnetic field-induced resistance changes in the ballistic transport regime is related to boundary scattering in mesoscopic channel samples [112]. In a conducting channel with a width W on the order of the mean free path, scattering with the channel walls can effectively decrease the mean free path of electrons. This is the case if the wall scattering is diffusive, i. e. randomizes the electron momentum. If the wall (or to be more precise, the confining potential) is sufficiently smooth, however, the scattering is specular and the electron motion can be described as a mirror reflection. Specular scattering does not affect the conductivity, since the electron motion parallel to the channel axis remains unchanged. In practice, both types of scattering occur and their relative importance depends on the details of the wall and the angle of incidence of electrons. For the simple case of fully diffusive boundary scattering in a channel confining a 2D EG with parabolic band dispersion, the resistivity can be approximated as [112]

$$\rho = \rho_0 \left(1 + \frac{4}{3\pi}\frac{l_{\mathrm{mfp}}}{W}\right), \tag{11.2}$$

where ρ_0 is the bulk resistivity of the sample. Equation 11.2 is valid for $l_{\mathrm{mfp}}/W << 1$ and deviates from the exact expression by less than 10 % for $l_{\mathrm{mfp}}/W \lesssim 10$ [112]. The boundary scattering effect also shows a pronounced magnetic field dependence. Upon applying a small magnetic field (which is not sufficient to induce quantum effects like SdH oscillations) the otherwise straight electron trajectories are bent and the carriers are forced to collide with the walls more frequently. Figure 11.1a) schematically shows two possible electron trajectories in a ballistic channel with fully diffusive walls with $W/R_{\mathrm{C}} = 0.55$. Both electrons enter the channel on the left with the same velocity and direction, but scattering at the walls causes backscattering for the red trace. The result is a positive magnetoresistance. At sufficiently high magnetic fields, the electrons start to move on so-called skipping orbit trajectories as shown in Figure 11.1b). In this situation the cyclotron radius is so small that electrons bounce along one wall of the system, but rarely encounter

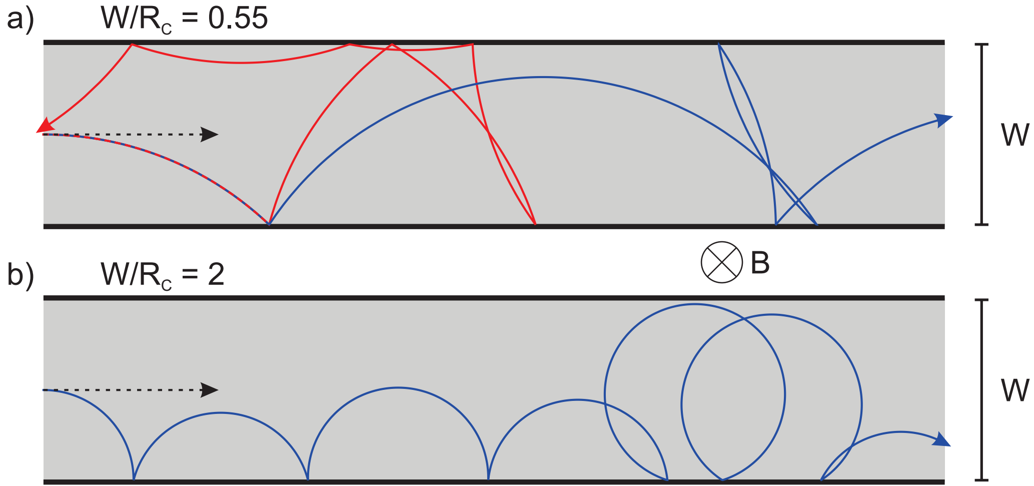

Figure 11.1: Schematic depiction of possible electron trajectories in a ballistic channel with width W, subjected to a small magnetic field B. This figure was inspired by Reference [112].

the opposite channel wall. The result is a negative magnetoresistance, giving rise to a pronounced peak in the magnetoresistance at the turnover point. Once the magnetic field is so strong that the cylotron radius is less than half of the channel width, $W > 2R_{\mathrm{C}}$, an electron cannot reach the opposite wall anymore and the bulk resistivity should be recovered [112].

This effect has famously been observed in high-mobility 2D EG samples [39]. It was found that the peak in magnetoresistance occurs at the magnetic field where $\alpha = W/R_{\mathrm{C}} = 0.55$, consistent with theory [114]. Furthermore, it was shown that properties of the channel walls crucially determine the strength of the effect. Perfectly smooth walls (created by split-gate technology) suppress this effect, since specular scattering dominates. Rough walls (created by low-energy ion exposure) lead to diffusive scattering, making the effect more pronounced [39]. Later on, the boundary scattering effect was also observed in graphene samples [115]. Graphene samples also show a pronounced magnetoresistance, which is suppressed for $W > 2R_{\mathrm{C}}$ as expected. However, the peak in the magnetoresistance occurs at $\alpha = 0.9$ in graphene, in contrast to $\alpha = 0.55$ observed in 2D EGs with parabolic energy dispersion. The reason for this discrepany is not fully clear as of now. It may be caused by the electronic band structure of graphene which gives rise to interference effects between incoming and outgoing electron wave functions [115]. This may change the scattering process at boundaries as compared to conventional 2D EGs. It has also been suggested that the difference arises from the differences in the confining potential, which may be considered parabolic in conventional 2D EGs, and hard wall in graphene [116].

One may expect that an effect of boundary scattering may be observable in high-mobility HgTe 3D TI samples as well. There are two important reasons to

verify this hypothesis experimentally. First, it may serve as a qualitative proof that ballistic transport can be achieved in HgTe 3D TI surface states and allow for a quantitative estimate of the transport mean free path. This information will be useful later on to interpret other transport data in microstructures (cf. Section 12.2). Second, one may expect that boundary scattering in the TSSs differs from the case of conventional 2D EGs, but also graphene (which also features Dirac carriers). One reason is the suppression of backscattering of helical edge states in 3D TIs [117]. The other reason is that the TSSs are "wrapped" around the insulating bulk. This raises the question of what boundary scattering actually is in the case of a 3D TI.

11.2 Magnetosize effect in HgTe 3D TI surface state transport

As discussed already in Chapter 7, substantial improvements in our lithographic techniques enable us to produce micrometer-sized HgTe structures, which retain a high device quality. Certain transport results are characteristic of small samples and not found in macroscopic Hall bars.

Figure 11.2 compares Hall measurements of samples *QC0509 HB ICP 1*, a 200 µm × 600 µm big Hall bar, and *QC0509 ch ICP 2*, a 2 µm × 10 µm sized channel sample. Both samples have been fabricated from the same wafer and with similar lithographic techniques, including ICP etching for structuring the mesa. The main difference is that the lift-off masks for the BaF_2 etch shield and the top gate metal electrode have been prepared by optical lithography on sample *QC0509 HB ICP 1* and by EBL on sample *QC0509 ch ICP 2*. The resistivity in the big sample, Figure 11.2a), shows almost no dependence on magnetic field before the onset of SdH oscillations around $B \approx 0.5\,\mathrm{T}$. The small dip around $B = 0\,\mathrm{T}$ may be attributed to multi-carrier behavior due to the presence of the top and bottom TSSs and conduction band states, which in general have a different mobility. From fitting the low-field Hall resistance (cf. gray dashed line) and the resistivity at 0 T one can deduce a total carrier density of $6.4 \times 10^{11}\,\mathrm{cm}^{-2}$ and a high mobility of $410 \times 10^3\,\mathrm{cm}^2(\mathrm{Vs})^{-1}$. The high quality is also reflected in the high-quality QHE which is observed at higher magnetic fields. The resistivity of the channel sample, Figure 11.2b), shows a very pronounced negative magnetoresistance around $B = 0\,\mathrm{T}$. From the low-magnetic-field data one finds a total carrier density of $6.7 \times 10^{11}\,\mathrm{cm}^{-2}$, which is comparable to the value in the big Hall bar. The mobility, however, is reduced to $160 \times 10^3\,\mathrm{cm}^2(\mathrm{Vs})^{-1}$, which is reflected in the overall higher resistivity in the channel sample. At magnetic fields as low as $B \approx 1\,\mathrm{T}$, contact problems distort the measurement in the channel sample.[2]

[2] Using the back gate, it has been verified that the deviations from the expected QHE behavior are most likely due to contact problems. Sample *QC0509 ch ICP 2* has large ungated areas, making this assumption very plausible (cf. Section 7.3).

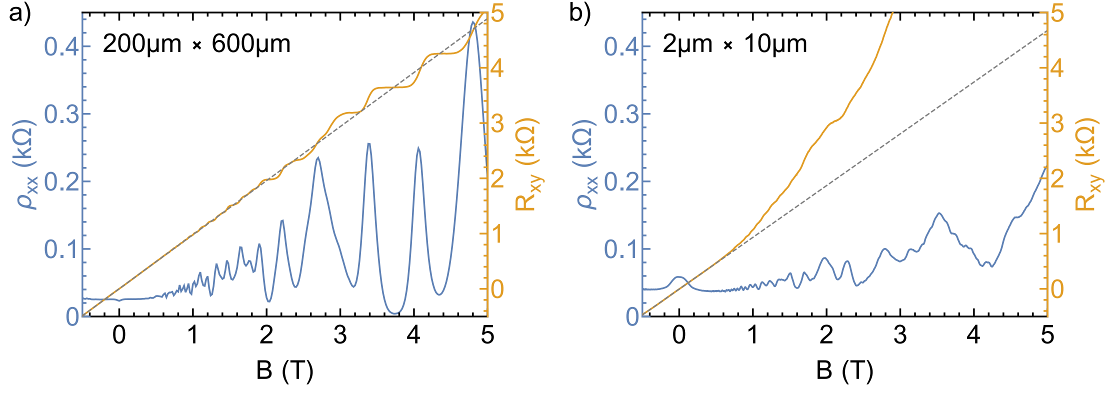

Figure 11.2: Comparison of macroscopic and microscopic samples. a) Longitudinal resistivity ρ_{xx} and Hall resistance R_{xy} for sample *QC0509 HB ICP 1*, a Hall bar with dimensions $200\,\mu\mathrm{m} \times 600\,\mu\mathrm{m}$. b) Longitudinal resistivity ρ_{xx} and Hall resistance R_{xy} for sample *QC0509 ch ICP 2*, a channel sample with dimensions $2\,\mu\mathrm{m} \times 10\,\mu\mathrm{m}$. The measurements were done at a sample temperature of $T = 1.4\,\mathrm{K}$, a top gate voltage of $V_{\mathrm{TG}} = 2\,\mathrm{V}$, and grounded back gate.

A similar increase of resistivity in small samples, together with a negative magnetoresistance, is also found in several comparable samples. It is reasonable to attribute this behavior to boundary scattering. A quantitative estimate supports this hypothesis: Using the mobility values from the big Hall bar, the bulk value for the mean free path in wafer *QC0509* can be estimated as [60]

$$l_{\mathrm{mfp}} \approx \frac{\mu_{\mathrm{av}} \hbar \sqrt{2\pi n_{\mathrm{tot}}}}{e}, \tag{11.3}$$

where μ_{av} is the average carrier mobility and n_{tot} is the total carrier density. Expression 11.3 does not take into account that several conduction channels participate and is strictly valid only for a 2D EG with parabolic band dispersion. Nevertheless, it should provide a reasonable order of magnitude estimate. The resulting bulk mean free path in wafer *QC0509* is on the order of $5.4\,\mu\mathrm{m}$ and thus larger than the width of the small channel sample. Based on Equation 11.2 a resistance increase by a factor of 2.1 might be expected from boundary scattering in this case. In the case of sample *QC0509 ch ICP 2* the resistivity is increased from a minimum of $\rho_{\mathrm{xx}}(0.62\,\mathrm{T}) = 37\,\Omega$ to $\rho_{\mathrm{xx}}(0\,\mathrm{T}) = 59\,\Omega$ at zero magnetic field, corresponding to a resistance increase by a factor of only 1.6. Note, however, that also the minimum resistivity in the channel sample is considerably higher than the minimum resistivity of $23\,\Omega$ found in the big Hall bar. This may be an indication that the EBL process has an impact on sample quality or that the channel sample was placed on a wafer part with reduced quality. Using the carrier mobility and density values from the channel sample in Equations 11.3 and 11.2 results in a predicted increase in resistance of only 1.5, which is comparable to the

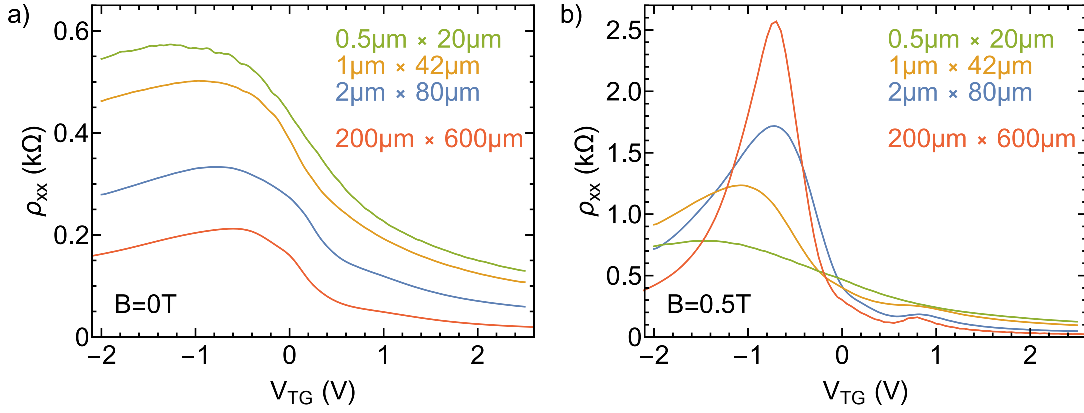

Figure 11.3: Comparison of microscopic channel structures and big Hall bar. a) Longitudinal resistivity ρ_{xx} as a function of top gate voltage V_{TG} at zero magnetic field for three channel structures on sample *QC0509 ch ICP 3* and the big Hall bar on sample *QC0509 HB ICP 1*. b) Same as in a), but at a magnetic field of $B = 0.5\,\mathrm{T}$. All measurements were done at 1.4 K and with grounded back gate.

experimentally observed value. On the whole, the quantitative estimates point towards boundary scattering of quasi-ballistic electrons as cause for the negative magnetoresistance.

To better understand this effect in HgTe 3D TIs, it is beneficial to consider channel samples with a larger aspect ratio and differing widths. Sample *QC0509 ch ICP 3* contains three channel structures, with dimensions $2\,\mu\mathrm{m} \times 80\,\mu\mathrm{m}$, $1\,\mu\mathrm{m} \times 42\,\mu\mathrm{m}$, and $0.5\,\mu\mathrm{m} \times 20\,\mu\mathrm{m}$. The lithographic process for this sample was mostly identical to the process for sample *QC0509 ch ICP 2*. The only difference is that the gate electrodes were structured with optical lithography and not EBL. The design allows to perform 4-terminal measurements of the longitudinal resistance, but not the Hall voltage (cf. Figure 7.3 for a similar device). Only in the 1 µm wide channel, one of the voltage probes failed, so that effectively a 3-terminal measurement was performed for this channel, resulting in a slightly differing aspect ratio. It is important to check that these small structures still have basic properties comparable to a macroscopic sample. Figure 11.3 compares the gate-dependent longitudinal resistivities of these channel samples with the resistivity of the $200\,\mu\mathrm{m} \times 600\,\mu\mathrm{m}$ big Hall bar on sample *QC0509 HB ICP 1*. The zero magnetic field curves are qualitatively similar for all samples, and notably all show a pronounced peak in the resistivity at a similar gate voltage. Quantitatively, the resistance increases for narrower channels. This is the expected behavior due to the classical size effect. The resistivities at a small magnetic field of $B = 0.5\,\mathrm{T}$ are still very similar for the big Hall bar and the 2 µm wide channel. Importantly, the peak positions, and thus the minimum density points, occur at a similar gate voltage. For the narrower channels, the peak positions in small magnetic field shift to slightly more negative gate voltages and broaden. Both changes indicate a slight sample degradation due to the lithographic

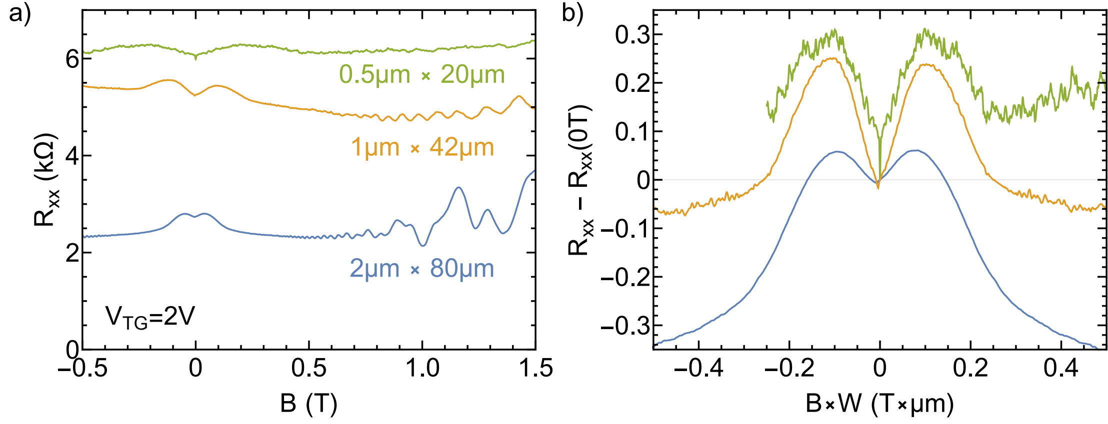

Figure 11.4: Low-field magnetoresistance of channel structures on sample *QC0509 ch ICP 3*. a) Longitudinal resistance R_{xx} as a function of magnetic field B for channels with differing widths W. b) Same data as in a), but shifted w. r. t. the zero-field resistance and plotted as a function of $B \times W$. For the 1 μm wide channel a linear background was subtracted. All measurements were done at 1.4 K and with grounded back gate.

process (cf. Section 7.2, but note the differences in sample widths). Even in the narrowest channel, it is still possible to gate from n-to p-regime. In the following it will be tacitly assumed that the density-to-gate voltage relation is similar in all samples. Based on previous discussions (cf. Chapter 8) it will further be assumed that the Fermi level is situated in the bulk band gap for gate voltages betwen 0 V and 0.6 V.

Figure 11.4a) shows the longitudinal resistance of the channel samples as a function of magnetic field at a top gate voltage of $V_{\mathrm{TG}} = 2\,\mathrm{V}$. In all channels, the resistance first increases with magnetic field, passes through a pronounced maximum and then decreases again. It then remains essentially flat up to the onset of SdH oscillations. Note that for the 1 μm wide channel the three-terminal configuration induces a slight asymmetry of the resistance. This is because a part of the Hall voltage is picked up in this measurement configuration as well. The positive magnetoresistance around $B = 0\,\mathrm{T}$, which could not be clearly resolved in sample *QC0509 ch ICP 2*, cf. Figure 11.2b), is fully consistent with a boundary scattering effect as explained before.

Further support for the importance of boundary scattering comes from the width dependence of the effect. The position of the maxima B_{max} shifts to higher magnetic field values as the channels become narrower. Figure 11.4b) shows the same data as a), but this time shifted w. r. t. the zero-field resistance and plotted as a function of $B \times W$. A linear background has been subtracted from the 1 μm data for clarity. According to Equation 11.1, the value

$$B \times W = \frac{\hbar k_F}{R_{\mathrm{C}} e} \times W = \alpha \cdot \frac{\hbar k_F}{e} \tag{11.4}$$

should be constant for the three channels of differing width, since k_F (which is not known a priori) should be the same. The rescaling reveals that the resistance maxima occur at a comparable value of α for all samples, despite the large differences in width. Also the transition from a negative magnetoresistance to an almost constant value occurs at a similar value of α. Both are expected for the boundary scattering effect, making this assignment conclusive.

What remains challenging in the case of HgTe 3D TIs is the assignment of the observed boundary scattering effect to the individual conduction channels participating in transport. Three carrier systems contribute in n-regime: The two TSSs on top and bottom surface of the HgTe layer, as well as n-type bulk carriers (cf. Chapter 8). To further clarify this point, Figure 11.5a) shows the magnetoresistance of the 2 µm wide channel for several top gate voltages. A clear resistance peak is observed for all gate voltages from 2.5 V down to 0.5 V. For still lower gate voltages a strong positive magnetoresistance dominates the overall signal, which can be attributed to the onset of p-conductance (cf. magnetoresistance in Figure 11.3 and discussion in Section 8.2). The magnetosize effect becomes more pronounced for higher positive gate voltages, i. e. for higher overall n-densities. It is reasonable to assume that in this regime the top TSS will dominate the conductivity. Wafer *QC0509* is undoped and the measurements were done with grounded back gate. Hence, the top TSS will accomodate most free carriers participating in transport. It is expected that resistance changes due to boundary scattering become less pronounced at lower carrier densities [39]. This implies that the influence of the bottom TSS and n-type bulk states are small. At higher fields ($B > 0.5\,\mathrm{T}$) the top TSS also dominates the SdH oscillations and its carrier density n_{TSS} can be obtained from a FFT analysis (cf. Section 8.2). The result is shown in the inset of Figure 11.5b). With this information, Equation 11.1, and $k_F = \sqrt{4\pi n_{\mathrm{TSS}}}$, one can now estimate the magnetic field at which $\alpha = W/R_{\mathrm{C}} = 2$. These points are marked in Figure 11.5a) with arrows. It is found that for $V_{\mathrm{TG}} \gtrsim 1\,\mathrm{V}$ the arrows roughly mark the transition points from a negative magnetoresistance to a constant or increasing magnetoresistance. This is the expected behavior, since at $W/R_{\mathrm{C}} \gtrsim 2$ the influence of the boundary scattering should become small.

The peaks in the magnetoresistance are expected to more strongly depend on the details of the boundary scattering and the electronic properties of the electron gas [116]. There is a general trend, though: With increasing carrier density, i. e. with increasing cyclotron radius, the resistance maxima should shift to higher magnetic fields. Figure 11.5b) shows the peak positions B_{max} as a function of gate voltage. It is found that the peak positions move to smaller magnetic fields for higher carrier densities in the top TSS. This behavior is found for all channel structures (note that for $V_{\mathrm{TG}} = 0.5\,\mathrm{V}$ and 1.0 V the peaks in the narrow channels were not clearly resolved and thus omitted). For comparison, the gray dashed lines show the expected peak positions for the 2 µm channel for $\alpha = 0.55$ (as found in conventional 2D EGs [39]) and $\alpha = 0.9$ (as found in graphene [115]). The orders of magnitude match in n-regime where the Fermi level is not situated in the bulk band gap anymore. However, the functional dependence on gate voltage is opposite

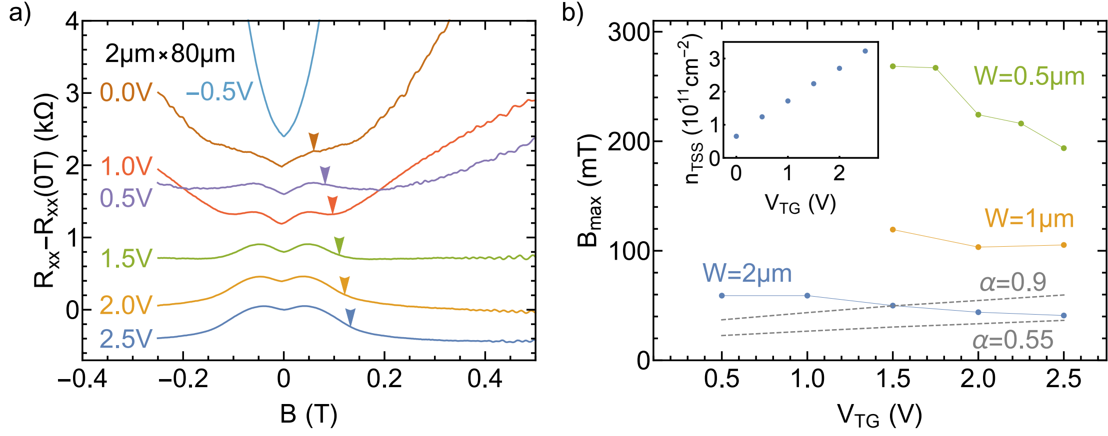

Figure 11.5: Gate dependence of the boundary scattering effect in sample *QC0509 ch ICP 3*. a) Longitudinal resistance R_{xx} of the 2 μm wide channel as a function of magnetic field B, shifted w. r. t. the zero-field resistance and stacked for clarity. Gate voltages are indicated in the figure. Arrows indicate the magnetic field where $\alpha = 2$, based on the densities for the top TSS. b) Position B_{max} of maxima in the resistance of channel structures as a function of top gate voltage. The dashed lines indicate expected maxima positions for the 2 μm wide channel. The inset shows the carrier density of the top TSS, n_{TSS}, as a function of top gate voltage.

to what is expected. The same behavior was observed in other channel samples made from HgTe 3D TI layers.

The most straightforward explanation for this discrepancy with conventional 2D EGs and graphene is the complicated interplay of different conduction channels with different carrier mobilities. As demonstrated in Figure 11.2a) and discussed in Section 8.2, even macroscopic Hall bar samples usually show a positive magnetoresistance. A positive magnetoresistance is characteristic for multi-carrier systems and has an amplitude related to the mobility difference of the individual carriers. This size-independent effect may well distort the size-induced magnetoresistance due to boundary scattering. As a result, maxima in the longitudinal resistance may be shifted to higher magnetic fields, making the overall interpretation very difficult. It is important to note, however, that multi-carrier behavior cannot be the only reason for the nonmonotonic magnetoresistance found in narrow channel structures. First of all, a strong nonmonotonic magnetoresistance is found only in narrow channel structures and not in macroscopic Hall bars. Second, a clear size-dependence of peak positions in narrow channels is observed (cf. Figure 11.5b)), which would not be expected from the multi-carrier behavior alone. Third, the superposition of different conduction channels will always lead to a positive magnetoresistance. The pronounced negative magnetoresistance observed in narrow channels has to be induced by the size effect.

In addition to the size-independent effect of multi-carrier transport, it is also possible that a size-dependent nonmonotonic magnetoresistance signal from the bottom TSS contributes to the overall signal. The bottom TSS has been neglected in the previous considerations since its carrier density is only on the order of $1 \times 10^{11}\,\mathrm{cm}^{-2}$ in wafer *QC0509* at grounded back gate.[3] At higher gate voltages, $V_{\mathrm{TG}} \gtrsim 1\,\mathrm{V}$, the boundary scattering of the top TSS should dominate the overall magnetoresistance. It is still possible, however, that the presence of the bottom TSS influences the overall signal and thus also complicates the interpretation. What makes the interpretation of the results especially challenging is the fact that the individual conduction channels might contribute slightly differently across a series of samples, or even from cooldown to cooldown. The exact configuration must be known, though, in order to properly disentangle the individual contributions. A more detailed understanding is necessary to assess whether the unusual density dependence of the boundary scattering effect in microsocpic HgTe 3D TI samples has a trivial explanation or whether it originates from the special properties of the surface states.

Future studies could shine light onto these open questions with a slightly different sample design. It would be beneficial to combine a macroscopic Hall bar structure as well as narrow channel structures on the same sample, so as to guarantee a maximum in comparability between the structures. It could also be beneficial to use a wafer material with higher quality than wafer *QC0509*, possibly comparable to wafer *Q2843*. In that case, it should be possible to properly disentangle and manipulate all contributing conduction channels by using top and back gates (cf. Section 8.2.2) with measurements of the macroscopic Hall bar. These findings might then be used to better understand the boundary scattering effect in the narrow channels. It could be interesting for example to tune both TSSs to the same densities when investigating the boundary scattering. This would remove the ambiguity of choosing the proper carrier densities to evaluate expressions like Equation 11.1.

Lastly, it remains to understand if there is a possibility to control the amount of (diffusive) boundary scattering in the system. In conventional 2D EGs this is achieved by structuring the channel either via ion etching (high amount of diffusive scattering) or split-gate technology (small amount of diffusive scattering) [39]. In our HgTe samples, it is expected that the amount of diffusive boundary scattering may scale with the roughness of the boundaries. In this case, boundary scattering should be more diffusive in samples structured with ICP etching as compared to samples structured with wet etching (cf. Section 4.3). Figure 11.6a) shows the longitudinal resistance of samples *QC0509 ch wet 1* and *QC0509 ch ICP 2* as a function of magnetic field, both at a top gate voltage of $V_{\mathrm{TG}} = 2\,\mathrm{V}$. These two samples are almost exact copies of each other in terms of sample layout and

[3]The density of the bottom TSS is not properly resolved in the FFT analysis, possibly due to insufficient sample quality. It can still be estimated by comparing the density of the top TSS with the total density.

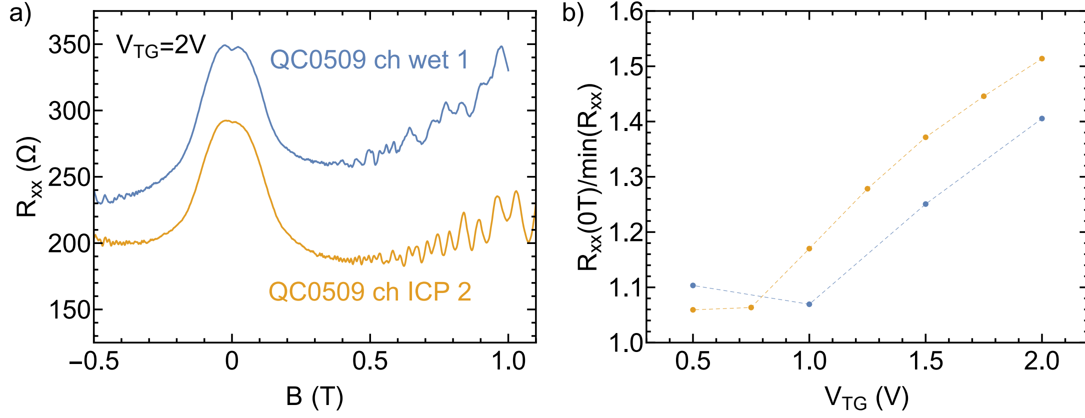

Figure 11.6: Influence of etching technique on the boundary scattering effect. a) Longitudinal resistance R_{xx} of samples *QC0509 ch wet 1* and *QC0509 ch ICP 2* as a function of magnetic field B, at a top gate voltage of $V_{\mathrm{TG}} = 2\,\mathrm{V}$ and with grounded back gate. b) Ratio of R_{xx} at zero magnetic field to the minimum R_{xx} as a function of top gate voltage. All measurements were done at 1.4 K.

lithography. The main difference is that the mesa of sample *QC0509 ch wet 1* was structured with the standard wet etching process, while sample *QC0509 ch ICP 2* was structured with the ICP process. Both have a nominal size of $2\,\mu\mathrm{m} \times 10\,\mu\mathrm{m}$ between voltage probes. Optical microscopy images indicate, however, that the actual width of the wet etched sample is $(1.6 \pm 0.1)\,\mu\mathrm{m}$ due to isotropic etching. The samples fabricated with ICP etching have a very high structural fidelity, which is confirmed by optical microscopy images. Both samples show the negative magnetoresistance which is the fingerprint of boundary scattering. The overall resistance (both at zero magnetic field and finite magnetic field) of the wet etched sample is higher than that of the dry etched sample as expected from the slight difference in aspect ratios. Due to this overall resistance difference one cannot directly compare the amplitude of the resistance peaks in both samples. It is more reasonable to compare the relative resistance increase due to boundary scattering. Figure 11.6b) shows $R_{\mathrm{xx}}(0\,\mathrm{T})/\min(R_{\mathrm{xx}})$ for both samples at top gate voltages where a clear peak is observed in the resistance. $R_{\mathrm{xx}}(0\,\mathrm{T})$ is the resistance at zero magnetic field. $\min(R_{\mathrm{xx}})$ is the minimum resistance for $|B| < 0.4\,\mathrm{T}$, averaged over both magnetic field directions to account for a slight asymmetry (possibly a Hall contribution) in the data. The relative resistance increase due to boundary scattering is slightly higher in the dry etched sample, consistent with the expectation. (The size effect becomes weak at small carrier densities, explaining the deviation at $V_{\mathrm{TG}} = 0.5\,\mathrm{V}$.) It is interesting that the wet etched sample also shows the boundary scattering effect, albeit somewhat less pronounced. This indicates that the amount of diffusive boundary scattering might be influenced by choosing a proper etching method. It seems unrealistic, though, to fully avoid this

effect in micrometer-sized HgTe samples.

On the whole, there is convincing evidence that the quasi-ballistic transport regime can be reached with high-mobility HgTe 3D TI samples. This becomes apparent by a nonmonotonic magnetoresistance in narrow channel samples, which is caused by diffusive scattering at the channel walls. The amount of diffusivity is smaller in wet-etched samples with smoother walls as compared to dry-etched samples with rough walls. It cannot be fully avoided, though. The effect of boundary scattering is qualitatively comparable to the observations made on conventional 2D EGs and graphene samples with high mobility. However, the density dependence of the effect is very different from the one observed in other systems and still not sufficiently understood. It remains an open question at this point whether this has a trivial cause or whether it is a consequence of the special properties of the TSSs.

12 Temperature-dependent transport in HgTe microstructures: Signatures of intercarrier scattering

In the previous section it was established that the quasiballistic transport regime can be observed in high-mobility HgTe 3D TI microstructures. This was proven by disturbing the semiclassical trajectories of electrons through the application of a small magnetic field. It is also possible, however, that scattering of electrons among each other increases the resistance by deflecting electrons to the dissipative channel walls. Whether or not this mechanism can be observed in HgTe 3D TIs will be discussed in the following.

12.1 Electron-electron scattering and its impact on resistance

Already more than 80 years ago, Baber (following a suggestion by Mott) investigated the influence of electron-electron scattering on the resistance of metals [118]. The commonly accepted fingerprint of this scattering mechanism is a quadratic increase of the resistance with temperature. This temperature dependence is related to the Pauli exclusion principle governing the behavior of a Fermi liquid. An electron e_1 can only scatter with another electron if the initial state at energy E_1 is occupied and the final state at energy E_1' is unoccupied. As a consequence of Fermi-Dirac statistics, both E_1 and E_1' have to lie in a thermal slice of width $\approx k_BT$ around the Fermi level, where k_B is the Boltzmann constant and T the electron temperature. The number of possible combinations of initial/final states for electron e_1 thus increases linearly with temperature. The same is true for electron e_2, so that the total scattering probability is approximately proportional to $(k_BT)^2$ [119]. The result of a detailed calculation may of course differ somewhat from the T^2 dependence. Additional restrictions due to energy and momentum conservation apply and modify the temperature dependence, especially in one- or two-dimensional systems [120]. Despite quantitative changes, an increase of the electron-electron scattering rate with increasing temperature is always expected. Identifying intercarrier scattering in an experiment is often possible by changing

the carrier temperature and thus the scattering rate.

However, an increase of the electron-electron scattering rate does not necessarily lead to an increase of resistance. Conservation of momentum implies conservation of current in the scattering event if the electrons involved all have the same properties. Still, two mechanisms are well-known to introduce a resistance due to electron-electron scattering: First, Umklapp scattering which involves the underlying lattice. In such a scattering event, the momentum is only conserved up to a reciprocal lattice vector G and both electrons may experience backscattering [120]. This is only possible of course, if the Fermi wave vector satisfies $k_F > G/4$, which is not the case in most low-density semiconductor systems. Second, if the electrons that scatter have vastly different properties, a redistribution of momentum can change the resistance. This is the case if the scattered electrons reside in two different bands (interband scattering), which differ significantly in effective mass. In this case, the "heavy" electrons can act as momentum sinks. In fact, this is the situation originally considered by Baber [118]. In many alkali and transition metals, a T^2 dependence of the resistance has been experimentally observed and attributed to electron-electron scattering involving these two mechanisms [121, 122].

In low-density semiconductor systems the effects of electron-electron scattering are usually more subtle. In conventional 2D EGs, for example, both Umklapp scattering and interband scattering are absent. In small samples intraband scattering may still have pronounced consequences, as first predicted by Gurzhi [123] and later shown experimentally by de Jong and Molenkamp [31, 32]. They investigated the temperature dependence of the resistance of quasiballistic 2D EG channel samples, in which the mean free path l_{mfp} is long in comparison to the channel width W. They changed the temperature of the electron gas by means of current heating, i. e. by passing a DC heating current through the channel. Due to the weak electron-phonon coupling at low temperatures it is possible to change the carrier temperature while leaving the lattice temperature virtually unchanged. This approach has the advantage that many effects of changing the sample temperature are avoided, including thermal activation of phonons and changes in the band structure. De Jong and Molenkamp found that the resistance first increases with increasing carrier temperature, reaches a pronounced maximum, and then decreases again. With a detailed model they were able to show that the increase in resistance is due to mutual deflection of ballistic electrons towards the dissipative channel walls. In this way, also momentum-conserving collisions can increase the overall resistance of the sample. This is reminiscent of the Knudsen flow regime in gases [124]. At still higher temperatures, the electron-electron scattering length becomes shorter than the channel width and a laminar (Poiseuille) flow develops. The effective interaction with the wall is reduced in this regime and the channel resistivity decreases. This transport regime is also known as "hydrodynamic electron flow", since the electron gas behaves like a classical fluid. More recently, effects of hydrodynamic electron flow have also been observed in graphene [33, 34] and attracted a considerable amount of attention (see e. g. [125, 126, 127]). Electron hydrodynamics is fascinating from a theoretical point of view since the behavior

of a complicated many-body electron system can conveniently be described by equations known from classical fluid dynamics.

One of the key questions that motivated the thesis at hand is “Is it possible to observe hydrodynamic electron flow also in the Dirac surface states of a 3D TI?” The most straightforward approach to answer this question is to follow the experimental approach by de Jong and Molenkamp and perform current heating experiments in HgTe channel samples like the ones described in the previous section. To advance our understanding of HgTe-based material systems, similar experiments were also conducted in thin HgTe layers and in bulk HgTe layers with compressive strain (Section 12.3). The central results of this chapter, summarized in Section 12.2, have been published already in Reference [36].

12.2 Temperature dependence of resistance in HgTe 3D TIs

12.2.1 Effect of current heating in HgTe - fingerprints of hydrodynamic electron flow?

Figures 12.1a) and b) compare the differential resistance dV/dI at different top gate voltages for two samples: A $W = 4\,\mu m$ wide channel on sample *Q2823 ch ICP B* and a $W = 2\,\mu m$ wide channel on sample *QC0509 ch ICP 2* (cf. Section 11.2). The two samples have an aspect ratio (length/width) of $L/W = 5$, i. e. total dimensions $4\,\mu m \times 20\,\mu m$ and $2\,\mu m \times 10\,\mu m$ between voltage probes. All measurements have been done at a sample temperature of 1.4 K, using standard low-frequency lock-in techniques. The current heating experiments were performed by adding a small AC voltage to the DC heating current, cf. inset of Figure 12.1a).

The black line shows the resistance at zero current heating, where the electron temperature equals the bath temperature of 1.4 K. It passes through a pronounced maximum when the sample is gated from n- to p-regime. For comparison between the two devices the gate voltages are presented with respect to this resistance maximum. $V^*_{TG} = 0\,V$ corresponds to an actual applied gate voltage of $V_{TG} = 0.8\,V$ in a) and $V_{TG} = -1\,V$ in b). The total density range shown here is similar for both samples, ranging from a high n-density ($5.7 \times 10^{11}\,cm^{-2}$ at $V^*_{TG} = 2.0\,V$ for *Q2823 ch ICP B*, $5.3 \times 10^{11}\,cm^{-2}$ at $V^*_{TG} = 2.5\,V$ for *QC0509 ch ICP 2*) to a moderate p-density ($-2.1 \times 10^{11}\,cm^{-2}$ at $V^*_{TG} = -0.5\,V$ for *Q2823 ch ICP B*, $-2.0 \times 10^{11}\,cm^{-2}$ at $V^*_{TG} = -0.9\,V$ for *QC0509 ch ICP 2*). The colored lines which run perpendicular to the gate voltage axis show the differential resistance as a function of heating current density $J = I/W$, where I is the applied DC current. Around the resistance maximum at $V^*_{TG} = 0\,V$, dV/dI first increases with increasing J, passes through a maximum and then decreases again for higher heating current densities. At positive gate voltages above 0.5 V, i. e. away from the resistance maximum, dV/dI decreases monotonically with heating current. Similar results as

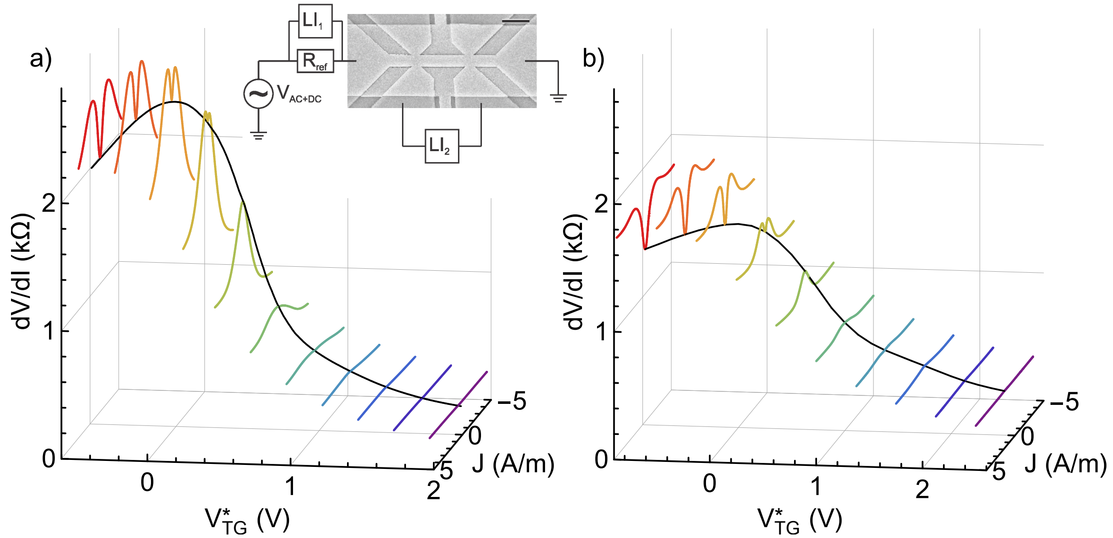

Figure 12.1: Differential resistance of HgTe 3D TI channel samples. a) and b) Colored traces show the differential resistance dV/dI as a function of heating current density J at different gate voltages for samples *Q2823 ch ICP B* and *QC0509 ch ICP 2*, respectively. The black line represents the resistance as a function of gate voltage for zero heating current at a bath temperature of 1.4 K. The inset shows a SEM image of sample *Q2823 ch ICP B*, together with a sketch of the circuit layout with two current contacts and four voltage probes. The top gate is recognizable by a lighter gray color. R_{ref} is an ohmic reference resistance and LI_1 and LI_2 are lock-in amplifiers. The scale bar has a width of 2 µm.

shown in Figure 12.1a) and b) have been obtained for all 3D TI channel samples investigated so far, including wet-etched samples. The peculiar nonmonotonic behavior of the differential resistance around the resistance maximum is very similar to the results described in References [31, 32] for the crossover from ballistic to hydrodynamic electron flow. These observations were the reason to commence a more thorough investigation of current heating in HgTe 3D TIs.

First it must be verified that the observed resistance changes are a carrier temperature-induced effect and not directly caused by the increased bias. Figure 12.2a) shows the differential resistance of the 4 µm wide channel on sample *Q2823 ch ICP B* at a fixed gate voltage of $V^{*}_{\mathrm{TG}} = 0.2\,\mathrm{V}$ for several sample temperatures T_s in the range 1.4 to 14 K. With increasing sample temperature the zero-bias resistance increases so that a peak in differential resistance is only observable up to $T_s = 8.9\,\mathrm{K}$. For higher temperatures, i. e. $T_s = 10.6\,\mathrm{K}$ and above, the nonmonotonic behavior is no longer observed and the differential resistance only decreases with increasing current. This observation indicates that the resulting carrier temperature is responsible for the differential resistance changes. One

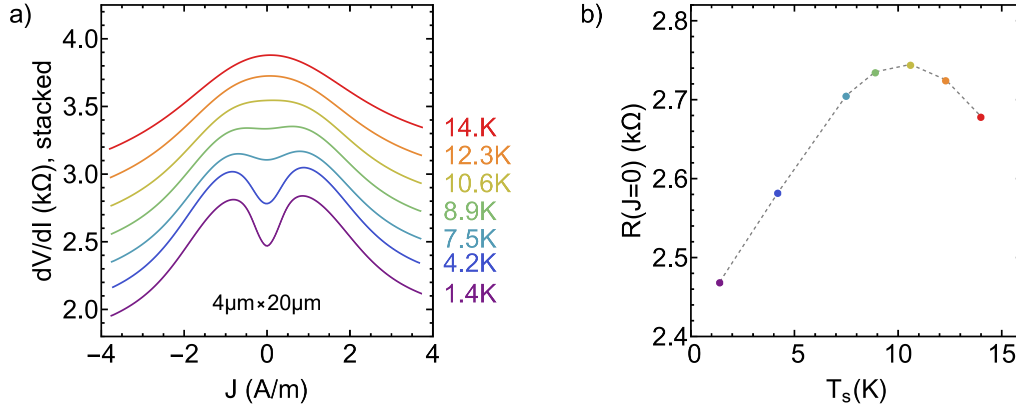

Figure 12.2: (Sample-) temperature dependence of differential resistance in a channel of 4 µm width on sample *Q2823 ch ICP B*. a) Differential resistance dV/dI as a function of heating current density J at different sample temperatures. The curves are vertically stacked by 0.4 kΩ for clarity. b) Resistance R at zero current heating as a function of sample temperature T_s, extracted from a).

can also trace the resistance of the channel for different sample temperatures, as shown in Figure 12.2b). The resistance increases up to a sample temperature of approximately 10.6 K and then decreases for higher temperatures. The sample temperature dependence of the resistance is thus qualitatively comparable to the carrier temperature dependence of the differential resistance. From the peak positions it can be estimated that a current density of 0.8 A/m (cf. purple line at 1.4 K in Figure 12.2a)) corresponds to an electron temperature of approximately 10 K (cf. Figure 12.2b)). This already demonstrates the temperature range relevant for the current heating experiments.

Second, the size dependence of the differential resistance changes needs to be considered. This is the most straightforward way to check if the nonmonotonic behavior of the differential resistance is caused by a transition from ballistic transport to another transport regime (e. g. hydrodynamic transport). If this was the case, the amplitude of the peak in the differential resistance should become more pronounced in smaller samples. Also the peak position should shift in carrier temperature, or heating current density. (It is tacitly assumed here that the current density essentially determines the carrier temperature.) Figure 12.3a) shows the differential resistance changes $\Delta dV/dI = dV/dI - dV/dI(J = 0)$ for two channel structures with widths 4 µm and 2 µm on sample *Q2823 ch ICP B*. All measurements are done at the same total carrier density of $-2.1 \times 10^{11}\,\mathrm{cm}^{-2}$. The 2 µm wide channel has been measured by using either the dedicated voltage probes (with a distance of 10 µm) or the current leads to measure the full channel length (20 µm). The latter is also a 4-terminal measurement since the current leads have two contacts each, but it may include channel entrance effects. The results show that the amplitude of the differential resistance changes is roughly

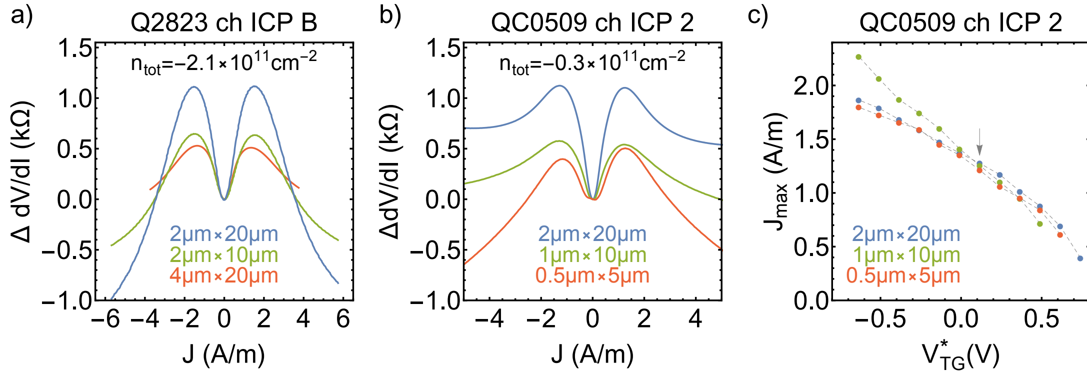

Figure 12.3: Size dependence of differential resistance changes $\Delta dV/dI$ of HgTe 3D TI channel samples. a) $\Delta dV/dI$ as a function of heating current density J for channel structures on sample *Q2823 ch ICP B*, all at the same total carrier density. b) $\Delta dV/dI$ as a function of heating current density for several channel structures on sample *QC0509 ch ICP 2*, all at the same total carrier density. c) Current density J_{max} at which the peak occurs in dV/dI as a function of top gate voltage V^*_{TG} in sample *QC0509 ch ICP 2*. The arrow marks the gate voltage for b). The 2 µm wide channels in a) were measured at a sample temperature of 2.5 K, all other measurements were done at 1.4 K.

proportional to the aspect ratio L/W (i. e. the number of squares) of the channel samples. Furthermore, a comparison of the 4 µm and 2 µm wide channels shows that the peak position occurs at approximately the same current density. The same holds for three channels of width 2 µm, 1 µm, and 0.5 µm on sample *QC0509 ch ICP 2*, as shown in Figure 12.3b) for one and the same carrier density. For the latter sample, the peak positions are also plotted as a function of top gate voltage in Figure 12.3c). For all gate voltages, at which a clear peak occurs in the differential resistance, these peaks occur at a similar heating current density. Overall, the differential resistance shows hardly any effect of the channel width.

The absence of a strong width dependence makes it very unlikely that the nonmonotonic behavior of the differential resistance in HgTe 3D TIs and conventional high-mobility 2D EGs share the same origin. This is further supported by the fact that wafers *Q2823* and *QC0509* differ considerably in carrier mobility. At comparable carrier densities (corresponding to $V^*_{\mathrm{TG}} = 1\,\mathrm{V}$ for both samples), *Q2823* has an average Drude mobility of $170 \times 10^3\,\mathrm{cm}^2(\mathrm{Vs})^{-1}$, while it is as high as $330 \times 10^3\,\mathrm{cm}^2(\mathrm{Vs})^{-1}$ for *QC0509*. Despite this difference, the differential resistance changes are similarly pronounced in both samples. To put these considerations on a more quantative basis, consider the modelling done by Kashuba, Trauzettel, and Molenkamp [129]. This work explicitly treats the effects of electron-electron scattering, impurity scattering, and (diffusive) boundary scattering on the temperature-dependent resistance of narrow channels made from a 2D Dirac material. Using the code that was developed by O. Kashuba

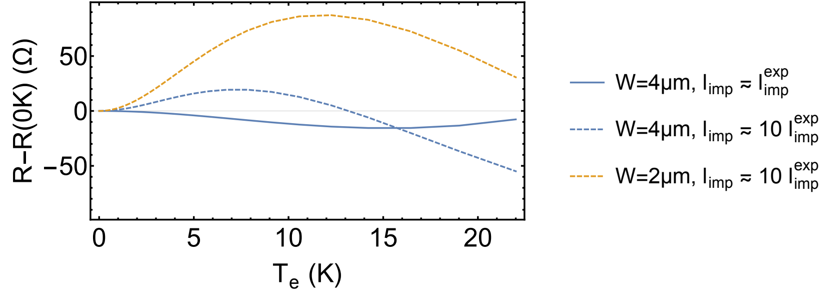

Figure 12.4: Simulated resistance changes in narrow channels made from a 2D Dirac material due to electron-electron scattering, impurity scattering, and (diffusive) boundary scattering. These results were obtained with code kindly provided by O. Kashuba [128].

for Reference [129], one can calculate the influence of electron-electron scattering for sample *Q2823 ch ICP B*. Figure 12.4 shows results obtained for 4 µm and 2 µm wide channels with an aspect ratio of 5 as in the experiment. For these calculations the Fermi velocity was set to $v_F = 0.5 \times 10^6\,\mathrm{m^2/s}$, the electron density to $n_e = 0.6 \times 10^{11}\,\mathrm{cm^{-2}}$, and the parameter of electromagnetic field coupling to $\alpha = 1.5$.[1] The solid blue curve shows results for an impurity scattering mean free path of 1.15 µm, which is comparable to the experimental value in wafer *Q2823*. Under these conditions, the transport is basically diffusive and the resistance only slightly decreases with increasing electron temperature. The interaction with the wall is not determining the overall behavior of the system. When the impurity scattering mean free path is increased by a factor of ten (which is unrealistically large for our HgTe samples but comparable to the high-mobility 2D EGs used in References [31, 32]), the temperature dependence of the calculated resistance (dashed lines in Figure 12.4) qualitatively resembles the experimental observations. However, the curves for the 4 µm and 2 µm wide channels differ substantially from each other, both in amplitude and in the temperature dependence. This is clearly not the case in the experiment (cf. Figure 12.3a)). Furthermore, the absolute change in the resistance that is predicted by the simulation is not at all comparable with the experimental observation. The experimentally observed increase in the differential resistance (which is not identical, but similar to the total resistance) for the 4 µm wide channel is roughly 25 times higher than the increase found in the simulation! These results clearly demonstrate that electron-electron scattering in combination with diffusive wall scattering may well be present in the HgTe channel samples considered here; however, it can by no means explain the observed temperature dependence. It seems more likely that the temperature dependence is an intrinsic effect and related to bulk properties of HgTe 3D TIs.

[1] The value of α determines the electron-electron scattering length. Its precise value is not known for the HgTe TSSs, but it should be on the order of 1 to 3 [129].

12.2.2 Semi-quantitative modelling of the temperature-dependent resistance

In order to develop a suitable model to describe the temperature dependence, it is important to understand how the transport results relate to the HgTe band structure. As discussed in detail in Part II, the low-temperature transport in HgTe 3D TIs can be subdivided into two regimes: The purely n-regime, in which only TSSs (bulk band gap) or conduction band states contribute to transport, and the low-density to high p-density regime, in which both n-type TSSs and p-type bulk states or VPSs are simultaneously present. The onset of bulk carriers is marked by an increase in the magnetoresistance, which is very pronounced for bulk hole carriers and less pronounced for conduction band states. Figure 12.5 compares the longitudinal resistance (both without magnetic field and with a small magnetic field of 0.3 T) to the normalized differential resistance of samples *Q2823 ch ICP B* and *QC0509 ch ICP 2*. In both samples, the onset of n-type bulk states is observed as a small increase in the magnetoresistance at $V_{\mathrm{TG}}^{*} \approx 1\,\mathrm{V}$ in a) and $V_{\mathrm{TG}}^{*} \approx 1.4\,\mathrm{V}$ in c). For gate voltages higher than that, the differential resistance shown in b) and d) shows hardly any change with heating current. For smaller gate voltages, where only TSSs contribute to transport, the differential resistance decreases with increasing heating current. At a top gate voltage of $V_{\mathrm{TG}}^{*} \approx 0.4\,\mathrm{V}$, the magnetoresistance starts to increase dramatically, marking the onset of bulk hole carriers. At this gate voltage the differential resistance starts

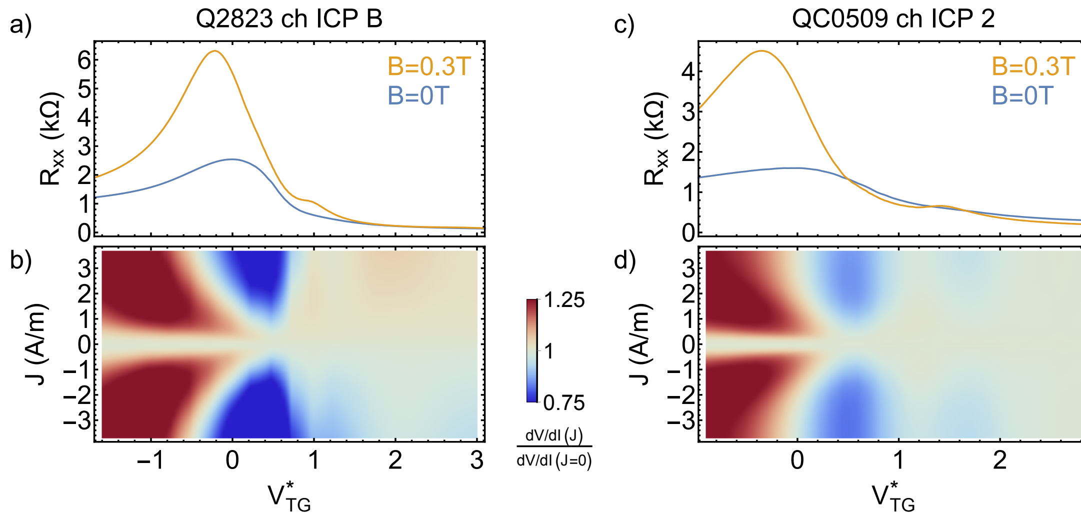

Figure 12.5: Comparison of low-temperature resistance and differential resistance. a) and c) Longitudinal resistance R_{xx} at magnetic fields of $B = 0\,\mathrm{T}$ and $B = 0.3\,\mathrm{T}$ as a function of top gate voltage V_{TG}^{*} for samples *Q2823 ch ICP B* and *QC0509 ch ICP 2*. b) and d) Normalized differential resistance as a function of heating current density J and top gate voltage for samples *Q2823 ch ICP B* and *QC0509 ch ICP 2*.

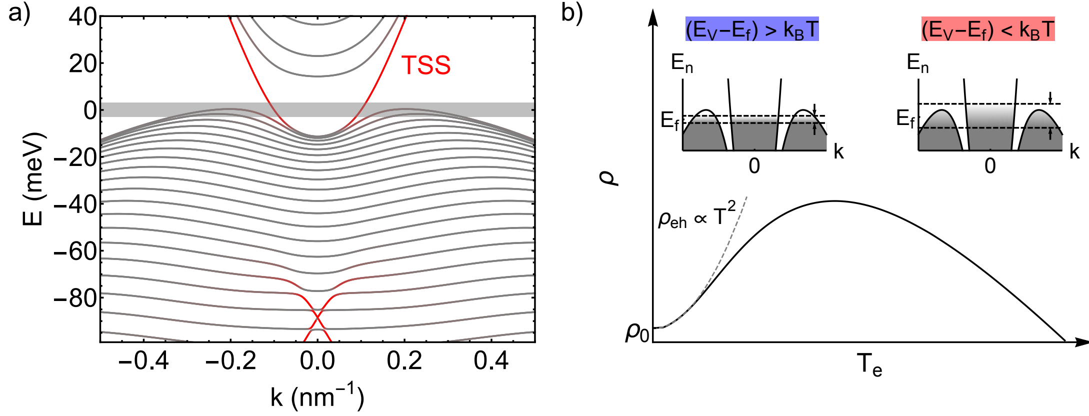

Figure 12.6: Qualitative model for explaining the temperature dependence of resistance in HgTe 3D TIs. a) Band structure of a 70 nm thick HgTe layer with CdTe lattice constant, calculated in a 8-band k·p model with the program *kdotpy* [99]. Gray shading marks the approximate energy window relevant for the nonmonotonic differential resistance. b) Schematic dependence of the resistivity ρ on the electron temperature T_e. The inset illustrates the situation for electron-hole scattering (low T_e, left) and increasing electron density (high T_e, right).

to develop a nonmonotonic behavior, which becomes more pronounced as the sample is gated further to p-regime. In other words: The peculiar nonmonotonic differential resistance is only observed when both TSS electrons and massive hole carriers are present simultaneously.

Figure 12.6a) shows the band structure of a 70 nm thick HgTe layer with the lattice constant of CdTe and sandwiched between CdHgTe protective layers, obtained by a k·p calculation using a basis of 8 orbitals [24, 97, 98, 99]. The TSSs are identified by their confinement close to the HgTe/CdHgTe interfaces (which is marked in red). The bulk states are shown in gray and the subband splitting relates to the finite layer width. A small bulk band gap opens between the valence and conduction band due to strain. The Dirac point is buried deep in the valence band, which has the characteristic "camel back" shape due to band inversion and hybridization of Γ_6 and Γ_8 bands [24, 80, 90]. From the presence of the camel back with a high DOS, one expects that the Fermi level E_f will be pinned to the valence band edge when gating the system from n- to p-regime. Once the Fermi level is pinned, electrons and holes are present in the system simultaneously. As demonstrated in Figure 12.5, the onset of two-carrier behavior coincides with the onset of a strongly nonmonotonic differential resistance. The relevant energy range for this effect is thus the region around the valence band maximum (cf. gray shading in Figure 12.6a)).

In such a highly asymmetric two-carrier system, increasing the carrier temperature has two effects. 1) When free electrons in the TSSs and free holes in

bulk states coexist, electron-hole scattering can occur. Since electrons and holes have opposite polarity, this scattering mechanism relaxes current, even though momentum is conserved [130, 131]. Furthermore, the heavy, low-mobility bulk holes in HgTe can effectively act as momentum sinks. This is reminiscent of s-d scattering in transition metals [120]. The electron-hole scattering rate, just as the electron-electron scattering rate discussed before, will increase with increasing carrier temperature T_e. It is reasonable to approximate the increase of the scattering rate as $\tau_{\mathrm{eh}} \propto T^2$. This mechanism can explain the experimental observation that the differential resistivity first increases with increasing temperature, cf. Figure 12.6b). 2) At higher carrier temperatures, the thermal smearing (of order $k_B T_e$) reaches the valence band edge. The insets of Figure 12.6b) illustrate the thermal smearing for low (left) and high (right) temperatures. At high temperatures, the phase space available for intercarrier scattering is truncated and the electron-hole scattering rate saturates. At the same time, the hole concentration continues to increase with carrier temperature when the Fermi level is sufficiently close to the valence band edge ($|E_V - E_f| \lesssim k_B T_e$, where E_V is the energy of the valence band maximum). Also the number of highly mobile electrons increases so as to keep the total charge (which is determined by the gate voltage) constant, and the overall resistivity decreases. The combination of these two effects results in a pronounced nonmonotonicity of the temperature-dependent resistivity.

The requirement of a constant total charge carrier density implies a shift in the Fermi level as a function of carrier temperature. This effect is commonly discussed in textbooks in the context of semiconductors, in which the valence and conduction bands differ substantially in effective mass [119]. In the HgTe system considered here, the implications of this effect are strongest when the Fermi level is in the bulk band gap and in close proximity to the valence band edge. In this situation electron-hole scattering is almost absent and the differential resistance only decreases with increasing heating current. When the Fermi level is further removed from the valence band edge (by gating to large positive gate voltages), the decrease in differential resistance becomes less pronounced.

These qualitative considerations can be checked for plausibility by developing a semi-quantitative model. The basis for this model is a band structure calculation similar to the one shown in Figure 12.6a). Some values (such as the relevant total carrier densities and carrier mobilities) need to be adapted from experimental results. In the following, this will be done based on data from the 4 µm wide channel on sample *Q2823 ch ICP B*.

The first step is to determine the electron and hole densities as a function of temperature for a set of given total carrier densities. For accurate results it is necessary to calculate the band structure in the two-dimensional k_x, k_y plane, since the dispersion is not rotationally symmetric, cf. inset of Figure 12.7a). From the band structure one can obtain the DOS as a function of energy E for each band. It is useful to define an "electron density of states", $D_e(E)$, and a "hole density of states", $D_h(E)$. $D_e(E)$ sums over all electron-like bands (i. e. the TSSs and conduction bands), while $D_h(E)$ sums over all hole-like bands (i. e. the valence

bands).[2] Figure 12.7a) shows the electron and hole DOS obtained in this way. The hole DOS is roughly one order of magnitude larger than the electron DOS. The electron DOS has a sharp increase when the bulk conduction band sets in. At energies smaller than 14 meV it is fully determined by the TSSs. The free carrier concentration can be calculated as [119]

$$n_{\text{tot}}(E_f, T) = \int_{-\infty}^{\infty} \left[D_e(E) f_e(E, E_f, T) - D_h(E)(1 - f_e(E, E_f, T)) \right] dE, \quad (12.1)$$

where $f_e(E, E_f, T) = 1/\left(e^{(E-E_f)/(k_B T)} + 1\right)$ is the Fermi-Dirac distribution function, E_f the Fermi level, and T the carrier temperature. The integration limits can be set to $-\infty$ and ∞, since the density of states D_e and D_h drop to zero below and above the band maxima. Equation 12.1 implicitly defines the chemical potential and the individual carrier densities from the requirement $n_{\text{tot}} = \text{constant}$. Figure 12.7b) shows the chemical potential as a function of temperature for a set of carrier densities in the range of $-1.3 \times 10^{11}\,\text{cm}^{-2}$ to $3.3 \times 10^{11}\,\text{cm}^{-2}$ with equidistant spacing in density. Due to the high DOS of the valence band the chemical potential is pinned there, so that the values of E_f almost fall on top of each other at small total carrier densities (purple and green curves). With increasing temperature the chemical potential drifts away from the bulk bands so as to keep the total charge constant. The increase of the electron and hole carrier densities (with respect to the low-temperature values) as a function of temperature is shown in Figure 12.7c). This effect is most pronounced for carrier densities, at which the chemical potential is close to the valence band maximum at low temperatures.

The next step is to calculate the resistivity. The intrinsic mobility of electrons, μ_e, is estimated from the experimental low-temperature resistivity at zero heating current and assumed to be constant. The hole contribution to conductance is small and thus neglected. The temperature-dependent resistivity can be calculated as

$$\rho_{\text{tot}} = \frac{1}{e n_e(T) \mu_e} + \rho_{\text{eh}}(T), \quad (12.2)$$

where ρ_{eh} is the additional resistance due to electron-hole scattering. It can be calculated using the coupled kinetic equation approach described in Reference [132] as[3]

$$\rho_{\text{eh}}(T) = \frac{m_e m_h n_h(T)}{e^2 n_e(T)(m_e n_e(T) + m_h n_h(T))} \times \frac{1}{\tau_{\text{eh}}(T)}, \quad (12.3)$$

where $m_e \approx 0.025\,\text{m}_0$ and $m_h \approx 0.2\,\text{m}_0$ are the effective masses of electrons and holes, respectively. m_0 is the rest mass of a free electron. The temperature

[2] From a practical point of view, all bands which lie fully below the bulk band gap are considered hole-like valence bands, all other bands are considered electron-like. This is not very rigorous of course, since deep in the valence band electron-like Dirac states coexist with hole-like states. However, for determining carrier densities only the cumulative DOS close to the band gap is important, so that the results obtained in this way are valid.

[3] Equation 12.3 is significantly simplified as compared to the general expression, Equation 29 in Reference [132], since the hole mobility is set to zero.

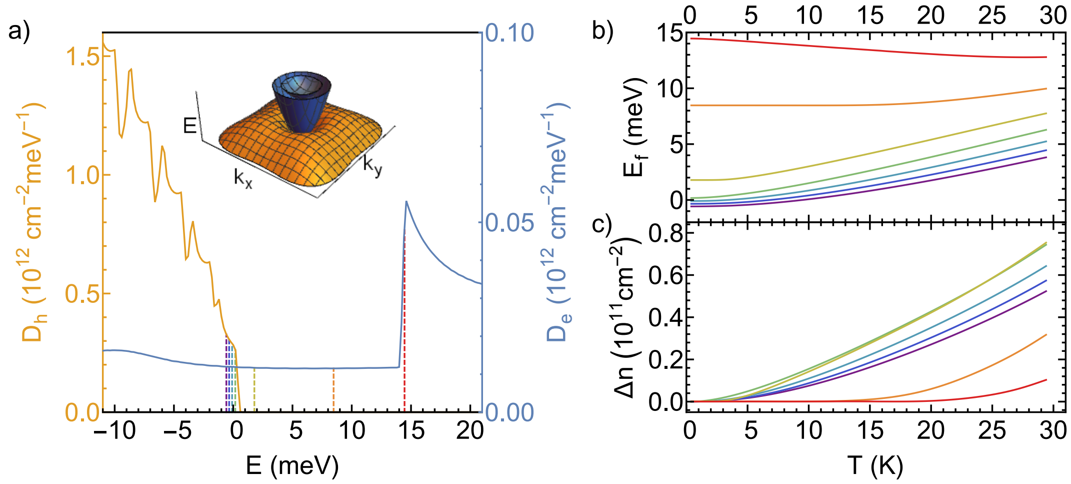

Figure 12.7: Temperature-induced chemical potential shift in HgTe 3D TIs. a) Density of states of electron bands, D_e, and hole bands, D_h, as a function of energy E. Note the different ordinate scales. Dashed lines indicate the chemical potential at 0.4 K for total carrier densities in the range $-1.3 \times 10^{11}\,\mathrm{cm}^{-2}$ (purple) to $3.3 \times 10^{11}\,\mathrm{cm}^{-2}$(red), with equidistant spacing. The inset shows the energy dispersion in k_x, k_y space used to determine the density of states. All results were obtained with the program *kdotpy* [99]. b) Chemical potential E_f as a function of temperature T for the same total densities as in a). c) Increase of (electron and hole) carrier density Δn as a function of temperature.

dependence of the resistivity is strongly influenced by the temperature dependence of the electron-hole scattering rate τ_{eh}^{-1}. The prefactor takes into account the effectiveness of momentum transfer due to electron-hole collisions, which crucially depends on the effective mass difference. In the limit of $m_h \to \infty$, Equation 12.3 reduces to the usual expression for impurity scattering, while in the limit of $m_h \to 0$ it vanishes. The electron-hole scattering rate itself is difficult to calculate directly. As discussed before, it is expected to follow a T^2-dependence at low temperatures and saturate at higher temperatures. Numerical studies, which deliberately avoid the usual assumptions leading to the T^2 dependence, show that the typical temperature scale for saturation is given by the Fermi temperature $T_f = (E_V - E_f)/k_B$, where E_V is the energy of the valence band edge [133, 134]. Adapting the numerical procedure for HgTe is beyond the scope of the current work, and instead the following heuristic expression will be used:

$$\tau_{\mathrm{eh}}^{-1} = CT^2 \left[1 - \exp\left(-\frac{E_V - E_f}{k_B T}\right)\right]^2, \quad \text{for} \quad E_V < E_f. \tag{12.4}$$

The constant $C = 4 \times 10^9\,\mathrm{s}^{-1}\mathrm{K}^{-2}$ is estimated by comparison to the experimental results. Figure 12.8a) shows the electron-hole scattering rate calculated with Equation 12.4 as a function of temperature in rescaled units. The log-log plot

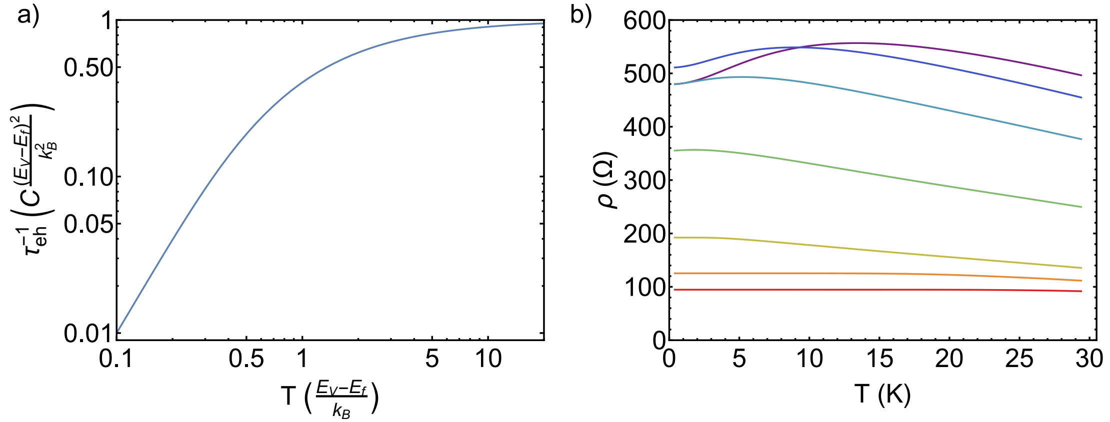

Figure 12.8: Semi-quantitative modelling results for electron-hole scattering in HgTe 3D TIs. a) Electron-hole scattering rate τ_{eh}^{-1} as a function of temperature T in rescaled units. b) Calculated resistivity ρ as a function of carrier temperature T for total carrier densities in the range $-1.3 \times 10^{11}\,\text{cm}^{-2}$ (purple) to $3.3 \times 10^{11}\,\text{cm}^{-2}$ (red).

illustrates the T^2 increase at low temperatures and the saturation at $T_f \approx (E_V - E_f)/k_B$.[4] Figure 12.8b) shows the resistivities, calculated with Equation 12.2, which already share many characteristics with the experimental results: The resistivity is hardly temperature-dependent in n-regime, decreases with temperature when the Fermi level is close to the bulk valence band maximum, and becomes non-monotonic in the low density-regime due to electron-hole scattering.

12.2.3 Calibration of carrier temperature as a function of heating current

In order to compare the heuristic model with the experimental results the resistivities as a function of carrier temperature need to be converted to differential resistance as a function of heating current. In other words: A detailed calibration of electron temperature as a function of heating current is needed.

A crude estimate can be obtained by comparing heating current-induced changes in the differential resistance to sample temperature-induced changes of the resistance. The relevant temperature range for the increase in resistance is on the order of 1.4 K to 10 K (cf. Figure 12.2). This kind of comparison can not be used for a more rigorous temperature calibration, though. First, it requires the resistance to be strongly dependent (and preferably nonmonotonic) on the temperature, which is not the case at most carrier densities. A weak (and monotonic)

[4] One subtle detail about Equation 12.4: For the calculation of τ_{eh}^{-1}, the chemical potential at zero temperature is used, i. e. the temperature-induced chemical potential shift is not included. This is necessary, since the shift is one of the reasons why the electron-hole scattering rate saturates. If the temperature-dependent E_f was used, the shift would be considered twice.

temperature dependence will introduce a large error bar in the calibration. Second, it is beneficial to use a carrier temperature calibration which is independent of the sample temperature. There are several independent effects of changing the sample temperature that change the carrier mobility. A calibration via the sample resistance may thus introduce a systematic error of unknown magnitude. In the pioneering work of de Jong and Molenkamp [31, 32] the electron temperature was determined by measuring the thermopower of a QPC, which was situated along the channel. For current heating experiments in HgTe this is not possible, since the technology for reliably structuring QPCs has only recently been developed for HgTe 2D EGs [48] and has not yet been implemented for bulk samples. Furthermore, the more complicated band structure of HgTe 3D TI layers can make it difficult to interpret results obtained in nanometer-sized constrictions (cf. Reference [30]). Two other methods are thus used for the current work: Temperature calibration via SdH oscillations and via Johnson noise thermometry.

The first approach makes use of the strong temperature dependence of SdH oscillations [135]. It requires two sets of measurements of the resistance as a function of magnetic field: First for several sample temperatures and second for several heating current densities, all with the same gate voltage settings. By comparing the amplitude of SdH oscillations as a function of sample temperature with those as a function of heating current density, one can construct a rough temperature calibration [136].

Figures 12.9a) and b) show the longitudinal resistance R_{xx} of sample *Q2808 ch ICP B*, a $1\,\mu\mathrm{m} \times 5\,\mu\mathrm{m}$ sized channel structure, as a function of magnetic field B and at a total carrier density between $6.1 \times 10^{11}\,\mathrm{cm}^{-2}$ and $7.3 \times 10^{11}\,\mathrm{cm}^{-2}$. The gate voltage is fixed to 3 V for all curves. Figure 12.9a) shows measurements at several sample temperatures T_s. As usual for high-mobility HgTe 3D TI samples in n-regime, a superposition of pronounced SdH oscillations of different carrier systems is observed. These oscillations decrease in amplitude with increasing sample temperature and are not observable anymore for temperatures of 30.3 K or higher. For all temperatures up to 20.6 K, the individual curves collapse onto a single line. For temperatures of 30.3 K and higher the curves shift to higher overall resistances. This may be an indication that gating changes at elevated temperatures. Figure 12.9a) shows measurements at several (average) DC heating current densities J, while the sample temperature was fixed to 1.4 K. Pronounced SdH oscillations are observable at small DC currents, albeit slightly changed as compared to Figure 12.9a). This, together with a small shift in total carrier density, indicates that the sample properties slightly changed at high sample temperatures or when applying high heating currents. At smallest DC currents, the measurements are quite noisy, which can be attributed to the small overall signal which is measured. At higher heating currents, the amplitude of SdH oscillations decreases and all curves eventually collapse onto one average curve without notable SdH oscillations. The amplitudes of SdH oscillations are extracted from these two datasets in the following way: In the field range between 2.05 T and 2.65 T (cf. gray shading) a linear background is subtracted from $R_{\mathrm{xx}}(B)$ and

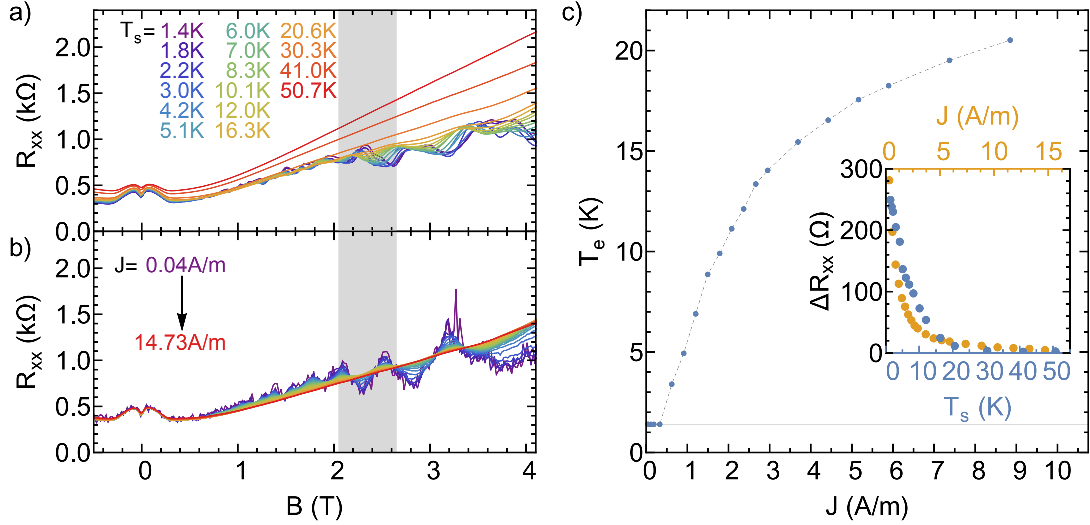

Figure 12.9: Calibration of carrier temperature as a function of heating current in sample *Q2808 ch ICP B* (1 µm × 5 µm) via SdH oscillations. a) and b) Longitudinal resistance R_{xx} as a function of magnetic field B at a fixed gate voltage of 3 V, for increasing sample temperatures T_s (a) or increasing heating current densities J (at $T_s = 1.4\,\mathrm{K}$) (b). c) Carrier temperature T_e as a function of heating current density at $T_s = 1.4\,\mathrm{K}$. Inset: Amplitude of SdH oscillations ΔR_{xx}, as a function of either sample temperature or heating current density.

the difference between the maximum value of R_{xx} and the minimum value of R_{xx} is taken as SdH amplitude ΔR_{xx}. This magnetic field range was the smallest for which pronounced SdH oscillations occur in all resistance curves. The results are shown in the inset of Figure 12.9c). It is then easy to identify a given heating current density with a certain carrier temperature by comparing $\Delta R_{\mathrm{xx}}(J)$ with $\Delta R_{\mathrm{xx}}(T_s)$, as shown in Figure 12.9c). Limiting cases here are the requirement that the minimum carrier temperature is equal to the sample temperature of 1.4 K and that a carrier temperature higher than 20 K can not be reliably calibrated with SdH oscillations (which are then not observable anymore). The results show that the carrier temperature does not increase quadratically over a wide current range, as for example in (Al, Ga)As channel samples [32]. For small heating current densities ($J \lesssim 1\,\mathrm{A/m}$), the results may be slightly biased due to the large noise in the signal. A quadratic increase in this range can neither be excluded nor confirmed. The data seems to indicate a saturation of the carrier temperature on the order of 20 K.

Temperature calibration via SdH oscillations is a good starting point since it requires little extra effort. On the other hand, it has some serious drawbacks. First, it relies on the observability of clear SdH oscillations. In most HgTe 3D TI samples this restricts the analysis to high n- or high p- densities, since quantum

oscillations are usually heavily distorted by the strong magnetoresistance at low total carrier densities. Furthermore, magnetic fields on the order of several T are required, which also affect other sample properties such as the current distribution, the density of states, and the overall resistance. It is thus not ideal for the current heating experiments discussed in this section, which are most interesting at small total densities and zero magnetic field.

A more sophisticated approach is a temperature calibration via Johnson noise thermometry (see e. g. [137] for a review). This approach relies on the random thermal motion of charge carriers, which results in a noise power spectral density of [137]

$$S_\nu(f) = 4k_B T R \tag{12.5}$$

for a pure resistance of magnitude R at a temperature T. If the resistance is known and the noise power can be measured accurately, the temperature can immediately be calculated with Equation 12.5. Importantly, the measured temperature is always the electron temperature, even if there is an imbalance between electron temperature and lattice temperature. From a practical point of view, determining the thermal noise power is a highly nontrivial task, though. First of all, the thermal noise has to be measured at high frequencies (on the order of MHz) in order to avoid contributions from $1/f$ noise. Special care is needed for the design of circuits which operate at such high frequencies. Second, the initial noise signal usually needs to be amplified in order to be measured reliably. Dedicated low-noise amplifiers are needed for this task and the gain of the amplifier chain has to be calibrated carefully. Figure 12.10a) shows a simplified schematic of a noise measurement setup which has been set up by Dr. Y. Yan and Dr. M. Abdelghany for our group. The sample has a high-frequency ground on one side in the form of a 100 nF capacitance. On the other side, a LC tank circuit selects the desired frequency band, which is on the order of 3 MHz in our setup. The thermal noise is amplified with a home built low-noise amplifier, which is kept at cryogenic temperatures to reduce the intrinsic noise of the amplifier. A second low-noise amplifier at room temperature further amplifies the signal, which is subsequently measured by a spectrum analyzer. The gain $G \approx 800$ and the equivalent noise $T_\mathrm{N} \approx 2.2\,\mathrm{K}$ of this system were calibrated with the help of a metal film resistor at different bath temperatures. This system allows for measuring the thermal noise also while applying a DC heating current. The electron temperature is then found from the relation $S_\nu = G^2 \times 4k_B(T_e + T_\mathrm{N})R$.

Figure 12.10b) shows the electron temperature as a function of heating current density in a 4 µm × 20 µm sized channel on sample *Q2823 ch Noise 1*, obtained from Johnson noise thermometry. The sample layout is identical to the 4 µm wide channel on sample *Q2823 ch ICP B*, which has been investigated in detail above and which shall be compared to the semi-quantitative modelling later on.[5] For all investigated carrier densities, the electron temperature rises with heating

[5] It is necessary to obtain the temperature calibration on a second sample, since our noise setup requires a special chip carrier.

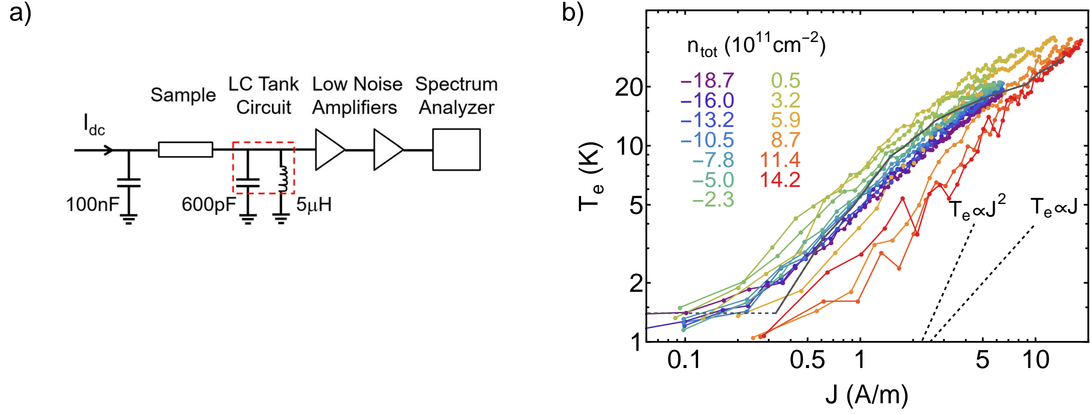

Figure 12.10: Calibration of carrier temperature as a function of heating current by means of Johnson noise thermometry. a) Schematic diagram of the Johnson noise thermometry setup used to measure the electron temperature in the sample. b) Colored data points: electron temperature T_e in sample *Q2823 ch Noise 1* as a function of heating current density J at different total carrier densities. The sample temperature was approximately 1.1 K. Colored lines are guides to the eye. The black dashed lines indicate the slope proportional to J or J^2. The superimposed gray line is the temperature calibration obtained via SdH oscillations on sample *Q2808 ch ICP B*, cf. Figure 12.9c). Figure a), as well as collection and analysis of data in Figure b) have been done by Dr. Y. Yan.

current density as expected. The slope is similar for all densities and indicates a temperature dependence between a J and J^2 dependence (cf. black dashed lines). Main deviations from this slope occur at low temperatures ($T_e \lesssim 2$ K), where the uncertainty of the noise calibration is highest, and at higher temperatures ($T_e \gtrsim 20$ K), where a saturation of the electron temperature seems to occur. The validity of this temperature calibration is supported by the similarity to the calibration obtained via SdH oscillations (cf. gray line in Figure 12.10b)). The orders of magnitude for the temperature rise as a function of heating current density are similar, despite the considerable difference in sample dimensions (4 µm × 20 µm vs. 1 µm × 5 µm). Important characteristics are comparable as well, including the deviation from a quadratic increase of the carrier temperature with heating current and the onset of carrier temperature saturation at approximately 20 K.

Understanding the details of current heating in HgTe is not the main aim of this thesis. It still is necessary, however, to briefly discuss the results of carrier temperature as a function of heating current. At first it seems surprising that the carrier temperature does not show a clear J^2 dependence as for example in (Al, Ga)As channel samples [32]. There are two important remarks in order: First, one of the main reasons for saturation of carrier temperature in polar semiconductors is

the energy loss to polar optical phonons, which is strongly temperature dependent [138]. In GaAs, for example, a significant increase in energy loss is obtained for carrier temperatures exceeding $T_e \approx 32\,\mathrm{K}$ (at a lattice temperature of 2 K) [138]. Due to the smaller energy of longitudinal-optical phonons in HgTe as compared to GaAs (17.01 meV in HgTe [12] vs. 36.74 meV in GaAs [138]), an increase in energy loss will occur at smaller temperatures. The electron temperature will thus begin to saturate at lower temperatures in HgTe than in GaAs, which may obscure a J^2 dependence. Second, it is not clear a priori how the electron temperature may vary along the channel. For long, quasi-ballistic channels it is expected that hot electrons will quickly distribute the excess energy across the electron system, so that the electron temperature is almost constant along the channel [32]. In small samples a temperature gradient may develop [34] and thus influence the average temperature in a more complicated manner. In the following discussion the temperature will be assumed to be constant, similar to the approach in previous studies. One has to keep in mind, however, that this is a simplification of the actual situation and may result in deviations from a pure J^2 dependence of the electron temperature. On the whole, the good agreement between the results from two entirely different methods for temperature calibration, even done in different samples, suggests that the calibrations are trustworthy. The orders of magnitude further agree with the estimated temperature ranges relevant for the nonmonotonic differential resistance measurements (cf. Figure 12.2). The temperature calibration obtained via Johnson noise thermometry will therefore be used in the following to compare the semi-quantitative modelling with experimental results.

12.2.4 Comparison between modelling and experiment

With the electron temperature calibration it is now possible to calculate the differential resistance as a function of heating current in the semi-quantitative model. The first step is to fit the experimentally determined electron temperatures with a suitable fit function, which will be used in the following conversion steps. This step is necessary because the experimental data points scatter considerably. The fit function used here is given by

$$T_e^{\mathrm{cal}}(P) = T_s + A_1 P^{B_1} + A_2 P^{B_2}, \tag{12.6}$$

where T_s is the sample temperature, $P = J^2\rho$ the applied power density, and A_1, A_2, B_1, B_2 the parameters which are adjusted with a standard least-square fit for each carrier density. Equation 12.6 is then used to convert the previously calculated resistivity as a function of carrier temperature $\rho(T)$, Figure 12.8b), to total resistance as a function of heating current $R(I)$. The differential resistance can be calculated as

$$\frac{dV}{dI} = R + I\frac{dR}{dI}. \tag{12.7}$$

The result of this calculation is shown in Figure 12.11a), next to the experimental results for the 4 µm wide channel on sample *Q2823 ch ICP B* for comparison.

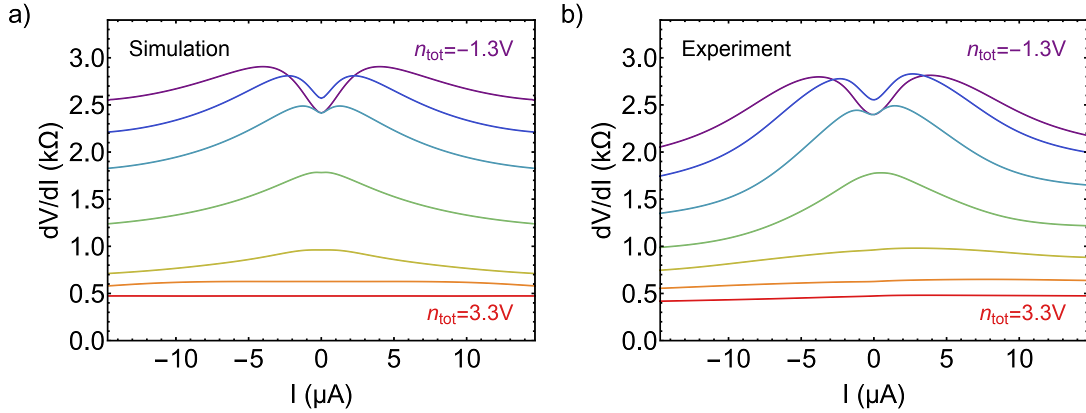

Figure 12.11: Calculated differential resistance compared with experimental results. a) Differential resistance dV/dI as a function of heating current I, calculated with a semi-quantitative model for several total densities with equidistant spacing. b) Differential resistance as a function of heating current of the 4 µm wide channel on sample *Q2823 ch ICP B* (same data as shown in Figure 12.1a)) for several total densities. The same color code has been used in a) and b).

The model qualitatively reproduces all aspects of the experimental data. The resistance decrease – both in the bulk band gap and for higher carrier temperatures in p-regime – is quantitatively comparable to the calculated and the experimental curves. This strongly indicates that the decrease in resistance is indeed determined by thermal redistribution of charge carriers to the high-mobility TSSs. The magnitude of the electron-hole scattering rate had to be adjusted by comparison with the experimental results. The current at which the electron-hole scattering rate saturates, however, also follows from the calculated band structure via Equation 12.4. The good quantitative agreement with the experiment strongly supports the proposed model based on electron-hole scattering.

12.2.5 The role of phonons

When discussing the temperature dependence of the resistance in semiconductors, it is usually necessary to explicitly take into account phonon scattering [119]. It is thus necessary to briefly discuss why the low-temperature resistance in HgTe 3D TIs is most likely not determined by phonon scattering.

Calculations for bulk HgTe indicate that scattering with polar optical phonons causes a pronounced decrease of the electron mobility for temperatures exceeding approximately 20 K [96]. For smaller temperatures, the carrier mobility is determined by impurity scattering [96]. It thus seems unlikely that a strong temperature dependence in the temperature range below 20 K can be solely explained by phonon scattering. Furthermore, phonon scattering will always increase the resistance with

increasing temperature. However, in the current heating experiments an increase in resistance is only observed when both electrons and holes are present in the channels. There is no reason why the presence of holes should suddenly "switch on" an interaction between TSS electrons and optical phonons. It can thus be rejected as an explanation for the nonmonotonic differential resistance.

Another possible explanation for a nonmonotonic temperature dependence is the crossover from the Bloch-Grüneisen regime to the quasielastic scattering regime [139]. In this scenario, scattering with acoustic phonons is responsible for a strong resistance increase below the Bloch-Grüneisen temperature $T_{\mathrm{BG}} = 2v_s\hbar k_F/k_B$, where v_s is the sound velocity and k_F the Fermi wave vector. Above the Bloch-Grüneisen temperature the resistance increase saturates, leading to a nonmonotonic dependence of resistance on temperature [139]. For TSSs in HgTe with a typical electron density of $\approx 0.7 \times 10^{11}\,\mathrm{cm}^{-2}$ and a velocity of sound of 2.6 km/s [140], the Bloch-Grüneisen temperature is only of order 3.7 K. This value is not large enough to explain the nonmonotonic differential resistance in HgTe 3D TIs. Furthermore, the resistance increase should become more pronounced and shift to higher electron temperatures when the electron density is increased. This is the opposite of what is observed in HgTe TSSs, so that Bloch-Grüneisen scattering can not explain the experimental results here.

12.2.6 Conclusion: Electron-hole scattering in HgTe

This section of the thesis was devoted to the effects of electron temperature on transport properties of the Dirac surface states of HgTe 3D TIs. Using the elegant technique of current heating in narrow channel structures it was possible to observe a pronounced nonmonotonic behavior of the differential resistance with heating current when both electrons and holes were present simultaneously. When only the TSSs contributed to transport, only a decrease of the differential resistance was observed. The striking similarity to the fingerprints of hydrodynamic electron flow in high-mobility 2D EGs motivated a more thorough investigation of this effect. Using (sample) temperature- and size-dependent measurements, it was possible to show that the temperature dependence in our HgTe samples is most likely caused by an intrinsic effect, which excludes hydrodynamic electron flow as an explanation. A qualitative model was developed, which includes both electron-hole scattering to explain the resistance increase and a temperature-induced redistribution of charge carriers to explain the resistance decrease. The validity of this model was proven by semi-quantitative calculations based on k·p band structure calculations, which agree well with the experimental results.

The observation of electron-hole scattering is quite remarkable in itself, since it adds a new material class – 3D topological insulators – to the slowly growing list of systems, in which intercarrier scattering considerably affects transport properties. HgTe may serve as a model system for these effects. It is a well-understood material system which can reliably be tuned over several very different density regimes. The carrier mobility can be quite high, so that effects of intercarrier scattering can easily

be separated from impurity scattering by temperature-dependent measurements. At the same time, the band structure of tensilely strained HgTe layers shares important similarities with other topological materials. Most striking is the occurrence of camel back - shaped bands, which often result from the combined effects of band inversion and hybridization [141]. It is thus likely that intercarrier scattering will play an important role in other topological materials as well.

Future studies should investigate electron-hole scattering in HgTe in a different experimental setup. For example, one could measure the so-called "bend resistance" [142] of cross-shaped mesa structures with dimensions similar to the impurity mean free path. A current is sent from one leg to an adjacent leg and a nonlocal voltage – which, divided by the current, gives the bend resistance – is picked up in the other two legs. If transport is ballistic, the bend resistance is negative, i. e. opposite in sign to what would be expected from a classical calculation of the current distribution. Upon warming the sample, scattering with holes would distort the ballistic electron trajectories, so that the bend resistance eventually becomes positive [131]. This would be yet another clear indication for the importance of electron-hole scattering in TSS transport.

12.3 Temperature dependence in other HgTe systems

The last section was devoted to a detailed study of current heating in HgTe 3D TIs. The technological advancements can also be used to perform similar experiments on other HgTe phases. The predictable differences and similarities in the band structure may help to confirm the interpretation developed above.

12.3.1 Current heating in zero-gap HgTe quantum wells

The thesis at hand is in general devoted to investigating transport properties of the Dirac surface states in HgTe 3D TIs. It is also possible, however, to obtain a single-valley, spin degenerate Dirac 2D EG in HgTe quantum wells [143]. Such a 2D EG occurs in HgTe QWs with critical thickness $d_c \approx 6.3\,\mathrm{nm}$, which separates QWs with noninverted ($d < d_c$) and inverted ($d > d_c$) subband ordering. In these "zero-gap" QWs linearly dispersing electron and hole bands touch in a single Dirac point at Γ. Such a system has experimentally been prepared before and described in detail in Reference [143]. It is reasonable to check for fingerprints of intercarrier scattering also in such zero-gap HgTe QWs. The obvious advantage over the 3D TI system is that the electrostatics is less complicated in QWs. Hence, the band structure can more directly be related to transport results.

One of the difficulties when preparing zero-gap QWs is the finite control of the layer thickness during growth. The usual approach is thus to grow a series of QWs and find one which is close to the critical thickness from a fan chart measurement, which gives access to the band gap. Figure 12.12a) shows a fan

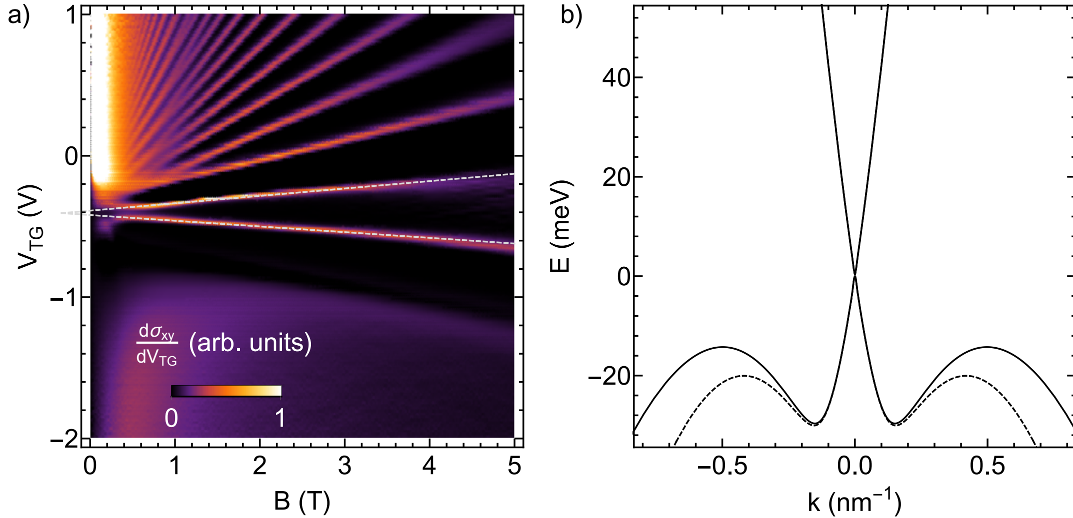

Figure 12.12: Landau level fan chart of wafer *Q2733* and corresponding band structure. a) Derivative of Hall conductivity σ_{xy} as a function of top gate voltage V_{TG} and magnetic field B at 4.2 K. Dashed lines highlight the $N = 0$ LLs. This Hall bar sample was measured by S. Hartinger. b) Band structure of a zero-gap HgTe QW, calculated with the program *kdotpy* [99]. Solid and dashed lines correspond to two directions in k-space, separated by 45°.

chart measurement of the characterization Hall bar (size 200 µm × 600 µm) of wafer *Q2733*, a nominally 7.5 nm thick HgTe QW, grown on a virtual CdTe substrate. The zero-mode LLs disperse above and below $V_{TG} \approx -0.4\,\mathrm{V}$ and are marked with dashed lines. In a true zero-gap QW, the crossing point of these LLs occurs at $B = 0\,\mathrm{T}$ [143]. In wafer *Q2733* the crossing point is found at a small negative magnetic field of $B \approx -0.3\,\mathrm{T}$, implying that this QW is slightly noninverted. The band gap can be estimated from the critical magnetic field (at which the two zero mode levels become degenerate): $B_c = \hbar E_g/(2eC)$, where E_g is the band gap and $C \approx -857\,\mathrm{meV} \cdot \mathrm{nm}^2$ [143]. The resulting band gap of approximately 0.9 meV is comparable to the typical electron temperature in current heating experiments. In the following, wafer *Q2733* will thus be regarded as a zero-gap QW.

Figure 12.12b) shows the band structure of a HgTe QW of critical thickness, found from a 8-orbital k·p calculation [99]. The Dirac point is situated at $E = 0\,\mathrm{meV}$. The conduction band has an almost linear, electron-like dispersion. The valence band is more complicated and contains several hole pockets. Around $k = 0$ the dispersion is almost linear as well. At −16 meV a flat maximum occurs at finite k, similar to the previously described camel back feature in HgTe 3D TIs (cf. Figure 12.6). This creates an interesting situation: The system allows direct access to a Dirac 2D EG, as well as a superposition of light- and heavy-mass holes.

In order to perform current heating experiments, it is necessary to work with small samples. The following results are based on sample *Q2733 ch ICP A*, a

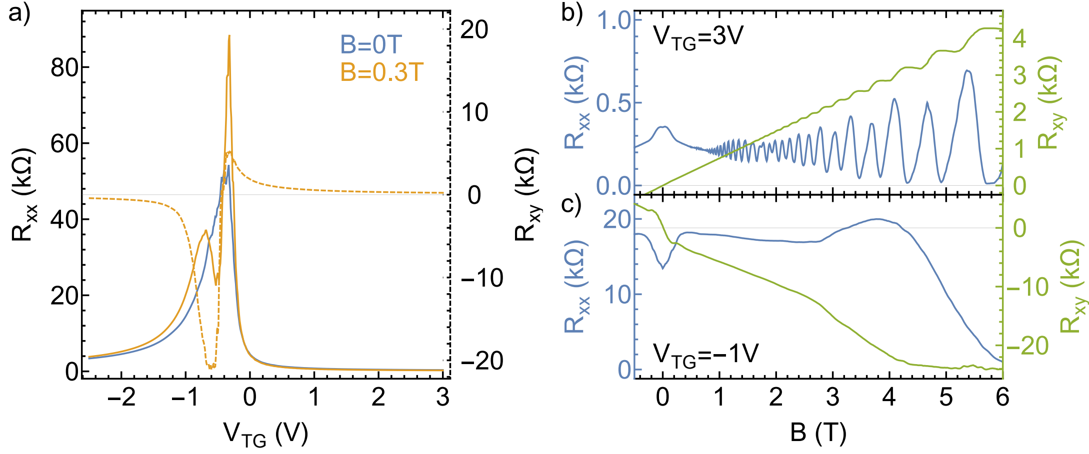

Figure 12.13: Characterization of sample *Q2733 ch ICP A* at 2 K. a) Longitudinal resistance R_{xx} and transverse resistance R_{xy} as a function of top gate voltage V_{TG} at zero magnetic field and $B = 0.3\,\mathrm{T}$. b) and c) R_{xx} and R_{xy} as a function of magnetic field at two top gate voltages.

$2\,\mu\mathrm{m} \times 10\,\mu\mathrm{m}$ sized channel structure, fabricated with the standard ICP process for channel samples, cf. Appendix A. Before discussing current heating experiments, it is necessary to thoroughly characterize this sample and relate the results to the band structure calculation.

Figure 12.13a) shows the longitudinal resistance R_{xx} as a function of top gate voltage V_{TG}. It shows a pronounced peak at $V_{\mathrm{TG}} = -0.3\,\mathrm{V}$. This maximum becomes even more pronounced in a small magnetic field. The zero-crossing of the transverse resistance R_{xy} in small magnetic fields indicates that this resistance maximum occurs roughly at the charge neutrality point. In other words, at this gate voltage the Fermi level crosses the Dirac point. Figure 12.13b) shows the longitudinal and transverse resistance as a function of the magnetic field at a top gate voltage of 3 V, corresponding to a high n-density of $8.5 \times 10^{11}\,\mathrm{cm}^{-2}$. The carrier mobility at this gate voltage is approximately $100 \times 10^{3}\,\mathrm{cm}^{2}(\mathrm{Vs})^{-1}$. The longitudinal resistance shows a negative magnetoresistance at magnetic fields smaller than 1 T, which is most likely caused by diffusive scattering on the channel walls (cf. Section 11.1). Pronounced SdH oscillations in R_{xx} and quantized steps in R_{xy} occur at magnetic fields higher than 1 T. In n-regime the sample shows all characteristics of a two-dimensional electron gas with high mobility.

Upon gating the sample to p-regime, the longitudinal resistance in a small magnetic field displays a second pronounced peak around $V_{\mathrm{TG}} = -0.6\,\mathrm{V}$, cf. Figure 12.13a). This second peak occurs when the Fermi level enters the camel back. The superposition of two carrier types with strongly differing mobilities – light Dirac holes and heavy camel back holes – leads to a pronounced positive magnetoresistance. This is confirmed by magnetic field dependent measurements at $V_{\mathrm{TG}} = -1\,\mathrm{V}$, shown in Figure 12.13c). The carrier mobility is reduced to

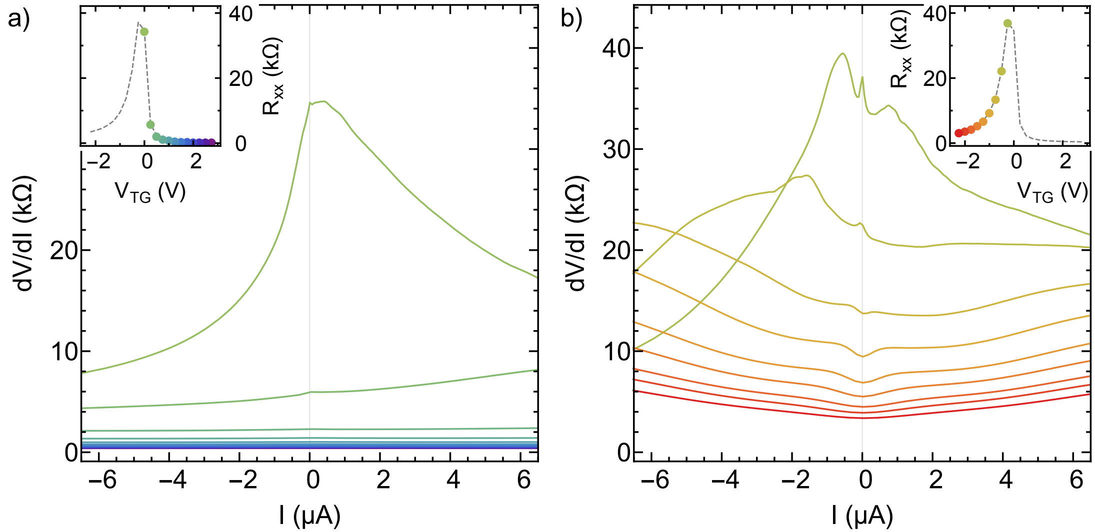

Figure 12.14: Current heating experiment in sample *Q2733 ch ICP A* at 2 K. a) and b) Differential resistance dV/dI as a function of heating current I in overall n- or p-regime, respectively. The color code corresponds to gate voltages as explained in the insets, which show the resistance at zero heating current as a function of top gate voltage.

$13 \times 10^3\,\mathrm{cm}^2(\mathrm{Vs})^{-1}$, indicating the presence of very low-mobility holes. The transverse resistance shows a pronounced kink at 0.15 T, which is accompanied by a positive magnetoresistance. Both is typical for a two-carrier system. In contrast to the situation in HgTe 3D TIs, both the low-field and the high-field slope are negative here.

On the whole, the characterization establishes a relation between different transport regimes and band structure features. The overall sample quality is high, with an impurity mean free path for high-mobility carriers on the order of the channel width. Sample *Q2733 ch ICP A* is thus suitable for current heating experiments similar to the ones performed with HgTe 3D TI samples.

Figure 12.14 shows the differential resistance as a function of heating current in sample *Q2733 ch ICP A*. The traces recorded in overall n-regime are shown in a), while those close to zero density and in p-regime are shown in b). The insets explain the corresponding color code. In high n-regime (purple and blue traces in a)), the differential resistance does not show a pronounced dependence on heating current. When gating closer to the Dirac point (green curves), a small cusp appears around zero heating current, the curves become highly asymmetric, and the differential resistance decreases considerably for high heating currents. In overall p-regime (orange to red curves), the differential resistance increases close to zero current heating and remains highly asymmetric for high heating currents.

Several very different effects contribute to these results. First, the asymmetry of the differential resistance around zero heating current as well as the pronounced

resistance decrease at high heating currents (close to charge neutrality) are both caused by the so-called "self-gating effect". Self-gating is sometimes also referred to as "circuit-induced asymmetry" [144, 145]. The application of a DC bias on one side of the channel effectively changes the (average) electrostatic potential inside the channel with respect to the gate electrode. Around charge neutrality a heating current of 2 µA requires a DC bias on the order of several tens of mV along the channel. This is equivalent to changing the top gate voltage by tens of mV. In HgTe 2D EGs the sample resistance undergoes large changes with varying gate voltage, resulting in substantial resistance changes due to self-gating. The measured differential resistance is thus determined by a superposition of changing the carrier temperature and varying the top gate voltage.[6] Second, and independent of self-gating, the resistance at these high heating currents can further increase due to scattering with optical phonons [96]. Due to all of these complications, the high-bias regime ($|I| \gtrsim 1\,\mu A$) will not be further discussed in the following.

Third, for small heating currents ($|I| \lesssim 1\,\mu A$) in p-regime ($V_{TG} < -0.75\,V$), the differential resistance shows a well-defined increase with heating current. The onset of an increasing differential resistance thus coincides with the onset of two-carrier behavior which occurs for gate voltages below $-0.6\,V$. Similar to the situation in 3D TIs, where TSS electrons scatter with bulk holes, the high-mobility holes in the zero-gap QW can scatter with low-mobility holes. The large mobility difference thus causes an increase in resistance. The (relative) resistance change is less dramatic as compared to the situation in 3D TIs, however. This is exactly as expected, since in the 2D EG discussed here, high mobility carriers scatter with low mobility carriers of the same polarity. Momentum conservation implies that these scattering events themselves cannot completely relax the current and the increase in resistance is thus only due to the mobility difference [118]. In HgTe 3D TIs, in contrast, scattering events involving electrons and holes can reverse the propagation direction of carriers and thereby reverse the current due to the different carrier polarity. Electron-hole scattering is thus more efficient in increasing resistance than the hole-hole scattering observed here.

Fourth, the origin of the small cusp around zero heating current, most pronounced at a gate voltage of $-0.25\,V$ (highest gate voltage in Figure 12.14b)), remains unknown. Several possible explanations can only be excluded. Current heating experiments in graphene have found a strikingly similar behavior, which could be attributed to a hot electron effect by temperature-dependent measurements [146]. In Reference [146] it is argued that a drop in resistance occurs due to weak localization (WL). It would be surprising if the resistance decrease in HgTe QWs could be explained with WL, though. In Reference [147] it was found that HgTe QWs exhibit weak anti-localization (WAL) instead, which can be attributed to the Dirac-like dispersion of the energy bands. Resistance changes due to WL and WAL are usually also observed upon applying a small magnetic field, which also

[6] This effect also occurs in current heating experiments in HgTe 3D TIs. There it is less pronounced, however, due to the small variation of resistance with gate voltage.

changes the electron phase and destroys the perfect constructive (or destructive) interference. At least in sample *Q2733 ch ICP A* such an effect is not observed in magnetic field-dependent measurements. Other HgTe 2D EG channel samples (see Reference [54]) also show a decrease in resistance in n-regime with heating current, which is stable in small magnetic fields ($B \lesssim 100\,\mathrm{mT}$). This is strong evidence that the resistance decrease is not caused by WL or WAL. It is also clear that the resistance decrease is not due to thermal activation of charge carriers as in HgTe 3D TIs. At $V_{\mathrm{TG}} = -0.25\,\mathrm{V}$, for example, the (electron-like) carrier density is as small as $0.2 \times 10^{11}\,\mathrm{cm}^{-2}$ and the initial decrease of resistance with heating current is very pronounced. According to the band structure calculation shown in Figure 12.12b), the Fermi level at this carrier density is still 14.9 meV away from the Dirac point. A considerable effect of thermal activation would thus be expected only for temperatures exceeding approximately 170 K at this gate voltage. As discussed in the context of 3D TIs, the relevant temperature range for current heating experiments in HgTe does not exceed 20 to 30 K. Thermal activation is thus irrelevant at the carrier densities where a resistance decrease is observed in QWs and can thus be rejected as explanation for the cusp around zero current heating. Further work is required to explain the origin of this effect.

To sum up, current heating experiments in a zero-gap HgTe 2D EG reveal an important similarity to current heating experiments in HgTe 3D TIs: The interaction between high-mobility carriers and low-mobility carriers results in a pronounced increase of the resistance with increasing carrier temperature. In the 2D EG sample discussed here, this interaction takes place between two kinds of hole carriers, but the basic model remains valid. Apparently, these effects are more difficult to single out in experiments with 2D EGs. This is in part due to a very strong self-gating effect, which could be reduced in future experiments by using samples without a top gate. A back gate (which has a much lower gate action) could still be used to tune the carrier density.

12.3.2 Current heating in compressively strained HgTe

Another interesting situation arises in thick HgTe layers, which are subject to a strain different from the tensile strain needed to induce the 3D TI phase. Applying compressive strain also lifts the degeneracy of the light and heavy Γ_8 bands at the Γ point by lowering the point group symmetry. Compressive strain does not lead to the formation of a bulk band gap, but rather linear crossing points in the band structure [10]. The HgTe layer features two of these doubly degenerate crossing points and is said to be in the Dirac semimetal phase.[7] The linear crossing points will be referred to as Dirac nodes in the following and should not be confused with the Dirac point in the TSSs mentioned in the context of the 3D TI phase of HgTe. At charge neutrality, and without introducing an electrostatic potential,

[7] To be precise, the two Dirac nodes are split into four Weyl points since the spatial inversion symmetry is broken in zinc blende crystals. In zero magnetic field, however, the splitting between the two Weyl points is too small to be detected experimentally [10].

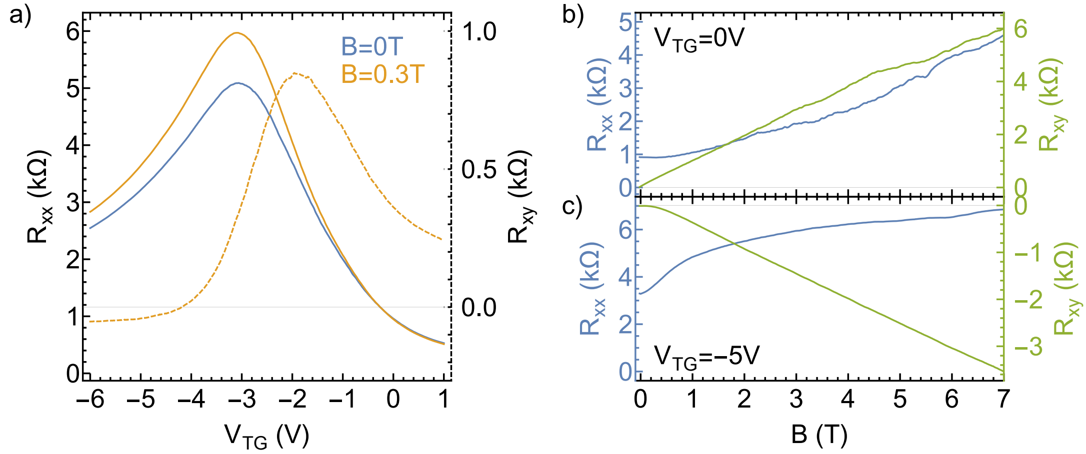

Figure 12.15: Characterization of sample *QC0340 ch ICP 1* at 1.4 K. a) Longitudinal resistance R_{xx} and transverse resistance R_{xy} as a function of top gate voltage V_{TG} at zero magnetic field and $B = 0.3\,\mathrm{T}$. b) and c) R_{xx} and R_{xy} as a function of magnetic field at two values of V_{TG}.

the Fermi energy is situated at these Dirac nodes. In gated devices this point can be identified by the minimum in conductance. Application of a strong negative gate potential leads to the formation of massive VPSs [10], similar to the situation in 3D TI layers. An important difference to the 3D TI phase is the absence of a camel back feature in the valence band, which is responsible for the occurrence of electron-hole scattering in tensilely strained HgTe layers. This difference is the motivation to compare current heating experiments in HgTe Dirac semimetals and 3D TIs. More information on the exciting physics of the HgTe Dirac semimetal phase can be found in References [10] and [79].

The current heating experiments were performed on channel samples fabricated from wafer *QC0340*, which features a 120 nm thick HgTe layer MBE-grown on a virtual substrate and sandwiched between 10 nm thick protective CdHgTe layers. The virtual substrate consists of a CdTe/$Cd_{0.5}Zn_{0.5}Te$ superlattice grown on a GaAs wafer [21, 148]. In this virtual substrate approach the thickness of the CdTe layers determines the overall lattice constant, which can be freely adjusted between the lattice constant of CdTe and $Cd_{0.5}Zn_{0.5}Te$. In wafer *QC0340* the virtual substrate has been adjusted to yield a compressive strain of 0.28 %. Sample *QC0340 ch ICP 1* contains a channel structure of size 2 µm × 10 µm between voltage probes. The sample layout and fabrication process are identical to the ones used for 3D TI channel structures (cf. Section 12.2.1).

Figure 12.15a) shows the longitudinal and transverse resistance of this device as a function of top gate voltage. At zero magnetic field, the resistance displays a pronounced maximum at $V_{\mathrm{TG}} = -3.2\,\mathrm{V}$. At a small magnetic field of 0.3 T the maximum resistance increases slightly while the peak position does not shift. The transverse resistance shows a sign reversal close to the peak position, indicating

the transition from n- to p-regime. Figure 12.15b) shows the longitudinal and transverse resistances as a function of magnetic field at zero gate voltage. The extracted total carrier density is $6.6 \times 10^{11}\,\mathrm{cm}^{-2}$ and the averaged Drude mobility $66 \times 10^{3}\,\mathrm{cm}^{2}\mathrm{V}^{-1}\mathrm{s}^{-1}$. Consistent with the low carrier mobility, the sample does not show SdH oscillations. At a top gate voltage of $V_{\mathrm{TG}} = -5\,\mathrm{V}$, Figure 12.15c), the sample is in p-regime with a total carrier density of $-11.2 \times 10^{11}\,\mathrm{cm}^{-2}$ and the Drude mobility is reduced to $8 \times 10^{3}\,\mathrm{cm}^{2}\mathrm{V}^{-1}\mathrm{s}^{-1}$. In overall p-regime the transverse resistance is slightly nonlinear at small magnetic fields. This nonlinearity is accompanied by an increase in the longitudinal resistance, which both indicates two-carrier behavior. In the compressively strained HgTe layer this behavior is less pronounced in comparison to tensilely strained HgTe. This is consistent with previous measurements on compressively strained HgTe layers [10, 79] and also reflected in the weak magnetoresistance in Figure 12.15a). In the 3D TI phase of HgTe, the superposition of almost localized bulk holes and high-mobility TSS electrons in p-regime is an unavoidable consequence of the band structure. In the Dirac semimetal phase, in contrast, there is no such superposition of dramatically different carrier types. The two-carrier behavior observed here is most likely due to the formation of massive VPSs close to the top gate, combined with a remaining n-type conductivity on the opposite side of the HgTe slab, which is less affected by the top gate.

Figure 12.16a) shows the results of current heating experiments in sample *QC0340 ch ICP 1*. The black dashed line shows the longitudinal resistance as a function of top gate voltage (with respect to the resistance maximum) for comparison. The colored lines show the differential resistance as a function of heating current density. Far in n-regime (purple line) there is no pronounced effect of current heating. Around the resistance maximum, as well as in overall p-regime, the differential resistance strongly decreases with increasing heating current. This is a remarkable difference to HgTe 3D TI samples, which show a pronounced nonmonotonic dependence of the resistance with heating current. Figure 12.16b) shows the differential resistance at the maximum resistance point (i. e. close to charge neutrality) for different sample temperatures in the range of 1.4 (purple) to 50 K (red). The sharp peak of the differential resistance becomes gradually more smeared upon increasing the sample temperature. Furthermore, the overall resistance drops with increasing sample temperature as summarized in the inset. On the whole, both current heating and changing the sample temperature have the same qualitative effect on the resistance. It can be concluded that the resistance decrease due to current heating is indeed a hot carrier effect. At $V^{*}_{\mathrm{TG}} = 0\,\mathrm{V}$, the measurement at 1.4 K has been repeated once more and extended to higher current densities (dashed line in Figure 12.16b)). The qualitative trend does not change at high current densities, but the slope of the differential resistance changes around 4 A/m. This, together with the sample temperature dependence of the other curves, indicates that a current density of order 4 A/m results in an electron temperature of approximately 20 to 30 K. For higher heating currents, the excess energy can effectively be dissipated by scattering with optical phonons and the resistance

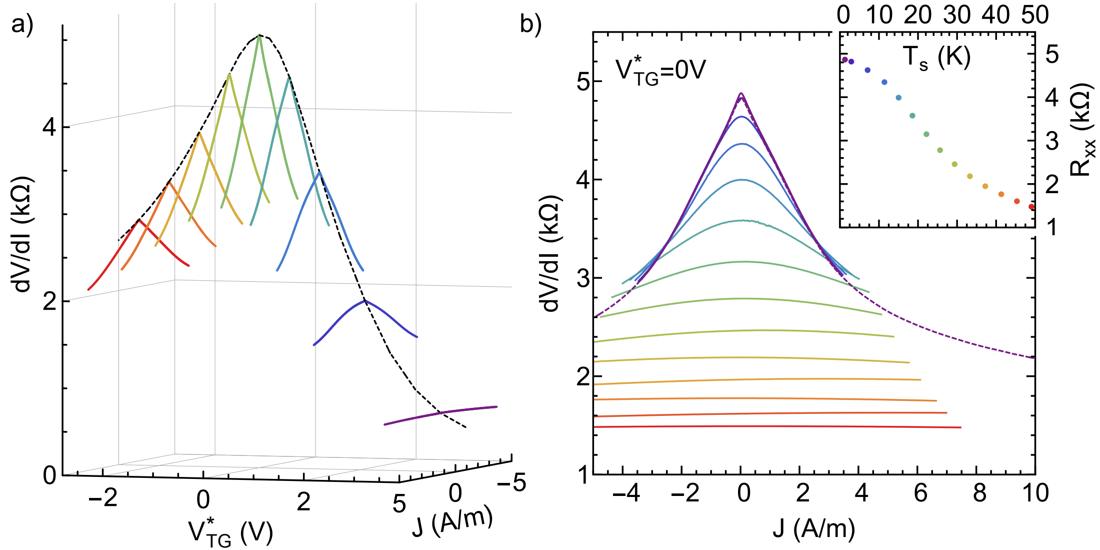

Figure 12.16: Current heating experiment in sample *QC0340 ch ICP 1*. a) Differential resistance dV/dI as a function of heating current density J and top gate voltage V^*_{TG} (colored lines) at 1.4 K. The dashed line is the gate-dependent resistance at zero heating current R_{xx}. b) Differential resistance as a function of heating current density at $V^*_{\mathrm{TG}} = 0\,\mathrm{V}$ and different sample temperatures T_s. The dashed line shows a high-bias measurement of the differential resistance at $T_s = 1.4\,\mathrm{K}$. The inset shows R_{xx} as a function of T_s and indicates the color code for b).

decrease changes. This estimated temperature range is consistent with the electron temperature calibration in HgTe 3D TI samples (cf. Section 12.2.3).

In order to understand the pronounced resistance decrease in the HgTe Dirac semimetal, it is again instructive to consider the actual band structure of the layer under consideration. Figure 12.17a) shows the band structure of a compressively strained HgTe layer, comparable to the layer stack of wafer *QC0340*. Bulk bands are shown in gray. The linear band crossing point (with vanishing DOS and total carrier density) is found at an energy of 0 meV and marked with a gray dashed line. The red color denotes two-dimensional states that are localized within 5 nm from the HgTe surfaces. According to Reference [10], these "massless Volkov-Pankratov states" originate from the band inversion between Γ_6 and Γ_8 bands. They will referred to as TSSs in the following due to the similarity to the TSSs of the 3D TI phase. The TSSs have a linear crossing point of their own, which is situated deep in the valence band at approximately $-105\,\mathrm{meV}$. The important difference to HgTe 3D TI layers is that the n-type TSSs do not coexist with low-mobility bulk hole states around the charge neutrality point. Thus, an absence of electron-hole scattering is expected; an assumption that agrees with experimental results. A similarity between the Dirac semimetal system and the 3D TI system is that increasing the carrier temperature leads to a significant increase in the (absolute)

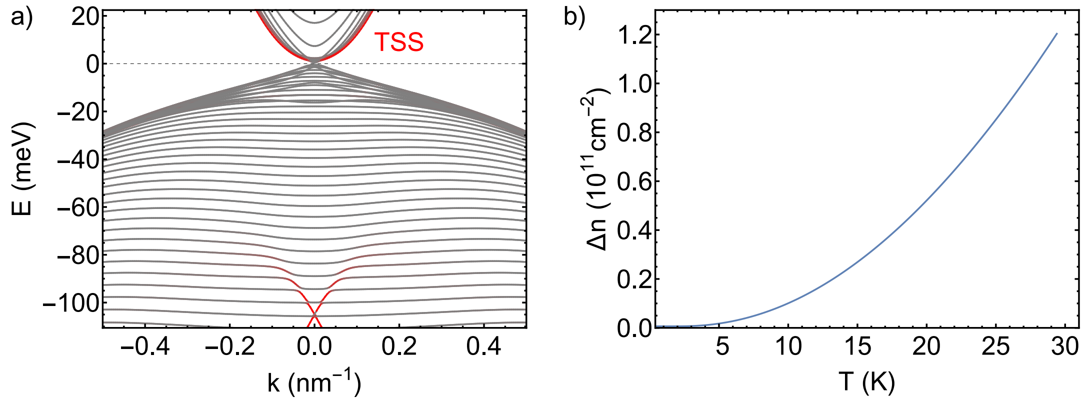

Figure 12.17: Band structure of HgTe Dirac semimetal slab and temperature-induced density shift. a) Band structure of a 120 nm thick HgTe layer with 0.3 % compressive strain, calculated with the program *kdotpy* [99]. Red color indicates that states are localized within 5 nm from the HgTe top and bottom surfaces. b) Shift of electron and hole densities Δn as a function of carrier temperature T, when the Fermi level is set to $E = 0\,\mathrm{meV}$ at low temperatures.

number of mobile charge carriers and thus a decrease in resistance. Figure 12.17b) shows the shift in electron and hole carrier densities with temperature, assuming that the low-temperature Fermi level is set to the zero-density point and that the total charge carrier density remains constant (cf. Equation 12.1). In the experimentally relevant temperature range, up to approximately 30 K, the number of free electrons and holes increases from zero to almost $1.2 \times 10^{11}\,\mathrm{cm}^{-2}$. This increase may well account for the decrease of the differential resistance found in the experiment. This mechanism could also explain why the decrease in resistance is most pronounced around the charge neutrality point and decreases (both in absolute and relative terms) at successively higher carrier densities, cf. Figure 12.16a). The decrease will not vanish completely, because the gate does not equally influence the entire HgTe layer. The part which is less affected by the gate will remain in a regime of low DOS and still experience a strong dependence on carrier temperature.

To sum up, the decrease of the differential resistance with heating current in compressively strained HgTe layers is likely caused by the vanishing DOS at the charge neutrality point and thermally activated transport. Most important is the absence of a resistance increase as observed in HgTe 3D TI layers, which can be explained by the absence of the camel back feature in the band structure – and thus the absence of electron-hole scattering. This observation is therefore another confirmation of the model of electron-hole scattering developed for transport experiments in 3D TIs.

13 Conclusion and outlook

This part of the thesis has been devoted to transport in HgTe based microstructures, with a particular focus on transport through the Dirac surface states of HgTe 3D TI layers. The preliminary work presented in Parts I and II was crucial in order to perform reliable experiments with microstructures and interpret the results consistently.

First, it was demonstrated that our high-mobility 3D TI samples can reach the quasiballistic transport regime, in which the scattering mean free path of electrons is larger than one of the device dimensions. The quasiballistic transport regime was experimentally identified in narrow channel samples by manipulating the electron trajectories with small magnetic fields. The enhanced boundary scattering led to a nonlinear magnetoresistance, which scaled in a predictable manner with sample size and was absent in macroscopic samples. The carrier density dependence of this effect was found to differ from the well-known results for conventional 2D EG samples and graphene. As of now it is unclear whether this difference follows trivially from the superposition of several conduction channels, or whether it is related to the special properties of the two-dimensional topological Dirac surface states. By using different lithographic methods to structure the HgTe channel samples it could be further shown that the edge roughness affects the boundary scattering effect. A considerable amount of diffusive boundary scattering could not be avoided, though. This finding may have important implications for nanostructured 3D TI devices like nanowires. In theoretical studies it is often assumed that the two-dimensional TSSs are wrapped homogeneously around the wire circumference [149]. In Reference [30] it is pointed out that real devices differ from the model situation due to inhomogeneous gating. Diffusive scattering at the device edges may add another imperfection which needs to be considered.

Next, it was investigated how increasing the carrier temperature by means of current heating affects transport in HgTe 3D TI microstructures. The original idea was to examine whether the hydrodynamic transport regime is accessible in TSS transport. A strong nonmonotonic temperature dependence of the resistance was found when both high-mobility electrons in the TSSs and low-mobility bulk holes were present simultaneously. By means of temperature- and size-dependent measurements this was shown to be a hot carrier effect, but not related to hydrodynamic electron transport. It was found that intercarrier scattering of free electrons and bulk holes can well explain the increase of resistance with carrier temperature. At higher temperatures, or if only a small number of bulk holes are present, a temperature-induced redistribution of charge carriers causes a resistance decrease. A semi-quantitative model based on these assumptions could reproduce

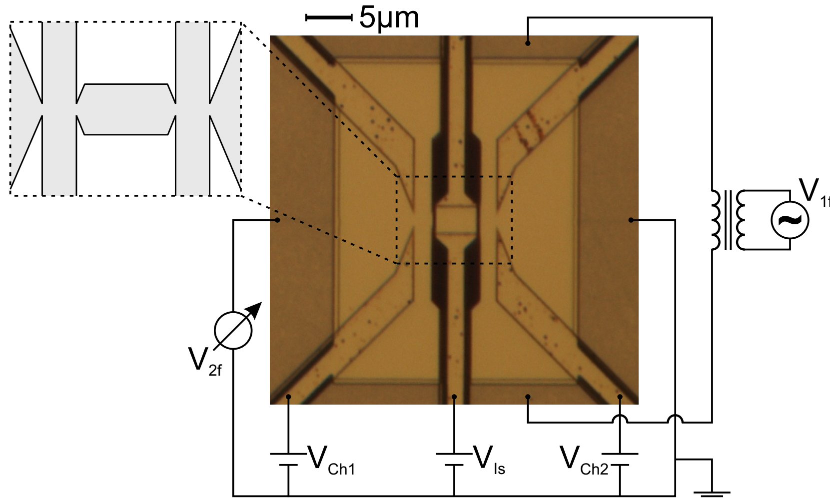

Figure 13.1: Optical image of sample *QC0340 Wthpow D*, together with the schematic circuit layout for thermopower measurements. $V_{1\mathrm{f}}$ is the AC excitation voltage at frequency f and $V_{2\mathrm{f}}$ the measured thermopower signal at frequency $2f$. V_{Ch1}, V_{Ch2}, and V_{Is} are the gate voltages for heating channels 1 and 2, and the central island, respectively. The magnification schematically shows the innermost part of the device mesa. The sample has been prepared and characterized by V. L. Müller and is currently measured in detail by A. A. Aravindnath.

all of the experimentally observed features, including the approximate amplitudes of the effects. It could further be shown that in zero-gap HgTe QWs the scattering of high-mobility Dirac holes with low-mobility camel back holes also leads to an increase of the resistance with temperature. In thick HgTe Dirac semimetal layers, in contrast, low-mobility (bulk) camel back holes are absent. Consistent with the expectation, it was found that in this system the resistance only decreases with increasing temperature due to thermal activation of free carriers. On the whole, the results of current heating experiments in HgTe microstructures have revealed the importance of intercarrier scattering as well as the nonconstant DOS for interpreting the temperature dependence of the resistance. Both are linked to the band structure and therefore unavoidable in experiments.

Further studies are currently underway in our group, which exploit the technique of current heating in more complex HgTe devices to perform accurate measurements of the thermopower and the thermal conductance. These experiments are motivated by the prediction of exotic effects like the mixed axial-gravitational anomaly in Weyl semimetals [150], signatures of which have been observed in NbP [151]. The fingerprint of this anomaly is an increase of the thermal conductance when a magnetic field is applied parallel to the thermal gradient [150]. Figure 13.1 shows an optical image of sample *QC0340 Wthpow D*, which is designed for measuring the thermopower and thermal conductance of a compressively strained HgTe layer.

The sample layout includes two heating channels, which are connected by a central island. With three separate gate electrodes the Fermi level in the two heating channels and the central island can be tuned independently. In the experiment a (carrier-) temperature gradient is created by passing an AC heating current at frequency f through one of the heating channels. The temperature of the other channel, which is not actively heated, remains close to the lattice temperature. The thermopower over the central island can conveniently be measured at frequency $2f$. In addition, the small temperature increase in the cold channel allows to estimate the thermal conductance of the central island. The advantage of this experimental approach is that the current heating technique avoids phonon drag contributions to thermal transport. This is not necessarily the case if the temperature gradient is created by heating the lattice on one side of the sample [152], another common approach to measure thermal transport properties.

A device like the one shown in Figure 13.1 would also allow for measuring the thermal conductance of HgTe 3D TIs, for example in dependence of carrier concentration or sample temperature. This would be an interesting experiment, since multiple bands can contribute to transport, which may further interacting through interband electron-hole scattering. Deviations from the Wiedemann-Franz law are expected in this case [153]. Such deviations have been observed in other 3D TIs [154], but also graphene [34], due to the decoupling of charge and heat currents. Experiments on HgTe, with its outstanding quality, could help to further understand details of the thermal properties of 3D TIs.

References

[1] K. von Klitzing, G. Dorda, and M. Pepper. New method for high-accuracy determination of the fine-structure constant based on quantized Hall resistance. *Phys. Rev. Lett.*, 45(6):494–497, 1980.

[2] C. L. Kane and E. J. Mele. Z_2 topological order and the quantum spin Hall effect. *Phys. Rev. Lett.*, 95(14):146802, 2005.

[3] B. A. Bernevig and S.-C. Zhang. Quantum spin Hall effect. *Phys. Rev. Lett.*, 96(10):106802, 2006.

[4] B. A. Bernevig, T. L. Hughes, and S.-C. Zhang. Quantum spin Hall effect and topological phase transition in HgTe quantum wells. *Science*, 314(5806):1757–1761, 2006.

[5] M. König, S. Wiedmann, C. Brüne, A. Roth, H. Buhmann, L. W. Molenkamp, X.-L. Qi, and S.-C. Zhang. Quantum spin Hall insulator state in HgTe quantum wells. *Science*, 318(5851):766–770, 2007.

[6] D. Hsieh, D. Qian, L. Wray, Y. Xia, Y. S. Hor, R. J. Cava, and M. Z. Hasan. A topological Dirac insulator in a quantum spin Hall phase. *Nature*, 452(7190):970–974, 2008.

[7] L. Fu and C. L. Kane. Topological insulators with inversion symmetry. *Phys. Rev. B*, 76(4):045302, 2007.

[8] C. Brüne, C. X. Liu, E. G. Novik, E. M. Hankiewicz, H. Buhmann, Y. L. Chen, X. L. Qi, Z. X. Shen, S. C. Zhang, and L. W. Molenkamp. Quantum Hall effect from the topological surface states of strained bulk HgTe. *Phys. Rev. Lett.*, 106(12):126803, 2011.

[9] P. Narang, C. A. C. Garcia, and C. Felser. The topology of electronic band structures. *Nat. Mater.*, 20(3):293–300, 2021.

[10] D. M. Mahler, J.-B. Mayer, P. Leubner, L. Lunczer, D. Di Sante, G. Sangiovanni, R. Thomale, E. M. Hankiewicz, H. Buhmann, C. Gould, and L. W. Molenkamp. Interplay of Dirac nodes and Volkov-Pankratov surface states in compressively strained HgTe. *Phys. Rev. X*, 9(3):031034, 2019.

[11] M. G. Vergniory, L. Elcoro, C. Felser, N. Regnault, B. A. Bernevig, and Z. Wang. A complete catalogue of high-quality topological materials. *Nature*, 566(7745):480–485, 2019.

[12] J. Chu and A. Sher. *Physics and Properties of Narrow Gap Semiconductors.* Springer, New York, 2008.

[13] B. A. Volkov and O. A. Pankratov. Two-dimensional massless electrons in an inverted contact. *J. Exp. Theor. Phys. Lett.*, 42(4):178–181, 1985. [*Pis'ma Zh. Eksp. Teor. Fiz.* 42(4):145–148, 1985].

[14] O. A. Pankratov, S. V. Pakhomov, and B. A. Volkov. Supersymmetry in heterojunctions: Band-inverting contact on the basis of $Pb_{1-x}Sn_xTe$ and $Hg_{1-x}Cd_xTe$. *Solid State Commun.*, 61(2):93–96, 1987.

[15] T. H. Hsieh, H. Lin, J. Liu, W. Duan, A. Bansil, and L. Fu. Topological crystalline insulators in the SnTe material class. *Nat. Commun.*, 3:982, 2012.

[16] B. A. Bernevig and T. L. Hughes. *Topological Insulators and Topological Superconductors.* Princeton University Press, Princeton, 2013.

[17] W. D. Lawson, S. Nielsen, E. H. Putley, and A. S. Young. Preparation and properties of HgTe and mixed crystals of HgTe-CdTe. *J. Phys. Chem. Solids*, 9(3):325–329, 1959.

[18] M. B. Reine. Foreword. In P. Capper and J. W. Garland, editors, *Mercury Cadmium Telluride: Growth, Properties and Applications*, pages xxvii–xxx. Wiley, New York, 2011.

[19] B. A. Joyce. Molecular beam epitaxy. *Rep. Prog. Phys.*, 48(12):1637–1697, 1985.

[20] C. Ames. *Molecular Beam Epitaxy of 2D and 3D HgTe, a Topological Insulator.* PhD thesis, Julius-Maximilians-Universität Würzburg, 2015.

[21] P. Leubner, L. Lunczer, C. Brüne, H. Buhmann, and L. W. Molenkamp. Strain engineering of the band gap of HgTe quantum wells using superlattice virtual substrates. *Phys. Rev. Lett.*, 117(8):086403, 2016.

[22] R. Schlereth. *New techniques and improvements in the MBE growth of Hg-containing narrow gap semiconductors.* PhD thesis, Julius-Maximilians-Universität Würzburg, 2019.

[23] JX Nippon Mining & Metals. Product catalog. `https://www.nmm.jx-group.co.jp/english/products/compound_semiconductor/`. Accessed: 2021-09-01.

[24] C. Brüne, C. Thienel, M. Stuiber, J. Böttcher, H. Buhmann, E. G. Novik, C.-X. Liu, E. M. Hankiewicz, and L. W. Molenkamp. Dirac-screening stabilized surface-state transport in a topological insulator. *Phys. Rev. X*, 4(4):041045, 2014.

[25] D. A. Kozlov, Z. D. Kvon, E. B. Olshanetsky, N. N. Mikhailov, S. A. Dvoretsky, and D. Weiss. Transport properties of a 3D topological insulator based on a strained high-mobility HgTe film. *Phys. Rev. Lett.*, 112(19):196801, 2014.

[26] J. B. Oostinga, L. Maier, P. Schüffelgen, D. Knott, C. Ames, C. Brüne, G. Tkachov, H. Buhmann, and L. W. Molenkamp. Josephson supercurrent through the topological surface states of strained bulk HgTe. *Phys. Rev. X*, 3(2):021007, 2013.

[27] J. Wiedenmann, E. Bocquillon, R. S. Deacon, S. Hartinger, O. Herrmann, T. M. Klapwijk, L. Maier, C. Ames, C. Brüne, C. Gould, A. Oiwa, K. Ishibashi, S. Tarucha, H. Buhmann, and L. W. Molenkamp. 4π-periodic Josephson supercurrent in HgTe-based topological Josephson junctions. *Nat. Commun.*, 7:10303, 2016.

[28] A. Jost, M. Bendias, J. Böttcher, E. Hankiewicz, C. Brüne, H. Buhmann, L. W. Molenkamp, J. C. Maan, U. Zeitler, N. Hussey, and S. Wiedmann. Electron-hole asymmetry of the topological surface states in strained HgTe. *Proc. Natl. Acad. Sci. U.S.A.*, 114(13):3381–3386, 2017.

[29] H. Maier, J. Ziegler, R. Fischer, D. Kozlov, Z. D. Kvon, N. Mikhailov, S. A. Dvoretsky, and D. Weiss. Ballistic geometric resistance resonances in a single surface of a topological insulator. *Nat. Commun.*, 8:2023, 2017.

[30] J. Ziegler, R. Kozlovsky, C. Gorini, M.-H. Liu, S. Weishäupl, H. Maier, R. Fischer, D. A. Kozlov, Z. D. Kvon, N. Mikhailov, S. A. Dvoretsky, K. Richter, and D. Weiss. Probing spin helical surface states in topological HgTe nanowires. *Phys. Rev. B*, 97(3):035157, 2018.

[31] L. W. Molenkamp and M. J. M. de Jong. Electron-electron-scattering-induced size effects in a two-dimensional wire. *Phys. Rev. B*, 49(7):5038–5041, 1994.

[32] M. J. M. de Jong and L. W. Molenkamp. Hydrodynamic electron flow in high-mobility wires. *Phys. Rev. B*, 51(19):13389–13402, 1995.

[33] D. A. Bandurin, I. Torre, R. K. Kumar, M. Ben Shalom, A. Tomadin, A. Principi, G. H. Auton, E. Khestanova, K. S. Novoselov, I. V. Grigorieva, L. A. Ponomarenko, A. K. Geim, and M. Polini. Negative local resistance caused by viscous electron backflow in graphene. *Science*, 351(6277):1055–1058, 2016.

[34] J. Crossno, J. K. Shi, K. Wang, X. Liu, A. Harzheim, A. Lucas, S. Sachdev, P. Kim, T. Taniguchi, K. Watanabe, T. A. Ohki, and K. C. Fong. Observation of the Dirac fluid and the breakdown of the Wiedemann-Franz law in graphene. *Science*, 351(6277):1058–1061, 2016.

[35] P. J. W. Moll, P. Kushwaha, N. Nandi, B. Schmidt, and A. P. Mackenzie. Evidence for hydrodynamic electron flow in $PdCoO_2$. *Science*, 351(6277):1061–1064, 2016.

[36] V. L. Müller, Y. Yan, O. Kashuba, B. Trauzettel, M. Abdelghany, J. Kleinlein, W. Beugeling, H. Buhmann, and L. W. Molenkamp. Electron-hole scattering limited transport of Dirac fermions in a topological insulator. *Nano Lett.*, 21(12):5195–5200, 2021.

[37] T. J. Thornton, M. Pepper, H. Ahmed, D. Andrews, and G. J. Davies. One-dimensional conduction in the 2D electron gas of a GaAs-AlGaAs heterojunction. *Phys. Rev. Lett.*, 56(11):1198–1201, 1986.

[38] B. J. van Wees, H. van Houten, C. W. J. Beenakker, J. G. Williamson, L. P. Kouwenhoven, D. van der Marel, and C. T. Foxon. Quantized conductance of point contacts in a two-dimensional electron gas. *Phys. Rev. Lett.*, 60(9):848–850, 1988.

[39] T. J. Thornton, M. L. Roukes, A. Scherer, and B. P. Van de Gaag. Boundary scattering in quantum wires. *Phys. Rev. Lett.*, 63(19):2128–2131, 1989.

[40] M. J. Mühlbauer. *Nanolithography on Mercury Telluride*. PhD thesis, Julius-Maximilians-Universität Würzburg, 2015.

[41] V. Srivastav, R. Pal, and H. P. Vyas. Overview of etching technologies used for HgCdTe. *Opto-Electron. Rev.*, 13(3):197–211, 2005.

[42] M. K. Bendias. *Quantum Spin Hall Effect – A new generation of microstructures*. PhD thesis, Julius-Maximilians-Universität Würzburg, 2017.

[43] M. K. Bendias. Lithographische Prozessoptimierung und Herstellung von Nanostrukturen zur Untersuchung von Spintransportphänomenen im topologischen Isolator HgTe. M. Sc. thesis, Julius-Maximilians-Universität Würzburg, 2012.

[44] J. L. Elkind. Ion mill damage in n-HgCdTe. *J. Vac. Sci. Technol. B*, 10(4):1460–1465, 1992.

[45] E. Belas, P. Höschl, R. Grill, J. Franc, P. Moravec, K. Lischka, H. Sitter, and A. Toth. Ultrafast diffusion of Hg in $Hg_{1-x}Cd_xTe$ ($x \approx 0.21$). *J. Cryst. Growth*, 138(1):940–943, 1994.

[46] K. Bendias, S. Shamim, O. Herrmann, A. Budewitz, P. Shekhar, P. Leubner, J. Kleinlein, E. Bocquillon, H. Buhmann, and L. W. Molenkamp. High mobility HgTe microstructures for quantum spin Hall studies. *Nano Lett.*, 18(8):4831–4836, 2018.

[47] P. W. Leech, M. H. Kibel, and P. J. Gwynn. The chemical etching of II-VI/GaAs heterostructures in aqueous I:KI:HBr solutions. *J. Electrochem. Soc.*, 137(2):705–707, 1990.

[48] J. Strunz, J. Wiedenmann, C. Fleckenstein, L. Lunczer, W. Beugeling, V. L. Müller, P. Shekhar, N. T. Ziani, S. Shamim, J. Kleinlein, H. Buhmann, B. Trauzettel, and L. W. Molenkamp. Interacting topological edge channels. *Nat. Phys.*, 16(1):83–88, 2020.

[49] H. K. Kuiken, J. J. Kelly, and P. H. L. Notten. Etching profiles at resist edges: I. mathematical models for diffusion-controlled cases. *J. Electrochem. Soc.*, 133(6):1217–1226, 1986.

[50] E. Kratschmer and M. Isaacson. Progress in self-developing metal fluoride resists. *J. Vac. Sci. Technol. B*, 5(1):369, 1987.

[51] A. Scherer and H. G. Graighead. Barium fluoride and strontium fluoride negative electron beam resists. *J. Vac. Sci. Technol. B*, 5(1):374–378, 1987.

[52] A. Scherer, B. P. Van der Gaag, E. D. Beebe, and P. S. D. Lin. Fluoride etch masks for high-resolution pattern transfer. *J. Vac. Sci. Technol. B*, 8(1):28–32, 1990.

[53] J. P. Kar, J. H. Choi, and J. M. Myoung. Feasibility study of barium fluoride films as a sacrificial layer for patterning of ZnO nanowire arrays. *J. Cryst. Growth.*, 311(8):2372–2376, 2009.

[54] J. Strunz. Optimierung von BaF_2-Masken zur Definition von Mikrokanalstrukturen für die Untersuchung hydrodynamischer Effekte in HgTe/HgCdTe-Heterostrukturen. M. Sc. thesis, Julius-Maximilians-Universität Würzburg, 2016.

[55] W. R. Fahrner, U. Hilleringmann, H.-C. Scheer, and A. D. Wieck. Nanostrukturierung. In W. Fahrner, editor, *Nanotechnologie und Nanoprozesse*, pages 167–242. Springer, Berlin, 2017.

[56] J. F. Moulder, W. F. Stickle, P. E. Sobol, and K. D. Bomben. *Handbook of X-ray Photoelectron Spectroscopy.* Perkin-Elmer Corporation, Eden Prairie, 1992.

[57] A. J. Stoltz, J. D. Benson, M. Jaime-Vasquez, P. J. Smith, L. A. Almeida, R. Jacobs, J. Markunas, K. Brogden, A. Brown, C. Lennon, P. Maloney, and N. Supola. A review of the characterization techniques for the analysis of etch processed surfaces of HgCdTe and related compounds. *J. Electron. Mater.*, 43(9):3708–3717, 2014.

[58] A. Zapata-Navarro, M. Zapata-Torres, V. Sosa, P. Bartolo-Perez, and J. L. Peña. CdTe oxide films grown by radio frequency sputtering utilizing argon–nitrous oxide plasma. *J. Vac. Sci. Technol. A*, 12(3):714–717, 1994.

[59] J. B. Varesi, J. D. Benson, M. Jaime-Vasquez, M. Martinka, A. J. Stoltz, and J. H. Dinan. Investigation of HgCdTe surface films and their removal. *J. Electron. Mater.*, 35(6):1443–1448, 2006.

[60] S. Datta. *Electronic Transport in Mesoscopic Systems*. Cambridge University Press, Cambridge, 1995.

[61] J. Hinz, H. Buhmann, M. Schäfer, V. Hock, C. R. Becker, and L. W. Molenkamp. Gate control of the giant Rashba effect in HgTe quantum wells. *Semicond. Sci. Technol.*, 21(4):501–506, 2006.

[62] L. Lunczer, P. Leubner, M. Endres, V. L. Müller, C. Brüne, H. Buhmann, and L. W. Molenkamp. Approaching quantization in macroscopic quantum spin Hall devices through gate training. *Phys. Rev. Lett.*, 123(4):047701, 2019.

[63] A. J. Stoltz. Dry plasma processing of mercury cadmium telluride and related II–VIs. In P. Capper and J. W. Garland, editors, *Mercury Cadmium Telluride: Growth, Properties and Applications*, pages 399–427. Wiley, New York, 2011.

[64] J. M. Werther. Induktiv gekoppeltes Plasmaätzen zur Strukturierung von CdHgTe/HgTe-Heterostrukturen. B. Sc. thesis, Julius-Maximilians-Universität Würzburg, 2017.

[65] M. A. Lieberman and A. J. Lichtenberg. *Principles of Plasma Discharges and Materials Processing*. Wiley, Hoboken, New Jersey, 2005.

[66] E. P. G. Smith, J. K. Gleason, L. T. Pham, E. A. Patten, and M. S. Welkowsky. Inductively coupled plasma etching of HgCdTe. *J. Electron. Mater.*, 32(7):816–820, 2003.

[67] E. Laffosse, J. Baylet, J. P. Chamonal, G. Destefanis, G. Cartry, and C. Cardinaud. Inductively coupled plasma etching of HgCdTe using a CH_4-based mixture. *J. Electron. Mater.*, 34(6):740–745, 2005.

[68] A. J. Stoltz, M. Jaime-Vasquez, J. D. Benson, J. B. Varesi, and M. Martinka. Examination of the effects of high-density plasmas on the surface of HgCdTe. *J. Electron. Mater.*, 35(6):1461–1464, 2006.

[69] F. Boulard, J. Baylet, and C. Cardinaud. Effect of Ar and N_2 addition on CH_4-H_2 based chemistry inductively coupled plasma etching of HgCdTe. *J. Vac. Sci. Technol. A*, 27(4):855–861, 2009.

[70] F. Boulard, J. Baylet, and C. Cardinaud. Influence of cadmium composition on CH_4-H_2-based inductively coupled plasma etching of $Hg_{1-x}Cd_xTe$. *J. Electron. Mater.*, 39(8):1256–1261, 2010.

[71] Y. Li, W. Hu, Z. Ye, Y. Chen, X. Chen, and W. Lu. Direct mapping and characterization of dry etch damage-induced PN junction for long-wavelength HgCdTe infrared detector arrays. *Opt. Lett.*, 42(7):1325–1328, 2017.

[72] L. F. Liu, Y. Y. Chen, Z. H. Ye, X. N. Hu, R. J. Ding, and L. He. Inductively coupled plasma-induced electrical damage on HgCdTe etched surface at cryogenic temperatures. *J. Electron. Mater.*, 47(10):5759–5762, 2018.

[73] D. V. Gorshkov, G. Y. Sidorov, V. S. Varavin, I. V. Sabinina, and M. V. Yakushev. Reconversion of the CdHgTe conductivity type after plasma etching process at low temperature. *Appl. Phys. Lett.*, 116(8):082102, 2020.

[74] V. M. Donnelly and A. Kornblit. Plasma etching: Yesterday, today, and tomorrow. *J. Vac. Sci. Technol. A*, 31(5):050825, 2013.

[75] P. Apte, K. Rybnicek, and A. Stoltz. Macro-loading effects in inductively coupled plasma etched mercury cadmium telluride. *J. Electron. Mater.*, 45(9):4497–4501, 2016.

[76] C. Thienel. *Exploring the transport properties of the three-dimensional topological insulator material HgTe.* PhD thesis, Julius-Maximilians-Universität Würzburg, 2014.

[77] Y. Baum, J. Böttcher, C. Brüne, C. Thienel, L. W. Molenkamp, A. Stern, and E. M. Hankiewicz. Self-consistent k·p calculations for gated thin layers of three-dimensional topological insulators. *Phys. Rev. B*, 89(24):245136, 2014.

[78] A. Inhofer, S. Tchoumakov, B. A. Assaf, G. Fève, J. M. Berroir, V. Jouffrey, D. Carpentier, M. O. Goerbig, B. Plaçais, K. Bendias, D. M. Mahler, E. Bocquillon, R. Schlereth, C. Brüne, H. Buhmann, and L. W. Molenkamp. Observation of Volkov-Pankratov states in topological HgTe heterojunctions using high-frequency compressibility. *Phys. Rev. B*, 96(19):195104, 2017.

[79] D. M. Mahler. *Surface states in the topological material HgTe.* PhD thesis, Julius-Maximilians-Universität Würzburg, Submitted (2021).

[80] D. M. Mahler, V. L. Müller, C. Thienel, J. Wiedenmann, W. Beugeling, H. Buhmann, and L. W. Molenkamp. Massive and topological surface states in tensile-strained HgTe. *Nano Lett.*, 21(23):9869–9874, 2021.

[81] C. R. Becker, C. Brüne, M. Schäfer, A. Roth, H. Buhmann, and L. W. Molenkamp. The influence of interfaces and the modulation doping technique

on the magneto-transport properties of HgTe based quantum wells. *Phys. Stat. Sol. C*, 4(9):3382–3389, 2007.

[82] J. Robertson. High dielectric constant oxides. *Eur. Phys. J. Appl. Phys.*, 28(3):265–291, 2004.

[83] B. J. Van Wees, E. M. M. Willems, L. P. Kouwenhoven, C. J. P. M. Harmans, J. G. Williamson, C. T. Foxon, and J. J. Harris. Suppression of Shubnikov-de Haas resistance oscillations due to selective population or detection of Landau levels: Absence of inter-Landau-level scattering on macroscopic length scales. *Phys. Rev. B*, 39(11):8066–8069, 1989.

[84] B. J. van Wees, L. P. Kouwenhoven, E. M. M. Willems, C. J. P. M. Harmans, J. E. Mooij, H. van Houten, C. W. J. Beenakker, J. G. Williamson, and C. T. Foxon. Quantum ballistic and adiabatic electron transport studied with quantum point contacts. *Phys. Rev. B*, 43(15):12431–12453, 1991.

[85] Stanford Research Systems, Sunnyvale (CA), USA. Analog lock-in amplifier SR124, operation and service manual, 2018.

[86] M. R. Calvo, F. de Juan, R. Ilan, E. J. Fox, A. J. Bestwick, M. Mühlbauer, J. Wang, C. Ames, P. Leubner, C. Brüne, S. C. Zhang, H. Buhmann, L. W. Molenkamp, and D. Goldhaber-Gordon. Interplay of chiral and helical states in a quantum spin Hall insulator lateral junction. *Phys. Rev. Lett.*, 119(22):226401, 2017.

[87] F. Goschenhofer, J. Gerschütz, A. Pfeuffer-Jeschke, R. Hellmig, C. R. Becker, and G. Landwehr. Investigation of iodine as a donor in MBE grown $Hg_{1-x}Cd_xTe$. *J. Electron. Mater.*, 27(6):532–535, 1998.

[88] F. Schmitt. *Transport properties of the three-dimensional topological insulator mercury telluride.* PhD thesis, Julius-Maximilians-Universität Würzburg, In preparation.

[89] J. Ziegler, D. A. Kozlov, N. N. Mikhailov, S. A. Dvoretsky, and D. Weiss. Quantum Hall effect and Landau levels in the 3D topological insulator HgTe. *Phys. Rev. Research*, 2(3):033003, 2020.

[90] S. Shamim, W. Beugeling, J. Böttcher, P. Shekhar, A. Budewitz, P. Leubner, L. Lunczer, E. M. Hankiewicz, H. Buhmann, and L. W. Molenkamp. Emergent quantum Hall effects below 50 mT in a two-dimensional topological insulator. *Sci. Adv.*, 6(26):eaba4625, 2020.

[91] T. Ihn. *Semiconductor Nanostructures.* Oxford University Press, New York, 2010.

[92] Wolfram Research, Inc., Champaign (IL), USA. Mathematica 12, 2019.

[93] X. Ying, S. R. Parihar, H. C. Manoharan, and M. Shayegan. Quantitative determination of many-body-induced interlayer charge transfer in bilayer electron systems via Shubnikov-de Haas measurements. *Phys. Rev. B*, 52(16):R11611–R11614, 1995.

[94] Y. Katayama, D. C. Tsui, H. C. Manoharan, S. Parihar, and M. Shayegan. Charge transfer at double-layer to single-layer transition in double-quantum-well systems. *Phys. Rev. B*, 52(20):14817–14824, 1995.

[95] N. Harrison, J. Caulfield, J. Singleton, P. H. P. Reinders, F. Herlach, W. Hayes, M. Kurmoo, and P. Day. Magnetic breakdown and quantum interference in the quasi-two-dimensional superconductor κ-(BEDT-TTF)$_2$Cu(NCS)$_2$ in high magnetic fields. *J. Phys.: Condens. Matter*, 8(29):5415–5435, 1996.

[96] J. J. Dubowski, T. Dietl, W. Szymańska, and R. R. Gałazka. Electron scattering in Cd$_x$Hg$_{1-x}$Te. *J. Phys. Chem. Solids*, 42(5):351–362, 1981.

[97] A. Pfeuffer-Jeschke. *Bandstruktur und Landau-Niveaus quecksilberhaltiger II-VI-Heterostrukturen.* PhD thesis, Julius-Maximilians-Universität Würzburg, 2000.

[98] E. G. Novik, A. Pfeuffer-Jeschke, T. Jungwirth, V. Latussek, C. R. Becker, G. Landwehr, H. Buhmann, and L. W. Molenkamp. Band structure of semimagnetic Hg$_{1-y}$Mn$_y$Te quantum wells. *Phys. Rev. B*, 72(3):035321, 2005.

[99] kdotpy: Program for k·p band structure calculations. Implemented in Python by W. Beugeling, and currently maintained by F. Bayer and W. Beugeling.

[100] W. Demtröder. *Experimentalphysik 3.* Springer, Berlin, 2010.

[101] D. A. Kozlov, D. Bauer, J. Ziegler, R. Fischer, M. L. Savchenko, Z. D. Kvon, N. N. Mikhailov, S. A. Dvoretsky, and D. Weiss. Probing quantum capacitance in a 3D topological insulator. *Phys. Rev. Lett.*, 116(16):166802, 2016.

[102] Y. Xu, I. Miotkowski, and Y. P. Chen. Quantum transport of two-species Dirac fermions in dual-gated three-dimensional topological insulators. *Nat. Commun.*, 7(1):11434, 2016.

[103] C. Li, B. de Ronde, A. Nikitin, Y. Huang, M. S. Golden, A. de Visser, and A. Brinkman. Interaction between counter-propagating quantum Hall edge channels in the 3D topological insulator BiSbTeSe$_2$. *Phys. Rev. B*, 96(19):195427, 2017.

[104] S. K. Chong, K. B. Han, T. D. Sparks, and V. V. Deshpande. Tunable coupling between surface states of a three-dimensional topological insulator in the quantum Hall regime. *Phys. Rev. Lett.*, 123(3):036804, 2019.

[105] Y. Xu, I. Miotkowski, C. Liu, J. Tian, H. Nam, N. Alidoust, J. Hu, C.-K. Shih, M. Z. Hasan, and Y. P. Chen. Observation of topological surface state quantum Hall effect in an intrinsic three-dimensional topological insulator. *Nat. Phys.*, 10(12):956–963, 2014.

[106] Y. Zhang, K. He, C.-Z. Chang, C.-L. Song, L.-L. Wang, X. Chen, J.-F. Jia, Z. Fang, X. Dai, W.-Y. Shan, S.-Q. Shen, Q. Niu, X.-L. Qi, S.-C. Zhang, X.-C. Ma, and Q.-K. Xue. Crossover of the three-dimensional topological insulator Bi_2Se_3 to the two-dimensional limit. *Nat. Phys.*, 6(8):584–588, 2010.

[107] J. P. Eisenstein and A. H. MacDonald. Bose–Einstein condensation of excitons in bilayer electron systems. *Nature*, 432(7018):691–694, 2004.

[108] B. Seradjeh, J. E. Moore, and M. Franz. Exciton condensation and charge fractionalization in a topological insulator film. *Phys. Rev. Lett.*, 103(6):066402, 2009.

[109] E. E. Mendez, L. Esaki, and L. L. Chang. Quantum Hall effect in a two-dimensional electron-hole gas. *Phys. Rev. Lett.*, 55(20):2216–2219, 1985.

[110] H. Deng, Y. Liu, I. Jo, L. N. Pfeiffer, K. W. West, K. W. Baldwin, and M. Shayegan. Interaction-induced interlayer charge transfer in the extreme quantum limit. *Phys. Rev. B*, 96(8):081102(R), 2017.

[111] L.-X. Wang, F. Schmitt, V. L. Müller, D. M. Mahler, L. Lunczer, W. Beugeling, H. Buhmann, and L. W. Molenkamp. Tunable inter-scattering between counter-propagating quantum Hall edge channels from surface states of a topological insulator. *Manuscript in preparation*, 2021.

[112] C. W. J. Beenakker and H. van Houten. Quantum transport in semiconductor nanostructures. In H. Ehrenreich and D. Turnbull, editors, *Semiconductor Heterostructures and Nanostructures*, volume 44 of *Solid State Physics*, pages 1–228. Academic Press, 1991.

[113] D. Weiss, M. L. Roukes, A. Menschig, P. Grambow, K. von Klitzing, and G. Weimann. Electron pinball and commensurate orbits in a periodic array of scatterers. *Phys. Rev. Lett.*, 66(21):2790–2793, 1991.

[114] E. Ditlefsen and J. Lothe. Theory of size effects in electrical conductivity. *Philos. Mag.*, 14(130):759–773, 1966.

[115] S. Masubuchi, K. Iguchi, T. Yamaguchi, M. Onuki, M. Arai, K. Watanabe, T. Taniguchi, and T. Machida. Boundary scattering in ballistic graphene. *Phys. Rev. Lett.*, 109(3):036601, 2012.

[116] H. Xu and T. Heinzel. Impurity and edge roughness scattering in graphene nanoribbons: The Boltzmann approach. *J. Phys.: Condens. Matter*, 24(45):455303, 2012.

[117] X.-L. Qi and S.-C. Zhang. Topological insulators and superconductors. *Rev. Mod. Phys.*, 83(4):1057–1110, 2011.

[118] W. G. Baber. The contribution to the electrical resistance of metals from collisions between electrons. *Proc. R. Soc. A*, 158(894):383–396, 1937.

[119] C. Kittel. *Introduction to Solid State Physics*. Wiley, New York, 2005.

[120] M. Kaveh and N. Wiser. Electron-electron scattering in conducting materials. *Adv. Phys.*, 33(4):257–372, 1984.

[121] J. Bass, W. P. Pratt, Jr., and P. A. Schroeder. The temperature-dependent electrical resistivities of the alkali metals. *Rev. Mod. Phys.*, 62(3):645–744, 1990.

[122] T. L. Ruthruff, C. G. Grenier, and R. G. Goodrich. Electron-electron scattering in transition metals. *Phys. Rev. B*, 17(8):3070–3073, 1978.

[123] R. N. Gurzhi. Minimum of resistance in impurity-free conductors. *J. Exp. Theor. Phys. Lett.*, 17:521–522, 1963. [*Pis'ma Zh. Eksp. Teor. Fiz.* 44:771–772, 1963].

[124] M. Knudsen. Die Gesetze der Molekularströmung und der inneren Reibungsströmung der Gase durch Röhren. *Ann. Phys.*, 333(1):75–130, 1909.

[125] A. Lucas and K. C. Fong. Hydrodynamics of electrons in graphene. *J. Phys.: Condens. Matter*, 30(5):053001, 2018.

[126] J. A. Sulpizio, L. Ella, A. Rozen, J. Birkbeck, D. J. Perello, D. Dutta, M. Ben-Shalom, T. Taniguchi, K. Watanabe, T. Holder, R. Queiroz, A. Principi, A. Stern, T. Scaffidi, A. K. Geim, and S. Ilani. Visualizing Poiseuille flow of hydrodynamic electrons. *Nature*, 576(7785):75–79, 2019.

[127] M. J. H. Ku, T. X. Zhou, Q. Li, Y. J. Shin, J. K. Shi, C. Burch, L. E. Anderson, A. T. Pierce, Y. Xie, A. Hamo, U. Vool, H. Zhang, F. Casola, T. Taniguchi, K. Watanabe, M. M. Fogler, P. Kim, A. Yacoby, and R. L. Walsworth. Imaging viscous flow of the Dirac fluid in graphene. *Nature*, 583(7817):537–541, 2020.

[128] O. Kashuba. Mathematica script for hydrodynamic flow simulation, 2019.

[129] O. Kashuba, B. Trauzettel, and L. W. Molenkamp. Relativistic Gurzhi effect in channels of Dirac materials. *Phys. Rev. B*, 97(20):205129, 2018.

[130] M. V. Entin, L. I. Magarill, E. B. Olshanetsky, Z. D. Kvon, N. N. Mikhailov, and S. A. Dvoretsky. The effect of electron-hole scattering on transport properties of a 2D semimetal in the HgTe quantum well. *J. Exp. Theor. Phys.*, 117(5):933–943, 2013.

[131] Y. Nam, D.-K. Ki, D. Soler-Delgado, and A. F. Morpurgo. Electron-hole collision limited transport in charge-neutral bilayer graphene. *Nat. Phys.*, 13(12):1207–1214, 2017.

[132] P. F. Maldague and C. A. Kukkonen. Electron-electron scattering and the electrical resistivity of metals. *Phys. Rev. B*, 19(12):6172–6185, 1979.

[133] T. Giamarchi and B. S. Shastry. Baber scattering and resistivity of a two-dimensional two-band model. *Phys. Rev. B*, 46(9):5528–5535, 1992.

[134] M. W. Swift and C. G. Van de Walle. Conditions for T^2 resistivity from electron-electron scattering. *Eur. Phys. J. B*, 90(8):151, 2017.

[135] D. Shoenberg. *Magnetic Oscillations in Metals*. Cambridge University Press, Cambridge, 1984.

[136] T. Neugebauer and G. Landwehr. Determination of the phonon modes involved in the carrier-phonon interaction in silicon inversion layers at low temperatures by nonohmic transport measurements. *Phys. Rev. B*, 21(2):702–708, 1980.

[137] J. F. Qu, S. P. Benz, H. Rogalla, W. L. Tew, D. R. White, and K. L. Zhou. Johnson noise thermometry. *Meas. Sci. Technol.*, 30(11):112001, 2019.

[138] R. Ulbrich. Energy relaxation of photoexcited hot electrons in GaAs. *Phys. Rev. B*, 8(12):5719–5727, 1973.

[139] O. E. Raichev, A. T. Hatke, M. A. Zudov, and J. L. Reno. Bloch-Grüneisen nonlinearity of electron transport in GaAs/AlGaAs heterostructures. *Phys. Rev. B*, 96(8):081407(R), 2017.

[140] M. Srećković, N. Ivanović, O. Žižić, and S. Bojanić. Electrical, optical, and thermodynamical aspects of sound propagation in HgTe, HgSe, $Hg_{1-x}Mn_xSe$, and MnZn spinel ferrites. *J. Electron. Mater.*, 32(4):208–214, 2003.

[141] B. Yan and C. Felser. Topological materials: Weyl semimetals. *Annu. Rev. Condens. Matter Phys.*, 8(1):337–354, 2017.

[142] S. Tarucha, T. Saku, Y. Hirayama, and Y. Horikoshi. Bend-resistance characteristics of macroscopic four-terminal devices with a high electron mobility. *Phys. Rev. B*, 45(23):13465–13468, 1992.

[143] B. Büttner, C. X. Liu, G. Tkachov, E. G. Novik, C. Brüne, H. Buhmann, E. M. Hankiewicz, P. Recher, B. Trauzettel, S. C. Zhang, and L. W. Molenkamp. Single valley Dirac fermions in zero-gap HgTe quantum wells. *Nat. Phys.*, 7(5):418–422, 2011.

[144] A. Kristensen, H. Bruus, A. E. Hansen, J. B. Jensen, P. E. Lindelof, C. J. Marckmann, J. Nygård, C. B. Sørensen, F. Beuscher, A. Forchel, and M. Michel. Bias and temperature dependence of the 0.7 conductance anomaly in quantum point contacts. *Phys. Rev. B*, 62(16):10950–10957, 2000.

[145] A. Löfgren, C. A. Marlow, I. Shorubalko, R. P. Taylor, P. Omling, L. Samuelson, and H. Linke. Symmetry of two-terminal nonlinear electric conduction. *Phys. Rev. Lett.*, 92(4):046803, 2004.

[146] A. S. Price, S. M. Hornett, A. V. Shytov, E. Hendry, and D. W. Horsell. Nonlinear resistivity and heat dissipation in monolayer graphene. *Phys. Rev. B*, 85(16):161411(R), 2012.

[147] M. Mühlbauer, A. Budewitz, B. Büttner, G. Tkachov, E. M. Hankiewicz, C. Brüne, H. Buhmann, and L. W. Molenkamp. One-dimensional weak antilocalization due to the Berry phase in HgTe wires. *Phys. Rev. Lett.*, 112(14):146803, 2014.

[148] P. Leubner. *Strain-engineering of the Topological Insulator HgTe*. PhD thesis, Julius-Maximilians-Universität Würzburg, 2016.

[149] J. H. Bardarson and R. Ilan. Transport in topological insulator nanowires. 2019. arXiv:1906.05192 [cond-mat.mes-hall].

[150] A. Lucas, R. A. Davison, and S. Sachdev. Hydrodynamic theory of thermoelectric transport and negative magnetoresistance in Weyl semimetals. *Proc. Natl. Acad. Sci. U.S.A.*, 113(34):9463–9468, 2016.

[151] J. Gooth, A. C. Niemann, T. Meng, A. G. Grushin, K. Landsteiner, B. Gotsmann, F. Menges, M. Schmidt, C. Shekhar, V. Süß, R. Hühne, B. Rellinghaus, C. Felser, B. Yan, and K. Nielsch. Experimental signatures of the mixed axial-gravitational anomaly in the Weyl semimetal NbP. *Nature*, 547(7663):324–327, 2017.

[152] R. Fletcher. Magnetothermoelectric effects in semiconductor systems. *Semicond. Sci. Technol.*, 14(4):R1–R15, 1999.

[153] M. Thesberg, H. Kosina, and N. Neophytou. On the Lorenz number of multiband materials. *Phys. Rev. B*, 95(12):125206, 2017.

[154] Z. Luo, J. Tian, S. Huang, M. Srinivasan, J. Maassen, Y. P. Chen, and X. Xu. Large enhancement of thermal conductivity and Lorenz number in topological insulator thin films. *ACS Nano*, 12(2):1120–1127, 2018.

Appendix

Appendix A: Recipes

The following pages give a detailed overview of the lithography processes used for this thesis. Note that this list is not complete. Some samples have been fabricated with slightly varying processes. If these deviations are expected to affect the experiments, they are mentioned in the main text.

These recipes are based on existing recipes. Noteworthy are the previous standard Hall bar process and the existing process for wet etched micro-Hall bars, developed in large parts by Dr. K. Bendias, Dr. T. Borzenko, and Dr. J. Kleinlein [42, 46]. Important input came also from P. Shekhar, as well as J. Strunz and J. Werther, and other colleagues working with HgTe.

For the sake of brevity, the following recipes contain several non-standard abbreviations, which are listed in the following:

Resists and developers	
ECI 3012	AZ ECI 3012, MicroChemicals GmbH, Ulm, Germany
AZ 726 MIF	AZ 726 MIF, MicroChemicals GmbH, Ulm, Germany
AR-N 4340	AR-N 4340, Allresist GmbH, Strausberg, Germany
AR 300-47	AR 300-47, Allresist GmbH, Strausberg, Germany
PMMA	950 k 3 %: AR-P 679.03, Allresist GmbH, Strausberg, Germany
PMMA	600 k 6 %: AR-P 669.06, Allresist GmbH, Strausberg, Germany
AR 600-56	AR 600-56, Allresist GmbH, Strausberg, Germany

Other chemicals	
ACE	Acetone
BOE 7:1	Buffered oxide etch, BOE 7-1, Technic, Noyarey, France
Crystalbond	Crystalbond 509, Aremco Products Inc., Valley Cottage (NY), US
Diluted HF	50 % hydrofluoric acid, diluted with DIW
DIW	Deionized water
IPA	Isopropanol
TSP1316	Technistrip P1316, Technic Inc., Cranston (RI), US

Miscellaneous	
AP	Aperture (EBL)
AV	Acceleration voltage (IBE)
EBL	Electron beam lithography
EV	Extraction voltage (IBE)
HP	Hot plate
N2 dry	Remove liquids from sample surface with a nitrogen spray gun
OL	Optical lithography
OM	Optical microscope
PEB	Post exposure bake
SB	Soft bake
USB	Ultrasonic bath
WD	Working distance (EBL)
WF	Writefield (EBL)

Some process steps are highly standardized and always done in a specific tool. The following table provides details for these processes, which are mentioned (without further details) in the recipes.

Inductively coupled plasma (ICP) etching process for CdHgTe	
Tool	PlasmaPro 100, Oxford instruments, Bristol, UK
Process details	Gas flux: 20 sccm Ar, 1 sccm CH_4 Chamber pressure: 13 µbar, Table temperature: 0 °C RF power: 1000 W to ICP coil, 15 W to sample table Duration: depends on desired etch depth

Installing samples in chip carrier	
Samples without back gate	Samples without back gate are glued to the chip carrier with insulating low-temperature GE varnish. Electrical connections are established via wedge bonding on the ohmic contact pads.
Samples with back gate	Samples with back gate are glued to the chip carrier with conducting glue to contact the substrate. Electrical connections to the device are established by gluing gold wires to the ohmic contact pads to avoid breaking the insulating CdTe buffer layer by wedge bonding.

Ion beam etching (IBE)	
Tool	Textra Gen2 plasma source, tectra GmbH, Frankfurt, Germany
Process details	Ar flux, extraction and acceleration voltage are process dependent

Miniclean process in reactive ion etching (RIE) tool	
Tool Process details	Non-commercial RIE tool with parallel plate geometry Gas flux: 50 sccm O_2 Chamber pressure: 50 µbar, Table temperature: room temperature RF power: 23 W to ICP coil Duration: 2 s, starting when the reflected power drops to zero

Plasma-enhanced chemical vapor depostion (PECVD) of gate insulator	
Tool	Plasmalab 80 plus, Oxford instruments, Bristol, UK
Process details (10 nm SiO_2)	Gas flux: 700 sccm N_2O, 150 sccm 5 % SiH_4/N_2 Chamber pressure: 1.3 mbar, Table temperature: 80 °C RF power: 30 W, Duration: 12 s
Process details (10 nm Si_3N_4)	Gas flux: 9 sccm 5 % SiH_4/NH_3, 400 sccm 5 % SiH_4/N_2 Chamber pressure: 1.3 mbar, Table temperature: 80 °C RF power: 20 W, Duration: 12 s

Wet etching process for CdHgTe[1]	
Prepare solution	Mix 37.5 ml DIW, 4.15 g KI, 0.1 g I_2 add 12.5 ml HBr, mix thoroughly dilute KI:I_2:HBr solution with 200 ml DIW
Etching process	The sample is fixed and wet etched under constant flow of wet etching solution

[1]These parameters were optimized by Dr. K. Bendias and P. Shekhar, see References [42, 46].

Recipes for HgTe Hall bars

Recipe H1: Standard dry etching recipe (until 2016) (see References [42] for a more detailed discussion).

A) Preparation	
Cleave wafer with scalpel, inspect sample in OM, clean if necessary	

B) Mesa (with OL)	
Spin-coating	ECI 3012, 20 s at 6000 rpm, SB for 2 min at 80 °C
Exposure 1	5.6 s
Exposure 2	up to 20 s with clearance rectangle
Development	22 s in AZ 726 MIF, stop in DIW, N_2 dry
Etching	Etch through the HgTe layer with IBE
	1.62 sccm Ar flux, 1.0 kV EV and AV, 8 mA emission current
Stripping	10 min in ACE (USB, 37 kHz, 100 % power), keep on 50 °C HP for 30 min
	rinse in IPA, rinse in DIW
	5 min in TSP1316 (USB, 37 kHz, 100 % power), keep on 50 °C HP for 5 min
	rinse in IPA, rinse in DIW, N_2 dry

C) Gate dielectric	
Pause	Keep sample in ambient conditions for one night to restore surface oxide
Deposition	apply 110 nm of SiO_2/Si_3N_4 insulator superlattice (PECVD tool)

D) Top gate (with OL)	
Spin-coating	AR-N 4340, 20 s at 6000 rpm, SB for 2 min at 80 °C
Exposure	20 s
PEB	6 min at 80 °C
Development	35-50 s in AR 300-475, stop in DIW, N_2 dry
Metallization	Deposit 5 nm Ti and 100 nm Au (from the top)
Lift-off	Immerse for 2-3 min in ACE on 50 °C HP, gently hose metal sheet away
	keep in ACE for 2 min, rinse in IPA, DIW, N_2 dry

E) Insulator etching (with OL)	
Spin-coating	ECI 3012, 20 s at 6000 rpm, SB for 2 min at 80 °C
Exposure	7 s
Development	22 s in AZ 726 MIF, stop in DIW, N_2 dry
Etching	13 s in BOE 7:1, stop in DIW and rinse thoroughly, N_2 dry
Stripping	rinse in ACE, rinse in IPA, rinse in DIW, N_2 dry

F) Ohmic contacts (with OL)	
Spin-coating	AR-N 4340, 20 s at 6000 rpm, SB for 2 min at 80 °C
Exposure	20 s
PEB	6 min at 80 °C
Development	35-50 s in AR 300-475, stop in DIW, N_2 dry
Cleaning	Etch 20 nm close to the HgTe layer with IBE
	3.5 sccm Ar flux, 0.4 kV EV and AV, 8 mA emission current
Metallization	Deposit (in situ) 50 nm AuGe and 50 nm Au, under 30° (from two sides)
Lift-off	Immerse for 2-3 min in ACE on 50 °C HP, gently hose metal sheet away
	keep in ACE for 2 min, rinse in IPA, DIW, N_2 dry

G) Glue sample to chip carrier and bond sample

Recipe H2: Standard dry etching recipe (2016 to 2019), using a BaF_2 etch mask

A) Preparation	
Cleave wafer with scalpel, inspect sample in OM, clean if necessary	
B) Mesa (with OL)	
Spin-coating	AR-N 4340, 20 s at 6000 rpm, SB for 2 min at 80 °C
Exposure	20 s
PEB	6 min at 80 °C
Development	40 s in AR 300-475, stop in DIW, N_2 dry
Mask deposition	Deposit 100 nm BaF_2
Lift-off	3 min in ACE (USB, 37 kHz, 100 % power), rinse in IPA, N_2 dry (if drying residues are visible, clean in ACE and IPA again)
Etching[2]	Etch through the HgTe layer with IBE 1.62 sccm Ar flux, 1.0 kV EV and AV, 8 mA emission current
Stripping	5 min in DIW (USB, 37 kHz, 100 % power), N_2 dry
C) Gate dielectric	
Cleaning	Descumming with miniclean program (RIE tool)
Deposition	apply 110 nm of SiO_2/Si_3N_4 insulator superlattice (PECVD tool)
D) Top gate (with OL): Same as Recipe H1	
E) Insulator etching (with OL): Same as Recipe H1	
F) Ohmic contacts (with OL): Same as Recipe H1	
G) Glue sample to chip carrier and bond sample	

Recipe H3: Wet-etched Hall bars

A) Preparation	
Cleave wafer with scalpel, inspect sample in OM, clean if necessary	
B) Mesa (with OL)	
Spin-coating	ECI 3012, 20 s at 6000 rpm, SB for 2 min at 80 °C
Exposure 1	5.6 s
Exposure 2	20 s with clearance rectangle
Development	25 s in AZ 726 MIF, stop in DIW, N_2 dry
Etching	Etch in standard wet solution, stop in DIW
Stripping	5 min in ACE on 50 °C HP, rinse in IPA, rinse in DIW, N_2 dry
C) Gate dielectric: Same as Recipe H2	
D) Top gate (with OL): Same as Recipe H1	
E) Insulator etching (with OL): Same as Recipe H1	
F) Ohmic contacts (with OL): Same as Recipe H1	
G) Glue sample to chip carrier and bond sample	

[2] The same recipe can been used for etching with the standard ICP etching process. In this case, the BaF_2 etch mask has to be reinforced with Ti and the stripping procedure extended to 15 min in DIW (USB, 37 kHz, 100 % power).

Recipes for HgTe microstructures

Recipe M1: ICP-etched channel samples with outer contacts only

A) Preparation	
Cleave wafer with scalpel, inspect sample in OM, clean if necessary	
B) Mesa (with EBL)	
Spin-coating	PMMA (950 k, 3 %), 40 s at 5000 rpm, SB for 30 min at 80 °C
Exposure	7 mm WD, 204.8 µm WF, 2.5 kV AV, 20 µm AP, 90 µC/cm^2 dose
Development	60 s in AR600-56:IPA (1:1), 60 s rinse in IPA, N_2 dry
Mask deposition	Deposit 80 nm BaF_2 and (in situ) 10 nm Ti
Lift-off	10 min in ACE (USB, 37 kHz, 100 % power), rinse in IPA, N_2 dry
Etching	Fix sample to carrier wafer with crystalbond etch with ICP etching process for CdHgTe
Stripping	15 min in DIW (USB, 37 kHz, 100 % power, 50 °C), rinse with DIW, N_2 dry
C) Gate dielectric	
Cleaning	Descumming with miniclean program (RIE tool)
Deposition	apply 110 nm of SiO_2/Si_3N_4 insulator superlattice (PECVD tool)
D) Top gate (inner part, with EBL)[3]	
Spin-coating	PMMA (600 k, 6 %), 40 s at 5000 rpm, SB for 10 min at 80 °C
Exposure	10 mm WD, 204.8 µm WF, 6.5 kV AV, 30 µm AP, 310 µC/cm^2 dose
Development	70 s in AR600-56:IPA (1:1), 60 s rinse in IPA, N_2 dry
Cleaning	Descumming with miniclean program (RIE tool)
Metallization	Deposit 10 nm Ti and 200 nm Au under 30° (from two sides)
Lift-off	Immerse for 10 min in ACE, gently hose metal sheet away rinse in IPA, DIW, N_2 dry
E) Top gate (outer contacts, with OL)	
Spin-coating	AR-N 4340, 20 s at 6000 rpm, SB for 2 min at 80 °C
Exposure	20 s
PEB	6 min at 80 °C
Development	40 s in AR 300-475, stop in DIW, N_2 dry
Cleaning	Descumming with miniclean program (RIE tool)
Metallization	Deposit 10 nm Ti and 200 nm Au (from the top)
Lift-off	Immerse for 5 min in ACE, gently hose metal sheet away rinse in IPA, DIW, N_2 dry
F) Ohmic contacts (outer contacts, with OL)	
Spin-coating	AR-N 4340, 20 s at 6000 rpm, SB for 2 min at 80 °C
Exposure	20 s
PEB	6 min at 80 °C
Development	40 s in AR 300-475, stop in DIW, N_2 dry
Cleaning	Descumming with miniclean program (RIE tool)
Etching	13 s in BOE 7:1, stop in DIW and rinse thoroughly, N_2 dry
Cleaning	Etch 20 nm close to the HgTe layer with IBE 3.5 sccm Ar flux, 0.4 kV EV and AV, 8 mA emission current
Metallization	Deposit (in situ) 50 nm AuGe and 50 nm Au, under 30° (from two sides)
Lift-off	Immerse for 5 min in ACE, gently hose metal sheet away rinse in IPA, DIW, N_2 dry
G) Glue sample to chip carrier and bond sample	

[3]The top gate lift-off process with PMMA (600 k, 6 %) was developed by P. Shekhar.

Recipe M2: wet-etched channel samples with outer contacts only

A1) Preparation	
Cleave wafer with scalpel, inspect sample in OM, clean if necessary	
A2) In removal (only for samples on GaAs substrates)[4]	
Spin-coating	ECI 3012, 20 s at 6000 rpm, SB for 4 min at 80 °C
Removal 1	mechanically scrape In from the backside of the sample
Cleaning	10 min in ACE (USB, 80 kHz, 80 % power), rinse in IPA, rinse in DIW, N_2 dry
Spin-coating	ECI 3012, 20 s at 6000 rpm, SB for 6 min at 80 °C
Removal 2	Immerse sample in HCl for 2 min, repeat until no bubbles are forming rinse in DIW, N_2 dry
Cleaning	10 min in ACE (USB, 80 kHz, 80 % power), rinse in IPA, rinse in DIW, N_2 dry

B1) Inner mesa (with EBL)	
Spin-coating	PMMA (950 k, 3 %), 40 s at 5000 rpm, SB for 30 min at 80 °C
Exposure	7 mm WD, 204.8 µm WF, 2.5 kV AV, 20 µm AP, 100 µC/cm^2 dose
Development	60 s in AR600-56:IPA (1:1), 60 s rinse in IPA, N_2 dry
Cleaning	Descumming with miniclean program (RIE tool)
Oxide removal	Immerse sample in diluted HF (1:200) for 50 s, rinse in DIW
Etching	Etch in standard wet solution, stop in DIW
Stripping	10 min in ACE on 50 °C HP, rinse in IPA, rinse in DIW, N_2 dry
B2) Outer mesa (with OL)	
Spin-coating	ECI 3012, 20 s at 6000 rpm, SB for 2 min at 80 °C
Exposure	10 s
Development	25 s in AZ 726 MIF, stop in DIW, N_2 dry
Etching	Etch in standard wet solution, stop in DIW
Stripping	5 min in ACE on 50 °C HP, rinse in IPA, rinse in DIW, N_2 dry

C) Gate dielectric: Same as Recipe M1

D) Top gate (inner part, with EBL): Same as Recipe M1

E) Top gate (outer contacts, with OL): Same as Recipe M1

F) Ohmic contacts (outer contacts, with OL): Same as Recipe M1

G) Glue sample to chip carrier and bond sample: Same as Recipe M1

[4] The process for In removal was developed by S. Upadhyay, P. Shekhar, and F. Schmitt.

Recipe M3: ICP-etched channel samples with inner contacts

A) Preparation: Same as Recipe M1	
B) Mesa (with EBL): Same as Recipe M1	
C) Ohmic contacts (inner contacts, with EBL)	
Spin-coating	PMMA (600 k, 6 %), 40 s at 5000 rpm, SB for 10 min at 80 °C
Exposure	10 mm WD, 204.8 µm WF, 6.5 kV AV, 30 µm AP, 310 µC/cm^2 dose
Development	70 s in AR600-56:IPA (1:1), 60 s rinse in IPA, N_2 dry
Cleaning	Etch 20 nm close to the HgTe layer with IBE 3.5 sccm Ar flux, 0.4 kV EV and AV, 8 mA emission current
Metallization	Deposit (in situ) 50 nm AuGe and 50 nm Au, under 30° (from two sides)
Lift-off	Immerse for 10 min in ACE, gently hose metal sheet away rinse in IPA, DIW, N_2 dry
D) Gate dielectric: Same as step C) in Recipe M1	
E) Top gate (inner part, with EBL): Same as step D) in Recipe M1	
F) Top gate (outer contacts, with OL): Same as step E) in Recipe M1	
G) Ohmic contacts (outer contacts, with OL)	
Spin-coating	AR-N 4340, 20 s at 6000 rpm, SB for 2 min at 80 °C
Exposure	20 s
PEB	6 min at 80 °C
Development	40 s in AR 300-475, stop in DIW, N_2 dry
Cleaning	Descumming with miniclean program (RIE tool)
Etching	13 s in BOE 7:1, stop in DIW and rinse thoroughly, N_2 dry
Metallization	Deposit 10 nm Ti and 200 nm Au, under 30° (from two sides)
Lift-off	Immerse for 5 min in ACE, gently hose metal sheet away rinse in IPA, DIW, N_2 dry
E) Glue sample to chip carrier and bond sample	

Recipe M4: Wet-etched channel samples with inner contacts

A1) Preparation: Same as Recipe M2
A2) In removal (only for samples on GaAs substrates): Same as Recipe M2
B1) Inner mesa (with EBL): Same as Recipe M2
B2) Outer mesa (with OL): Same as Recipe M2
C) Ohmic contacts (inner contacts, with EBL): Same as Recipe M3
D) Gate dielectric: Same as step C) in Recipe M1
E) Top gate (inner part, with EBL): Same as step D) in Recipe M1
F) Top gate (outer contacts, with OL): Same as step E) in Recipe M1
G) Ohmic contacts (outer contacts, with OL): Same as Recipe M3
E) Glue sample to chip carrier and bond sample

Appendix B: List of material

The following table gives an overview of the CdHgTe/HgTe wafers used in this thesis. The table indicates the substrate for growing the heterostructure, the thicknesses of the CdHgTe and HgTe layers (denoted d_{CdHgTe} and d_{HgTe}, respectively), as well as the colleague growing the material and the growth date. The substrate may either be a commercial CdTe or $\mathrm{Cd_{0.96}Zn_{0.04}Te}$ wafer, a relaxed CdTe buffer layer MBE-grown on a GaAs wafer (denoted VS-CdTe), or a $\mathrm{CdTe/Cd_{0.5}Zn_{0.5}Te}$ superlattice grown on a GaAs wafer (denoted SLS-CdTe/CdZnTe). Note that the MBE-growth of the CdHgTe/HgTe heterostructure may include additional layers, which are not mentioned explicitly in the following table. An I-doped barrier layer is denoted as $d_{\mathrm{CdHgTe}}/d_{\mathrm{CdHgTe}} : I/d_{\mathrm{CdHgTe}}$, where $d_{\mathrm{CdHgTe}} : I$ is the thickness of the I-doped layer.

Note that wafers *Q2971*, *QC0364*, and *QC0441* appear in this thesis only for the purpose of lithography tests. All other wafers were used to build transport devices.

The colleagues who grew the material are Dr. C. Ames (CA), L. Fürst (LF), Dr. P. Leubner (PL), L. Lunczer (LL), and Dr. R. Schlereth (RS).

Wafer	Substrate	Bot. barrier d_{CdHgTe} (nm)	HgTe d_{HgTe} (nm)	Cap layer d_{CdHgTe} (nm)	Grower	Growth date
Q2696	CdTe	75	73	75	PL	01.12.2012
Q2733	VS-CdTe	100	7.5	50	CA	22.05.2013
Q2808	VS-CdTe	50	70	50	CA	21.03.2014
Q2823	VS-CdTe	50	70	10	CA	26.06.2014
Q2843	VS-CdTe	80	70	80	CA/RS	05.11.2014
Q2958	CdTe	75	9.5	75	RS/LF	27.03.2017
Q2959	CdTe	72.5	9.5	72.5	RS/LF	28.03.2017
QC0327	CdZnTe	93	9	93	LL	06.08.2015
QC0331	CdZnTe	81	8	81	PL	14.08.2015
QC0332	CdZnTe	100	8	100	PL	21.08.2015
QC0333	CdZnTe	150	7.5	50	PL	09.09.2015
QC0336	CdZnTe	124	9.2	42	LL	17.09.2015
QC0340	SLS-CdTe/ CdZnTe	10	120	10	PL/LL	30.09.2015
QC0501	CdTe	18/9/65	67	49.5	LL	04.07.2018
QC0502	CdTe	19/10/67	67	50	LL	05.07.2018
QC0509	VS-CdTe	75	75	75	LL	09.08.2018
Q2971	VS-CdTe	200	-	-	RS/LF	11.05.2017
QC0364	VS-CdTe	360	-	-	LL	04.03.2016
QC0441	VS-CdTe	70/10/70	9	50	LL	08.08.2017

Appendix C: List of samples

The table on the following page gives an overview of the samples for transport experiments, which appear in this thesis. Each sample name includes the corresponding wafer number and a unique sample name.

Sample *Q2733 HB* was fabricated by S. Hartinger, and samples *QC0327 HB 1*, *QC0327 HB 2*, *QC0332 HB 1*, *QC0332 HB 2*, *QC0336 HB 1*, and *QC0336 HB 2* were fabricated by J. Strunz. All other samples were fabricated by V. L. Müller.

The table provides information about the dimensions of transport devices on a sample, the date on which the sample fabrication was started, the etch mask and etching method for structuring the mesa, as well as other important information. The listed device dimensions refer to dimensions in between voltage probes in 4-terminal measurements. Device dimensions in brackets indicate that the device can be measured only in a 2-terminal configuration. If not mentioned otherwise, the samples were equipped with a top gate stack including a SiO_2/Si_3N_4 insulator layer, deposited by PECVD. "OG yes" indicates that the device is equipped with inner AuGe/Au ohmic contacts and an overlapping top gate design. "OG no" indicates that the ohmic contacts are far from the top gate, resulting in ungated mesa areas. The latter is the standard design and not mentioned explicitly for all Hall bar samples.

Sample	Dev. Dim. µm	Fabr. start	Etching Mask	Etching Method	Remarks
Hall bar samples, fabricated by optical lithography					
Q2696 HB ICP	200x600, 10x30	17.04.2018	BaF_2/Ti	ICP	
Q2733 HB	200x600, 10x30	05.08.2013	ECI3012	IBE	Old HB design
Q2843 HB IBE	200x600, 10x30	15.11.2017	BaF_2/Ti	IBE	
Q2843 HB ICP	200x600, 10x30	15.11.2017	BaF_2/Ti	ICP	
Q2843 HB ICP 2	200x600, 200x600	01.03.2019	BaF_2/Ti	ICP	HfOx insulator, new 8-term. HB design
Q2958 HB 1	200x600, 10x30	06.04.2017	BaF_2	IBE	
Q2958 HB 2	200x600, 10x30	06.04.2017	BaF_2	ICP	
Q2958 HB 3	200x600, 10x30	29.11.2018	ECI3012	wet	
Q2959 HB 1	200x600, 10x30	06.04.2017	BaF_2	IBE	
Q2959 HB 2	200x600, 10x30	06.04.2017	BaF_2	ICP	
Q2959 HB 3	200x600, 10x30	29.11.2018	ECI3012	wet	
QC0327 HB 1	200x600, 10x30	20.01.2016	ECI3012	IBE	Small HB: Shorted
QC0327 HB 2	200x600, 10x30	16.02.2016	BaF_2	IBE	
QC0331 HB 1	200x600, 10x30	17.02.2016	BaF_2	IBE	
QC0331 HB 2	200x600, 10x30	17.02.2016	ECI3012	IBE	
QC0332 HB 1	200x600, 10x30	22.02.2016	ECI3012	IBE	
QC0332 HB 2	200x600, 10x30	22.02.2016	BaF_2	IBE	
QC0333 HB 1	200x600, 10x30	22.02.2016	BaF_2	IBE	
QC0333 HB 2	200x600, 10x30	22.02.2016	ECI3012	IBE	
QC0336 HB 1	200x600, 10x30	14.03.2016	ECI3012	IBE	
QC0336 HB 2	200x600, 10x30	14.03.2016	BaF_2	IBE	
QC0501 HB ICP	200x600, 10x30	25.07.2018	BaF_2/Ti	ICP	Big HB: One current contact not working
QC0502 HB ICP	200x600, 10x30	25.07.2018	BaF_2/Ti	ICP	
QC0509 HB ICP 1	200x600, 10x30	05.09.2018	BaF_2/Ti	ICP	
Channel samples, fabricated by electron beam and optical lithography					
Q2696 ch 1	16x160, 8x80, 4x40, 2x20	13.01.2017	PMMA	wet	OG yes, HfOx insulator, 2 µm channel: shorted
Q2696 ch 2	16x160, 8x80, 4x40, 2x20	10.02.2017	BaF_2	IBE	OG yes
Q2733 ch ICP A	1x5/(1x10), 2x10/(2x20)	01.02.2018	BaF_2/Ti	ICP	OG yes, 1 µm channel: gate not working
Q2808 ch ICP B	1x5, 2x10	11.06.2017	BaF_2	ICP	OG yes
Q2823 ch ICP B	2x10/(2x20), 4x20/(4x40)	21.12.2017	BaF_2/Ti	ICP	OG no
Q2823 ch noise 1	4x20/(4x40), (10x10), (4x40)	07.06.2018	BaF_2/Ti	ICP	OG yes
QC0336 ch 2	2x20,4x20	26.09.2016	PMMA	wet	OG yes, 4 µm channel: gate not working
QC0336 ch ICP	1x5, 2x10	25.04.2017	BaF_2	ICP	OG yes
QC0340 ch ICP 1	2x10/(2x20), 4x20/(4x40)	15.10.2018	BaF_2/Ti	ICP	OG no
QC0509 ch ICP 2	2x10/(2x20), (0.5x5), (1x10), (2x20)	27.02.2019	BaF_2/Ti	ICP	OG no
QC0509 ch ICP 3	16x160, 2x80, 1x40, 0.5x20	14.03.2019	BaF_2/Ti	ICP	OG yes, EBL only for mesa, 16 µm channel: shorted, 1 µm channel: only one voltage probe working
QC0509 ch wet 1	2x10/(2x20), (0.5x5), (1x10), (2x20)	19.02.2019	PMMA	wet	OG no, AR not as intended due to wet etching
Other samples					
QC0340 Wthpow D	island: 3x5	07.06.2018	BaF_2/Ti	ICP	OG yes

Appendix D: Details of transport measurements

The following appendix provides experimental details regarding the transport measurements for this thesis.

Different cryostats were used for these experiments: A ^{4}He bath cryostat ("5T") for measurements at a fixed temperature of 4.2 K, several ^{4}He cryostats with a variable temperature insert for measurements at ≈ 1.4 K and higher temperatures ("Gilgamesh", "Long John", "10T", "King Louie"), and a ^{3}He/^{4}He dilution refrigerator for measurements at ≈ 25 mK and ≈ 150 mK ("18T").

The measurements of longitudinal and transverse resistance were done according to Figure 3.5b). The total excitation voltage over the reference resistor and the sample was either a DC voltage on the order of 10 mV, or an AC voltage on the order of 200 µV to 2 mV and frequencies of ≈ 13 Hz, ≈ 37 Hz or ≈ 113 Hz, depending on the sample resistance. DC excitation and gate voltages were supplied either with dedicated computer cards or voltage supplies and appropriate low-pass filters as needed. AC excitation voltages were supplied with the reference output of the lock-in amplifiers used for the measurement. For differential resistance measurements, a small AC voltage on the order of ≈ 100 µV to ≈ 1 mV was superimposed onto the DC excitation voltage by means of a transformer. DC voltages were measured with tabletop digital multimeters (Agilent 34420A, Agilent Technologies, Loveland (CO), USA; or Keysight 34460A, Keysight Technologies, Loveland (CO), USA; or Agilent 34970A, Agilent Technologies, Loveland (CO), USA) via high-input-impedance preamplifiers (gain 1x, home-built). AC voltages were measured with analog lock-in amplifiers (SR124, Stanford Research Systems, Sunnyvale (CA), USA; or PAR124A, EG&G Princeton Applied Research, Princeton (NJ), USA) in combination with tabletop digital multimeters (see above).

The table on the following page lists the setup(s) used for the measurements discussed in this thesis and whether these measurements were performed with DC excitation, AC excitation, or DC+AC excitation (for differential resistance measurements). Sample *Q2823 ch noise 1* is not listed here. It was measured in a setup dedicated to Johnson noise thermometry measurements, which is briefly described in Section 12.2.3.

Sample	Setup	Measurement type(s)
Hall bar samples		
Q2696 HB ICP	18T	AC
Q2733 HB	5T	DC
Q2843 HB IBE	10T	DC
Q2843 HB ICP	10T	DC
Q2843 HB ICP 2	18T	AC
Q2958 HB 1	5T	DC
Q2958 HB 2	5T	DC
Q2958 HB 3	5T	DC
Q2959 HB 1	5T	DC
Q2959 HB 2	5T	DC
Q2959 HB 3	5T	DC
QC0327 HB 1	5T	DC
QC0327 HB 2	5T	DC
QC0331 HB 1	5T	DC
QC0331 HB 2	5T	DC
QC0332 HB 1	5T	DC
QC0332 HB 2	5T	DC
QC0333 HB 1	5T	DC
QC0333 HB 2	5T	DC
QC0336 HB 1	5T	DC
QC0336 HB 2	5T	DC
QC0501 HB ICP	18T	AC
QC0502 HB ICP	18T	AC
QC0509 HB ICP 1	Gilgamesh	AC
Channel samples		
Q2696 ch 1	Gilgamesh	AC
Q2696 ch 2	Gilgamesh	AC
Q2733 ch ICP A	King Louie	AC, DC+AC
Q2808 ch ICP B	Gilgamesh	AC, DC
Q2823 ch ICP B	Long John, King Louie	AC, DC+AC
QC0336 ch 2	Gilgamesh	AC
QC0336 ch ICP	Gilgamesh	AC
QC0340 ch ICP 1	Gilgamesh	AC, DC+AC
QC0509 ch ICP 2	Gilgamesh	AC, DC+AC
QC0509 ch ICP 3	Gilgamesh	AC
QC0509 ch wet 1	Gilgamesh	AC

List of publications

The following list contains all peer-reviewed journal articles, which I have been working on as a coauthor as part of my PhD project. The list does not contain manuscripts which are submitted or in preparation, but not published yet.

- L. Lunczer, P. Leubner, M. Endres, **V. L. Müller**, C. Brüne, H. Buhmann, and L. W. Molenkamp. Approaching quantization in macroscopic quantum spin Hall devices through gate training. *Phys. Rev. Lett.*, 123(4):047701, 2019.

- J. Strunz, J. Wiedenmann, C. Fleckenstein, L. Lunczer, W. Beugeling, **V. L. Müller**, P. Shekhar, N. T. Ziani, S. Shamim, J. Kleinlein, H. Buhmann, B. Trauzettel, and L. W. Molenkamp. Interacting topological edge channels. *Nat. Physics*, 16(1):83–88, 2020.

- **V. L. Müller**[1], Y. Yan[1], O. Kashuba, B. Trauzettel, M. Abdelghany, J. Kleinlein, W. Beugeling, H. Buhmann, and L. W. Molenkamp. Electron-hole scattering limited transport of Dirac fermions in a topological insulator. *Nano Lett.*, 21(12):5195–5200, 2021.

- D. M. Mahler, **V. L. Müller**, C. Thienel, J. Wiedenmann, W. Beugeling, H. Buhmann, and L. W. Molenkamp. Massive and topological surface states in tensile-strained HgTe. *Nano Lett.*, 21(23):9869–9874, 2021.

[1] These authors contributed equally.

Acknowledgments

Scientific progress is hardly ever the achievement of a single, isolated person. The thesis at hand is the result of a long, and sometimes challenging, process. Many people contributed to the work, either very directly or due to their more general support. At this point I would like to thank all of you. I am especially grateful to

- Prof. Laurens Molenkamp for accepting me as Ph. D. student at your chair and for your guidance throughout this project.
- Prof. Hartmut Buhmann, my “Doktorvater”, for your continuous support and guidance at every step of this dissertation. My understanding of the physics involved has greatly improved through the numerous discussions we had. At the same time, your open and friendly manner has set the framework for the collaborative way of working with all members of your group. I also appreciate your willingness to initiate, support, and be an active member of the “legendary” EP3-band, the successor of which is still an important part of my life outside the university.
- Prof. Björn Trauzettel for your invaluable and persistent support for interpreting and modeling our experimental results. Our discussions greatly benefited from your constructive attitude and your ability to translate between theoretical and experimental physicists. Thank you also for accepting to be the second referee of the thesis committee.
- Prof. Friedrich Reinert for accepting to be the third referee for the defense.
- Dr. Johannes Kleinlein for teaching me so much about lithography and your continuous guidance with every lithography-related issue. The lithography part of this thesis is based on your suggestions and ideas.
- Dr. Yuan Yan for the fruitful collaboration to understand HgTe-based microstructures and the help in the lab. Thank you for setting up the system and performing thermal noise measurements, which turned out to be a crucial ingredient for understanding our results.
- Dr. Oleksiy (”Alex“) Kashuba for providing sound theoretical (and moral) support when we struggled to understand HgTe microstructures. Thank you for your refreshing way of looking at things.
- Dr. Wouter Beugeling for sharing your powerful, yet very user-friendly, band structure calculation program with us. My understanding of the HgTe band structure and our experimental results benefited considerably from the band structure results and related discussions with you.
- Dr. Li-Xian Wang for many fruitful discussions about HgTe 3D TIs.

- Dr. Tanja Borzenko for providing lithography-related help whenever needed.
- Dr. Mohamed Abdelghany for your help in setting up the noise measurement system and understanding the experimental results.
- David Mahler; starting from my first day in EP3 you have been a great mentor and colleague. It was actually you who introduced me to many of the practical aspects of our work in the lab, and I could always rely on your help. We also had a good amount of fruitful discussions about physics and I learned a lot from you about solid state physics and HgTe in particular.
- The MBE-experts, who have grown the HgTe layers which are literally the basis for all experimental results in this thesis: Dr. Christopher Ames, Lena Fürst, Dr. Phillip Leubner, Lukas Lunczer, and Dr. Raimund Schlereth.
- Pragya Shekhar, you have been a great colleague to share an office with. Thank you for numerous discussions about lithography, physics, and everything else. Too bad that we had to spent so much time in home office!
- Jonas Strunz and Julian Werther, for your great help in improving lithographic techniques as part of your master's and bachelor's theses, respectively. It was a pleasure to work with you!
- My fellow Ph. D. students and postdoctoral researchers who supported me by kindly sharing their invaluable experience, especially: Andreas Budewitz, Simon Hartinger, and Dr. Saquib Shamim.
- All the people who persistently keep the lab infrastructure running and the physicists from breaking things (– not always successfully unfortunately...), especially: Volkmar Hock, thank you for fixing every imaginable (!) issue in the cleanroom and for sharing your healthy sense of humor with your colleagues; Carmen Bundschuh and Petra Wolf-Müller, thank you for your practical help in the cleanroom; Roland Ebert and Cornelius Ziga, thank you for reliably providing liquid Helium and good advice in the transport labs.
- Angelika Berger for your support with all the – sometimes confusing – organizational issues related to the work at the university.
- All my other nice colleagues at the university, who created a supportive and pleasant work atmosphere.

Lastly, but most importantly, I would like to thank my family for supporting me in so many different ways. Pauline, thank you for sharing your life with me, for being my most important companion, and for patiently encouraging me through all the highs and lows I encountered in the last couple of years. Fridolin, thank you for bringing us unlimited happiness and for reminding us of what is truly important in life. Mama, Johannes, Anke, Leonhard, Ulrike, Christian, and Henny, thank you for your genuine interest in my project and your moral support. Henny and Pauline, thank you for "fearlessly" proof-reading this thesis with great care. I am very lucky to have such a great family!